DYNAMIC MASKLESS HOLOGRAPHIC LITHOGRAPHY AND APPLICATIONS

by

Daniel R. McAdams

B.S. in Physics, Pennsylvania State University, 2006

M.S. in Mechanical Engineering, University of Pittsburgh, 2009

Submitted to the Graduate Faculty of

the Swanson School of Engineering in partial fulfillment

of the requirements for the degree of

Doctor of Philosophy

University of Pittsburgh

2012

UNIVERSITY OF PITTSBURGH

SWANSON SCHOOL OF ENGINEERING

This dissertation was presented

by

Daniel R. McAdams

It was defended on

August 21, 2012

and approved by

Daniel G. Cole, Ph. D., Professor

Sung Kwon Cho, Ph. D., Professor

William W. Clark, Ph. D., Professor

Kevin P. Chen, Ph. D., Professor

Dissertation Director: Daniel G. Cole, Ph. D., Professor

DYNAMIC MASKLESS HOLOGRAPHIC LITHOGRAPHY AND APPLICATIONS

Daniel R. McAdams, PhD

University of Pittsburgh, 2012

The purpose of this research is to improve the resolution of dynamic maskless holographic lithography (DMHL) by using two-photon absorption, to provide a more thorough characterization of the process, and to expand the functionality of the process by adding previously undemonstrated patterning modes. Two-photon DMHL will be performed in both 2D and 3D configurations with specific characterization relating to process resolution and repeatability. The physical limits of DMHL will be discussed and ways to circumvent them will be proposed and tested.

DMHL eliminates the need for a separate mask for every different pattern exposure and allows for real-time shaping of the exposure pattern. It uses an electrically addressable spatial light modulator (SLM) to create an arbitrary intensity pattern at the specimen plane. The SLM is a phase mask that displays a hologram. An algorithm is used to find an appropriate phase hologram for each desired intensity pattern. Each pixel of the SLM shapes the wavefront of the incoming laser light so that the natural Fourier transforming property of a lens causes the desired image to appear in the specimen plane. The process enables one-off projects to be done without the cost of fabricating a mask, and makes it possible to perform lithography with fewer (or even no) moving parts.

TABLE OF CONTENTS

1.0 INTRODUCTION 1

1.1 State of the Art and Background 4

1.1.1 DMHL 4

1.1.1.1 DMHL State of the Art 4

1.1.1.2 DMHL Background 5

1.1.2 Two-photon Absorption 8

1.2 Research Objectives 12

1.2.1 Objectives 12

1.3 Research Impact 14

1.4 Document Structure 15

2.0 HOLOGRAPHY THEORY 16

2.1 Gratings for Serial Patterning 18

2.1.1 The Grating Equation 18

2.1.2 Diffraction Gratings 19

2.1.3 Diffraction pattern due to grid of pixels 25

2.1.4 Phase gratings 26

2.1.4.1 Sinusoidal Phase Grating 28

2.1.4.2 Blazed phase grating 29

2.2 Fresnel lenses for serial patterning 35

2.2.1 Gratings and Lenses 36

2.3 Gerchberg Saxton Algorithm for 2D Parallel Patterning 37

2.4 Multiplexing holograms (Moving from Parallel 2D to Parallel 3D Exposures) 39

2.5 Creating 3D Light Intensity Patterns for 3D Parallel Patterning 40
2.5.1 3D Parallel Patterning with Gratings and Lenses 41
2.5.2 3D Gerchberg Saxton algorithm for 3D Parallel Patterning 41
2.5.2.1 3DGS Implementation 44
3.0 TWO-PHOTON LITHOGRAPHY THEORY 53
3.1 Two-photon absorption 53
3.1.1 Benefits of Two-photon photolithography 56
3.1.2 Verifying two-photon absorption 58
3.1.3 Excited State absorption 58
3.2 Photoinitiator Chemistry 60
3.2.1 Explanation of Ciba Irgacure 369 photochemistry 61
3.3 Calculation of voxel size 64
4.0 DESIGN CONSIDERATIONS FOR THE DMHL SYSTEM 67
4.1 Resolution 69
4.1.1 Position accuracy limits of beam 72
4.1.2 Relating C_{lens} to real image displacement 73
4.2 Optical Aberrations 78
4.2.1 Spherical Aberration 79
4.2.2 Astigmatism 81
4.3 Physics of SLMs 82
4.3.1 Polarization Eigenstates 85
4.3.2 Birefringence 86
4.4 SLM Device Limitations 87
4.4.1 Asymmetry of SLM diffraction efficiency 87
4.4.1.1 Average phase change per pixel within a hologram 90
4.4.2 SLM time response 90
4.5 Characterizing the SLM 92
4.5.1 Phase Calibration 92
4.5.2 Intensity fluctuations 94
4.6 Characterizing the laser 95

4.6.1 Beam Quality . . . 98
4.6.2 Measuring Laser Pulsewidth . . . 98
4.6.3 Laser Power Budget . . . 100
4.7 Preliminary Experiments . . . 105
4.7.1 Sputter coating process and SEM induced damage . . . 106
5.0 2D PATTERNING RESULTS AND DISCUSSION . . . 108
5.1 2D Serial Patterning . . . 108
5.1.1 Experimental results . . . 109
5.1.1.1 Sensitivity to Objective Axial Position . . . 109
5.1.1.2 Possible Thermal Curing . . . 110
5.1.1.3 Shape of the voxel . . . 111
5.1.2 Patterning resolution . . . 113
5.1.2.1 Small Area Linewidth . . . 113
5.1.2.2 Large Area Linewidth . . . 119
5.1.2.3 Minimum Pitch . . . 119
5.1.3 Dwell-time Compensation . . . 121
5.1.3.1 Actual vs. Theoretical Patterning Beam Intensity . . . 123
5.1.3.2 Implementing Dwell-time Compensation . . . 123
5.1.3.3 Experimental Results . . . 125
5.2 2D Parallel Patterning . . . 128
5.2.1 Speckle Reduction . . . 132
5.2.2 Experimental Results . . . 133
5.3 In between 2D and 3D . . . 140
6.0 3D PATTERNING RESULTS AND DISCUSSION . . . 143
6.1 3D Serial Patterning . . . 143
6.1.1 Measuring Axial Voxel Length . . . 143
6.1.2 Aspect ratio limit . . . 147
6.1.3 Patterning volume - Aberration correction for DMHL . . . 149
6.1.3.1 Sharpness Metrics . . . 151
6.1.3.2 Experimental results . . . 152

6.1.4 Anomalous curing - height of features . . . 160
6.2 3D Parallel Patterning . . . 162
6.2.1 Gratings and Lenses Approach . . . 163
6.2.1.1 Results and Discussion . . . 164
6.2.2 3D Gerchberg Saxton Algorithm . . . 166
6.2.3 Ways to improve uniformity . . . 169
7.0 SUMMARY AND CONCLUSION . . . 171
7.1 Future work and Recommendations . . . 173
APPENDIX A. SLM BACKGROUND . . . 174
A.1 SLM Theory and Characterization . . . 174
A.1.1 Phase-mostly operation . . . 177
A.1.2 Differences between Parallel aligned and Twisted LC cells . . . 178
A.1.3 Fringing Fields . . . 179
A.1.4 Flyback . . . 179
APPENDIX B. MATLAB CODE . . . 181
B.1 Average phase change . . . 181
B.2 Making phase gratings . . . 183
B.3 Measuring phase response of SLM . . . 186
B.4 Mapping Diffraction Intensity in Patterning Field . . . 187
B.5 3DGS . . . 195
BIBLIOGRAPHY . . . 200

LIST OF TABLES

1 ND filter transmission. 102

2 Parameters for determining upper bound of peak intensity for each objective (assuming 14.4 kW peak power and 100 % transmission through each objective). The +1st order of the phase grating is the "strong" first order beam. . 104

3 Parameters for determining upper bound of peak intensity for each objective (assuming 14.4 kW peak power and 70 % transmission through each objective). The +1st order of the phase grating is the "strong" first order beam. 104

4 Resolution for 2D serial DMHL. 121

5 Dwell-time compensation derived from measured patterning intensity. 126

6 Dwell-time overcompensation 126

7 Number of pixels for certain patterns (Parallel Patterning). These are assumed to be made with images that are 512×512 pixels using the strong first diffraction order. 131

8 Patterning conditions for anomalous curing experiment. 160

LIST OF FIGURES

1 These rods were made using DMHL (*source* [45]). 5

2 The top row of images shows 9 micro-components made with 9 parallel, serially scanning holographic beams in Norland optical adhesive 63 (*source* [41]). The bottom row shows a bridge made in SU-8 2010. These components were made with many holograms. 6

3 This is a schematic diagram of the DMHL set up. The laser is expanded into a collimated beam that is the input to the SLM. The exposure of the substrate is switched on and off by the shutter. The SLM is transmissive and only changes the phase of the incident light. After the SLM, the light propagates to the specimen plane through three lenses. The first lens is placed about one focal length away from the SLM to perform the Fourier transform explained in Figure 4. The lenses also scale the desired intensity pattern. 7

4 The lens Fourier transforms whatever is in its front focal plane at its back focal plane. 9

5 Energy diagram of both absorption processes. The two lower energy photons must be absorbed "simultaneously" to make the necessary energy transition. The two-photon process requires photons that are twice the wavelength of the single-photon process. 11

6 Demonstration of a Gaussian beam having smaller full width at half maximum (FWHM) for the square of the intensity (inside curve). There is a 40% reduction in feature width. Two-photon absorption goes as the intensity squared because two photons must be absorbed almost simultaneously. This effectively makes the dimensions of the exposing light beam smaller. 13
7 Geometry for grating equation. 19
8 This is a schematic diagram of the DMHL set up. The laser is expanded into a collimated beam that is the input to the SLM. The exposure of the substrate is switched on and off by the shutter. The SLM is transmissive and only changes the phase of the incident light. After the SLM, the light propagates to the specimen plane through three lenses. The first lens is placed about one focal length away from the SLM to perform the Fourier transform. The lenses also scale the desired intensity pattern. 21
9 The Fourier transform will be explained using this set of coordinate axes. . . 22
10 A plot of the 2D Fourier transform for a single square aperture (analytical solution). 24
11 The dimensions of a SLM array of pixels. These are used to calculate the expected zero order diffraction pattern. 24
12 Intensity diffraction pattern from grid of SLM pixels in normalized units (in this case 10 pixels in each direction). The black oval is the portion of the diffraction pattern that is transmitted by the mirror after the SLM. The circular mirror acts as an elliptical pupil because the mirror is rotated about the vertical axis to deflect the light. 27
13 The blazed phase grating displayed on the SLM diffracts light from the zero order into other diffractive orders. In principal the blazed grating can deflect all the light into an arbitrary diffraction order. 30
14 The SLM can be used to deflect light in the same way as a prism. 31
15 The diffraction efficiency of the phase staircase that can be displayed by the SLM is derived from the subtraction of the "error" from the desired blazed grating (adapted from [98]). 33

16 This is an example of a MATLAB-generated blazed phase grating. The phase level is given in the sidebar. 34
17 Displaying a Fresnel lens on the SLM moves the light in each diffraction order axially. Differently signed orders move in opposite directions. 36
18 The GS algorithm takes the input on the left and creates the hologram on the right. When the hologram is displayed on the SLM, the target intensity pattern is visible in the specimen plane. 38
19 This is a simple diagram of the GS algorithm from. 39
20 Error reduction algorithm for three dimensional beam shaping (*source* [92]). . 46
21 Blazed grating derived with 3DGS algorithm when the ratio between the maximum wavenumber on any axis, k_x, k_y, or k_z, and the wavenumber, k, of the patterning light is 1. Note that the nature of the algorithm causes the hologram to have a circular shape, and this ratio of wavenumbers makes a circle that almost exactly circumscribes the square "aperture" of the hologram. . . 48
22 Blazed grating derived with 3DGS algorithm when the ratio between the maximum wavenumber on any axis, k_x, k_y, or k_z, and the wavenumber, k, of the patterning light is 2. Note that the nature of the algorithm causes the hologram to have a circular shape, and this ratio of wavenumbers makes a circle with a diameter of about half that of the circle in Figure 21. 49
23 Fresnel lens derived with 3DGS algorithm when the ratio between the maximum wavenumber on any axis, k_x, k_y, or k_z, and the wavenumber, k, of the patterning light is 1. 50
24 Fresnel lens derived with 3DGS algorithm when the ratio between the maximum wavenumber on any axis, k_x, k_y, or k_z, and the wavenumber, k, of the patterning light to be 2. Note that the nature of the algorithm causes the hologram to have a circular shape, and this ratio of wavenumbers makes a circle with a diameter of about half that of the circle in Figure 23. 51
25 Fresnel lens derived with 3DGS algorithm when the ratio between the maximum wavenumber, k_x and k_y, and the wavenumber, k, of the patterning light is 1, while the ratio between the maximum k_z and k is 2. 52

26 Energy diagram of both absorption processes. The two lower energy photons must be absorbed "simultaneously" to make the necessary energy transition. The two-photon process requires photons that are twice the wavelength of the single-photon process. 55

27 The topmost curve is the absorption spectrum for Ciba Irgacure 369 (*source* [12]). It has an absorbance of about 0.2 at 266 nm. 56

28 Absorption spectrum for Ormocomp© resist (*source* [72]). 57

29 These are results from OrmoComp© with a 20× objective at various intensities. They are not made holographically, but simply with the laser going through the objective. The polymerization rate vs. intensity plot in Figure 30 was derived from this sample to imply two-photon absorption. 59

30 This is a plot of the average polymerization rate ($\mu m^3/s$) vs. exposure intensity for a two second exposure. For two-photon absorption, a linear dependence is expected. If the reaction involved single-photon absorption, the dependence would be square root. It can be seen that the fit to a line is much better. . . 59

31 Irgacure 369 molecule undergoing photocleavage and causing photopolymerization of ORMOCER (adapted from [48]). The benzoyl radical is circled. . . 62

32 The chemical structure of an acrylate monomer (*source* [84]). The reactive species attaches to the left side of the monomer, and opens up a bond on the right side for it to react with another monomer. The polymer is built in this way. 63

33 Each point on a ray can be described by two variables, x and θ. Two example points are given before and after a ray has traversed a lens. 68

34 This is a schematic diagram of the DMHL set up. The laser is expanded into a collimated beam that is the input to the SLM. The exposure of the substrate is switched on and off by the shutter. A neutral density filter (ND) is used to control the laser intensity. The half-wave plate rotates the linear polarization of the laser to maximize the diffraction efficiency into the first diffraction order. The SLM is transmissive. After the SLM, the light propagates to the specimen plane through three lenses. The first lens is placed about one focal length away from the SLM to perform the Fourier transform. The lenses also scale the desired intensity pattern. 70
35 Explanation of reduced effective patterning area. 74
36 Light from other diffracted orders can interfere with the intended patterning beam. 75
37 As C_{lens} increases, the effective focal length decreases as $1/C_{\text{lens}}$. 76
38 This plot shows a model of how the first order beam should move axially with increasing C_{lens}. The solid line is for an LC layer thickness of 10 μm and the dashed line is for an LC layer thickness of 8.5 μm. The measured data is plotted as stars. The measured data appears to match the thinner LC layer thickness, and this thickness is feasible. The model has a step-like nature at high C_{lens} because of the pixelation of the SLM. 78
39 Examples of Zernike polynomials. 80
40 Effect of electric field on liquid crystals between transparent electrodes in an SLM. The dotted lines are the alignment directions for the liquid crystals in contact with the electrodes. This shows a 90 degree twist. 83
41 The diffraction efficiency for gratings along one axis of the SLM varies much more rapidly and drops off much more quickly than the other. The dashed line shows the normalized diffraction efficiency of a range of vertical blazed gratings while the solid lines is for horizontal gratings. This is mostly due to the asymmetry in the drive circuitry. Note: Grating constants are proportional to spatial frequency. Here 50 grating constants is equal to a blazed grating with 100 periods. 89

42 This is a plot of average phase change per pixel as spatial frequency increases in the y-direction. N_λ is the number of wavelengths or periods in the displayed grating. 91

43 This is a plot of average phase change per pixel as lens constant, C_{lens} increases. 91

44 Phase response of SLM for different gray level values (Brightness:100, Contrast:255, polarizer before SLM:0° and polarizer after SLM:45°) 93

45 This is the side view of a serially cured square. It shows small intensity fluctuations. It was made with a scan speed of about 0.85 μm/s. 95

46 This is an attempt to show the whole patterning area with a grid. The two dark bands in which there is not enough light to pattern are clearly evident. The large mess on the left is from the zero order causing the resist to boil, and can be eliminated. 96

47 A plot of the normalized intensity due to the first diffraction order. There is a larger drop-off in intensity in the x-direction than the y-direction because it extends further from the zero order and requires a higher spatial frequency grating. The magnitude of the coordinates on the x- and y-axes are proportional to the spatial frequency of the displayed gratings (in this case, one X_{offset} or Y_{offset} is equal to two periods in a displayed blazed grating. 97

48 Autocorrelator setup with beam trace showing how the beam is split, the path length is varied, and the beam is recombined for SHG in the BBO crystal (point where beam converges). 99

49 Explanation of how to angle tune the BBO crystal after determining the polarization of the laser. 100

50 Autocorrelation curves with Gaussian fit. 101

51 Both images are from the ESEM before the sample was coated with palladium. On the left is the sample viewed with a 20 kV electron beam early in viewing. On the right is the same area viewed about 10 minutes later. There seems to be damage done by the electron beam. 107

52 On the left is the optical microscope image taken after development with the 40x objective. In the center is the early (before electron beam damage) ESEM image. On the right is the same area viewed with the SEM. 107

53 The upper-left trio of squares was serially scanned at a shallow depth, while the set of 10 on the lower right were made with a deeper focus. 110

54 These lines were made with increasing depth into the sample from left to right. The contrast of the lines is proportional to their axial height and it can be seen that the width of the most shallow line is wider than the middle line. 111

55 This is a schematic explanation of possible thermal curing when the focus is too deep within the substrate. Once the centroid of the focus is closer than some threshold distance, normal photocuring begins to occur. 112

56 These lines were made with a peak intensity of about 3.1 GW/cm^2 and an exposure time of 0.3 sec. per voxel. The objective was moved up about 500 nm between each line. 114

57 This set of lines was made with a peak intensity of about 2.7 GW/cm^2 and an exposure time of 0.3 sec. per voxel. 115

58 This is a fit of theoretical voxel diameter for constant exposure time at several peak intensities. 115

59 This is a fit of theoretical voxel diameter for two constant exposure peak intensities at several exposure times. 116

60 This square was made with a peak intensity of about 2.7 GW/cm^2 and an exposure time of 0.1 sec. 116

61 These squares were made with a peak intensity of about 2.7 GW/cm^2 and an exposure time of 0.1 sec. Only the bottom left feature was cured as designed. 117

62 This set of lines was made with a peak intensity of about 2.7 GW/cm^2 and an exposure time of 0.15 sec. per voxel. 118

63 These linewidth data points were used for the determination of the small area patterning resolution. The two lines on the right of both sets were underexposed. 118

64 These squares were used to find the large area patterning resolution. Dwell-time compensation was used. The two squares on the right had an exposure time of 0.2 sec. per voxel, then the middle was 0.3 sec, the next was 0.55 sec. and the last was 0.7 sec. 120

65 The data points for the determination of the minimum pitch come from these line pairs. 122

66 The normalized diffraction efficiency for the patterning beam (first diffraction order) compared with that derived from the model. The beam power was measured with a power meter. The number of periods in the displayed horizontal blazed grating is twice the number of X_{offset} units. 124

67a Top and side view of uncompensated lines. 126

67b Top and side view of dwell-time compensated lines. 127

67c Top and side view of overcompensated lines. 127

68 Normalized height of cured lines made at different distances from the zero order. The $X_{textoffset}$ value is proportional to spatial frequency of the grating in the x-direction and also the displacement of the beam from the zero order. Here, the number of periods in the blazed grating is twice the value of the corresponding $X_{textoffset}$. As the distance increases, the patterning intensity decreases and dwell-time compensation becomes necessary. It can be seen that dwell-time compensation significantly improves the uniformity of features. By definition, theory predicts that all compensated features should have a normalized height of 1. Performance is even better if even more dwell-time is added (overcompensation). 129

69 This is the whole Litho 43 sample. The three sets of interest have boxes around them. Clockwise from the top left are 10x10 squares, 30x30 squares, and 20x20 squares. This is the first instance of a parallel feature being exposed properly (20x20 squares in bottom left). 134

70 The two good-looking squares were made with $ND = 0$ and 10 holograms each exposed for 0.2 seconds. The top one was exposed twice. 135

71 Segments of circles (Top: $N = 10$, Bottom: $N = 5$) in parallel exposures. . . . 135

72 These circles were exposed separately, with the objective being moved between exposures. . . . 136
73 This set was made with $N = 10$ holograms and an exposure time per hologram of 0.3 sec. . . . 136
74 This set was made with $N = 10$ holograms. The top left set had an exposure time of 0.25 sec. per hologram, the middle set, 0.2 sec. per hologram, and the bottom right set, 0.15 sec. per hologram. . . . 137
75 This plot shows how the available peak intensity in the strong first diffraction order changes as the flat graylevel applied to the target image is changed. . . . 138
76 This set was made with $N = 10$ holograms each exposed for 0.25 sec. The graylevel decreases from left to right with increasing distance from the zero order. . . . 139
77 Several parallel-exposed circles made with Bessel beams. Each column is a separate exposure with the Bessel beam of a different r_o value. The center row is the over exposed zero order. . . . 140
78 One parallel line segment was exposed, then an orthogonal line segment was cured at various depths to create a cross ($N = 5$ holograms with an exposure time of 0.15 sec.). . . . 141
79 One parallel line segment was exposed, then an orthogonal line segment was cured at various depths to create a cross. . . . 141
80 Cured lines were hung in the air using 3D serial patterning. . . . 144
81 This set of lines was made with an exposure time of 0.15 sec. per dot and a peak intensity of about 2.7 GW/cm^2. The line on the left has fallen over indicating that the axial voxel length is being approached. . . . 145
82 This set of lines was made with an exposure time of 0.3 sec. per dot a peak intensity of about 2.7 GW/cm^2. The line on the left has fallen over indicating that the axial voxel length is being approached. . . . 146
83 Plot of axial voxel length vs. exposure peak intensity for two different dwell times. The data is fit to an equation for the axial voxel length given in Chapter 3. . . . 146

84 Sets of pillars were made from which to hang parallel-exposed features. The horizontal beam connecting the two vertical pillars is one voxel thick. Both hanging features were made with two separate exposures. The feature on the left was made with a horizontal beam exposed first and an orthogonally placed beam exposed next that did not cure. Each exposure was with $N = 5$ holograms and an exposure time of 0.15 sec. each. The feature on the right is similar except that the second exposure was of a Bessel beam, which also appears not to have cured. 148

85 The pillar made with 6.78 GW/cm^2 peak intensity and 0.3 sec. exposure per voxel. 149

86 The pillar was not made with DMHL. With no SLM, the 10× objective created a free standing pillar with an aspect ratio of 12. This gives a better idea of the physical limits of the mechanical strength of the resist. 150

87 The first lens after the SLM is placed about one focal length away to perform a Fourier transform and is rotated by about 10 degrees to add enough aberration to the system to affect patterning. 153

88 Maximum intensity of laser spot from CCD image for different degrees of aberration correction. The patterning volume is proportional to the maximum laser intensity. Therefore it is best to find a set of aberration correction coefficients that also provide high intensity along with sharpness. 154

89 Sharpness of laser spot from CCD image for different degrees of aberration correction. The most efficient use of laser power is to focus the light into the sharpest point possible. 155

90 The determined aberration corrections. X-astigmatism with -0.81λ (top left) and Y-astigmatism with -0.25λ (top right) are added to get the total correction (center). The color relates to the phase of the pixel. Black corresponds to a delay of 0 and white corresponds to a delay of 2π. 156

91 This is an oblique view of four features made with a varying amount of aberration correction. The aberration correction increases from the top left to the bottom right, and there is clear evidence that aberration correction improves pattern fidelity. 158

92 This is a side view of four features made with varying amount of aberration correction. The aberration correction increases from the left to the right. . . . 158

93 This is a side view of the two features made with the most aberration correction applied. There is still a significant improvement from $W_{\text{ast}} = -0.34\lambda$ on the left and $W_{\text{ast}} = -0.85\lambda$ on the right. 159

94 Set A was made with the shortest exposure time and has pillars that are closest to the designed height. 161

95 This plot shows the effect of different 3D serial patterning methods. The axial spacing between layers and the exposure time per voxel was varied. All methods produced pillars much taller than designed, but longer exposure time per voxel (set C) and more voxels in a given volume (set B) produce larger deviations from design. 161

96 Model of desired feature. Each oval corresponds to a voxel and the color corresponds to the weight. White is the highest intensity. The highest weights are at the base of the feature because the voxels at the base have the fewest near neighbors. 165

97 Examples of hollow tripods made with a single exposure with 3D volumetric holograms. Two orthogonal views are given. From left to right, the value of c increases from 0 to 0.1 to 0.2. The application of weights reduces the overexposure at the top of the feature. Each tripod was made in a separate exposure. On the right, the corresponding views of the ideal morphology are given. 167

98 This is the projection from above of the 128×128 pixel input pattern. The input is actually a set of 8 images at different axial displacements. 168

99 This is a top view of the set of 3 tripods made with the 3DGS algorithm. The top left tripod did not had no weights applied, the middle tripod had $c = 0.2$ and the bottom right tripod had $c = 0.4$. It seems that a weight of $c = 0.2$ is sufficient to make the tripod come out as designed. 170

100 This is a set of 3 tripods made with the 3DGS algorithm. The top left tripod did not had no weights applied, the middle tripod had $c = 0.2$ and the bottom right tripod had $c = 0.4$. It seems that a weight of $c = 0.2$ is sufficient to make the tripod come out as designed. 170

1.0 INTRODUCTION

Lithography is used in a wide variety of situations from major industrial-scale processes to simple one-off lab projects. Not only is lithography used for making integrated circuits through subtractive processes, but by making micro-components out of the photopolymerized resist itself through additive processes. Advances in resolution and throughput have been made steadily for the last few decades [39]. As the physical limits of lithography are reached, more adaptable and cheaper approaches are needed to increase its availability. Dynamic Maskless Holographic Lithography (DMHL) is one such approach. DMHL allows for the exposure pattern to be changed in real-time and for three dimensional control of light intensity with no moving parts. The focus of this research will be to improve the resolution and reproducibility of the DMHL process and to extend its capabilities. Both 2D and 3D components will be made that either cannot be made with traditional lithography, or can only be made through a complicated registration process. Methods to improve uniformity over a large patterning field, increase patterning volume, and improve 3D pattern fidelity will also be discussed.

Dynamic maskless holographic lithography uses an electrically addressable spatial light modulator (SLM) to create an arbitrary intensity pattern at the specimen plane. The SLM is a phase mask that displays a hologram. The SLM can be used to steer a single beam (usually the first diffraction order) or to display a hologram that creates an almost-arbitrary intensity pattern in the focal volume. An algorithm is used to find an appropriate phase hologram for each desired intensity pattern. Each pixel of the SLM shapes the wavefront of the incoming laser light so that the natural Fourier transforming property of a lens causes

the desired image to appear in the specimen plane. The process enables one-off projects to be done *without the cost of fabricating a mask*, and makes it possible to perform lithography with fewer (or even no) moving parts.

One main goal of this research is to improve the resolution of the DMHL process by using two-photon absorption. In principle there can be a 40% decrease in feature size through the use of two-photon absorption. Instead of one UV photon being absorbed by the photo-active component of the resist, two longer wavelength photons are absorbed simultaneously. This only happens at the high peak intensities provided by a pulsed laser. The absorption of the photoinitiator molecules in the resist then depend on the square of the intensity, resulting in smaller features.

DMHL makes it possible to create 3D structures in the resist. This can be done in a single shot if available laser intensity is high enough, or through a serial scanning process. Holograms can contain information in three dimensions, and thus can be used to add a third dimension to lithographic features. It is impossible to make 3D structures with a mask without moving the substrate axially with an expensive translation stage. By adding a quadratic phase grating to a hologram, the focus of the laser beam can be made to go deeper into the sample without moving the objective lens. The micro-component can then be made to have a third dimension thicker than a single axial voxel. A voxel (*vo*lume pi*xel*) is the three-dimensional volume of resist cured by a laser focused to a single point. It is the basic unit of lithography.

The DMHL process has several inherent limits. The pixelation of the SLM reduces diffraction efficiency in phase gratings with high spatial frequency. This reduces pattern uniformity over large patterning areas. A method will be demonstrated that compensates for this reduced efficiency and restores pattern uniformity. Optical aberrations in the optical system, and unavoidable mismatches in refractive index between oil immersion objectives and the photoresist can degrade resolution and reduce potential patterning volume. An aberration correction algorithm will be implemented that compensates for the aberrations in the DMHL system.

The design of almost-arbitrary 3D light intensity patterns for lithographic use is a new area of research. Two methods are demonstrated here. Constructive and destructive in-

terference complicate the design of 3D light intensity patterns and cause defects in cured features. Defects are reduced or eliminated in both methods by applying appropriate weights to each voxel in the pattern. A set of design considerations are defined to avoid problems inherent to 3D DMHL and guide future work.

On top of the improvement in resolution, the project will more accurately characterize the 2D and 3D results of DMHL. The reproducibility of the cured structures will be quantified as an uncertainty in lateral and axial dimensions. Several papers have been written on DMHL, but few, if any, numbers are given for the variation from feature to feature. Differences in the resolution of serial versus parallel patterning processes will be discussed. The effect of speckle was found to be the limiting factor for parallel patterning.

The most common uses for devices made from photoresist are in "lab-on-a-chip" devices. Labs-on-a-chip are normally microfluidic in nature, and can incorporate laser inputs for manipulation and fluorescence/spectroscopy. As the number of uses for lab-on-a-chip devices increases, their complexity will also increase. Simple lines/troughs and pumps will not be adequate. DMHL described here will allow for the creation of a toolbox of parts necessary for the next generation of labs-on-a-chip and micromachines [27, 63, 44, 66]. Micromachines can be manipulated with optical traps. Gears can even be spun with a transfer of angular momentum. Microlens arrays can be created and used for near field microscopy [70, 53]. The integration of silicon electronics with photonics is also a possible application for DMHL. IR and optical metamaterials can be made by filling the voids in micro-component arrays with metals like gold [29]. These metamaterials can form optical devices like polarizers that are much smaller than those currently available.

The research described here will push the state of the art in lithography in several ways. The production of 3D features made from a single hologram will be the major contribution with the implementation of methods to increase patterning area uniformity and patterning area volume being secondary improvements. All of these process extensions will increase throughput.

1.1 STATE OF THE ART AND BACKGROUND

In this section, the process of DMHL will be broken down and discussed. Justification for the project is provided by the improvement in effective resolution using two-photon absorption, the extension of the process with 3D intensity patterns, and process improvements like aberration correction. Several different ways of making the holograms will be explained. Finally the state of the art will be given in comparison with the proposed research.

Most papers only give the resolution, while repeatability is more difficult to find in the literature. Though several authors claim to have performed two-photon DMHL, very little, if any information is given on how two-photon absorption has been verified. This work will also be the first instance of curing a non-periodic 3D micro-component with a single hologram.

1.1.1 DMHL

DMHL uses a computer generated hologram to create a target image in the specimen plane of the microscope. The phase hologram is displayed on a liquid-crystal spatial light modulator (SLM). The hologram can be a simple grating or Fresnel lens or can be created using an algorithm that takes a target image and Fourier transforms it into an array of phase delays. DMHL eliminates the need for a separate mask for every different pattern exposure and allows for real-time shaping of the exposure pattern. In recent years, research similar to that proposed here was done with dynamic amplitude masks [8, 95], but those methods lose light whenever a pixel is opaque, and because they do not use holograms, the image cannot be moved in 3D.

1.1.1.1 DMHL State of the Art The first applications related to DMHL were in the creation of little holes in glass using femtosecond lasers [100, 35, 36, 37]. One of the early papers even involved the multiplexing of several Fresnel lenses to create a 3D array of bright spots for making holes in different planes simultaneously [35]. Moreover, there was progress into making actual micro-components out of resist, as will be done in this research. Work was done on making lines [101], helical pillars [45], bridges and variously shaped prisms

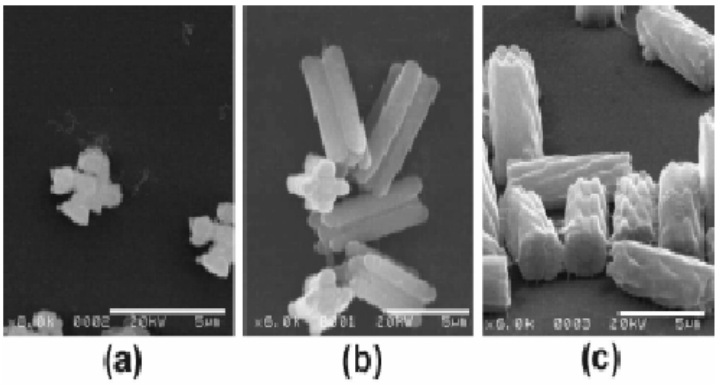

Figure 1: These rods were made using DMHL (*source* [45]).

with specifically designed heights [41], and 2D coats of arms [4]. Both Takahashi et al. and Kelemen et al. claim two-photon absorption, but do not use lens functions to add a third dimension to their features [101, 45]. The lines had a minimum width of 230 nm. The widths of the helical pillars were about 700 nm and are shown in Figure 1. Two-photon absorption was not confirmed in either of these papers [101, 45], but was assumed due to the low absorption of the resist at the single photon wavelength. Jenness defined resolution as the size of a feature corresponding to a single pixel width in the target image. The features in his work also have a resolution of about 700 nm. The micro-components shown in Figure 2 are made using a pulsed green laser with 18 ns pulses (60 times longer than the pulsewidth used here) and a peak power of 22 kW. The laser used in this research has a peak power around 80 kW. The axial voxel size is about 2.5 μm [41]. The highest magnification objective used by Jenness was 100$\times$ with NA= 1.4, which is identical to the objective used in this research. All these parameters imply that the features created in this research should be similar to those created by Jenness, but with improved resolution due to the higher peak powers (the curing threshold can be achieved in a smaller volume).

1.1.1.2 DMHL Background In this research, DMHL is performed by expanding and collimating the pulsed laser light so that it fills much of the face of the transmissive SLM.

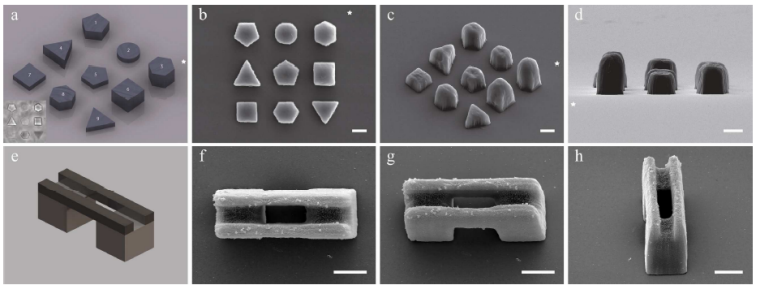

Figure 2: The top row of images shows 9 micro-components made with 9 parallel, serially scanning holographic beams in Norland optical adhesive 63 (*source* [41]). The bottom row shows a bridge made in SU-8 2010. These components were made with many holograms.

The SLM pattern is Fourier transformed by a lens, and the resulting pattern is imaged to the specimen plane of the microscope to cure photoresist. The experimental setup used to perform DMHL is given in Figure 3.

The SLM has electrically addressable pixels that can be changed in real time through almost a full 360 degrees of phase delay. The SLM is 8-bit and therefore can cut the phase delay into 256 levels. Phase gratings and Fresnel lenses can move single diffraction orders in space. By designing the array of pixels in the phase mask to be the Fourier transform of some target image, it is also possible to create a whole intensity pattern in the specimen plane which can be used to expose a resist. The design of the hologram is done using the Gerchberg-Saxton (GS) algorithm, a type of phase retrieval program. A 3D light intensity pattern can also be produced by a single 2D phase hologram.

The complex light field at a given axial position, $u(x, y)$, is defined at all locations by a magnitude, $A(x, y)$, and a phase, $\phi(x, y)$:

$$u(x, y) = A(x, y)e^{j\phi(x,y)} \tag{1.1}$$

though in this case, the amplitude is assumed to be constant over the face of the SLM.

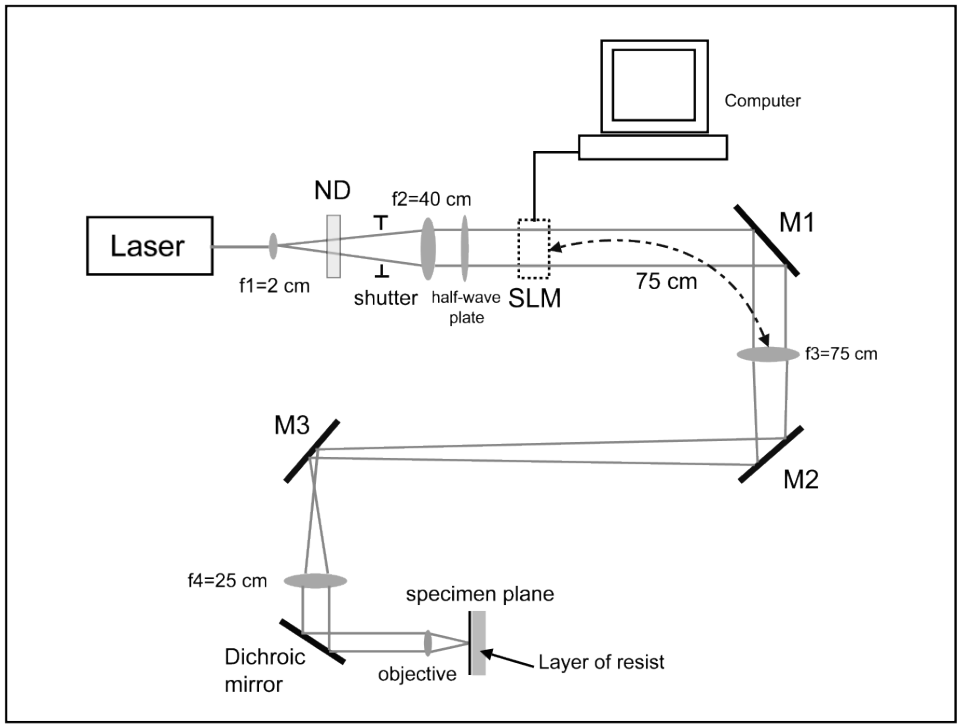

Figure 3: This is a schematic diagram of the DMHL set up. The laser is expanded into a collimated beam that is the input to the SLM. The exposure of the substrate is switched on and off by the shutter. The SLM is transmissive and only changes the phase of the incident light. After the SLM, the light propagates to the specimen plane through three lenses. The first lens is placed about one focal length away from the SLM to perform the Fourier transform explained in Figure 4. The lenses also scale the desired intensity pattern.

A lens takes a complex input field, u_{in}, and Fourier transforms it into a complex output, u_{out}, at the back focal plane of the lens as shown in Figure 4. The Fourier transform is explicitly given as:

$$u_{\text{out}}(u,v) = \frac{1}{j\lambda f}\iint_{-\infty}^{\infty} u_{\text{in}}(x,y)\exp\left(-j\frac{2\pi}{\lambda f}(xu+yv)\right)dxdy \tag{1.2}$$

where f is the focal length of the lens, (u,v) are the new coordinates at the back focal plane [32]. The GS algorithm makes use of the Fourier transform to find an array of phases that when combined with a flat amplitude profile (from the collimated laser beam) will produce the desired image in the focal plane after a lens. A 3D version of the GS version of the GS algorithm can create 3D light intensity patterns using similar principles [92, 107].

The use of holograms also allows for many process improvements. Aberration correction can be done to compensate for any aberrations in the optical system. Mathematical adjustments can be made during hologram calculation to account for nonuniformity of the patterning field and interference effects in 3D light intensity patterns.

1.1.2 Two-photon Absorption

The resolution, R, of a lithographic process is defined as:

$$R = \frac{k_1\lambda}{\text{NA}} \tag{1.3}$$

where k_1 is process dependent but is usually between 0.5 and 1, and λ is the wavelength of light. The definition of resolution that pertains to DMHL will be discussed in more depth later. According to equation 1.3, the most direct way to improve the resolution of a lithographic process is to use a shorter wavelength to expose the pattern. As the wavelength gets shorter, the photons carry more energy, doing damage to the experimental apparatus, and can be absorbed by the air which then requires the use of a vacuum. Conventional lenses also absorb UV which then requires the use of reflective optics. This means that the experimental set up gets more expensive and complicated. One possible solution is to use two-photon absorption which gives improved resolution without the need for new optics or a vacuum.

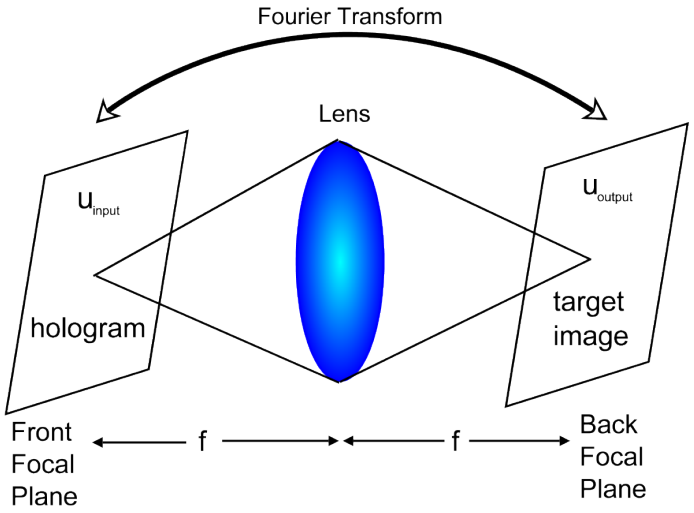

Figure 4: The lens Fourier transforms whatever is in its front focal plane at its back focal plane.

The absorption of light in the photoresist is usually done one photon at a time, at a specific wavelength at which the photoactive part of the resist has a high absorption cross-section. The curing of the resist happens linearly with the intensity of the light. Two-photon absorption (see Figure 5) increases the resolution of a lithographic process by using light that is twice the wavelength of the absorption peak in the resist. The photoinitiator only reacts if two photons are absorbed simultaneously. This requires very high intensities. The feature sizes will then be based on the square of the intensity. The square of the intensity is sharper and smaller in lateral dimension. Figure 6 shows that the FWHM of the intensity for two-photon absorption gives a 40% reduction in feature size compared to the single photon case.

The intensity of light varies quadratically with axial distance from the focus. The benefit of two-photon lithography is that because the light is absorbed based on the square of the intensity, the photoinitiator's absorption varies with axial distance, z, as z^{-4}. The region of intensity high enough to cure the resist has a volume on the order of λ^3 where λ wavelength of the patterning laser [88]. Light scattering can cause areas around the intended feature to be cured, reducing resolution and making critical dimension control difficult. Two photon excitation helps mitigate this problem because light scattering scales as $1/\lambda^4$. By doubling the effective exposure wavelength, scattering is decreased by a factor of 16. Another benefit to two-photon absorption is that the beam is less distorted by already-cured structures due to lower scattering of longer wavelengths [64]. This aids in making 3D structures that will involve building above or below previously exposed areas.

Almost all two-photon absorption papers use a femtosecond pulsed Ti:saphire laser that is tunable through the visible and near-IR range. Because most commercially available resists are cured by UV light on the I-line (365 nm), experiments involve using light from about 700-800 nm. Results of this research show that this tunability is unnecessary even for UV resists. The pulsed green (532 nm) laser used in this project is an order of magnitude cheaper than a pulsed Ti:sapphire laser system, and can achieve results with comparable or better resolution. It has pulse widths of about 300 ps and a repetition rate of 500 Hz. It has an average power of 12 mW and a pulse energy of 24 μJ. This gives a peak power of 80 kW.

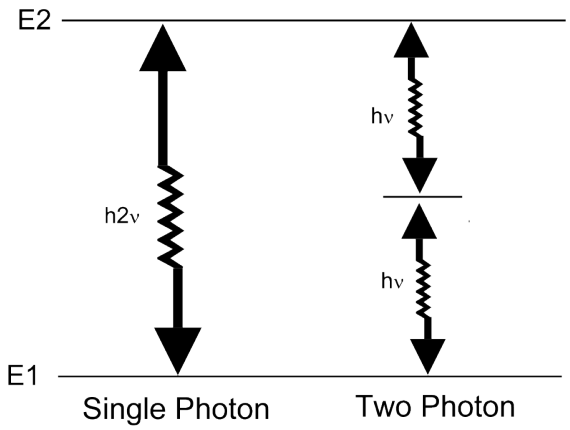

Figure 5: Energy diagram of both absorption processes. The two lower energy photons must be absorbed "simultaneously" to make the necessary energy transition. The two-photon process requires photons that are twice the wavelength of the single-photon process.

1.2 RESEARCH OBJECTIVES

The project can be broken down into two main objectives: 2D and 3D DMHL and each includes a series of sub-objectives. Both objectives will also involve characterization of the DMHL process so that users can make more educated design choices. Characterization involves quantifying the resolution and defining uncertainty. A set of design rules similar to what is available for conventional photolithography will enable a much greater number of people to use DMHL to its full capability.

1.2.1 Objectives

1. **Two-Photon Dynamic Maskless Holographic Lithograpy in 2D** - The first objective of the project is to demonstrate two-photon DMHL in two dimensions (in both serial and parallel modes) and characterize the process in more detail than has been done to date. Also methods to compensate for inherent physical limits of the system will be applied (dwell-time compensation and speckle mitigation).

    a. **Two Photon** - In holographic lithography, much of the laser light is lost due to diffraction at the SLM, therefore it must be done on very sensitive photoresists. The obvious solution to resolution improvement is to use a shorter wavelength to expose the resist, but many liquid crystal SLM displays would be damaged by light of UV wavelengths or shorter. UV wavelengths can also require reflective optics and a vacuum environment due to absorption by air and glass. Two-photon absorption bypasses this problem by using a longer wavelength of light.

    b. **Evaluation of DMHL Process Resolution** - The lateral resolution can be quantified by measuring the width of a line that is made holographically. The axial resolution can be quantified by a combination of measuring the height of lines that have been cured hanging in the air, and by measuring how tall a single line can be before it falls over. By taking the standard deviation in the measurements of a large number of lines (from several different samples), the reproducibility can be defined.

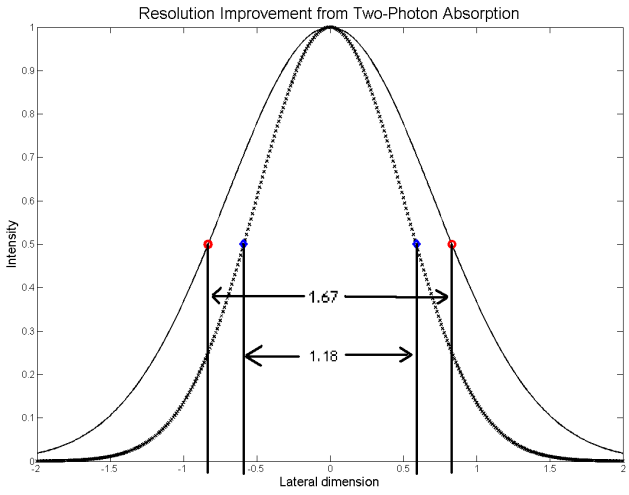

Figure 6: Demonstration of a Gaussian beam having smaller full width at half maximum (FWHM) for the square of the intensity (inside curve). There is a 40% reduction in feature width. Two-photon absorption goes as the intensity squared because two photons must be absorbed almost simultaneously. This effectively makes the dimensions of the exposing light beam smaller.

Reproducibility of DMHL-produced features have not been published in currently available papers. Proper characterization of DMHL-produced features will aid in the making of a set of design rules for future users.

2. **3D Lithography** Adding a third dimension to microstructures can increase their functionality and density. There are two ways to cure objects holographically in 3D: 1) scan a holographic dot (any image) through the whole volume of the feature using lens functions to displace the image axially, or 2) use a hologram that shapes the light in all three dimensions. Both sub-objectives will also include characterization and compensation methods that account for interference effects.

   a. **Using Rapid Prototyping** - The easiest way to make a 3D object is to take a point of light and scan it through the resist in the shape of the desired feature. This is the first step in making complex, high-resolution, 3D micro-components. This method will also be used to demonstrate aberration correction.

   b. **Using a Single 3D Hologram** - Holograms can contain information in three dimensions. This fact allows for 3D intensity patterns to be generated and used for curing micro-components in a single shot. Although 3D light intensity patterns have been used in holographic optical traps (HOTs)[57, 16], the design considerations are different for lithographic applications. Interference effects can cause parts of a feature to be under- or overexposed. A major difference between DMHL and HOT is that adjacent voxels must be close enough and with high enough intensity to make sure the cured voxels are attached to each other.

1.3 RESEARCH IMPACT

The intellectual merit of this project involves determining the resolution of DMHL in all three dimensions and advancing the state of the art in the complexity and quality of micro/nano components. The focus of this research will be to more thoroughly characterize the DMHL process, add improvements and extend with a new patterning mode. After demonstrating 2D DMHL, micro-components with a third dimension will be made using a single hologram.

This has never been demonstrated before. Also methods to improve pattern uniformity and pattern fidelity will be tested. These include compensation for non-uniform diffraction efficiency throughout the patterning area, aberration correction in the optical system and accounting for interference effects in 3D patterning.

The broader impacts of this project are in benefits to society that come from increasing the availability and versatility of lithographic processes. This is done by eliminating the need for a separate mask for each designed pattern. Making unlimited numbers of patterns without a mask significantly reduces the cost of a lithographic project. Technologies like microfluidic "labs-on-a-chip" and micromachines [27, 63, 44, 66] can be developed faster, by more people using flexible maskless lithography. Potentially devices like, microlens arrays could be created and used for near field microscopy [70, 53]. Also, IR and optical metamaterials could be made by coating arrays of micro-components with metals like gold [29]. The methods developed to improve pattern uniformity and fidelity can be applied to other SLM-based technologies.

1.4 DOCUMENT STRUCTURE

Below is a list describing the structure of this dissertation. The first several sections will describe the theory behind the DMHL process. The next will explain design decisions. Finally there will be several sections on experimental results and discussion.

1. The theory of holography and an explanation of how a phase hologram can move light in three dimensions.
2. The theory of two-photon absorption and the physical process behind how light interacts with photoresists to cause curing.
3. Design of the experimental setup and of the characterization of its components.
4. Results from 2D and then 3D patterning including DMHL process improvements like aberration correction and dwell-time compensation.
5. Discussion of major contributions and future work.

2.0 HOLOGRAPHY THEORY

A hologram is defined as an image that is created by the interference of a reference beam and an object beam. The interference pattern is normally recorded on some intensity-sensitive medium like photographic film, and contains information about the phase of the incident light. In the case of DMHL, the hologram is the array of pixels with different phase delays that creates an intensity pattern in the far field through diffraction.

The patterning will be done by two methods, one is serial, and involves scanning a single beam made by a series of phase grating and Fresnel lens combinations, while the other is parallel and involves projecting a whole image. The image will be made from a single hologram that has been determined with an algorithm that optimizes the match between the desired intensity pattern and the intensity pattern achieved in the specimen plane. This chapter will explain both processes.

Holograms can be categorized as "thick" or "thin" depending the relationship between the highest spatial frequency content and the thickness of the holographic medium. The SLM contains a layer of liquid crystals that is about 10 μm thick. A parameter, Q, can be used to determine whether the holograms displayed on the SLM can be thought of as thick or thin. This Q parameter is defined by [32]:

$$Q = \frac{2\pi\lambda_o d}{n\Gamma^2} \tag{2.1}$$

where λ_o is the vacuum wavelength of the light used during reconstruction, n is the refractive index of the medium, Γ is the period of a sinusoidal grating, and d is the thickness of the medium. This can be thought of as the optical phase delay of the hologram ($\phi = 2\pi dn/\lambda$) multiplied by the square of the ratio of the wavelength of light in the hologram ($\lambda_n = \lambda_0/n$) and the grating period,Λ. If Q$< 2\pi$ then the grating is thin, while Q$> 2\pi$ means the hologram

is thick [32]. For the holograms on the SLM to be categorized as thick, the smallest period in a phase grating would have to be 2 μm. The pixel pitch is about 32 μm meaning that the holograms in this research are well into the "thin" range. The main result of this designation is a lower maximum diffraction efficiency, where diffraction efficiency is the ratio of input light to output light in a certain diffraction order. Thick phase gratings can achieve 100% diffraction efficiency.

The holograms displayed on the SLM can also be categorized as Fourier holograms [32]. This simply means that the hologram is located in a plane that will result in the Fourier transform of the complex field in the object/specimen plane. Each set of sinusoidal fringes (with a specific spatial frequency and angle) in a Fourier hologram corresponds to a point in the object image. In this way a sinusoidal phase grating directs light to one point in the object plane. The greatest benefit to using a Fourier hologram is that the pixels of the SLM can be larger for a given desired bandwidth [32].

Holograms normally create twin images, one of which is real and the other is virtual. The twin images correspond to the complex conjugates of the wave that is scattered by the hologram (as opposed to the light that is simply transmitted). Many times these images are separated angularly. The following equation can be used to determine the axial separation of the two images:

$$z_i = \left(\frac{1}{z_p} \pm \frac{\lambda_2}{\lambda_1 z_r} \mp \frac{\lambda_2}{\lambda_1 z_o} \right)^{-1} \tag{2.2}$$

where the upper set of signs corresponds to one image and the lower to the other, z_i is the axial distance of the image points, z_r is the axial location of the reference source, z_o is the axial location of the object, z_p is the axial distance to the reconstruction source, λ_1 is the recording wavelength, and λ_2 is the reconstruction wavelength [32]. In the case of this research, $\lambda_1 = \lambda_2$ and $z_r = z_o$ which puts both images in the same plane (the object plane). It is known that phase holograms made with multiple phase levels theoretically produce no conjugate image (unlike amplitude or binary phase holograms), but phase errors in the SLM cause these images to appear in practice [4]. As long as the images are offset enough, they can be separated by using an iris to block one.

2.1 GRATINGS FOR SERIAL PATTERNING

The SLM used for displaying holograms is a twisted-nematic liquid-crystal device. The SLM itself is a diffraction grating made of an array of rectangular apertures. Each pixel has driving electronics around it, and a transparent window in the center which can have its refractive index changed by an applied voltage. For serial patterning, a phase grating and a Fresnel lens must be applied to the pixels to steer a single beam of light around. This beam is used for patterning. The following sections will explain the theory of how this is physically possible.

2.1.1 The Grating Equation

Any grating (amplitude, phase or any combination of the two) can be described by a simple equation called the grating equation [32]:

$$n_2 \Lambda \sin\theta_2 - n_1 \Lambda \sin\theta_1 = m\lambda \tag{2.3}$$

where Λ is the grating period, n_1 is the refractive index on the incident side of the grating, θ_1 is the angle of incidence of the ray of light, n_2 is the refractive index on the exiting side of the grating, θ_2 is the angle with the grating normal at which the exiting ray leaves, and m is the diffractive order. The difference on the left side of the equation is the optical path length difference of two rays. The rays interfere with each other, and therefore, a diffractive order m is only visible when the difference is an integer multiple of the wavelength, and constructive interference occurs. Using the above equation, and assuming ($n_1 = n_2 = 1$), the spacing between orders, d, in an image plane is given as $d = L\lambda/\Lambda$ where L is the distance from the grating to the image plane.

Taking into account the geometry of the experimental set up used here, it is possible to define a maximum diffraction angle, $\theta_{\max}$ due to the particular pixel pitch, Λ_p:

$$\frac{\lambda}{2\Lambda_p} = \sin\theta_{\max} \tag{2.4}$$

assuming just the first diffraction order ($m = 1$). The reason for the factor of 2 is that the minimum grating period is two pixels. The geometry of the set up includes light with

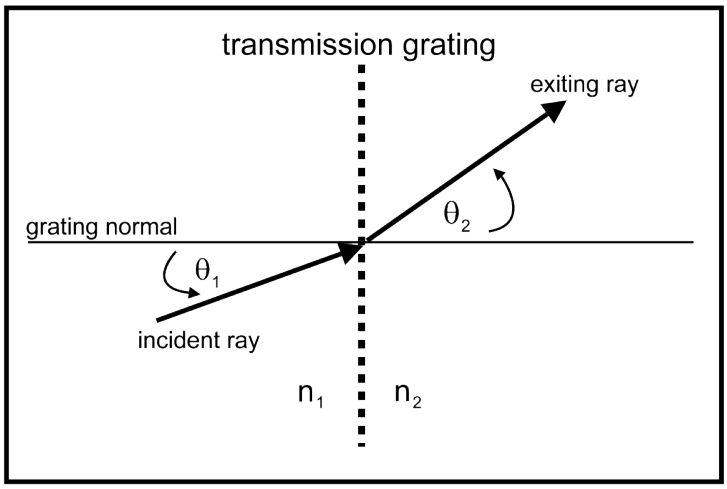

Figure 7: Geometry for grating equation.

an incident angle, θ_1 of zero degrees (normal incidence on the grating). The pixel pitch of this particular SLM is 32 μm. This works out to $\theta_{\max} = 0.48°$. The combination of this maximum deflection angle and the pupil function of the set of lenses and mirrors after the SLM define the limits of the patterning area.

2.1.2 Diffraction Gratings

Without the grating equation, it is still possible to derive the transmission properties of a grating based on diffraction theory. The incident laser light is simply diffracted by an aperture that has a specific transmittance function $t(x, y)$. In the case of the SLM, there is an opaque rectangular grid (the transistors controlling each pixel) and inside each cell, there is a smaller rectangular aperture that is transparent with a variable refractive index. In reality, the pixels do not behave like they are completely transparent. This is because the twisted nature of the liquid crystal cell causes the light to be elliptically polarized, and some of the outgoing light gets absorbed on its way through the LC cell. In the following

calculations, the pixels will be assumed to be completely transmissive. First, the effect of the static grid of driving circuitry will be derived, then the effect of the phase patterns that are displayed on the pixels.

Using diffraction and propagation theory, it can be shown that a lens that has an image one focal length before it, creates a Fourier transform of that image one focal length after it. The input image will be defined by an amplitude transmittance function, $t_a(x, y)$ that is then illuminated by a normally incident plane wave of amplitude A [32]. For this analysis, the only approximation that must be valid is the Fresnel or paraxial approximation. This requires that only small angles of diffraction be included ($<\sim 15°$). As mentioned above, the largest angle at which the SLM can deflect the first diffraction order is only $\theta_{\max} = 0.48°$. Also, the size of the lenses and mirrors used in this experiment cutoff much of the higher order diffraction effects, and allow for only small angle diffraction patterns to make it to the specimen plane.

The geometry of the experimental system is shown in Figure 8. The following explanation is from Goodman's Fourier Optics Chapter 5 [32]. The pertinent planes of this analysis are given in Figure 9.

The input image (the SLM plane) will be defined by an amplitude transmittance function, $t_a(x', y')$ that is then illuminated by a normally incident plane wave of amplitude A [32]. The light transmitted by the SLM has an angular spectrum of:

$$F_i(f_x, f_y) = \mathcal{F}[At_a] \tag{2.5}$$

where $\mathcal{F}$ denotes a Fourier transform, $f_x = x/\lambda f$ and $f_y = y/\lambda f$ and the angular spectrum of the light incident on the lens is:

$$F_l(f_x, f_y) = \mathcal{F}[U_l] \tag{2.6}$$

where U_l is the field immediately before the lens. F_l can be found by propagating the light from the input to the lens (assuming the paraxial approximation) using:

$$F_l(f_x, f_y) = F_i(f_x, f_y) \exp[-j\pi\lambda d(f_x^2 + f_y^2)] \tag{2.7}$$

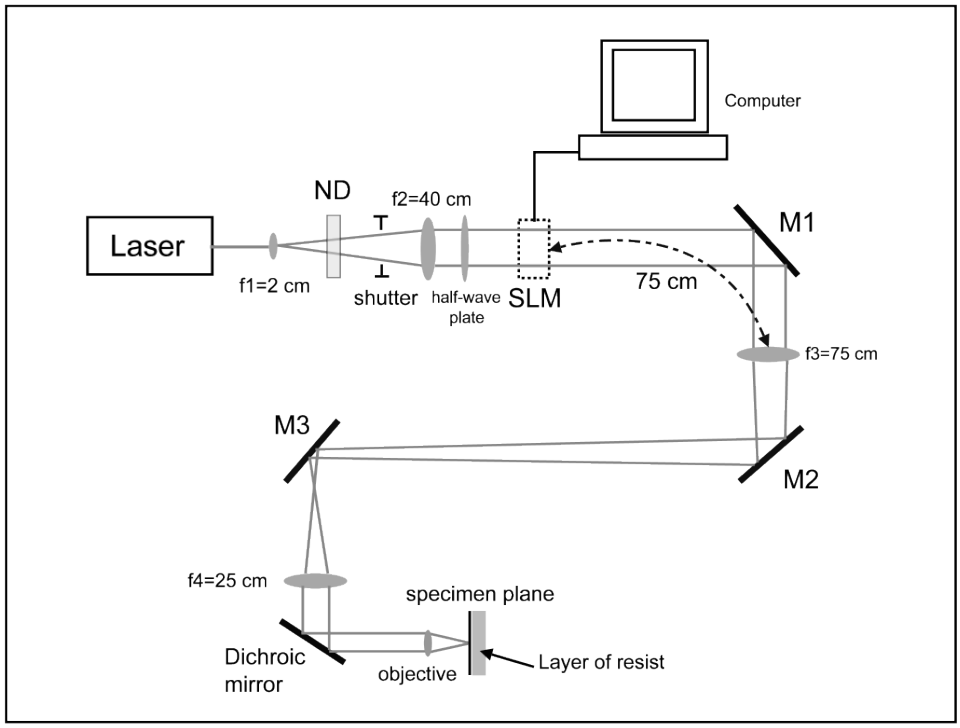

Figure 8: This is a schematic diagram of the DMHL set up. The laser is expanded into a collimated beam that is the input to the SLM. The exposure of the substrate is switched on and off by the shutter. The SLM is transmissive and only changes the phase of the incident light. After the SLM, the light propagates to the specimen plane through three lenses. The first lens is placed about one focal length away from the SLM to perform the Fourier transform. The lenses also scale the desired intensity pattern.

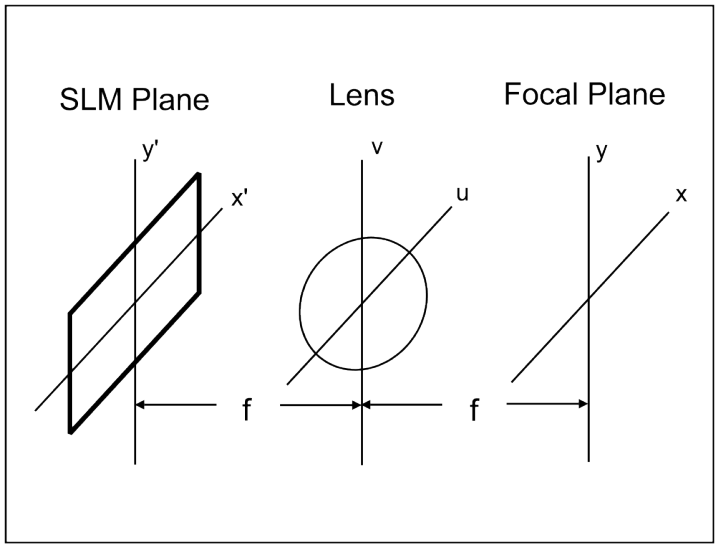

Figure 9: The Fourier transform will be explained using this set of coordinate axes.

where d is the propagation distance between the input and the lens and the constant phase delay ($\exp[jkd]$) is dropped. In the case of this experiment, the input will be a focal length away from the lens ($d = f$). The field immediately after the lens is identical to U_l except for an additional quadratic phase factor that gets canceled by the other quadratic phase factor in the Fresnel diffraction integral.

The field distribution $U_f(x, y)$ in the focal plane (after the lens) is given by the Fresnel diffraction formula with $z = f$ (assuming no pupil effects):

$$U_f(x,y) = \frac{\exp[j\frac{k}{2f}(x^2+y^2)]}{j\lambda f}\int\int_{-\infty}^{\infty} U_l(u,v)\exp[-j\frac{2\pi}{\lambda f}(xu+yv)]dudv \tag{2.8}$$

which simplifies to:

$$U_f(x,y) = \frac{\exp[j\frac{k}{2f}(x^2+y^2)]}{j\lambda f}F_l(\frac{x}{\lambda f},\frac{y}{\lambda f}) \tag{2.9}$$

When the relation between the input spectrum, F_i, and the spectrum at the lens, F_l, from equation 2.7 is substituted into equation 2.9, the result is:

$$U_f(x,y) = \frac{\exp[\frac{jk}{2f}(x^2+y^2)(1-\frac{d}{f})]}{j\lambda f}F_i(\frac{x}{\lambda f},\frac{y}{\lambda f}) \tag{2.10}$$

and when $d = f$, this simplifies to:

$$U_f(x,y) = \frac{A}{j\lambda f}\int\int_{-\infty}^{\infty} t_a(x',y')\exp[-j\frac{2\pi}{\lambda f}(x'x+y'y)]dx'dy' \tag{2.11}$$

which is a Fourier transform of the field at the SLM plane.

Now that the relationship between the arbitrary input field one focal plane before a lens and the field at the focal plane after a lens has been established, it is time to examine what to expect from the SLM. To begin, the intensity pattern from a single rectangular aperture will be derived. For monochromatic, normally incident, plane wave illumination, the field at the aperture, $U(x',y')$ is equal to the transmittance function, $t(x',y')$ given by:

$$t(x',y') = \text{rect}\left(\frac{x'}{w_{px}}\right)\text{rect}\left(\frac{y'}{w_{py}}\right) \tag{2.12}$$

where w_{px} and w_{py} are the dimensions of the pixel in the x- and y-directions respectively.

The Fourier transform of a rectangular aperture is:

$$\mathcal{F}[t(x',y')] = (2w_{px})(2w_{py})\,\text{sinc}\left(\frac{2w_{px}x}{\lambda z}\right)\text{sinc}\left(\frac{2w_{py}y}{\lambda z}\right) \tag{2.13}$$

making the field in the focal plane after the lens:

$$U(x,y) = \frac{e^{jkz}e^{j\frac{k}{2z}(x^2+y^2)}}{j\lambda z}4w_{px}w_{py}\,\text{sinc}\left(\frac{2w_{px}x}{\lambda z}\right)\text{sinc}\left(\frac{2w_{py}y}{\lambda z}\right) \tag{2.14}$$

The relationship between the instantaneous intensity of the light, $I(x,y)$, (which is measured by a camera, and which causes photopolymerization) and the instantaneous field, $U(x,y)$ is:

$$I(x,y) = |U(x,y)|^2 \tag{2.15}$$

This makes the intensity in the focal plane:

$$I(x,y) = \frac{16w_{px}^2w_{py}^2}{\lambda^2z^2}\,\text{sinc}^2\left(\frac{2w_{px}x}{\lambda z}\right)\text{sinc}^2\left(\frac{2w_{py}y}{\lambda z}\right) \tag{2.16}$$

A plot of this analytical solution is shown in Figure 10.

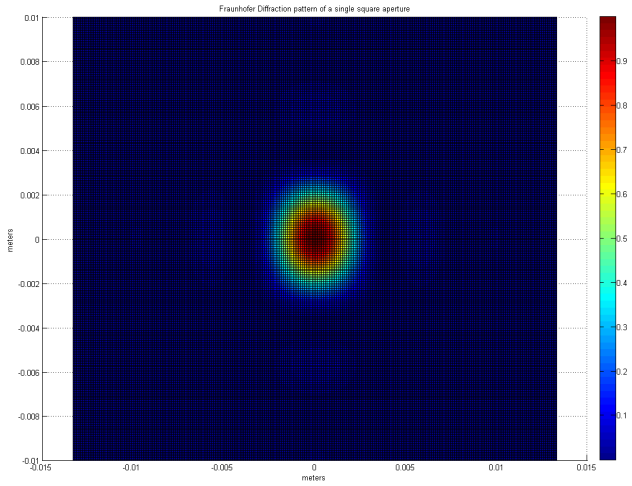

Figure 10: A plot of the 2D Fourier transform for a single square aperture (analytical solution).

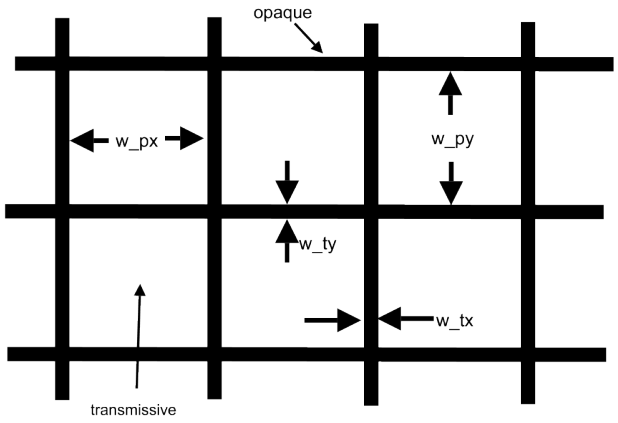

Figure 11: The dimensions of a SLM array of pixels. These are used to calculate the expected zero order diffraction pattern.

2.1.3 Diffraction pattern due to grid of pixels

The aperture of the SLM is simply a array of rectangular apertures that are separated by some opaque material (see Figure 11). The thickness of the opaque material in the x- and y-direction are w_{tx} and w_{ty}, respectively. The values for the four variables in Figure 11 can be found using the fill factor and the pixel pitch. The fill factor of the SLM is 55%, and the pixel pitch is 32 μm. Therefore:

$$w_{px} + w_{tx} = 32\mu\text{m} \tag{2.17}$$

and

$$\frac{w_{px}w_{py}}{(w_{px} + w_{tx})(w_{py} + w_{ty})} = 0.55 \tag{2.18}$$

Assuming that $w_{px} = w_{py}$ and $w_{tx} = w_{ty}$, this results in, $w_{px} = w_{py} = 24$ μm and $w_{tx} = w_{ty} = 8$ μm. The fill factor is also equal to the diffraction efficiency of all the diffractive orders combined [15]:

$$\eta_{total} = \left(\frac{w_{px}}{w_{px} + w_{tx}}\right)^2 \tag{2.19}$$

The transmittance function of the SLM with no voltage applied is:

$$\begin{aligned} t_A(\xi,\eta) = \text{rect}\left(\frac{\xi}{N_x\Delta}\right)\text{rect}\left(\frac{\eta}{N_y\Delta}\right)\text{rect}\left(\frac{\xi}{w_{px}}\right)\text{rect}\left(\frac{\eta}{w_{py}}\right) \\ \otimes\left(\left[\frac{1}{\Delta}\,\text{comb}\left(\frac{\xi}{\Delta}\right)\delta(\eta)\right]\otimes\left[\frac{1}{\Delta}\,\text{comb}\left(\frac{\eta}{\Delta}\right)\delta(\xi)\right]\right) \end{aligned} \tag{2.20}$$

where $\otimes$ denotes a convolution, N_x is the number of of pixels in the x-direction on the SLM, N_y is the number of pixels in the y-direction, and Δ is the pixel pitch, assumed to be equal in both directions. The comb function is defined as:

$$\text{comb}(x) = \sum_{n=-\infty}^{\infty}\delta(x-n) \tag{2.21}$$

The transmittance function is separable into $t_A(\xi,\eta) = t_x(\xi)t_y(\eta)$:

$$t_x(\xi) = \left[\text{rect}\left(\frac{\xi}{w_{px}}\right)\otimes\frac{1}{\Delta}\,\text{comb}\left(\frac{\xi}{\Delta}\right)\otimes\delta(\xi)\right]\text{rect}\left(\frac{\xi}{N_x\Delta}\right) \tag{2.22}$$

and

$$t_y(\eta) = \left[\text{rect}\left(\frac{\eta}{w_{py}}\right) \otimes \frac{1}{\Delta}\,\text{comb}\left(\frac{\eta}{\Delta}\right) \otimes \delta(\eta)\right] \text{rect}\left(\frac{\eta}{N_y\Delta}\right) \tag{2.23}$$

Fourier transforming the transmittance functions to get the field in the focal plane, and then squaring them to get the intensity gives a diffraction pattern of:

$$I(x,y) = \left(\frac{N_x N_y \Delta^2 w_{px} w_{py}}{\lambda z}\right)^2 \left[\sum_{m=-\infty}^{\infty}\sum_{n=-\infty}^{\infty} \text{sinc}\left(\frac{m w_{px}}{\Delta}\right) \right.$$
$$\left. \times \,\text{sinc}\left[\frac{N_x\Delta}{\lambda z}\left(x - m\frac{\lambda z}{\Delta}\right)\right] \text{sinc}\left(\frac{n w_{py}}{\Delta}\right) \text{sinc}\left[\frac{N_y\Delta}{\lambda z}\left(y - n\frac{\lambda z}{\Delta}\right)\right]\right]^2 \tag{2.24}$$

The holograms that are displayed on the SLM will act on each of the diffracted orders from the static grid of pixels. It can be thought of as many copies of the displayed hologram. The diffraction pattern of the grid of pixels will be superimposed on anything meant to be displayed in the specimen plane for patterning, but the series of mirrors and lenses act as pupils on this complex pattern of light. Due to the size of the first mirror after the SLM, only the static zero order and the two static first orders on the vertical laboratory axis is allowed through (see Figure 12). Further down the optical train, these static first orders are blocked (for the most part, as will be discussed in the section on designing the experimental set up). Note again that the patterning is done with the first diffraction order (within the static zero order).

2.1.4 Phase gratings

A phase grating is used to move the patterning beam (or a whole image) laterally in the specimen plane. Two basic types of phase gratings will be analyzed, and the one with the best diffraction efficiency will be used for patterning. The two types of grating are a sinusoidal phase grating and a blazed phase grating. The twist of the twisted nematic liquid crystal SLM causes intensity and phase modulation to be coupled, so the phase gratings used in practice can be thought of as "phase-mostly" gratings.

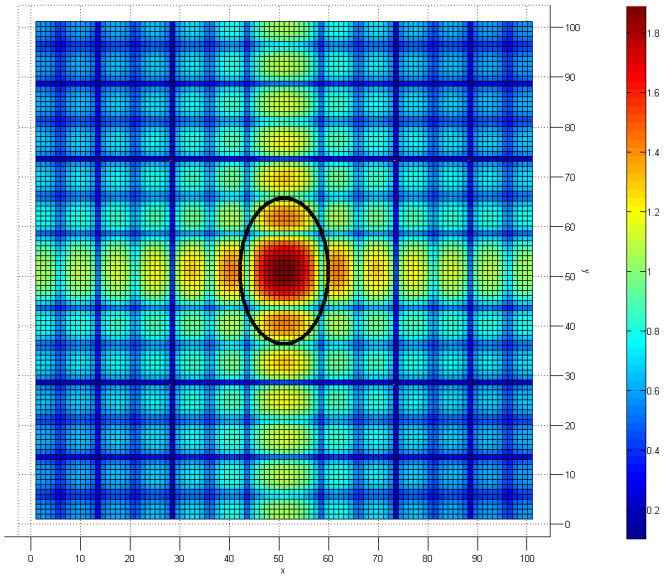

Figure 12: Intensity diffraction pattern from grid of SLM pixels in normalized units (in this case 10 pixels in each direction). The black oval is the portion of the diffraction pattern that is transmitted by the mirror after the SLM. The circular mirror acts as an elliptical pupil because the mirror is rotated about the vertical axis to deflect the light.

2.1.4.1 Sinusoidal Phase Grating The SLM can be used to display an approximation of a sinusoidal phase grating. To decide whether this is the better type of grating to use, a derivation of the first order diffraction efficiency will be done for a continuous sinusoidal phase grating (from [32]). The amplitude transmittance function is:

$$t_A(\xi,\eta) = \exp\left[j\frac{m}{2}\sin(2\pi f_0\xi)\right]\text{rect}\left(\frac{\xi}{2w}\right)\text{rect}\left(\frac{\eta}{2w}\right) \tag{2.25}$$

where the aperture is square ($2w \times 2w$), f_0 is the spatial frequency of the grating, and m is the peak-to-peak change in phase. The exponential term in the transmittance function can also be expressed as:

$$\exp\left[j\frac{m}{2}\sin(2\pi f_0\xi)\right] = \sum_{q=-\infty}^{\infty} J_q\left(\frac{m}{2}\right)\exp(j2\pi q f_0\xi) \tag{2.26}$$

where J_q is a Bessel function of the first kind, order q. This means that the Fourier transform of that part of the amplitude transmittance function is:

$$\mathcal{F}\left[\exp\left[j\frac{m}{2}\sin(2\pi f_0\xi)\right]\right] = \sum_{q=-\infty}^{\infty} J_q\left(\frac{m}{2}\right)\delta(f_X - qf_0, f_Y) \tag{2.27}$$

Assuming the grating is illuminated by a unit-amplitude, normally incident plane wave, and is one focal length from a lens, the diffraction pattern in the focal plane after the lens will be:

$$\begin{aligned}\mathcal{F}[t_a(\xi,\eta)] = \mathcal{F}[U(\xi,\eta)] &= [A\,\text{sinc}(2wf_X)\,\text{sinc}(2wf_Y)] \otimes \\ &\quad \left[\sum_{q=-\infty}^{\infty} J_q\left(\frac{m}{2}\right)\delta(f_X - qf_0, f_Y)\right] \qquad (2.28)\\ &= \sum_{q=-\infty}^{\infty} AJ_q\left(\frac{m}{2}\right)\text{sinc}[2w(f_X - qf_0)]\,\text{sinc}(2wf_Y) \qquad (2.29)\end{aligned}$$

The field in the focal plane after the lens is then:

$$U(x,y) = \frac{A}{j\lambda z}\exp[jkz]\exp\left[j\frac{k}{2z}(x^2+y^2)\right]\sum_{q=-\infty}^{\infty} J_q\left(\frac{m}{2}\right)\text{sinc}\left[\frac{2w}{\lambda z}(x - qf_0\lambda z)\right]\text{sinc}\left(\frac{2wy}{\lambda z}\right) \tag{2.30}$$

If there are many periods within the aperture of the grating ($f_0 \gg 1/w$), then the argument of the x-axis sinc term will be large, and the diffraction orders will not overlap, resulting in:

$$I(x,y) \approx \left(\frac{A}{\lambda z}\right)^2 \Sigma_{q=-\infty}^{\infty} J_q^2\left(\frac{m}{2}\right) \mathrm{sinc}^2\left[\frac{2w}{\lambda z}(x - q f_0 \lambda z)\right] \mathrm{sinc}^2\left(\frac{2wy}{\lambda z}\right) \tag{2.31}$$

This makes the peak intensity of the qth order $[AJ_q(m/2)/\lambda z]^2$ [32].

According to this approximation, the diffraction efficiency is independent of the spatial frequency as long as there are many periods within the SLM aperture. The maximum phase excursion for the SLM is a little less than 2π. The optimum phase excursion for the first order is about 3.69 radians (211°) which is within the capabilities of the SLM, and provides a diffraction efficiency of about 33.8% according to:

$$\eta_q = J_q^2(m/2) \tag{2.32}$$

This will now be compared with the model of a blazed grating.

2.1.4.2 Blazed phase grating Is it possible to do any better than 33.8% diffraction efficiency into the first order? A prism theoretically deflects 100% of light into its "first" diffraction order. A prism (or a lens) can be described by a thickness function, that defines the optical thickness with position in a plane perpendicular to the optic axis. Because the thickness for a prism varies linearly, a simple amplitude transmittance function could be:

$$t_p(y) = \exp[-jk\alpha y] \tag{2.33}$$

where α is some constant that determines the slope of the prism. The SLM can be made to function like a prism by displaying a linear phase profile. The SLM has a limited range of possible phase values. For good performance (i.e. good diffraction efficiency), it is desirable to have at least 2π of phase delay for the wavelength of light that will be used. In this way the linear phase ramp can be broken into smaller ramps modulo-2π (see Figure 13). The smaller the period of the phase ramps, the greater the deflection of the beam. This is because the phase grating imitates a thicker prism with a larger phase delay.

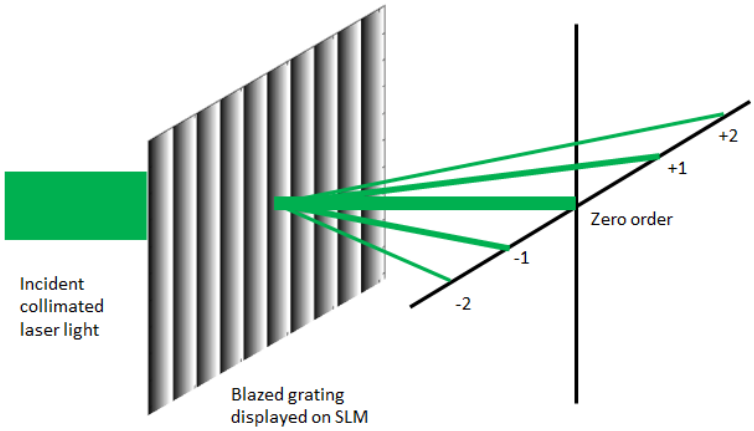

Figure 13: The blazed phase grating displayed on the SLM diffracts light from the zero order into other diffractive orders. In principal the blazed grating can deflect all the light into an arbitrary diffraction order.

A one-dimensional array of small linear phase ramps can be described by the transmittance function [98]:

$$t_a(y) = \sum_{m=-\infty}^{\infty} \delta(y - mT) \otimes \text{rect}\left(\frac{y}{T}\right) \exp(i2\pi\beta y) \tag{2.34}$$

where T is the grating period, $\beta = (n-1)d/\lambda T$, n is the refractive index of the material the blazed phase grating is made of, d is the thickness the phase ramp portion of the grating and $\otimes$ represents the convolution operator. Figure 14 shows how this transmittance function can act like a prism.

The Fourier transform of this transmittance function is given by:

$$\mathcal{F}[t_a(y)] = \sum_{m=-\infty}^{\infty} \delta(f - m/T)\,\text{sinc}(T(\beta - f)) \tag{2.35}$$

where $f = \sin(\theta)/\lambda$ and θ is the angle between each diffraction order. This gives a diffraction efficiency of the mth order of:

$$\eta_m = \text{sinc}(T(\beta - m/T))^2 \tag{2.36}$$

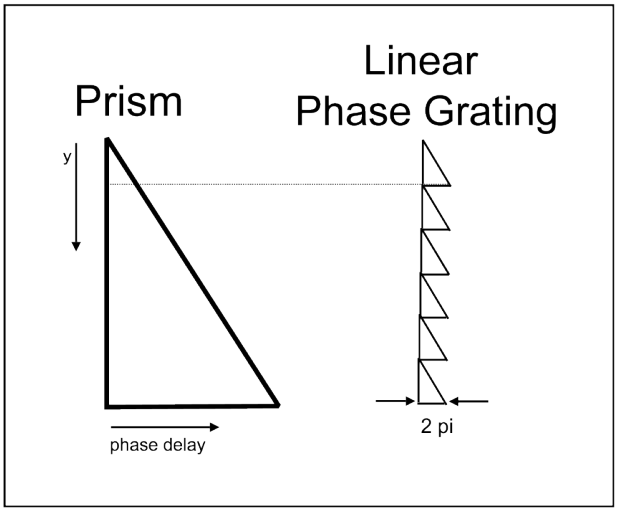

Figure 14: The SLM can be used to deflect light in the same way as a prism.

When $\beta = 1/T$, i.e., when there is 2π of optical phase delay in one period of the grating, the diffraction efficiency can be 100%. Even with the reduced phase excursion of this SLM (1.82π radians), the theoretical first order efficiency is 97%. Because the theoretical maximum first order diffraction efficiency of the blazed grating is much higher than that of the sinusoidal grating, it was chosen for use in lateral beam displacement.

The previous calculations assume a perfect linear phase ramp. This cannot be implemented by a pixelated SLM. The SLM can only display a certain discrete number of phases, and each period of the grating is made of a certain number of pixels depending on the spatial frequency of the grating. The limit of the spatial frequency of a grating is a binary grating with a period of two pixels. A binary grating puts a symmetric amount of power in both the $+1$ and -1 orders. Non-binary blazed gratings preferentially put power in either the positive or negative order.

The diffraction efficiency of a pixelated blazed grating can be derived by breaking the grating into two parts and deriving a diffraction efficiency for each [98]. The phase staircase that can be implemented with the SLM can be represented by the desired blazed grating

minus an "error" blazed grating (see Figure 15). Each pixel will have the correct phase value only at its center. The edges of each pixel will either be too high or too low. The error grating has a period and phase depth that is a factor of $1/N$ of the desired blazed grating, where N is the number of pixels per grating period [98]. The displayed phase grating then has a diffraction efficiency of the product of the diffraction efficiency of the particular order of the desired blazed grating and the zero-order diffraction efficiency of the error grating. The diffraction efficiency of a blazed phase grating with a period of N pixels (assuming that the phase levels of the pixels are evenly spaced between zero and 2π) is given by:

$$\eta_m^N = \mathrm{sinc}(\beta T - m)^2 \,\mathrm{sinc}\left(\frac{\beta T}{N}\right)^2 \tag{2.37}$$

which gives a first order diffraction efficiency of about 47% even for a binary grating. In general, the first order diffraction efficiency is [98]:

$$\eta_1 = \mathrm{sinc}\left(\frac{1}{N}\right)^2 \tag{2.38}$$

where N is the number of steps in the blaze profile. At higher deflections, the diffraction efficiency drops as the diffractive orders become more symmetrical and the blazing effect fades. As the beam is scanned during patterning, the parts of the pattern that are further from the zero order (requiring higher spatial frequencies) will receive less intensity. This must be compensated in some way to ensure uniform features over the whole patterning area and will be discussed in Chapter 5.

The gratings move the first order beam laterally and can be set using the following equation:

$$\phi_{lat}(x, y) = [2\pi(xX_o + yY_o)] \bmod 2\pi \tag{2.39}$$

where $\phi_{lat}(x, y)$ is the phase delay of the grating at a certain pixel on the SLM, x and y are pixel locations on the SLM, and $X_o = N_{\lambda x}/N_{px}$ and $Y_o = N_{\lambda y}/N_{py}$ determine the slope of the hypothetical prism (how many full wavelengths of phase delay, N_λ, across the hologram which is $N_p \times N_p$) in the x- and y- directions respectively. The displacement of the first order beam in the focal plane is proportional to the slope of the prism. The 512×512 pixel grating in Figure 16 has a slope of $X_o = 0$ and $Y_o = 20/512$ which would create a prism

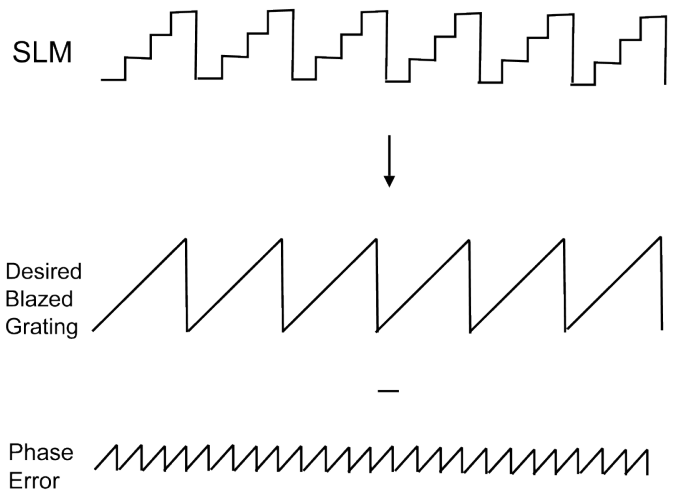

Figure 15: The diffraction efficiency of the phase staircase that can be displayed by the SLM is derived from the subtraction of the "error" from the desired blazed grating (adapted from [98]).

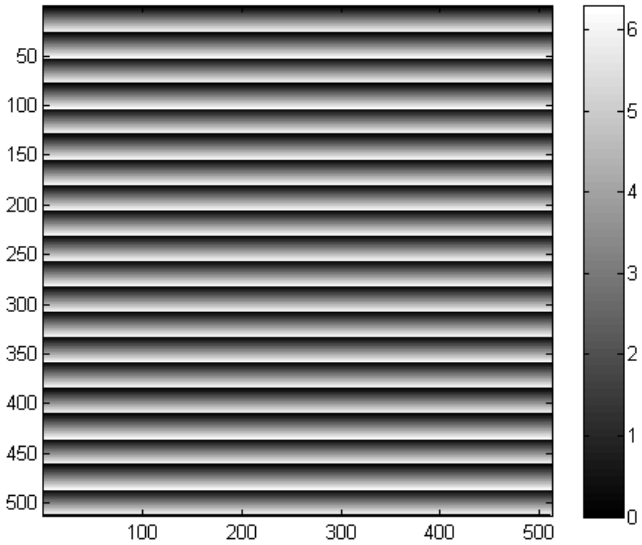

Figure 16: This is an example of a MATLAB-generated blazed phase grating. The phase level is given in the sidebar.

with a delay of 20λ at its thickest point. Because the SLM cannot create phase delays of 20λ, the modulo-2π function breaks the prism into 20 grating periods of λ, or 2π radians. In practice, the gratings displayed on an SLM can have grating periods with non-integer average numbers of pixels which allows for continuous patterning. This results in aliasing and reduced efficiency.

Finally the effect of the circuitry controlling each pixel must be taken into account. This particular SLM has a fill factor of $(w_{px}/(w_{px} + w_{tx}))^2 = 0.55$ as mentioned above. The first order diffraction efficiency is scaled by this factor, spreading the sinc-squared function as [15]:

$$\eta_1 = \left(\frac{w_{px}}{w_{px} + w_{tx}}\right)^2 \operatorname{sinc}\left(\frac{w_{px}}{(w_{px} + w_{tx})N}\right)^2 \tag{2.40}$$

2.2 FRESNEL LENSES FOR SERIAL PATTERNING

A lens is a device that imparts a quadratic phase on light that travels through it. A converging lens is thicker in the middle, and therefore has the largest phase delay there. The SLM can be used as a lens if the phase delay is designed to have a large value in the center with a radially decreasing phase that varies quadratically. Because the SLM is limited in the amount of phase delay it can cause for light of a certain wavelength, it is usually necessary to display the phase modulo-2π in the same way as the blazed grating explained above. This use of the modulo-2π function to provide the same focal length as a much thicker lens makes the lens displayed on the SLM a Fresnel lens.

The Fresnel lens displayed on the SLM can be described as a thin lens. A thin lens is one in which light enters and exits at almost the exact same lateral position [32]. Fresnel lenses can be used to move the first order beam axially (see Figure 17) and the equation describing the phase delay imparted by a thin lens is:

$$\phi_{ax}(x,y) = \frac{k}{2f}(x^2+y^2) \tag{2.41}$$

where $\phi_{ax}(x,y)$ is the phase delay at each pixel on the SLM, $k = 2\pi/\lambda$ and f is the focal length of the displayed lens. Again the SLM cannot provide phase delays greater than 2π radians, and for convenience, the factor in front of the quadratic index terms can be condensed into a single number, C_{lens} as:

$$\phi_{ax}(x,y) = [C_{\text{lens}}(x^2+y^2)] \bmod 2\pi \tag{2.42}$$

where C_{lens} is proportional to the axial displacement of the first diffraction order beam in the focal volume as explained below. The focal length of the Fresnel lens, f_{SLM}, can vary anywhere from infinity to some minimum value given by [51]:

$$\frac{r_0^2}{2\Delta(n_e-n_o)} < f \leq \infty, \tag{2.43}$$

where Δ is the liquid crystal film thickness, n_e is the extraordinary refractive index of the LC layer, n_o is the ordinary refractive index, and r_0 radius over which there is a 2π phase

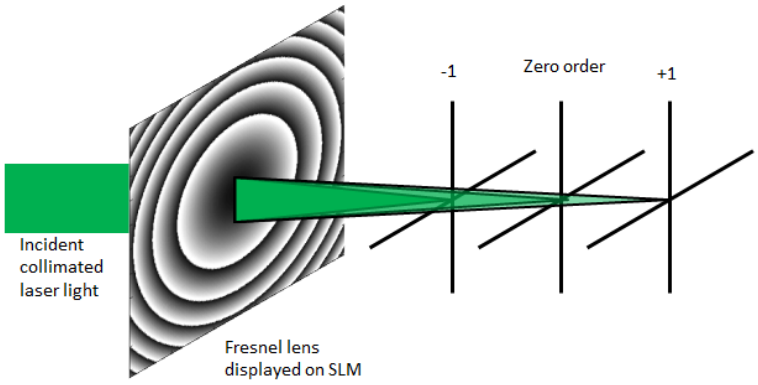

Figure 17: Displaying a Fresnel lens on the SLM moves the light in each diffraction order axially. Differently signed orders move in opposite directions.

change in the displayed pattern. The absolute minimum value this could be is two pixels, but a more realistic minimum is about 8 pixels which is $8 \times 32 = 256$ μm. This gives:

$$f_{\text{SLM min}} = \frac{r_0^2}{2\Delta(n_o - n_e)} = \frac{[(256) \times 10^{-6}]^2}{2 \times 10 \times 10^{-6}(0.05)} = 66 \text{ mm} \tag{2.44}$$

which puts a limit on the maximum axial displacement of the first diffraction order beam. The LC layer is specified as 10 micrometers thick by Holoeye. The difference between the extraordinary and ordinary refractive indices is about 0.05.

2.2.1 Gratings and Lenses

For 3D serial patterning, it is necessary to scan the beam through the volume of the desired feature. This can be done by combining a blazed grating with a Fresnel lens in what is known as the "gratings and lenses approach" as follows [57]:

$$\varphi(x, y) = [\phi_{lat}(x, y) + \phi_{ax}(x, y)] \bmod 2\pi \tag{2.45}$$

where $\varphi(x, y)$ is the phase at each pixel in the combined hologram. A movie of holograms can be made to scan the beam to each location.

Scanning can be done in 2D and 3D patterning and is necessary when available beam power is low, but higher throughput can be achieved by exposing whole patterns at once. Several algorithms have been developed to take an input target intensity pattern (2D or 3D) and give a corresponding phase hologram as an output that achieves the target pattern in the focal volume. The following sections reviews these algorithms.

2.3 GERCHBERG SAXTON ALGORITHM FOR 2D PARALLEL PATTERNING

Knowledge of the phase and amplitude of a field, $U(x, y)$ in one plane is enough to determine the phase and amplitude of the field in all other planes by using diffraction theory. When the two planes involved have a Fourier transform relationship between them (for example in the case of planes one focal length away on either side of a lens), a phase retrieval algorithm known as the Gerchberg-Saxton (GS) algorithm can be used to find a phase hologram (in the input plane) that will create a desired intensity pattern (in the output plane) [30]. The GS algorithm takes a target image (light intensity) in one plane and determines a phase hologram that transforms an input plane wave into a target intensity pattern in the far field [30]. In this case the phase hologram is displayed on an SLM. The phase delay added to the light can be changed between zero and 2π at each pixel. The phase at the specimen plane can be arbitrary. Figure 19 shows a simple graphical way to understand the algorithm and it is given more explicitly as follows (see target image and result in Figure 18):

1. Make an array of random phases to start with.
2. The intensity is 1 (due to the plane wave input) with the phase as the random array, ψ_1 ($1 \exp[i\psi_1]$).
3. Then the discrete FFT is taken of ($\exp[i\psi_1]$). This simulates what the intensity would look like at the conjugate Fourier plane.
4. Next the phase of each value in the transformed image is saved into a new phase array, ϕ_1.

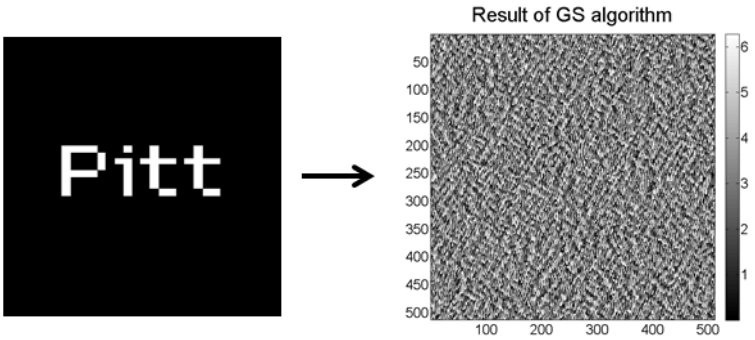

Figure 18: The GS algorithm takes the input on the left and creates the hologram on the right. When the hologram is displayed on the SLM, the target intensity pattern is visible in the specimen plane.

5. Now the intensity of the target image, A_{target} is "enforced" by multiplying it with the phase array ($A_{\text{target}} \exp[i\phi_1]$) The magnitude of ($\exp[i\phi_1]$) is of course one, so the intensity pattern looks exactly like the target image.

6. Now this new array of phases and magnitudes is inverse Fourier transformed with an FFT.

7. The phase of this array is now substituted as the initial phase at the beginning of the next iteration, ψ_2.

8. This algorithm can iterate for a given number of times, or some error value can be used as a cutoff.

Many times the output is acceptable after only 8 iterations. Errors can be induced by the fact that the GS algorithm assumes that a continuum of phase angles is available to the SLM. More computationally expensive algorithms that take into account the limited number of phase values belong to the family of direct search algorithms. Hybrid methods that add multiple holograms in different planes serve as a way to bridge the gap between 2D and 3D patterning.

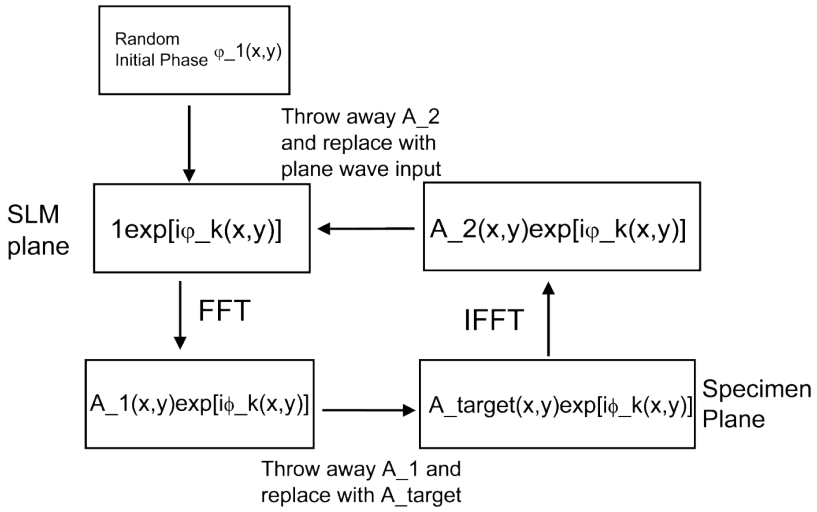

Figure 19: This is a simple diagram of the GS algorithm from.

2.4 MULTIPLEXING HOLOGRAMS (MOVING FROM PARALLEL 2D TO PARALLEL 3D EXPOSURES)

Besides adding individual voxels, it is possible to add holograms that were determined with phase retrieval algorithms like the GS algorithm. The simplest way is to add the holograms pixel by pixel. Because a Fourier hologram is distributed, the change in each pixel value leaves the image in the specimen plane intact (for a small number of summed holograms). It is possible to weight the holograms so that one contributes more to the value of a certain pixel more than another, but the process as a whole is nonlinear [17]. This creates spurious cross terms. A way to solve this problem is to separate all the holograms by assigning each hologram to a separate region of the SLM [17]. By assigning the regions randomly, the output is not convolved with any aperture functions. The weights of the holograms are now controlled by how many pixels each random mask occupies.

By adding a Fresnel lens to a precalculated hologram (from the GS algorithm), it can be displaced axially from the specimen plane. Now a 3D intensity pattern can be made by placing cross-sections of the target pattern throughout some focal volume. Another more rigorous method is to numerically propagate the light field iteratively between each target plane. In this way a more physically realizable field is created [109, 60, 61]. Both of these methods are limited by the spacing between cross-sections because the field is not specified in these regions. Another practical suggestion in the literature is to avoid using equally-spaced planes [56]. Finally, the entire 3D volume can be included in the calculation using a 3D phase retrieval algorithm. The GS algorithm can be adapted to make a single hologram that creates a 3D light intensity pattern [34, 57, 92, 107].

2.5 CREATING 3D LIGHT INTENSITY PATTERNS FOR 3D PARALLEL PATTERNING

Adding a third dimension to lithographic features allows for increased throughput and functionality. Assuming industrial strength lasers are used in the future, a limiting factor for throughput could be the number of beams that can fit in the patterning field without causing laser-induced damage to the resist. By spreading the laser power over a greater volume, more features can be made per patterning field. The SLM can be used to create a 3D intensity pattern in the specimen volume without the need to translate the substrate up and down. There are two ways to do this, either by a complex summation of phase gratings and Fresnel lenses that each correspond to a single voxel location (gratings and lenses [57, 16]), or by using some continuous 3D shape that can be replicated with almost complete fidelity (3D GS algorithm [92]). Computer generated 3D holograms have been demonstrated [107] but not used for lithography.

2.5.1 3D Parallel Patterning with Gratings and Lenses

The gratings and lenses approach described above can also be used to create 3D light intensity patterns by placing sets of voxels within a volume [57, 16]. This method only specifies where light intensity should be high, but does not specify darkness around the pattern. Unintended destructive and constructive interference can cause features cured with this approach to have defects. On the other hand, the approach is very straightforward to implement. It is possible to mitigate the interference effects by translating the phase hologram in the hologram plane during exposure, thereby dynamically changing the locations of interference. With the laser energy "smeared" in this way, only the intended feature receives the required dose for curing.

To create a single hologram that places N voxels in the focal volume, the holograms corresponding to each individual voxel must be summed in the complex plane and then the resulting hologram is the argument of that complex function [57]:

$$\phi(x,y) = \arg\left(\sum_{j=1}^{N} \exp[i\varphi_j(x,y)]\right) \tag{2.46}$$

2.5.2 3D Gerchberg Saxton algorithm for 3D Parallel Patterning

Instead of adding several holograms to create a series of cross-sections, there exist 3D phase retrieval algorithms similar to the GS algorithm that can take a target 3D light intensity pattern and derive an appropriate 2D phase hologram [56, 92, 107]. Previous methods involved taking the field in one plane, propagating it, applying constraints, propagating it more, etc., while the methods described here involve a 3D Fourier transform that does all the propagation and constraining in parallel. The algorithm in [56] is a hybrid between these two methods in that it specifies target intensity cross-sections, while [92, 107] use a 3D Fourier transform over a whole volume. This 3D Fourier transform is what defines a 3D Gerchberg Saxton (3DGS) algorithm. It should be noted that the algorithm described by Shabtay [92] requires two SLMs, while that described by Whyte and Courtial [107] does not. In the 3DGS algorithm, the constraints are imposed on the spectrum of the light, not the field.

The 3DGS algorithm uses a geometric representation of the wave equation to constrain the spectrum of the image [92]. It was implemented experimentally by [107] but was not used for lithography.

The main difficulty in creating 3D light intensity patterns is that the pattern must obey the wave equation, therefore, a given arbitrary pattern is not necessarily possible. In these algorithms, the fewer constraints, the better the results [56]. If some region outside the designed feature does not need to be completely dark, it is best not to include it in the target volume.

The 3DGS algorithm differs from the gratings and lenses algorithm in that a 3D volume is the input instead of a set of single points. In this way, the contrast around the pattern should be increased because the hologram is designed to have darkness around the desired feature. Also, the 3DGS algorithm takes the wave equation, and therefore interference effects into account, and should provide the closest realizable light intensity pattern to the target intensity pattern.

In 2D, the GS algorithm works with a Fourier transform between a pair of fields (intensity and phase), while the 3D version uses the concept of the Ewald sphere and works with a Fourier transform between a 3D intensity pattern and its k-space representation (spectrum) [107]. The Ewald sphere is the set of points that are a certain distance, $|\vec{k}|$, from the origin in k-space. The set of wavevectors that describe the spectrum of monochromatic light fall on an Ewald sphere. An Ewald sphere can be used to represent a linear differential equation [58]. For example, the Helmholtz wave equation is:

$$\nabla^2 u(x,y,z) + k^2 u(x,y,z) = 0 \tag{2.47}$$

where ∇^2 is the Laplacian operator, $u(x,y,z)$ is an electric field, and $k = 2\pi/\lambda$ is a wavenumber. The electric field, $u(x,y,z)$ can also be represented by a Fourier transform of its angular spectrum:

$$u(x,y,z) = \int_{-\infty}^{\infty}\int_{-\infty}^{\infty}\int_{-\infty}^{\infty} \tilde{u}(\nu_x,\nu_y,\nu_z) \times \exp[2\pi i(x\nu_x + y\nu_y + z\nu_z)] d\nu_x d\nu_y d\nu_z \tag{2.48}$$

where ν_x, ν_y, and ν_z are the components of the angular spectrum of $u(x, y, z)$ in spatial frequency space. Inserting equation 2.48 into equation 2.47 yields:

$$\int_{-\infty}^{\infty}\int_{-\infty}^{\infty}\int_{-\infty}^{\infty}\left[(2\pi i\nu_x)^2+(2\pi i\nu_y)^2+(2\pi i\nu_z)^2+k^2\right] \times\tilde{u}(\nu_x,\nu_y,\nu_z)\exp[2\pi i(x\nu_x+y\nu_y+z\nu_z)]d\nu_x d\nu_y d\nu_z \tag{2.49}$$

which requires that the 3D spatial frequency spectrum vector $\tilde{u}$ have a length of $1/\lambda$ if it is to be nonzero. The relationship between ν and k is $k = 2\pi\nu$, therefore another way of describing the constraint on the angular spectrum of the light is:

$$|\vec{k}|^2 = k_x^2 + k_y^2 + k_z^2 = k^2 \tag{2.50}$$

The 3DGS algorithm is similar to the GS algorithm used in earlier parts of the research, except that now, the constraint is that the k-space representation of the 3-D target intensity sits on the surface of an Ewald sphere. The algorithm tries to minimize the error between what is desired and what is physically possible given the phase delay and pixel size available to the SLM.

Each point on the Ewald sphere corresponds to a plane wave with a certain frequency and direction. A point source in the front focal plane of a lens becomes a plane wave in the back focal plane and vice versa. The SLM in the front focal plane of the Fourier transforming lens can then be thought of as modulating the phases of an array of plane waves that each correspond to a point on the Ewald sphere and come to a focus at a point in the target intensity pattern. The relationship between real-space and k-space is a Fourier transform [99].

The phase hologram displayed on the SLM cannot change the magnitude of the wavevector of the incident light, therefore the relationship between each photon's incident wavevector, $\vec{k}_{in}$ and output wavevector, $\vec{k}_{out}$ is [33]:

$$\vec{k}_{in} + \vec{k}_h = \vec{k}_{out} \text{ with } \quad |\vec{k}_{in}| = |\vec{k}_{out}| \tag{2.51}$$

where $\vec{k}_h$ is the grating vector of the hologram. In this way, the 3DGS algorithm finds a hologram that imparts a physically realizable spectrum on the outgoing light that also has the desired intensity pattern.

The three papers this analysis is based on [56, 92, 107] all involve only modeling or measuring light patterns outside of a microscope on the millimeter to meter range. What makes the work here different is that it is done with a high-NA microscope objective with the purpose of micro-manufacturing.

2.5.2.1 3DGS Implementation The 3DGS algorithm was implemented in MATLAB in the following steps (see Figure 20 for a flow chart):

1. The target intensity pattern is provided with a series of bitmap images.
2. Several parameters are defined:
   a. λ is the wavelength of light.
   b. τ is proportional to the "thickness" of the Ewald sphere. It determines how much each k-space element is weighted depending on its distance from k (the infinitesimally thick surface of the Ewald sphere).
   c. The number of pixels in the target intensity volume (in each direction).
   d. The "physical size" of the target intensity pattern.
3. The target intensity volume, $A(x, y, z)$, (in this case $128 \times 128 \times 128$ pixels) is set to a small non-zero number.
4. The target intensity bitmaps are inserted as cross-sections into $A(x, y, z)$. It was found that the performance of the algorithm was better when the number of pixels in the target intensity volume in each direction, were the same, $N_x = N_y = N_z$, which is the number of pixels in the x-direction, y-direction, and z-direction, respectively.
5. An `fftshift` function is applied to $A(x, y, z)$.
6. The last step before the algorithm starts iterating, is to set the phase of each point in the target volume, $\varphi(x, y, z)$, to a random value.
7. The 3DGS algorithm is implemented iteratively with the kth iteration looking like,

$$u_k^d(x, y, z) = A(x, y, z)exp[i\varphi_k(x, y, z)], \tag{2.52}$$

   where $A(x, y, z)$ is the desired amplitude distribution, $\varphi_k(x, y, z)$ is derived from the previous iteration, and $u_k^d(x, y, z)$ is a field distribution that has the desired amplitude but does not satisfy the wave equation [92].

8. The next step in the algorithm involves performing a 3D Fourier transform of $u_k^d(x, y, z)$ to get $\tilde{u}_k^d(k_x, k_y, k_z)$.
9. The constraint that makes the field physical is then applied by requiring that all spectral components fall on an Ewald sphere, S:

$$\tilde{u}_k^c(k_x, k_y, k_z) = \tilde{u}_k^d(k_x, k_y, k_z), \quad (k_x, k_y, k_z) \in S \tag{2.53}$$

with all other elements being set to zero. In practice this looks like:

$$\tilde{u}_k^c(k_x, k_y, k_z) = W(k_x, k_y, k_z)\tilde{u}_k^d(k_x, k_y, k_z) \tag{2.54}$$

where $W(k_x, k_y, k_z)$ is a matrix of weights determined by the magnitude of $\vec{k}$. Because of the discrete nature of the target volume, it is better to apply a nonzero weight to all the elements in the k-space volume. Whyte and Courtial use the following function [107]:

$$W(k_x, k_y, k_z) = \exp\left[\frac{-|\vec{k}(k_x, k_y, k_z)| - k)^2}{2\tau^2}\right] \tag{2.55}$$

where τ is a constant that determines the "thickness" of the Ewald sphere. By setting more elements to nonzero values, the algorithm has more degrees of freedom with which to approximate the target intensity pattern. Theoretically larger values of τ provide for a better approximation of the target intensity, but in practice, larger τ values cause the final hologram to be very noisy. All $W(k_x, k_y, k_z)$ values corresponding to elements with $k_z < 0$ were set to zero to eliminate plane waves propagating backward.
10. After that, $\tilde{u}_k^c(k_x, k_y, k_z)$ is 3D inverse Fourier transformed to obtain $u_{k+1}(x, y, z)$ which is physically realizable.
11. The $\varphi_{k+1}(x, y, z)$ for the next iteration is:

$$\varphi_{k+1} = \text{ang}[u_{k+1}(x, y, z)] \tag{2.56}$$

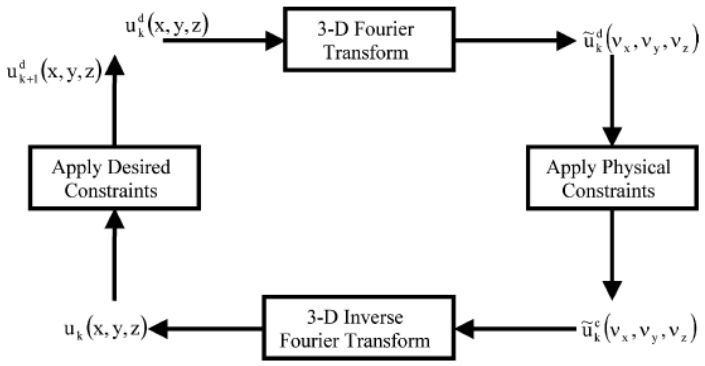

Figure 20: Error reduction algorithm for three dimensional beam shaping (*source* [92]).

Finally, a given number of iterations results in a final $u_k(x, y, z)$ which would be a physically realizable array of electric field elements in the focal volume if a 3D SLM existed to provide the correct phase values from $\tilde{u}_k^c(k_x, k_y, k_z)$. The SLM is two dimensional, and therefore cannot display a volume of phase elements. Instead, a projection $\phi_p(x, y)$ must be made for display. This projection is derived [107]:

$$\phi_p(x, y) = \text{ang}\left[\sum_{m=1}^{N_z} \tilde{u}_k^c(k_x, k_y, m)\right] \tag{2.57}$$

where N_z is the number of k-space elements in the k_z-direction. This approximation introduces errors, but they are small.

Even though Whyte and Courtial [107] describe choosing seemingly arbitrary dimensions of the target intensity pattern, it is the size and number of the SLM pixels that determines what target intensity patterns are possible. The 3DGS algorithm uses the relationship between the wavenumber of the patterning light, k, and the wavenumbers associated with the grid of points in the target intensity pattern. To use the full dynamic range of the SLM, a grid spacing that makes the largest k_x, k_y, or k_z about equal in magnitude to k, must be used. Changing the target intensity pattern dimensions does not change where light is placed in the focal volume, but the derived hologram can look different. For example, for a blazed grating with 10 periods across the SLM face, which corresponds to a target intensity

pattern with a single dot 10 pixels from the center, the amount of the grating that was displayed would change based on the chosen grid spacing (see Figures 21 and 22), but the displacement of the beam would be unchanged. The grid spacing is equal in each direction for the derived holograms in the figures. The reason the blazed grating is cutoff in Figure 22 is that the magnitude of the maximum k_x, k_y, and k_z is twice that of k, and the way the hologram is derived is based on how close each k-space triplet is to having the same magnitude as k. Fewer triplets with a magnitude near k means less nonzero values in the hologram. The projection at the end of the 3DGS algorithm results in the circular nature of the displayed hologram. There is really only a small range of grid spacings that utilize the full aperture of the hologram.

The displacement of the beam in the lateral direction is also independent of the number of pixels in the hologram. The number of pixels in the hologram (and the input target images) only limits the extent of the patterning area. The more pixels there are, further the beam can be moved.

For the axial direction, the holograms in Figures 23 and 24 were made with a target intensity of a single dot 10 pixels above the center of the target volume. The grid spacing is equal for all axes. It should be noted that the situation is different than for lateral displacement. Here the behavior of the circular "aperture" cutting off the hologram is the same as the lateral displacement case, but the displayed Fresnel lenses are not the same.

On the other hand, the derived Fresnel lenses do behave as expected with respect to the axial grid spacing. When the axial grid spacing is reduced by half, therefore increasing k_z by a factor of 2 as in Figure 25 the hologram looks identical as in Figure 24 except stretched to fill the hologram aperture. The size of the smallest circle on a Fresnel lens is inversely proportional to the axial displacement it provides.

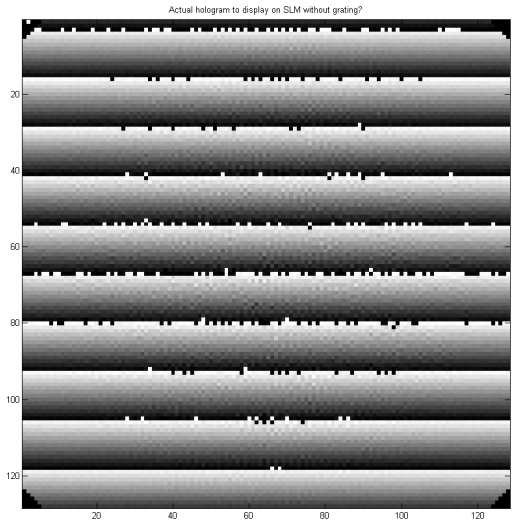

Figure 21: Blazed grating derived with 3DGS algorithm when the ratio between the maximum wavenumber on any axis, k_x, k_y, or k_z, and the wavenumber, k, of the patterning light is 1. Note that the nature of the algorithm causes the hologram to have a circular shape, and this ratio of wavenumbers makes a circle that almost exactly circumscribes the square "aperture" of the hologram.

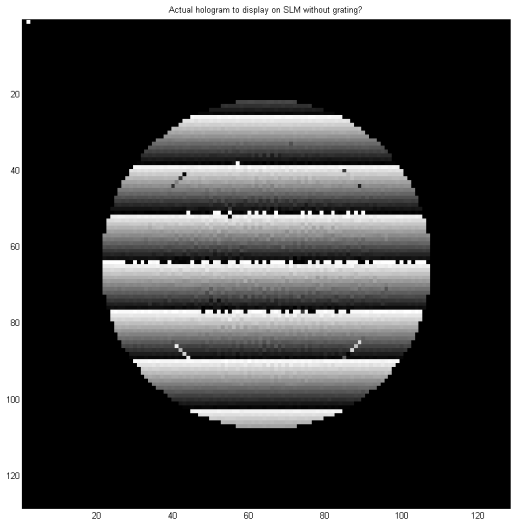

Figure 22: Blazed grating derived with 3DGS algorithm when the ratio between the maximum wavenumber on any axis, k_x, k_y, or k_z, and the wavenumber, k, of the patterning light is 2. Note that the nature of the algorithm causes the hologram to have a circular shape, and this ratio of wavenumbers makes a circle with a diameter of about half that of the circle in Figure 21.

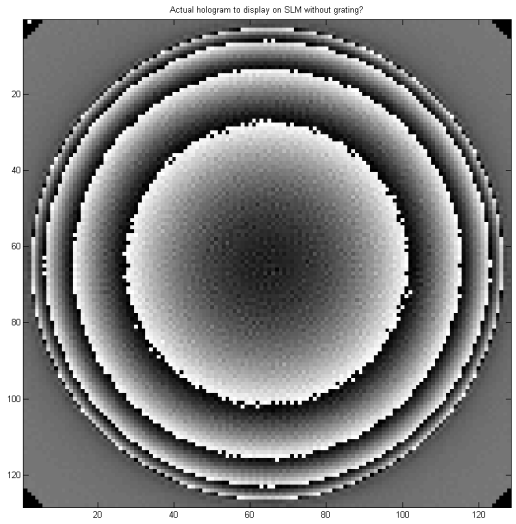

Figure 23: Fresnel lens derived with 3DGS algorithm when the ratio between the maximum wavenumber on any axis, k_x, k_y, or k_z, and the wavenumber, k, of the patterning light is 1.

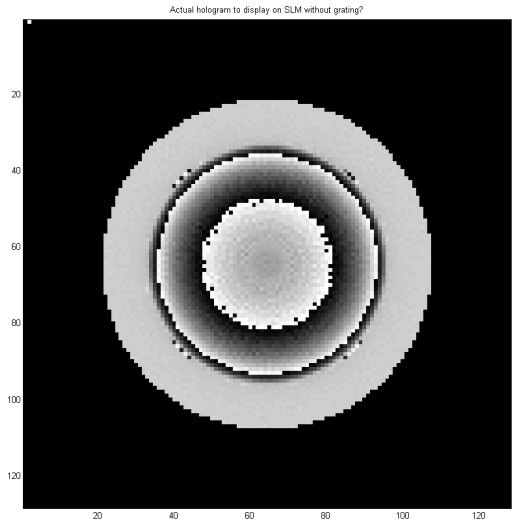

Figure 24: Fresnel lens derived with 3DGS algorithm when the ratio between the maximum wavenumber on any axis, k_x, k_y, or k_z, and the wavenumber, k, of the patterning light to be 2. Note that the nature of the algorithm causes the hologram to have a circular shape, and this ratio of wavenumbers makes a circle with a diameter of about half that of the circle in Figure 23.

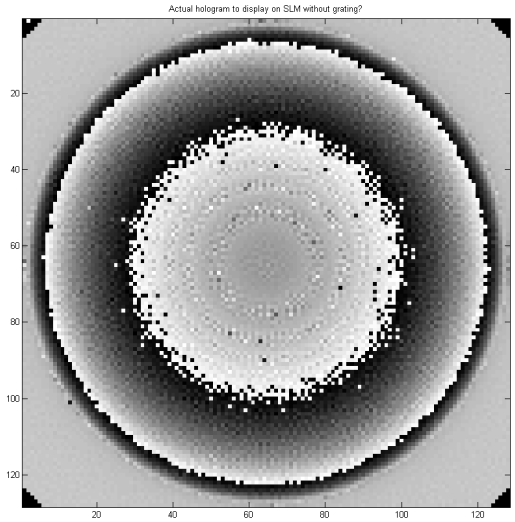

Figure 25: Fresnel lens derived with 3DGS algorithm when the ratio between the maximum wavenumber, k_x and k_y, and the wavenumber, k, of the patterning light is 1, while the ratio between the maximum k_z and k is 2.

3.0 TWO-PHOTON LITHOGRAPHY THEORY

Two-photon absorption (TPA) causes the same photopolymerization reaction in resist as single photon absorption. The only difference is that two photons are absorbed simultaneously, requiring high intensity and therefore also occurring in a smaller volume. TPA is used in this work to improve the resolution of the DMHL process. The process of photopolymerization differs depending on the chemistry of the resist/laser pair. This chapter will provide the necessary theoretical background on lithography and photopolymerization.

The fundamental unit of lithography is the voxel. It is approximately ellipsoidal and much larger axially than laterally. The properties of the cured voxel will also be discussed.

3.1 TWO-PHOTON ABSORPTION

A molecule must absorb a specific amount of energy for a certain chemical reaction to occur. In a single photon process, all of that energy is provided by the absorption of a single photon. In some cases is it advantageous to achieve the chemical reaction with light that does not correspond to that exact reaction energy (explained below). Luckily it is also possible for multiple photons to be absorbed (effectively simultaneously) to the same effect. The same amount of energy must be provided, so only certain combinations of photons will work. The probability of absorption of n photons at one time scales as I^n.

A two-photon absorption process involves the absorption of two photons simultaneously. These two photons have less energy and a larger wavelength than those in a single-photon process. In a single-photon lithographic process, the patterning resolution is proportional to

the intensity of the exposure light, while in a two-photon process, the resolution is proportional to the intensity squared as mentioned above. Figure 26 shows a comparison of energy level diagrams for both absorption processes.

There are two types of two-photon processes: degenerate and non-degenerate. Degenerate TPA occurs when two photons of the same energy (wavelength) cause a molecule to enter an excited state. Non-degenerate TPA occurs when two photons of different energy (wavelength) are used [5]. The molecule enters a "virtual state" when the first photon is absorbed, and then immediately moves to an excited state when the second photon is absorbed [5]. A degenerate two photon process is used here because the photons can be provided by the same laser source.

TPA spectra are usually taken with optical Kerr ellipsometry. TPA cross-sections are given in units of Goeppert-Mayers (GM) where 1 GM = 10^{-50}cm^{4}s per photon. If the TPA coefficient, β, is known, the TPA cross-section, $\sigma^{(2)}$ can be found (in units of GM) by [47]:

$$\beta = \frac{(\sigma^{(2)} N_A d)\text{x}10^{-3}}{h\nu} \tag{3.1}$$

where N_A is Avogadro's number, d is the concentration of the two photon absorption compound, h is Planck's constant, and ν is the frequency of the incident laser beam.

Kleinman gives an equation for the two-photon absorption cross-section:

$$\sigma^{(2)} = (\frac{e^2}{mc^2})^2 \frac{c^2}{n^2 \nu_b^2} F g(2\nu_b - \nu_c) \tag{3.2}$$

where F is the photon flux (photons/cm^2 sec), ν_b is the frequency of the laser, ν_c is the absorption frequency of the material, n is the index of refraction of the material, and $g(2\nu_b - \nu_c)$ is a function that describes the absorption band of the material also known as its *spectral lineshape* [49]. The efficiency of the two-photon process increases when a system with a narrower absorption band is used [43].

Single photon absorption spectra are readily available for many photoinitiators. In general, the single-photon absorption data cannot be used by just doubling the wavelength to obtain two-photon absorption data (LaPorte's rule). These rules are not strictly followed in asymmetric molecules, meaning single-photon and two-photon absorption spectra can be equivalent in some cases [22]. The Irgacure 369 molecule used in this research is asymmetric

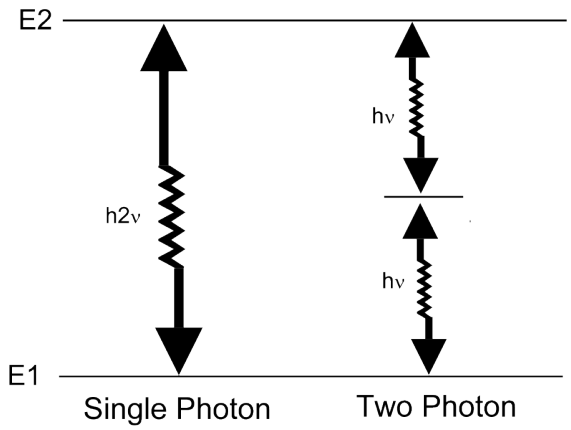

Figure 26: Energy diagram of both absorption processes. The two lower energy photons must be absorbed "simultaneously" to make the necessary energy transition. The two-photon process requires photons that are twice the wavelength of the single-photon process.

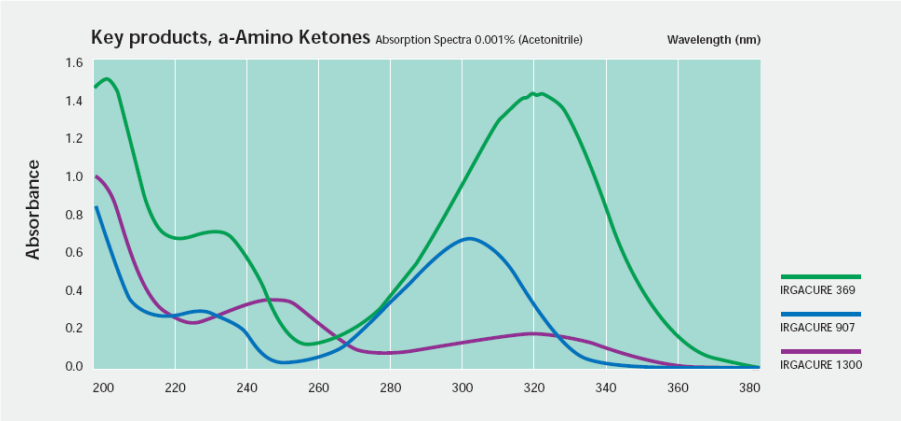

Figure 27: The topmost curve is the absorption spectrum for Ciba Irgacure 369 (*source* [12]). It has an absorbance of about 0.2 at 266 nm.

as shown in Figure 31. The laser used in this work has a wavelength of 532 nm, which means its two-photon wavelength is 266 nm. The absorption spectrum for Irgacure 369 is given in Figure 27. The absorption at 266 nm is lower than its peak value around 320 nm, but it is still high enough for the purposes of this research. For two-photon lithography, a photoinitiator with a low exposure threshold and a resist with a high damage threshold is desirable because of the high intensities involved with patterning.

3.1.1 Benefits of Two-photon photolithography

This research uses TPA because it provides process-related and result-related benefits over single-photon photolithography. DMHL requires the use of wavelengths longer than UV because the SLM can be damaged by short wavelengths. Also the threshold power for curing resist decreases with increasing concentration of photoinitiator. It is specifically possible to use higher concentrations of photoinitiator when doing TPA because the resist/photoinitiator system is more transparent to the laser wavelength and cured regions do not block deeper regions from illumination [3]. Finally, the absorption of the resist itself can limit the depth into which patterning is possible. The particular resist used here has much higher absorption in UV (see Figure 28).

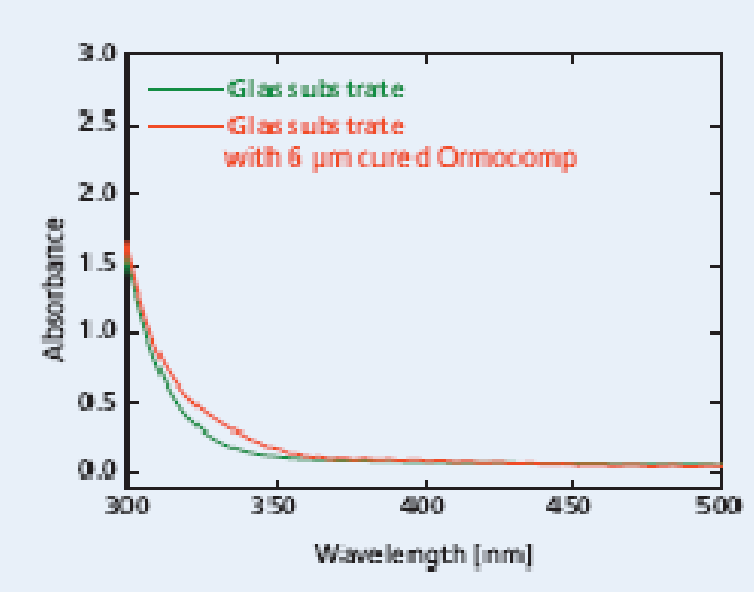

Figure 28: Absorption spectrum for Ormocomp© resist (*source* [72]).

The diffraction limited focal volume of visible light is bigger than the diffraction limited focal volume of UV light, so how much improvement results from using two-photon absorption with visible light as opposed to single-photon absorption with UV light? The improvement in the size of the photopolymerized area is mostly along the optical axis [65]. In other words, the axial resolution is better with two-photon lithography. The rate at which photoinitiator molecules are excited decreases quickly (as z^{-4}) with the distance from the focus. This is due to the quadratic dependence on the intensity. Also the exposure is confined to a small volume around the focus (on the order of λ^3, where λ is the wavelength of the incident beam) [88]. Finally, Rayleigh scattering varies as $1/\lambda^4$ and the increase in patterning wavelength by a factor of 2 reduces scattering by a factor of 16.

3.1.2 Verifying two-photon absorption

Several experiments can be done to confirm that TPA is actually taking place. Sometimes TPA can be confused with thermal curing, excited state absorption (as explained below), or even single photon absorption if the photoinitiator has weak absorption at the patterning wavelength and high intensities are used.

A simple test was done by Belfield et al. [5] in which the same photopolymerization experiment was done using a pulsed laser and a CW laser of the same wavelength. If there was no polymerization with the CW laser, then it was assumed that two-photon absorption was the only explanation. This could also be explained by the fact that the absorption at that wavelength was very low, and only significant at high intensity. Another TPA confirmation experiment is to plot excitation intensity vs. emission intensity (of the photoinitiator) and show that there is a slope of 2 on a log-log plot [22]. These two methods could not be used because no CW UV laser was available at 266 nm and there was no way to measure the photoluminescence of the photoinitiator.

One way that was possible with the available lab equipment was to check that the polymerization rate (volume/sec) is linear with laser power as it should be for two-photon processes (at least in liquid acrylates like those used here [52]). It is proportional to the square root of laser power for one-photon processes [52, 11]. The data in Figure 30 is taken from the results shown in Figure 29. It can be seen that the data fit a linear fit much better than the square-root fit, showing that it is likely a two-photon process is occurring.

3.1.3 Excited State absorption

Excited state absorption is a two-photon process where a molecule is excited in a single-photon process, and then its excited state absorbs another photon. This is different than a virtual state absorbing a photon [5].

The measurement of a photoinitiator's two-photon cross section can be difficult to interpret because of excited state absorption. When measurements are made with different pulsewidths, different cross-sections can be found. It is possible that some excited states have a long lifetime, and as the pulse gets longer, more and more molecules are pushed into

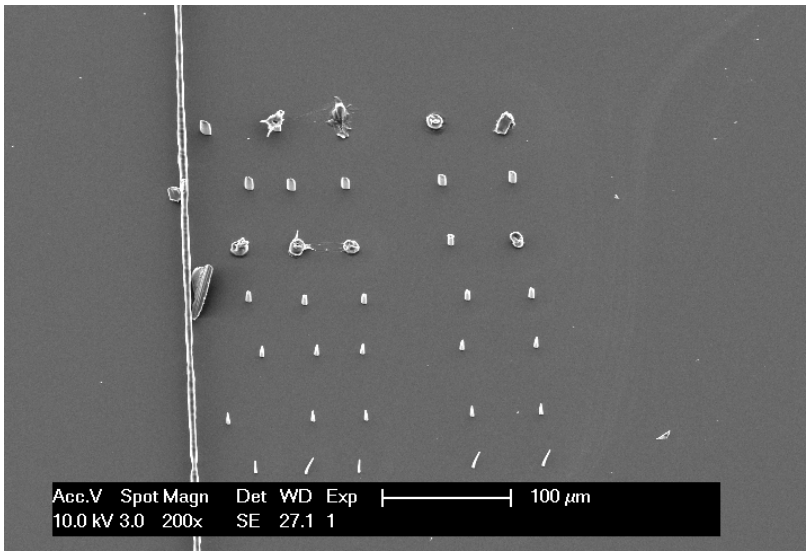

Figure 29: These are results from OrmoComp© with a 20× objective at various intensities. They are not made holographically, but simply with the laser going through the objective. The polymerization rate vs. intensity plot in Figure 30 was derived from this sample to imply two-photon absorption.

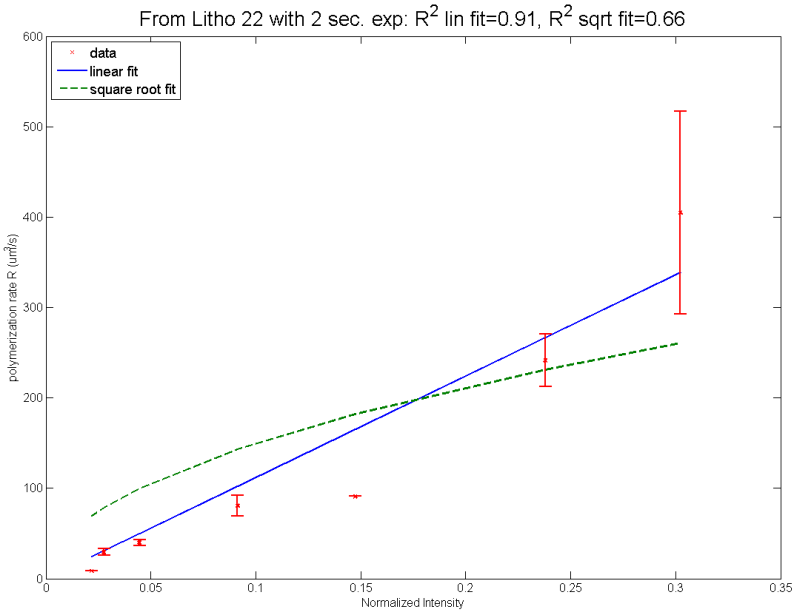

Figure 30: This is a plot of the average polymerization rate (μm^3/s) vs. exposure intensity for a two second exposure. For two-photon absorption, a linear dependence is expected. If the reaction involved single-photon absorption, the dependence would be square root. It can be seen that the fit to a line is much better.

the excited state, and then can absorb at approximately the same wavelength as what would be expected for two-photon absorption [67]. This can cause longer pulses to result in much higher values of measured two-photon absorption cross-sections.

Thermally assisted one-photon excitation can also cause photopolymerization instead of by TPA, but have less of an effect when pulsed lasers are used [46]. Without a dedicated set of experiments, it is difficult to determine if any of these absorption processes are occurring in the DHML patterning performed here.

3.2 PHOTOINITIATOR CHEMISTRY

The mechanism of photolithography is that a photoinitiator in the resist absorbs light and causes a change in the solubility of the resist. A positive photoresist is one in which the regions exposed to light become *more* soluble in the developer and a negative photoresist becomes *less* soluble. There are two common types of photoinitiator chemistries used in photolithography: photoinduced free-radical polymerization (used here) and cationic polymerization [14]. Free radical-based systems should normally be kept away from oxygen. The cationic polymerization can be of two types: vinyl and ring-opening [14]. Cationic photopolymerization is insensitive to oxygen, and therefore convenient to use in air [5]. Cationic photopolymerization has a nearly first-order dependence on light intensity, while free-radical photopolymerization has a half-order dependence. The rate of cationic photopolymerization is also much more temperature dependent than the rate of free-radical photopolymerization [14]. The most important difference pertaining to the resolution of a lithographic process is that cationic photopolymerizations can keep going even after the exposure is over while most free-radical photopolymerizations stop within a millisecond due to termination processes [14].

One reason that free-radical systems could be used in air (as they are here) is that the reaction kinetics of the cross-linking reaction are faster than those of the reaction with oxygen. There also could be something in the resist that reacts with oxygen to protect the radicals so they can participate in the cross-linking reaction. When the resist is irradiated above

a certain threshold intensity, the photolysis takes place as if there were no oxygen [105]. Even better results might be obtained by purging the photoresist of oxygen radicals but this adds complexity and expense to the process.

3.2.1 Explanation of Ciba Irgacure 369 photochemistry

The resist used in this research is OrmoComp© with 1.8% Ciba Irgacure 369, or 2-Benzyl-2-dimethylamino-1-(4-morpholinophenyl)-butanone-1 with a CAS No: 119313-12-1 as the photoinitiator. As mentioned above OrmoComp© is an inorganic-organic hybrid polymer. It is a combination of 2,2-bis(acryloyloxymethyl)butylacrylate and trimethylopropane triacrylate. It is synthesized by sol-gel chemistry [48]. The hybrid polymers are organically functionalized. ORMOCERs were developed by the Fraunhofer Institute. They have properties that make them ideal for nanomanufacturing. They have limited shrinkage and are biocompatible.

Irgacure 369 is a ketone and it takes part in free-radical photopolymerization (see Figure 31) [76]. It forms radicals by α-cleavage, β-cleavage and/or Norrish II hydrogen abstraction [76]. α-cleavage is the act of breaking a carbon-carbon bond adjacent to the carbon bearing a specified functional group. A β-cleavage is a type of bond breaking in which the bond breaks between atoms two bonds and three bonds from the carbon bearing the functional group. Hydrogen abstraction is the process by which a free radical removes a hydrogen atom from another molecule, transforming the second molecule into a free radical. The reactive species is a benzoyl radical [48].

The absorption of light by the Ciba Irgacure 369 molecule leads to polymerization in the resist. In this case, it is "radical chain polymerization". Radical chain polymerization is a chain reaction that has three phases: initiation, propagation and termination [79]. Irgacure 369 only creates one benzoyl radical per photoinitiator molecule. The photoinitiator molecule is transformed into or creates a reactive species. The reaction propagates as the growing polymer chain keeps attaching monomers. An acrylate monomer is shown in Figure 32. There are two ways that the reaction can terminate, either, two growing monomers attach to each other, or occlusion. Occlusion is heterogeneous polymerization [79]. There are three

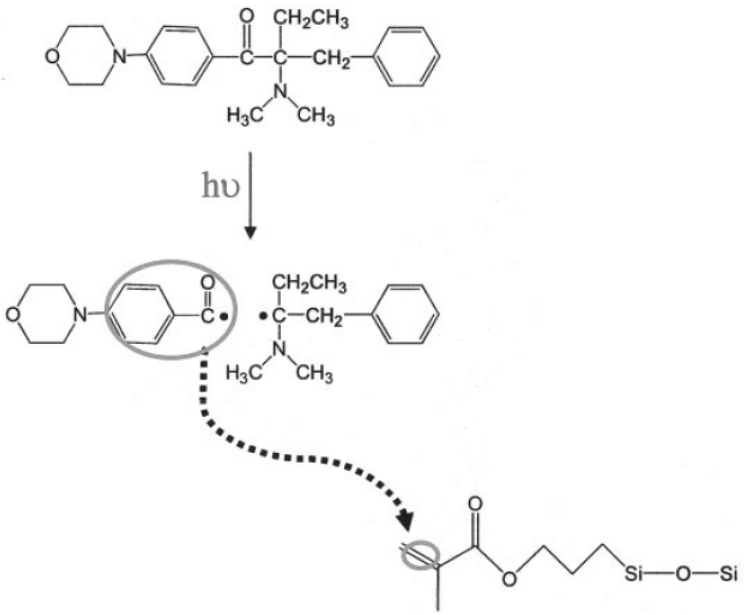

Figure 31: Irgacure 369 molecule undergoing photocleavage and causing photopolymerization of ORMOCER (adapted from [48]). The benzoyl radical is circled.

important rate constants, k_i, the reaction rate of the initiator with a monomer, k_p, the reaction rate of a growing chain with a monomer, and k_t, the rate constant associated with termination. The rate constant, k_t is and is usually orders of magnitude larger than k_p [79]. This is why the chains don't just grow until all the monomer is gone. This also likely increases the resolution of the TPA photolithography process.

The *polymerization rate* is the same as the *rate of monomer disappearance* given by:

$$\frac{-d[M]}{dt} = R_i + R_p \tag{3.3}$$

where $[M]$ is the concentration of monomer, R_i is the rate of initiation and R_p is the rate of propagation [79]. Because the polymers are much longer than two monomers, $R_p \gg R_i$. This means that the polymerization rate can be expressed as [79]:

$$R_p = k_p[M\cdot][M] \tag{3.4}$$

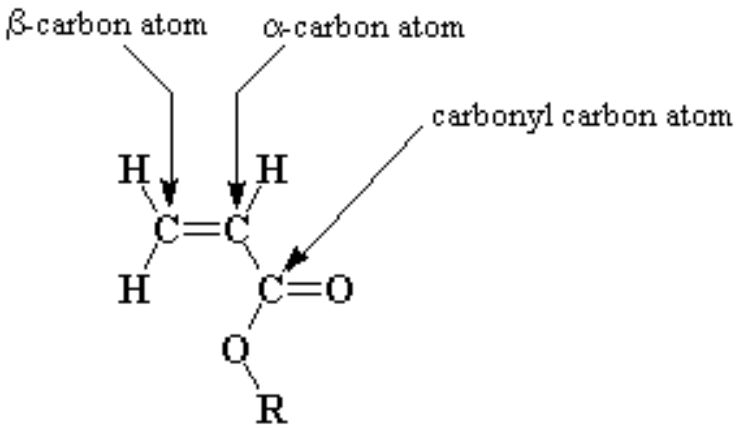

Figure 32: The chemical structure of an acrylate monomer (*source* [84]). The reactive species attaches to the left side of the monomer, and opens up a bond on the right side for it to react with another monomer. The polymer is built in this way.

where $[M]$ is the monomer concentration and $[M\cdot]$ is the total concentration of all chain radicals. After assuming that the concentration of radicals $[M\cdot]$ is constant [79]:

$$R_p = k_p[M]\left(\frac{R_i}{2k_t}\right)^{1/2} \tag{3.5}$$

This is the polymerization rate and the rate of propagation. The square root dependence on the termination rate constant is due to the fact that radicals normally terminate with other radicals, eliminating two at a time.

The rate at which the initiator dissociates into radicals has a rate constant of k_d. The rate at which the initiator produces radicals is R_d:

$$R_d = fk_d[I] \tag{3.6}$$

where f is the initiator efficiency, and $[I]$ is the initiator concentration. This equation assumes that the initiator molecule dissociates into one radical. The initiation reaction involves two separate reactions (the dissociation of the initiator into a radical and the reaction of the radical with a monomer) and the second step is normally much faster, so the rate determining

step is the dissociation of the initiator into a radical. This means R_i can be replaced with R_d, yielding a new equation for the polymerization rate:

$$R_p = k_p[M]\sqrt{\frac{fk_d[I]}{2k_t}} \tag{3.7}$$

The photopolymerization rate for a single-photon absorption system is [79]:

$$R_p = k_p[M]\sqrt{\frac{\phi\epsilon I_o[A]b}{2k_t}} \tag{3.8}$$

where ϕ is the quantum yield for initiation (the number of propagating chains initiated per light photon absorbed), ϵ is the molar absorptivity (extinction coefficient) of the photoinitiator, I_o is the intensity of light, $[A]$ is the concentration of the photoinitiator, and b is the thickness of the reaction system being irradiated. For two photon absorption, the I_o term is squared and R_p becomes a linear function of intensity.

3.3 CALCULATION OF VOXEL SIZE

There is a set of equations that explains how to predict the voxel diameter and height for two-photon absorption lithography using the laser intensity and exposure time [54, 96, 102, 97, 55, 91]. The intensity of the laser is:

$$I(r,z) = \frac{2P_t}{\pi w(z)^2}\exp\left[\frac{-2r^2}{w(z)^2}\right] \tag{3.9}$$

where P_t is the average power of the laser, $w(z)$ is the radius of the beam at a particular axial distance from the focus, and r is the radial position [54].

By assuming the geometry of the Gaussian beam shape is hyperbolic (in a cross-section along the optic axis), the intensity and radius of the beam are:

$$w(z) = \frac{\lambda}{\pi\tan\theta}\left[1+\left(\frac{\lambda z}{\pi w_0^2}\right)^2\right]^{1/2} \tag{3.10}$$

where λ is the wavelength of light,$\theta = \sin^{-1}(\mathrm{NA}/n)$ is the angular aperture of the objective, n is the index of refraction of the immersion oil, NA is the numerical aperture, and w_0 is the beam radius at the focus [54].

The rate of change of the density of radicals, ρ, produced by laser pulses in the polymerization process goes as [91]:

$$\frac{\mathrm{d}\rho}{\mathrm{d}t} = (\rho_0 - \rho)\sigma_2 \cdot N^2 \tag{3.11}$$

where ρ_0 is the primary initiator particle density, σ_2 is the effective two-photon cross-section for the generation of radicals and N is the photon flux.

Using the above three equations, Lee derives equations for the diameter and height of a voxel [54]:

$$d(P_t, t) = \frac{\lambda}{\pi \tan\theta}\left[\ln\left(\frac{4\pi^2 P_t^2 t[\tan\theta]^4}{E_{th}\lambda^4}\right)\right]^{1/2} \tag{3.12}$$

$$l(P_t, t) = 2z = \frac{2\lambda}{\pi[\tan\theta]^2}\left[\left(\frac{4\pi^2 P_t^2 t[\tan\theta]^4}{\lambda^4 E_{th}}\right)^{1/2} - 1\right]^{1/2} \tag{3.13}$$

where d is the voxel diameter, l is the voxel length, E_{th} is the threshold energy, P_t is the laser power, and t is the exposure time. The plots of these equations imply that the voxel length (height) is more sensitive to the laser power than to the exposure time [54].

The diameter of the voxel for constant intensity varies as [54, 91]:

$$d(t) = A_1\sqrt{\ln B_1 t} \tag{3.14}$$

where t is the exposure time and A_1 and B_1 are constants determined by the laser parameters and the photochemistry. The diameter of the voxel for constant exposure time varies as:

$$d(I) = A_1\sqrt{\ln B_2 I^2} \tag{3.15}$$

where I is the average intensity of the laser. Note that the constant A_1 should be the same for both fits. It is defined as [55]:

$$A_1 = \frac{\lambda}{\pi \tan(\sin^{-1}(\mathrm{NA}/n))} \tag{3.16}$$

From these derivations, it can be seen that the way to get the minimum voxel size is to use a scheme called "minimum power, minimum exposure time"[54]. There are two regimes

in which voxels grow: focal spot duplication and voxel growth [54]. In the first, the voxel size is more dependent on intensity, but in the second mode, the shape of the voxel is more exposure time dependent. At high exposure intensities, as intensity is increased, the voxel grows more axially than laterally for a given exposure time. The voxel can be thought of replicating the focal spot in three dimensions. At lower intensities and longer exposures, the voxel grows isotropically with time as radicals diffuse outward [55]. This means that to form voxels that are axially smaller, it is best to find a low exposure intensity and use a longer exposure time rather than a high exposure intensity with shorter exposure time.

The theory presented in Chapters 2 and 3 assumes perfect performance of all experimental components. This does not happen in reality, and certain adjustments and considerations must be made to improve the quality of the micro-manufactured features. The next chapter deals with these design considerations.

4.0 DESIGN CONSIDERATIONS FOR THE DMHL SYSTEM

To apply the theory that has been laid out, experimental realities must be considered. The particular SLM, laser, and resist have physical limits that determine what types of microstructures can be made. The optical system has inherent aberrations. The effective resolution of the experimental setup determines the smallest critical dimension of a feature and how close two separate features can be placed. The physics of liquid crystals (interaction with light, response to voltage, etc.) and the nature of the driving electronics also affect the patterning capabilities of the experimental system.

As with most laser systems, the size of the beam at each point in the optical train must be designed with all system apertures in mind. The beam comes out of the laser with a diameter of about 0.8 mm. Ray transfer matrices can be used to show the effect of each lens and each segment of beam propagation. Each point on a ray is described by two variables, its distance from the optical axis, x and the angle it makes with the optic axis, θ (see Figure 33). This is assuming a radially symmetric beam. The following sets of matrices show the effect of propagation and of a lens on these variables:

$$\begin{bmatrix} 1 & d \\ 0 & 1 \end{bmatrix} \begin{pmatrix} x \\ \theta \end{pmatrix} = \begin{pmatrix} x' \\ \theta' \end{pmatrix} \tag{4.1}$$

$$\begin{bmatrix} 1 & 0 \\ \frac{-1}{f} & 1 \end{bmatrix} \begin{pmatrix} x \\ \theta \end{pmatrix} = \begin{pmatrix} x' \\ \theta' \end{pmatrix} \tag{4.2}$$

The first equation is for the propagation of a ray. The second is for a lens. Propagation changes only the x value of the ray, while a lens changes only the angle.

As seen in Figure 34, the first apertures to be considered are the shutter and ND filter apertures. They are placed inside the beam expander because the Thorlabs beam shutter

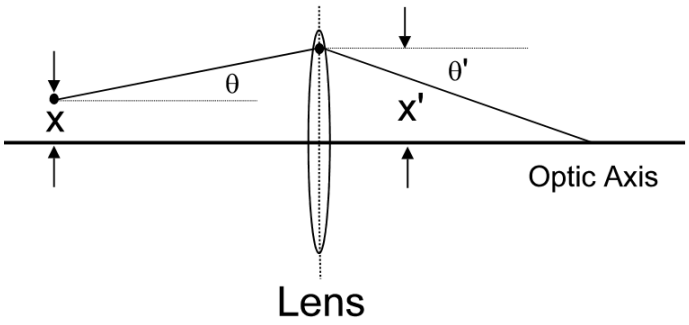

Figure 33: Each point on a ray can be described by two variables, x and θ. Two example points are given before and after a ray has traversed a lens.

aperture is only 1.26 cm in diameter and the beam must be expanded beyond this to illuminate the phase hologram displayed on the SLM. After the beam expander, but before the SLM, a half-wave plate is placed. The half-wave plate is set to 26 degrees off fast axis vertical and is used to rotate the linear polarization of the laser light to maximize the diffraction efficiency in the patterning beam (first order). The diameter that the beam must be expanded to is determined by the fact that the holograms to be displayed on the SLM will be 512×512 pixels. This choice was made for ease of computation with fast Fourier transforms (FFTs). The holograms will therefore take up an area 1.64 cm by 1.64 cm (pixel pitch is 32 μm). The beam expander is designed to expand the beam by a factor of $f_2/f_1 = 400/20 = 20$ to a diameter of 1.6 cm which almost fills the hologram (keeping almost all of the laser intensity going through the hologram).

The holographic phase gratings displayed on the SLM can diffract the first order through a range of angles. Where each hologram directs the beam in the specimen plane of the objective is determined by the location, number, and focal lengths of the lenses after the SLM. An odd number of lenses transforms the diffraction angles created by each phase grating into a beam displacement in the specimen plane. Three lenses were chosen because

a single lens (the objective) does not allow for scaling the beam to fit in the back aperture of the objective. The beam is too large after transmission through the SLM. For a three lens system, the transfer function for a ray looks like:

$$\begin{bmatrix} 0 & \frac{-f_1 f_3}{f_2} \\ \frac{f_2}{f_1 f_3} & 0 \end{bmatrix} \quad \begin{pmatrix} x \\ \theta \end{pmatrix} = \begin{pmatrix} x' \\ \theta' \end{pmatrix} \tag{4.3}$$

The first diffraction order must make it from the SLM to the microscope objective aperture (5 mm diameter for the 100× objective). The distance between the first two lenses after the SLM is the sum of their focal lengths, so it acts to compress the beam by a factor of $f_4/f_3 = 25/75 = 0.33$ to 5.3 mm which just overfills the 100× microscope objective aperture. Overfilling the back aperture of the objective improves the resolution of the polymerization by increasing the power in the rays coming from the greatest angles [3]. Most of these decisions are constrained by the fact that only a small set of lens focal lengths are available. Also, it is important for the beam to not come to a focus on any of the mirrors because the beam is powerful enough to damage them.

Losses of light due to the use of the SLM come from various sources. The circuitry around each pixel is opaque and blocks light. There is light reflected off the front and back faces of the SLM. The array of pixels acts like a 2D diffraction grating, which diffracts light into higher orders that are then lost due to the finite apertures of the mirrors and lenses. The following sections will discuss the resolution of the experimental system, the physics and characterization of the SLM, and the characterization of the laser.

4.1 RESOLUTION

The resolution of a lithographic process is usually determined by measuring the width of a cured line of resist. For serial patterning, this corresponds to a line one voxel thick, and for parallel patterning, the standard will be the width of a cured line made with an input image one pixel thick. The axial resolution will be found by making a series of lines at increasing depth. When the line either falls over or does not appear after development because it did not attach to the substrate, the height of the previous feature will define the axial

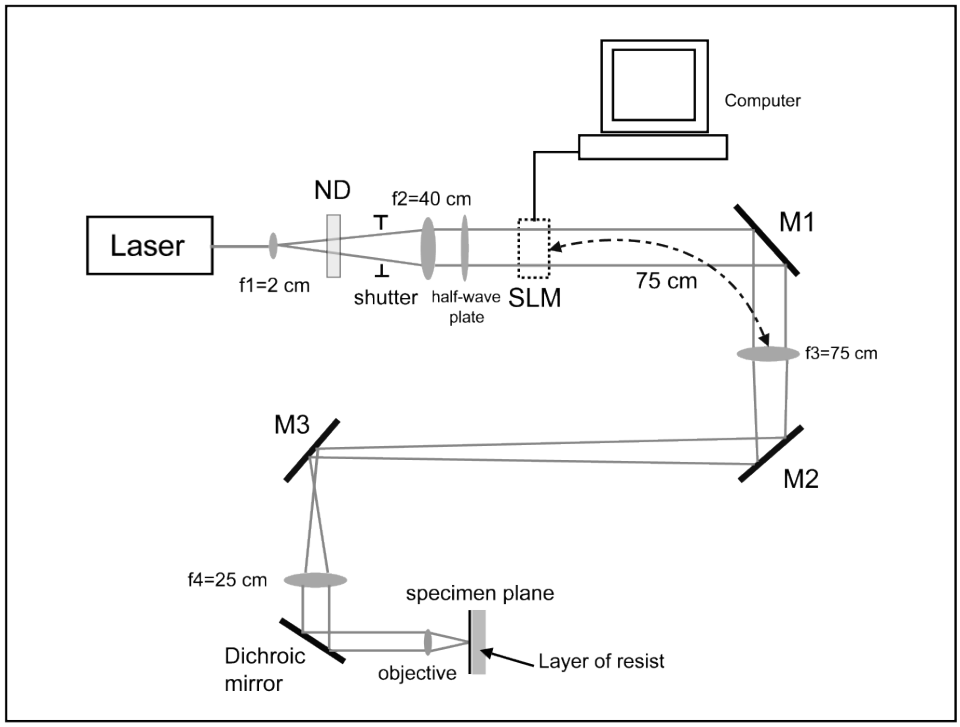

Figure 34: This is a schematic diagram of the DMHL set up. The laser is expanded into a collimated beam that is the input to the SLM. The exposure of the substrate is switched on and off by the shutter. A neutral density filter (ND) is used to control the laser intensity. The half-wave plate rotates the linear polarization of the laser to maximize the diffraction efficiency into the first diffraction order. The SLM is transmissive. After the SLM, the light propagates to the specimen plane through three lenses. The first lens is placed about one focal length away from the SLM to perform the Fourier transform. The lenses also scale the desired intensity pattern.

resolution. It is also possible to measure the axial thickness of a line of resist hanging in the air between two pillars. Both measurements give important information about the 3D patterning capabilities of the system.

The equation for resolution in image formation is a good place to start in setting expectations on the resolution of the lithographic process. It is based on the ability to distinguish between two adjacent points of light. The intensity of the cross-section perpendicular to the direction of propagation of every point of light is described by a sinc-squared function and the distance between the center of the first point and the first minimum in the second point's intensity defines the resolution, R:

$$R = \frac{k_1 \lambda}{\mathrm{NA}} \tag{4.4}$$

where k_1 is process dependent but is usually between 0.5 and 1, and λ is the wavelength of light. Using NA= 1.4 and λ = 532 nm, the resolution of the process described here is theoretically 232 nm, but the actual process resolution must be measured. The NA is:

$$\mathrm{NA} = n \sin \theta_a \tag{4.5}$$

where n is the refractive index of the medium (air or immersion oil depending on the objective lens) and θ_a is half the angular aperture of the objective.

The resolution in the third dimension (axial resolution) is related to the depth of field of the experimental set up. The depth of field is related to wavelength and NA by:

$$z = \frac{k_2 \lambda}{(\mathrm{NA})^2} \tag{4.6}$$

where k_2 is another process-dependent constant with a value of about 0.5. This implies an expected axial voxel length of about 0.5 μm using λ = 532nm and NA= 0.75, and 0.13 μm if the NA= 1.4 objective is used. These imaging-derived values do not take into account curing thresholds in the resist. Jenness achieved an axial voxel of about 2 microns in cured resist [41]. This value will be used as a benchmark.

4.1.1 Position accuracy limits of beam

There are two beam positioning resolutions pertinent to the experimental design. The first is the limit for FFT-based algorithms like the GS algorithm and the second is for arbitrary blazed phase gratings. A blazed phase grating was described in Chapter 2. Fundamental increments in a blazed grating are integer wavelengths of optical path length. It is well known that FFT-based algorithms can only place voxels on a grid of points corresponding to these fundamental increments [89].

The FFT-based limit can be found by first calculating the theoretical extent of the first order patterning area, and then dividing by the number of pixels in the phase hologram. For a three lens system, the transfer function for a ray is given above. Then the equation for the maximum displacement of the beam in the patterning field (for a ray coming from the center of the SLM) is given by:

$$\frac{-f_1 f_{\text{obj}}}{f_2}\theta_{\max} = 41\mu\text{m} \tag{4.7}$$

where $f_1 = 75$ cm, $f_2 = 25$ cm, $f_3 = f_{\text{obj}} = 1.645$ mm for the 100× objective, and $\theta = \theta_{max} = 0.48°$. This gives a theoretical patterning area of 82×82 μm =6724 μm^2 and allows for the calculation of the parallel patterning (FFT-based) resolution with a 512×512 pixel input image [4]. This resolution is 160 nm.

By using a hologram calculating algorithm like the GS algorithm that uses FFTs, points of light can only be placed on a grid with this 160 nm spacing. This is the best theoretical resolution achievable in the parallel patterning mode. The field of view of the CCD when the 100× objective is in use is about 42 μm by 56 μm which makes the rest of the patterning area difficult to use. A different set of lenses could be used to compress this patterning area to fit completely in the CCD field of view, but it is unnecessary. The lateral dimension of a cured voxel of resist is much larger than 160 nm.

With reference to the X_o and Y_o values that determine how many periods the blazed gratings have (see Chapter 2), each wavelength's worth of phase across the SLM face moves the first order beam by 160 nm for the 100× objective. The actual beam steering resolution for serial patterning is even better than this 160 nm limit because phase gratings can be

displayed that have a non-integer number of wavelengths across their face. Beam steering is effectively continuous in this mode [89, 104, 71]. The ultimate resolution of the DMHL process is determined by the size of the smallest curable voxel of resist (∼300 nm).

This research involves patterning with the zero order of the grid of pixels, but the first order of the phase hologram. The pixelation causes higher order copies of the hologram image. The result is that the effective patterning area is smaller than stated above. The zero order is located at the center of this area and must be blocked in some way. This makes the central region of the patterning area unusable. Also, because the conjugate first order sometimes has enough power in it to induce photopolymerization, the usable patterning area is a little less than half of the theoretical patterning area (see Figure 35). Note that it is possible to place the zero order outside the CCD field of view and have the entire CCD field of view be available for patterning, but the limited laser power available makes this unnecessary. Uniform patterning at the best achievable resolution is only possible near the zero order. This will be explained below.

There is another reason to limit the patterning field. The first diffraction order that is used for patterning is not the only diffraction order deflecting light onto the specimen plane. Opening up the iris to let the first diffraction order move around a larger area also allows other orders to make spurious features (see Figure 36).

4.1.2 Relating $C_{\mathbf{lens}}$ to real image displacement

It is also important for the design of micro-manufactured features, to know the conversion between C_{lens} and axial displacement of the patterning beam in the specimen plane. Ray and lens matrices can be used to find this relationship. The SLM must be counted as a lens.

The first important parameter to be found is the radius of the smallest circle displayed in the Fresnel lens. This allows for the calculation of the focal length. Because a modulo-2π function is used, the smallest circle will have a boundary when the phase reaches 2π. The smallest circle of a displayed Fresnel lens is:

$$r_0 = \text{floor}\left(\sqrt{\frac{2\pi}{C_{\text{lens}}}}/\Delta x\right) p \tag{4.8}$$

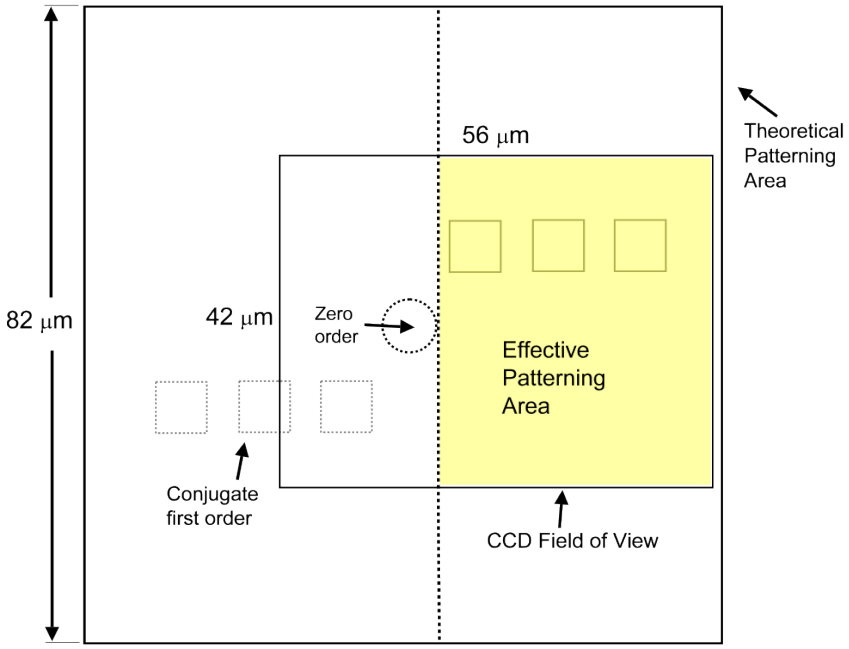

Figure 35: Explanation of reduced effective patterning area.

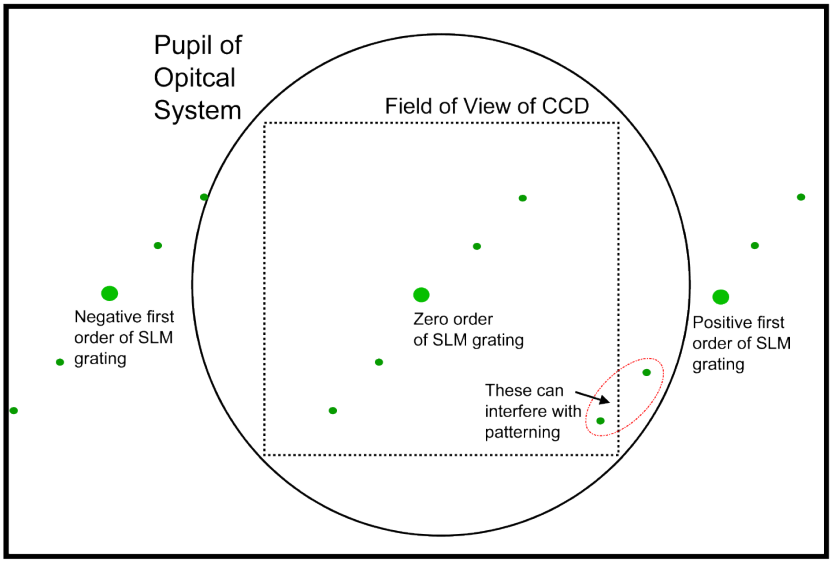

Figure 36: Light from other diffracted orders can interfere with the intended patterning beam.

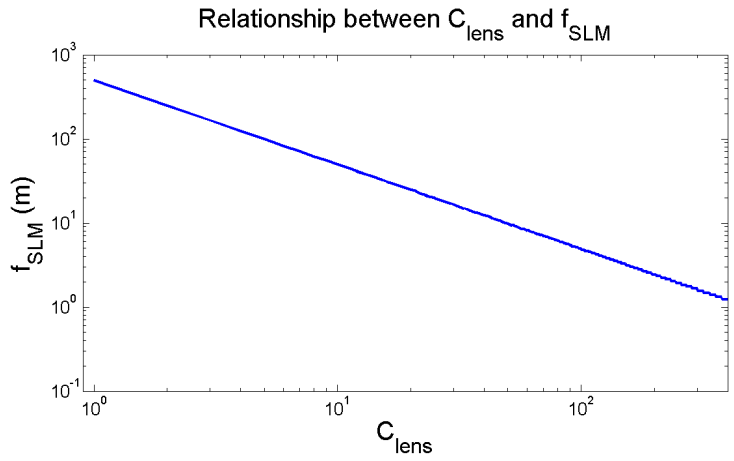

Figure 37: As C_{lens} increases, the effective focal length decreases as $1/C_{\text{lens}}$.

where Δx is the size of one pixel according to the definition in the MATLAB script (in this case from a `linspace` command) and $p = 32$ μm is the pixel pitch of the SLM. Then the equation for the effective focal length of the SLM, f_{SLM} is given by (also given in equation 2.43):

$$f_{SLM} = \frac{r_0^2}{2\Delta(n_e - n_o)} \tag{4.9}$$

The relationship between C_{lens} and f_{SLM} is plotted in Figure 37.

The relationship between C_{lens} and actual image displacement can then be found through a set of ray matrices. The input of the system is defined here as the outer ray of a collimated beam with a radius of 1.27 cm. This looks like:

$$\begin{pmatrix} x \\ \theta \end{pmatrix} = \begin{pmatrix} 0.0127 \text{ m} \\ 0^\circ \end{pmatrix} \tag{4.10}$$

After accounting for all but the propagation from the objective to the specimen plane, we have:

$$\begin{bmatrix} 1 & f_{\text{obj}} + \Delta z \\ 0 & 1 \end{bmatrix} \begin{pmatrix} A \\ B \end{pmatrix} = \begin{pmatrix} 0 \\ \theta' \end{pmatrix} \tag{4.11}$$

where A and B are constants that depend on the derived f_{SLM}, f_{obj} is the focal length of the microscope objective, θ' is an unconstrained angle at which the outermost ray of light

intersects the focus, and Δz is the axial displacement of the first order beam. The focal length of the objective can be related to the tube lens and magnification by:

$$f_{\text{obj}} = f_T/M \tag{4.12}$$

where f_T is the focal length of the tube lens of the microscope and M is the magnification. The tube lens of the Zeiss microscope used here has a focal length of 164.5 mm. The displayed hologram must be sized correctly so that each pixel correspond to a pixel on the SLM. The axial displacement can then be found by solving for Δz in Equation 4.11. Conveniently, the axial displacement of the first order beam is linear with C_{lens} (see Figure 38). The calculated conversion between C_{lens} and axial displacement in the specimen plane is:

$$50 \text{ nm per } C_{\text{lens}} \text{ for } 100\times \text{ objective} \tag{4.13}$$

$$124 \text{ nm per } C_{\text{lens}} \text{ for } 63\times \text{ objective} \tag{4.14}$$

The theoretical limit for axial displacement with this SLM occurs at the smallest possible radius of the Fresnel lens that can be displayed. The calculated minimum focal length possible for a Fresnel lens displayed on the SLM in this experiment corresponds to an axial displacement of about 400 μm using the 100× objective. This limit is not possible in practice because of aliasing and reduced diffraction efficiency due to high spatial frequencies in the Fresnel lens. Also, as explained below, asymmetry in the SLM drive circuitry limits the spatial frequency even more along one axis. This can create highly astigmatized beams. Finally spherical aberration of the objective lens limits the axial displacement long before the SLM's limitations do.

Another parameter that affects the movement of the beam is the number of electrodes over which the phase change is implemented [90]. As seen in plot of the axial displacements versus C_{lens} shown in 38, at high spatial frequencies, the displacement (axial or lateral) becomes more discrete. This reduces positioning resolution at high displacements.

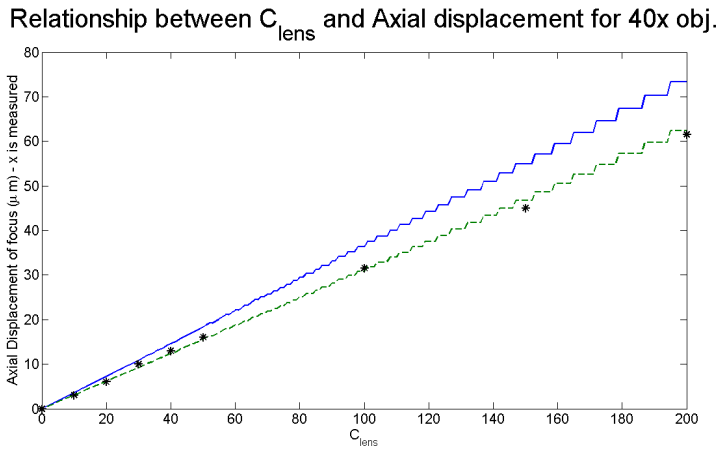

Figure 38: This plot shows a model of how the first order beam should move axially with increasing C_{lens}. The solid line is for an LC layer thickness of 10 μm and the dashed line is for an LC layer thickness of 8.5 μm. The measured data is plotted as stars. The measured data appears to match the thinner LC layer thickness, and this thickness is feasible. The model has a step-like nature at high C_{lens} because of the pixelation of the SLM.

4.2 OPTICAL ABERRATIONS

Optical aberrations are deviations from a perfect spherical wave focusing to a diffraction limited point. Any optical aberration can be expanded in terms of a complete set of polynomials that are orthogonal over the interior of the unit circle [10]. The Zernike polynomials (see Figure 39) are one such set, and will be used to compensate for aberrations in the DMHL system described here [77]. In theory any aberration that is separable can be fully compensated and each aberration can be corrected independently [71]. The main aberrations experienced in DMHL and other holographic systems (holographic optical traps) are spherical aberration and astigmatism.

The Zernike polynomial index j, as defined by Noll [77], depends upon the aberration order n and azimuthal index m by

$$j = \tfrac{1}{2}(m + n(n+2)) \tag{4.15}$$

With this ordering, there are even and odd Zernike polynomials defined as:

$$Z_j(r,\theta) = \begin{cases} \sqrt{n+1}R_n^0(r), & m = 0 \\ \sqrt{2(n+1)}R_n^m(r)\cos(m\theta), & m \neq 0, j \text{ even} \\ \sqrt{2(n+1)}R_n^m(r)\sin(m\theta), & m \neq 0, j \text{ odd} \end{cases} \tag{4.16}$$

where

$$R_n^m(r) = \sum_{s=0}^{(n-m)/2} \frac{(-1)^s(n-s)!}{s![(n+m)/s-s]![(n-m)/2-s]!} r^{n-2s} \tag{4.17}$$

in which r is a radial coordinate and the values of n and m are always integers and satisfy $m \leq n$ and $n - |m|$ =even. For example, the Zernike polynomials for astigmatism in polar coordinates are:

$$Z_5(r,\theta) = \sqrt{6}r^2 \sin 2\theta \tag{4.18}$$

and

$$Z_6(r,\theta) = \sqrt{6}r^2 \cos 2\theta \tag{4.19}$$

respectively, where $r = \sqrt{x^2+y^2}$ and θ is the angle with the horizontal axis of some pixel (x,y) on the SLM taking (0,0) as the center of the SLM. The value of the polynomial, Z_5, Z_6, etc. is multiplied by some coefficient, a_5, a_6, etc. to provide a certain amount of aberration compensation. The Zernike coefficients can be related to physical values. For example, astigmatism coefficients can be given in units of wavelengths. The number of wavelengths of a certain aberration is derived by taking the unwrapped phase of the hologram and dividing the maximum phase delay by 2π i.e., $a_5/2\pi$ is the number of wavelengths of x-astigmatism. The gratings and Fresnel lenses used to move the light can be thought of as the first three Zernike polynomials (tilt in x and y, and defocus).

4.2.1 Spherical Aberration

Spherical aberrations occur when a beam of light travels through media of differing refractive index on its way to a focal point. Spherical aberrations decrease optical resolution. Most oil immersion, high-NA microscope objectives are designed to observe a specimen that is surrounded by a material with about the same refractive index as glass, $n_g = 1.52$ [86]. In

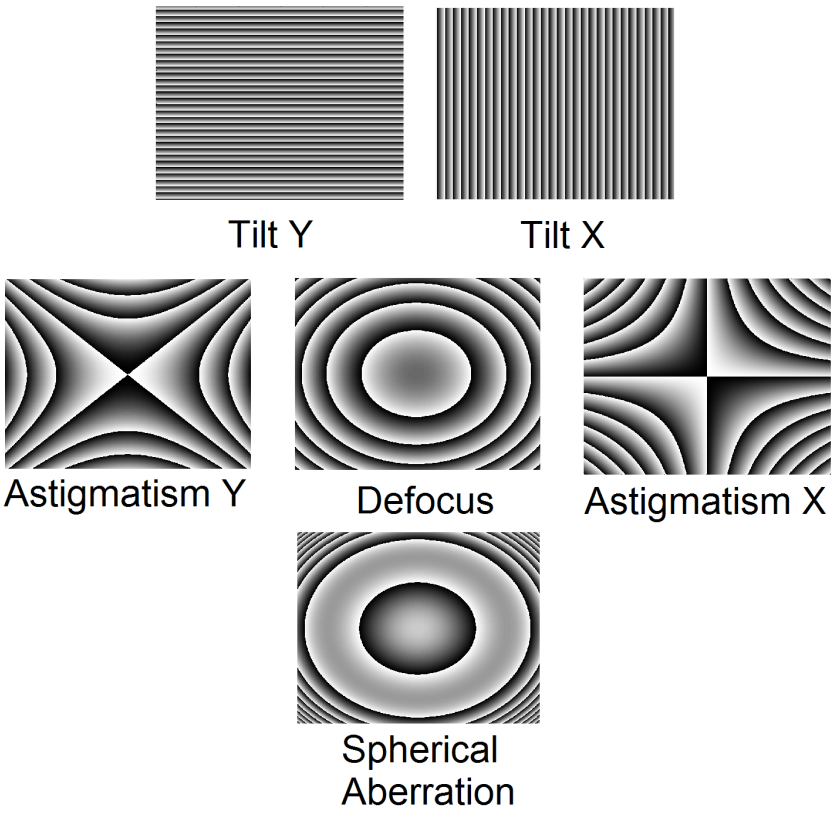

Figure 39: Examples of Zernike polynomials.

many cases the specimen is in an aqueous solution with an index of $n_m = 1.33 - 1.35$. Light travels through the objective, the immersion oil, the glass coverslip (all of the same index), and then as it traverses the interface between the coverslip glass to the aqueous solution, the wavefront experiences spherical aberration. In the case of DMHL, the index of the medium on the other side of the coverslip is actually slightly higher ($n_{\text{resist}} = 1.56$) than that of glass.

There are two main effects of spherical aberration on the intensity distribution of light in the patterning volume. The axial location where the light comes to a focus in the patterning volume is angle dependent and therefore spreads axially for high-NA objectives. [86] Also, as the desired focus location moves deeper into the resist, the actual focus location moves increasingly further away from the coverslip for ($n_g < n_{\text{resist}}$) [86]. As Fresnel lenses are used to focus light deeper into the sample, the actual focus keeps getting further and further from the nominal focus. The lateral extent of the focus does not change very much but the axial extent increases rapidly with distance from the coverslip. [86]

The higher the NA, the worse the spherical aberration, although high-NA is desirable for high resolution patterning. Even experiments with stages that can scan in three dimensions, allowing for axial movement of the objective, are limited by spherical aberration [65]. By applying a conjugate spherical aberration to the optical system it should be possible to negate the effects of the index mismatch. Though the effects of spherical aberration increase with axial distance into the patterning volume, a *single* aberration correction value can simulate the resist having the same refractive index as glass. The small magnitude of refractive index mismatch in this particular situation makes spherical aberration insignificant for DMHL performed here.

4.2.2 Astigmatism

Astigmatism can result from lenses being tilted in the optical train [87]. Corrections of several optical wavelengths can be necessary to compensate for the imperfect flatness of the SLM in holographic optical tweezer experiments [108]. Corrections of astigmatism can also

be necessary for 3D lithographic patterning. In astigmatism, the beam comes to a focus along the x-axis and the y-axis in different planes. The focus is therefore elongated, less intense, and creates a cross-like pattern in space.

The astigmatism found in this optical system was found to be negligible with respect to its effect on patterning. Because of the thresholding effect of photopolymerization, it is difficult to measure small differences in patterning intensity through its effect on cured feature dimensions. For this reason, to demonstrate the effect of aberration correction in a DMHL system, a severe astigmatism aberration was added to the system by rotating one of the lenses in the optical train (the 75 cm focal length lens in Figure 34) by about 10 degrees with respect to an axis perpendicular to the optical table (see Chapter 6). Higher order aberrations like coma and trefoil were also measured and found to be insignificant.

4.3 PHYSICS OF SLMS

Many SLM-related factors can affect the performance of a DMHL system: [111] modulation properties of the SLM, the number and geometry of the pixels, scattering and absorption by the SLM, discretization and quantization, fringing field effects, time-dependent variation (due to pixel refresh rates), temperature dependence (the temperature of the liquid crystals can increase due to absorption, changing their optical properties). The most significant factors will be discussed below with others being relegated to an appendix.

This research involves the use of a transmissive Holoeye LC 2002. It is a twisted nematic liquid crystal spatial light modulator (TLC-SLM) with a twist angle of 90 degrees. In a TLC-SLM a layer of liquid crystals (LC) is deposited between two transparent electrodes. The side of the electrode in contact with the LCs is processed in such a way to provide a row of grooves to anchor the first layer of LC molecules (see Figure 40). This set of grooves is called the director. The twist angle is the angle separating the grooves on one electrode from the grooves on the opposite electrode. Voltage applied across the electrodes rotates the angle at which the liquid crystals are aligned, and changes the optical properties of the LC layer. In a nematic LC layer, LC molecules that are not physically in contact

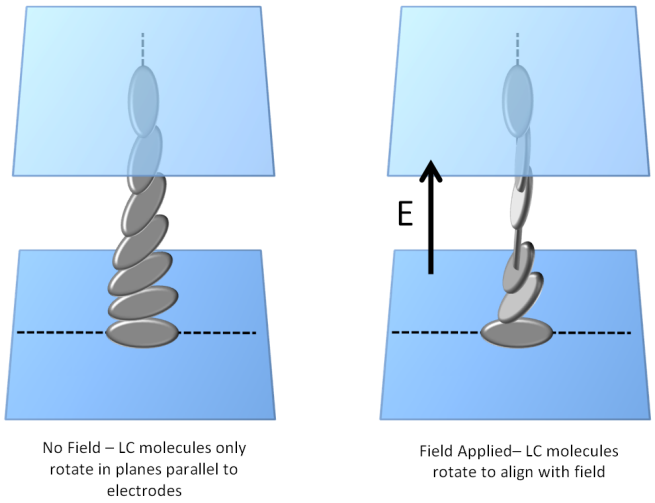

Figure 40: Effect of electric field on liquid crystals between transparent electrodes in an SLM. The dotted lines are the alignment directions for the liquid crystals in contact with the electrodes. This shows a 90 degree twist.

with the electrodes can rotate to align themselves with the electric field [32]. To display a phase hologram it is important that an applied voltage changes the optical path length or phase delay associated with each individual pixel. Optical path length changes with index of refraction of the LC layer. The elongated shape of LC molecules causes them to have a different index of refraction depending on the direction of polarization of the incident light. This is called birefringence which is explained in more detail below.

The main optical property that changes with voltage is the extraordinary index of refraction of the LC layer. The relationship between applied voltage and the extraordinary index of refraction can be defined as [85]:

$$\frac{1}{n_e^2(\tau)} = \frac{\sin^2\tau}{n_o^2} + \frac{\cos^2\tau}{n_e^2} \tag{4.20}$$

where τ is the angle at which the LC molecules rotate, n_e is the extraordinary index of refraction and n_o is the ordinary index of refraction. The ordinary index of refraction is experienced by light that is polarized normal to the long axis of the LC molecule and the extraordinary index of refraction is experienced by light that is polarized parallel to the long

axis of the LC molecule [32]. Because the LC molecules near the electrodes don't rotate to the same degree as those in the center of the layer, it is not possible to model the device as a uniaxial crystal.

According to Holoeye, the LC 2002 always has a coupled amplitude/phase modulation (there are no polarizers embedded in the device). It is possible to use it in a "phase-mostly" configuration with certain polarization configurations and Brightness/Contrast settings. The brightness setting determines the bias voltage that is added to the driving AC voltage while the contrast setting controls the voltage swing.

A nematic liquid crystal SLM is usually driven with an AC voltage to avoid permanent chemical changes in the the liquid crystals [32]. Although the driving voltage is AC, it does not rotate the LC molecules back and forth between two extremes. The LC molecules rotate with the absolute value of the applied voltage because their dipole moment is induced rather than permanent [32].

The LC 2002 has a fill factor of 55%, approximately 2π phase shift at 532 nm, and an aperture of 21 mm x 26 mm. The thickness of the liquid crystal layer is about 10 micrometers. This gives a birefringence (the difference between ordinary and extraordinary refractive indices) of $\Delta n \approx 0.05$. More detail on birefringence is given below. The liquid crystal layer needs to be at least $\lambda/\Delta n$ meters thick to provide 2π radians of phase delay.

Microfabrication takes place when the intensity of light is high enough to cause the resist to polymerize. DMHL uses an SLM to shape the light intensity pattern in three dimensions. There are limits to this process due to the size of the field of view, the depth of focus of the objective, spherical aberration, pixel size of the SLM, amount of phase delay each pixel can provide, etc. Each SLM pixel can be thought of as providing a complex transmittance [2]:

$$M_g = |M_g| e^{i\theta_g} \tag{4.21}$$

where the index g is the graylevel value which varies from 0 to 255 for an 8-bit display. Below is a brief explanation of what effect liquid crystals have on light. A more in-depth discussion is provided in Appendix A.

4.3.1 Polarization Eigenstates

As light passes through a liquid crystal cell, its polarization eigenstate (the complete description of the light's polarization) rotates through the twist angle, α [74]. In earlier, thicker SLMs, linearly polarized light would simply be rotated by this twist angle. Now that SLMs are thinner, the polarization eigenvectors are elliptically polarized because a higher percentage of the liquid crystals are anchored to the director and not affected by the applied voltage [74]. Input light from the laser that starts out linearly polarized now has the major axis of its polarization eigenstate rotated through the twist angle, but the output light is elliptically polarized. This elliptical polarization means that the phase and amplitude modulation of the SLM become coupled. As SLMs get thinner, the effects of the LC molecules that aren't affected by voltage (touching the directors) play a bigger role, and can need to be compensated with wave plates. Early, thicker SLMs could be used for phase-only modulation with linearly polarized light.

Because the birefringence depends on the voltage applied to the display, the ellipticity of the polarization eigenvectors also varies with voltage. The polarization eigenvector is linearly polarized for large birefringence values because the applied voltage is large enough to rotate LC molecules near the director [74]. For optimal phase-mostly operation, the ellipticity for the input light needs to be the average elliptical polarization eigenvector in order to best compensate for the polarizing qualities of the SLM [19]. This average eigenvector can be generated by a combination of waveplates and polarizers [19, 74, 85, 2]. This is explained in more detail in Appendix A. Several polarization compensation setups were tested for this work but provided only minimal improvement over the use of a single half-wave plate to rotate the linear polarization of the laser light in such a way as to maximize the diffraction efficiency into the first order.

4.3.2 Birefringence

Birefringence is the difference in refractive indices for ordinarily and extraordinarily polarized light [42]. There is a complex relationship between birefringence and phase delay. The relative retardation, β, (in units of radians per meter) between the ordinarily and extraordinarily polarized components of a light beam is defined as [32]:

$$\beta(V) = \frac{2\pi(n_e(V) - n_o)}{\lambda_o} \tag{4.22}$$

where n_e is the voltage-dependent extraordinary index of refraction of the liquid crystal material, n_o is the ordinary index of refraction and λ_o is the wavelength of light. The index of refraction experienced by the light is dependent on its polarization. The ordinary index of refraction remains constant with applied voltage for each pixel. The light going through the birefringent material only experiences the maximum delay if it is aligned with the ordinary or extraordinary axis. This can then be converted into the phase delay (in radians) by multiplying by the thickness of the LC layer, d. It should be noted that the phase difference between two gray levels, and the difference between each of those gray levels with zero is not equal ($\phi_1 - \phi_2 \neq (\phi_1 - \phi_0) - (\phi_2 - \phi_0)$) due to "polarization dependent geometric phase" [111].

There is some critical voltage, V_c, below which molecular reorientation does not occur. This voltage is based on physical constants of the liquid crystals [42]. The phase delay as a function of voltage (note: this is for parallel-aligned LC cells) is: [25]

$$\Delta\phi = \kappa_1\phi_m(V/V_c - 1) \text{ for } \quad \frac{V - V_c}{V_c} \ll 1, \tag{4.23}$$

where κ_1 is a constant based on the physical constants of the liquid crystals, V_c is the threshold voltage and ϕ_m is the maximum phase delay given by:

$$\phi_m = 2\pi d\Delta n/\lambda \tag{4.24}$$

and

$$\Delta\phi = \phi_m\left(1 - \frac{\kappa_2}{V}\right) \text{ for high fields } \quad \frac{V - V_c}{V_c} \gg 1 \tag{4.25}$$

where κ_2 is another constant determined by the physical properties of the liquid crystals. In the low voltage region, the phase delay is linear with voltage, while at higher voltages, the phase delay levels off to the maximum possible delay. Both of these behaviors can be seen in Figure 44. This model also assumes that the molecules all tilt at the same angle when the electric field is applied.

The physical properties of an LC cell vary spatially [94]. It is assumed that the variation is due to a change in off-state birefringence most likely caused by a change in the thickness of the LC layer. There is evidence that β can vary by almost a factor of 2 across a square inch of area due most likely to "bowing" of the glass sandwich that contains the liquid crystals [94]. This is just one of many physical limitations to the SLM. Several more will be discussed in the following section.

4.4 SLM DEVICE LIMITATIONS

Beside the physical effects mentioned in Chapter 2, there are limitations specific to the Holoeye device itself due to its design. Many anomalous behaviors described in the next section are due to these experimental realities. The layout of the driving electronics cause an asymmetry in the diffraction efficiency of displayed gratings. The time response of the SLM can be an important factor in determining the maximum frame rate for movies of holograms being displayed during micro-manufacturing.

4.4.1 Asymmetry of SLM diffraction efficiency

For the type of SLM used here, the rms voltage applied across a pixel is much lower than the peak driving voltage because each pixel is updated/refreshed sequentially (in a raster scan) [59]. Because of this property of the driving circuitry, at high spatial frequencies, vertical gratings have much less phase excursion than horizontal gratings. According to a measurement made with a Thorlabs power meter, this drop off in diffraction efficiency occurs around a period of 4 pixels for holograms that are 512x512 (see Figure 41). The axis

corresponds to the low-frequency scanning signal of the SLM [2]. This explains why the displayed Fresnel lenses in this research become more astigmatized with depth.

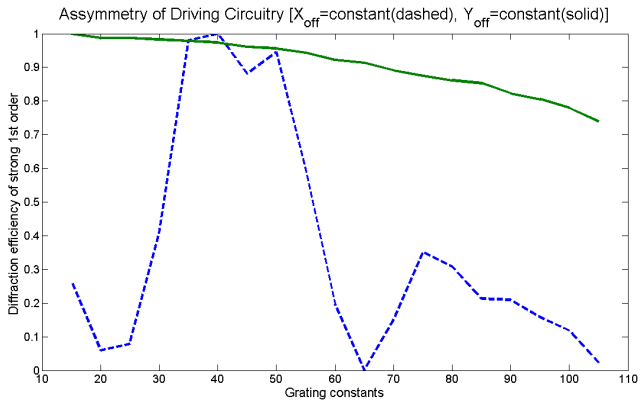

Figure 41: The diffraction efficiency for gratings along one axis of the SLM varies much more rapidly and drops off much more quickly than the other. The dashed line shows the normalized diffraction efficiency of a range of vertical blazed gratings while the solid lines is for horizontal gratings. This is mostly due to the asymmetry in the drive circuitry. Note: Grating constants are proportional to spatial frequency. Here 50 grating constants is equal to a blazed grating with 100 periods.

The first step in compensating for this spatial frequency dependence of the phase depth is to calculate the local horizontal frequency value in the neighborhood of each pixel. This can be done by taking cross-sections of the hologram at a few points to check if the maximum spatial frequency of 110 periods of 2π phase shift across the hologram on the y-axis has been exceeded. This works out to about 4 pixels per period.

4.4.1.1 Average phase change per pixel within a hologram

Because of the asymmetry in the SLM driving circuitry, there is a more strict limit on spatial frequency along one axis than the other [62]. This also means that there is a maximum average local phase gradient (difference in phase between two adjacent pixels) that can be displayed on the SLM before diffraction efficiency starts to roll off. The plot of average local phase change vs. grating frequency (see Figure 42) shows that the known spatial frequency limit corresponds to a local average phase value of about 2 radians. The plot was made with MATLAB script, `avgphasechange.m`. This script finds the average rms change in phase per pixel of a specific hologram. According to this script, Fresnel lenses with lens constants up to $C_{\text{lens}} = 350$ which corresponds to an axial displacement of about 17.5 μm, do not cross the limit of 2 radians of average local phase change (see Figure 43).

4.4.2 SLM time response

The time response of a liquid crystal device is proportional to the square of the thickness of the LC layer (this makes a reflective device faster than a transmissive device) [68]. The LC 2002 is quoted to have a maximum frame rate of 60 Hz. The display rate of the MATLAB figures appears to limit the rate at which holograms can be changed before the SLM switching limit is reached. The effective frame rate limit for this system was found to be around 10 Hz.

The intensity in a laser spot that is created by a computer generated hologram can vary as a movie of holograms is displayed to move a dot [26, 82]. The amount the intensity changes in between holograms is proportional to the average change in phase per pixel. This change in intensity occurs because the pixels can only change phase values so quickly. For

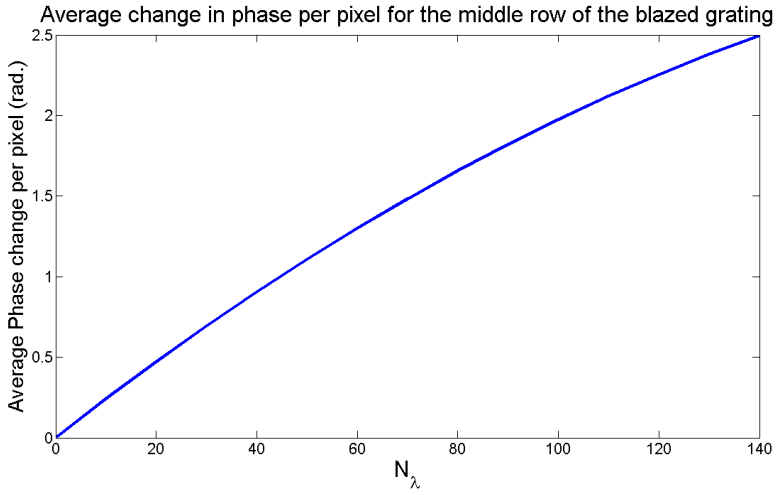

Figure 42: This is a plot of average phase change per pixel as spatial frequency increases in the y-direction. N_λ is the number of wavelengths or periods in the displayed grating.

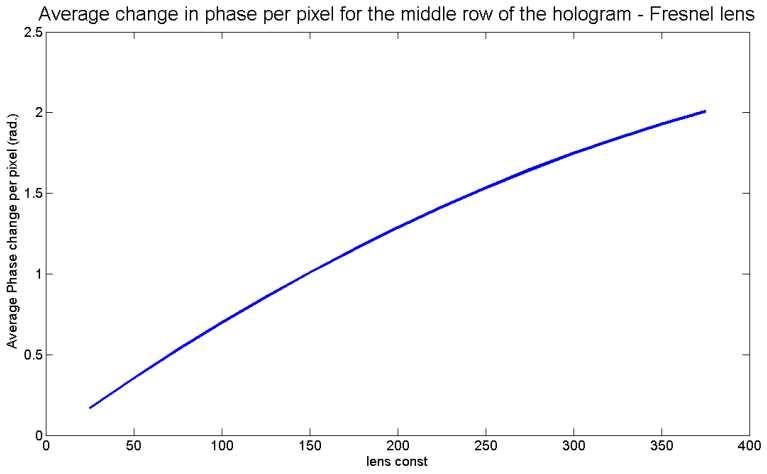

Figure 43: This is a plot of average phase change per pixel as lens constant, C_{lens} increases.

serial patterning with gratings, the best thing to do is use small step sizes. It is also possible to mitigate this limitation by implementing an extra step in a GS algorithm to minimize the amount of phase change from hologram to hologram for each pixel.

4.5 CHARACTERIZING THE SLM

Several characterization and calibration experiments were done to confirm that the SLM could be used with minimal changes to the device and the displayed holograms.

A half-wave plate setting of 26° off the fast axis provides the maximum diffraction efficiency to both the positive and negative first order when using `adaptivegratinghigh.m` create blazed gratings. The half-wave plate rotates linear polarization of the incident laser light. Rotating the half-wave plate has a proportional effect on both the strong and weak first order (both maxima/minima at the same rotation angles).

The computer screen and the SLM are both 800×600 pixels. To ensure that the hologram pixels correspond to the SLM pixels one to one, images of the holograms displayed on the screen were analyzed. The holograms are 512×512 pixels and the MATLAB commands that create this one to one correspondence are: `axis('square')` and `set(gcf, 'Position', [1338 383 661 661])`.

4.5.1 Phase Calibration

There are many ways to measure the phase response of an SLM described in the literature [110, 74, 83, 7]. Some phase response curves are derived from the use of a Mach-Zehnder interferometer and others use Ronchi (binary) diffraction gratings.

Laser light was sent through a polarizer set to zero degrees, then through a mask with two pinholes in a piece of aluminum foil that was placed over the SLM. There are no polarizers in the SLM. The beam from one pinhole fell on a constant phase while the other fell on the other half of the SLM which had a variable phase. After the SLM was another polarizer set to 45 degrees. The external polarizers on the input and output sides of the SLM should

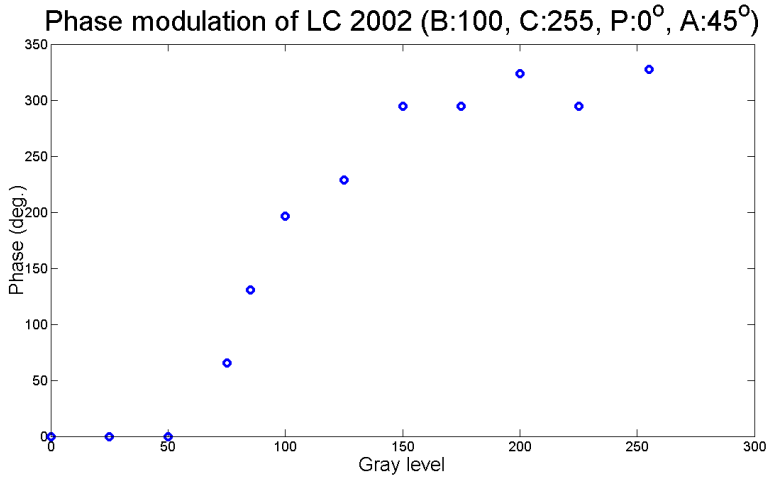

Figure 44: Phase response of SLM for different gray level values (Brightness:100, Contrast:255, polarizer before SLM:0° and polarizer after SLM:45°)

be adjusted to obtain the maximum fringe pattern translation for the whole grayness level range. Maximizing the fringe-pattern contrast in the phase measurement simultaneously minimizes coupled amplitude modulation [7]. As the phase was changed on the variable half, interference fringes translated in the specimen plane of the microscope according to the phase difference between the two halves. CCD images of the fringes for 12 different gray level values from 0 to 255 were taken. MATLAB code, `fringedisplacement.m` was used to analyze the results. The equation for deriving the phase was $\phi = 2\pi(p_{\text{shift}}/p_{\text{period}})$ where p_{shift} is the number of pixels the fringe is shifted and p_{period} is the number of pixels in one fringe period. The resolution on the measurement was not very high because the number of pixels per fringe period was only 12 pixels. The architecture described here only permits characterization of a small region of the SLM due the to use of the pinholes.

The measured phase vs. graylevel curve shown in Figure 44 is expected from equation 4.20 because the index of refraction changes slowly for either large or small tilt angles. This also explains why the slope of the retardance with grayness level has three regions, the first which has a shallow slope as retardance and the extraordinary index change slowly, the

second which has a steep slope as the retardance and the extraordinary index change quickly, and then leveling off again to a gentle slope as the retardance and extraordinary index change slowly with increasing voltage. Graylevel is proportional to applied voltage.

4.5.2 Intensity fluctuations

As the beam is scanned across the patterning area, there are periodic intensity fluctuations that can cause features to have lumps (see Figure 45). These fluctuations are spatial, not temporal. They are caused by fluctuations in diffraction efficiency as the spatial period and angle of the phase gratings are changed. On top of the small fluctuations, there are two large dark bands going across the patterning area where the diffraction efficiency drops to about zero for the first order (see Figure 46). An experiment was done in which the SLM was physically rotated to test the source of the dark bands. The dark bands rotated with the SLM and occurred around $N_\lambda = 44$ (number of grating periods across the hologram in the y-direction) implying that the dark bands come from the SLM and not from inhomogeneities in the beam, which was not rotated. By changing colormaps (the relationship between designed phase and displayed graylevel of a grating made with MATLAB), the location of the dark band can be shifted, but no way was found to eliminate it. There is another dark band when $N_\lambda = 130$ in the y-direction, but this is outside the effective patterning area.

The period of the small intensity fluctuation was found to be relatively constant (1.5-1.8 μm), but because it changes depending on the alignment of the setup, it can only be compensated by measuring before each sample is made. This mapping is done with `mapdiffeff pupil polarize.m` (see Figure 47). This is most likely due to the fact that the actual phase patterns displayed on the SLM cause aliasing and loss of efficiency for certain values of grating period. The fact that small misalignments change the location of the fluctuations implies they could be related to quality of the beam coming from the laser. The beam is not perfectly spatially homogeneous (as discussed below). When a complicated spatial filter was incorporated into the experimental setup, the beam looked cleaner, but the dark bands were still present. Some anomalous behavior can be attributed to nonuniform phase variation among individual pixels [20].

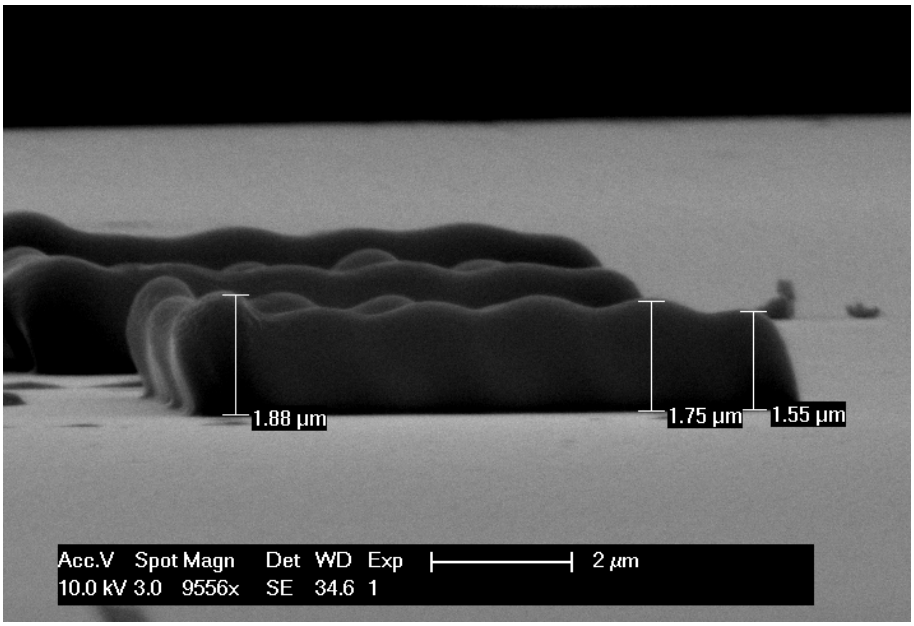

Figure 45: This is the side view of a serially cured square. It shows small intensity fluctuations. It was made with a scan speed of about 0.85 μm/s.

The angle with which the displayed grating makes with the natural direction of the liquid crystals changes the polarization sensitivity [40]. This could explain some anomalous behavior of certain displayed phase gratings (dips in diffraction efficiency that do not match monotonic pixelation-related drop-off). Polarization sensitivity increases as the number of pixels per grating period decreases exacerbating any diffraction efficiency drop off.

4.6 CHARACTERIZING THE LASER

The laser used in this research is a pulsed green laser from Teem Photonics (PNG-M04005-100). The laser is specified to have an average power of 20 mW, but was measured to have an average power of about 12 mW. It has a repetition rate of 500 Hz, and pulsewidths of 300 ps. This works out to about (12mW/500=) 24 μJ per pulse. It is specified as linearly polarized.

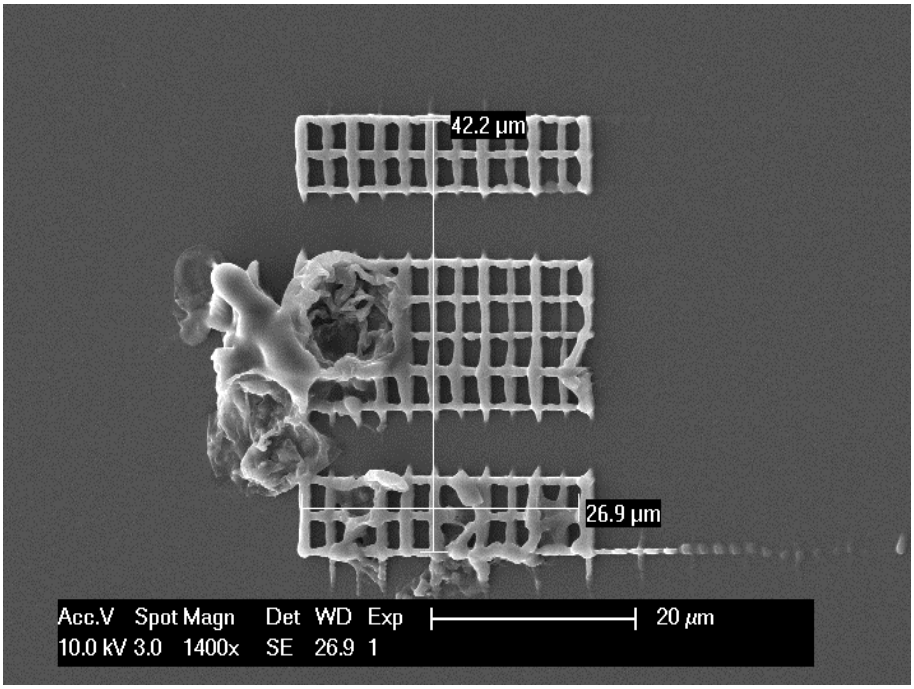

Figure 46: This is an attempt to show the whole patterning area with a grid. The two dark bands in which there is not enough light to pattern are clearly evident. The large mess on the left is from the zero order causing the resist to boil, and can be eliminated.

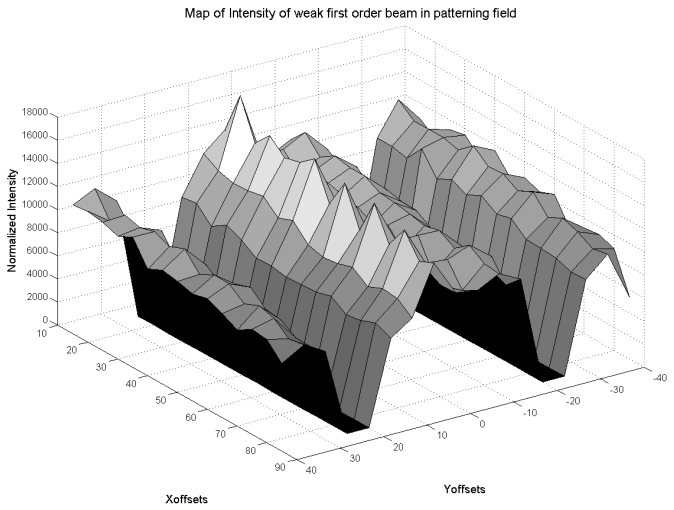

Figure 47: A plot of the normalized intensity due to the first diffraction order. There is a larger drop-off in intensity in the x-direction than the y-direction because it extends further from the zero order and requires a higher spatial frequency grating. The magnitude of the coordinates on the x- and y-axes are proportional to the spatial frequency of the displayed gratings (in this case, one X_{offset} or Y_{offset} is equal to two periods in a displayed blazed grating.

A discussion of the beam quality, the measurement of the pulsewidth with an autocorrelator, and the beam intensity in the specimen plane with different objectives, is given below. It was confirmed with a quadrant photodiode that the repetition rate was 500 Hz.

4.6.1 Beam Quality

When the beam was expanded, it appeared to have an amplitude grating superimposed on it. This was due to interference of multiple plane waves coming out of the laser head (possibly due to reflections from small misalignments in the nonlinear crystal inside laser). By placing an iris near the beam waist of the laser, it was possible to remove this effect, although the beam was still not perfectly Gaussian. The beam waist is specified to be 7.7 cm away from the laser head output and the iris is placed about 10 cm further down the optical train.

4.6.2 Measuring Laser Pulsewidth

Autocorrelation experiments were performed to verify the pulsewidth of the pulsed 532 nm laser. The concept is to split a beam in two in an interferometer, and vary the optical path length of one leg (see Figure 48). When the beams are recombined inside a nonlinear crystal, they create light at twice the frequency if the pulses overlap enough. This setup uses a β-barium borate (BBO) crystal from Gooch and Housego for second harmonic generation (SHG). As the path length is varied, the amount of second harmonic light varies. By fitting a Gaussian curve to the SHG intensity at different path lengths and using the speed of light, it is possible to calculate the length of the pulse in time. Building an autocorrelator is easy, but getting it to work is difficult. A UV sensor is used to measure second harmonic light (wavelength of 266 nm). The most important thing is to have the SHG crystal mounted on a stage that has 5 degrees of freedom (XYZ, pitch, and rotation). This is because the crystal must be rotationally aligned with the polarization of the pulses for Type 1 SHG. Also, the distance the nonlinear crystal is placed from focusing lens is important because the intensity is high enough only exactly at the focus. By luck, the polarization of the laser was perpendicular to the optical table and therefore it was possible to angle tune the pitch of the crystal (see Figure 49) while it was in the rotation stage. If this had not been the

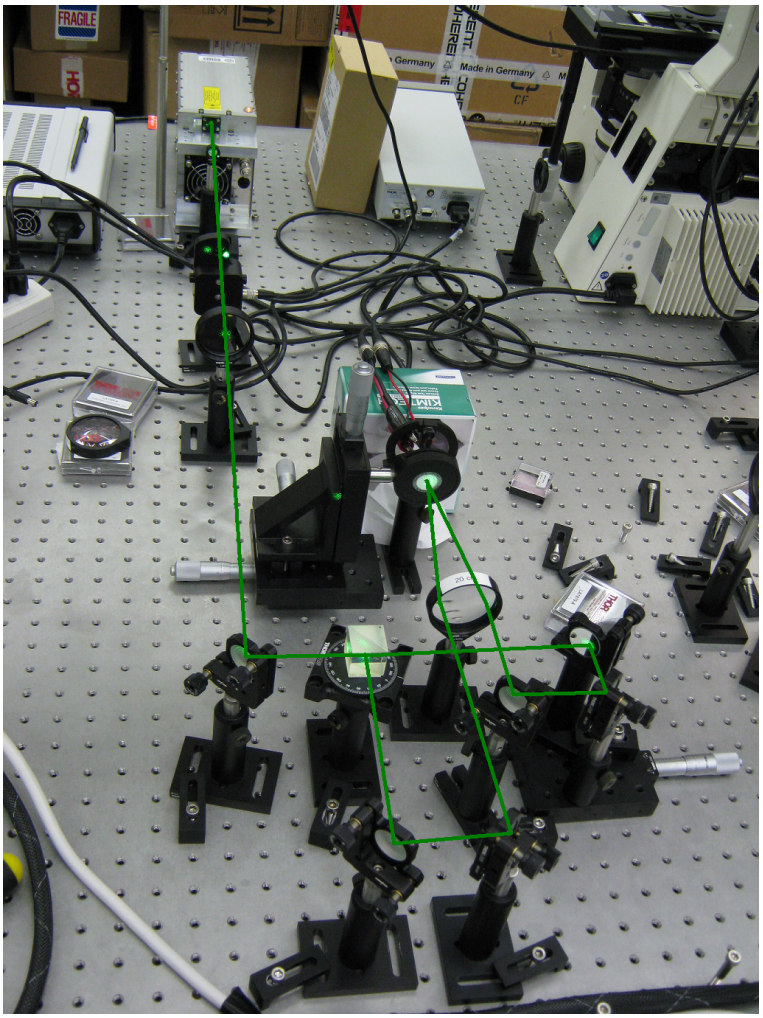

Figure 48: Autocorrelator setup with beam trace showing how the beam is split, the path length is varied, and the beam is recombined for SHG in the BBO crystal (point where beam converges).

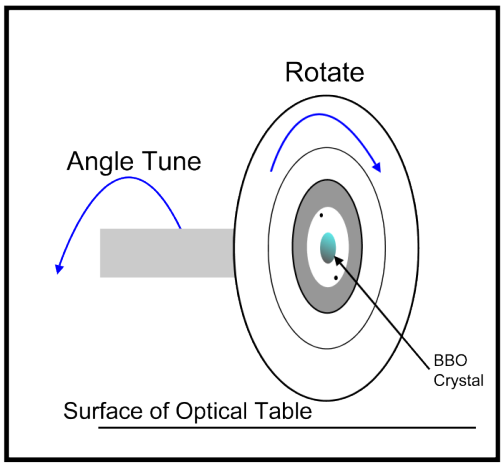

Figure 49: Explanation of how to angle tune the BBO crystal after determining the polarization of the laser.

case, a half-wave plate could have been used to rotate the laser polarization. The average pulse width of the three autocorrelations is 339 ps (see data in Figure 50). The standard deviation of the three is 29 ps.

4.6.3 Laser Power Budget

The important parameter that determines whether a certain resist is cured with two-photon absorption is the peak intensity achieved by a certain laser/objective lens combination. As the beam travels through the optical system, losses occur. When the beam gets to the dichroic mirror inside the microscope, it still has over 80% of its original intensity (without the SLM). After the dichroic mirror, the amount of light reaching the specimen plane is cut to about 18% its original value from 12 mW to about 2.21 mW with no SLM, no objective, an iris blocking the "extra" beams from the laser as mentioned above and the half-wave plate set to 26° off the fast axis. The insertion of the SLM increases these losses because most of the light is diffracted into higher orders that are cutoff by the apertures in the system.

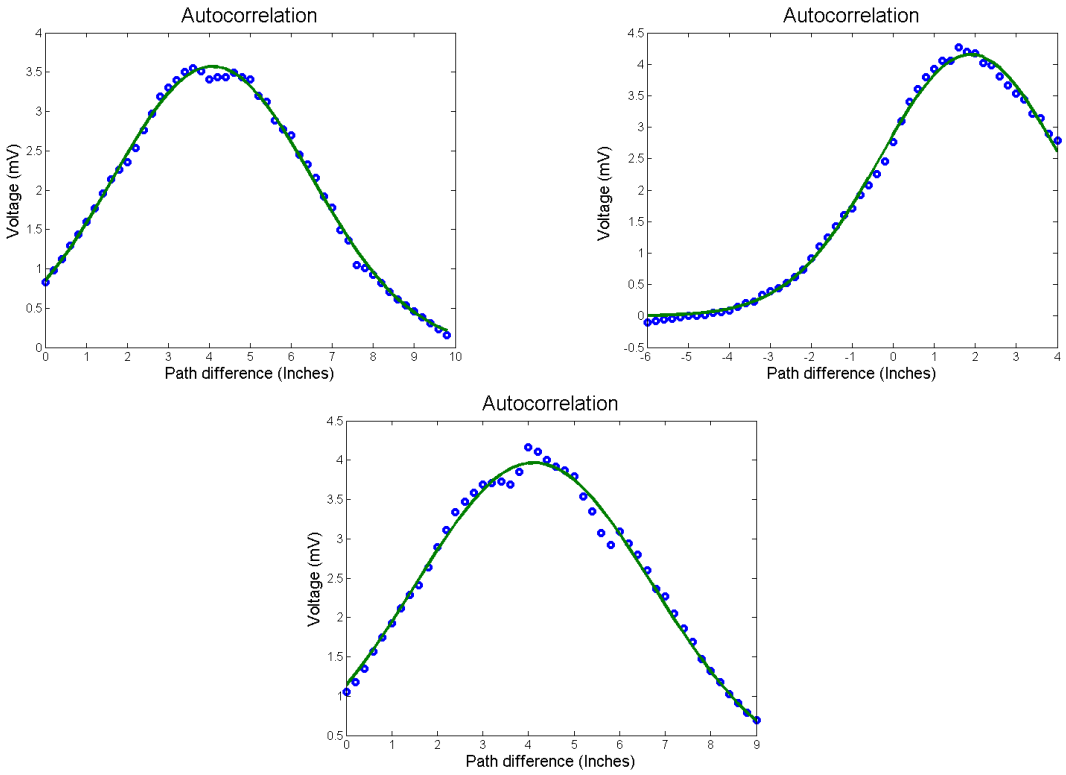

Figure 50: Autocorrelation curves with Gaussian fit.

Table 1: ND filter transmission.

ND (Optical Density)	Nominal Transmission (%)	Measured Transmission (%)
0	100	100
0.1	79	85.5
0.2	63	72.4
0.3	50	57.5
0.4	40	47.5
0.5	32	36.2
0.6	25	26.7
1.0	10	12.2
2.0	1	1.72
3.0	0.1	0.14
4.0	0.01	0.005

An assortment of Thorlabs metallic neutral density (ND) filters are used to attenuate the laser because it does not have a knob to change the power. The rating on the ND filter corresponds to its optical density at 546 nm. The optical density, D is defined by:

$$D = \log_{10}(1/T) \tag{4.26}$$

where T is the transmittance. The transfer function between input power and output power for the ND filters was measured to be:

$$P_o = 1.086 P_i e^{-2.393\text{ND}} \tag{4.27}$$

where P_o is the output power, P_i is the input power, and ND is the ND filter value. The equation was found using a best-fit of the data to a single term exponential (`exp1`) in MATLAB.

The nominal and measured transmission of each ND filter is given in Table 1. Both of these equations are equivalent within a few percent. The ND filters have transmissions consistently higher than their nominal value.

Table 2 shows the peak intensities possible for various microscope objectives and with various loss inducing elements, assuming 18% transmission through the optical system (except the objective). The middle column can be thought of as upper bounds for the system (no SLM). The peak power is about $(0.18 \times 24\mu\text{J}/300\text{ps}=)14.4$ kW. The peak intensity numbers given in Table 2 are assuming a flat profile. This is not the case in reality. A Gaussian profile would mean that there is a higher peak intensity at the center of the beam than the edges. The first column of peak intensities are for the laser going directly to the specimen plane (no objective). Only about 18% of the laser light makes it to the specimen plane (mostly due to the dichroic mirror). The second column of peak intensities includes the losses incurred when the SLM is added to the setup. The SLM reduces the available power at the specimen plane to about 4% of the power coming from the laser. This is in the static zero order, the light that goes straight through the SLM without being diffracted. The phase holograms used for patterning will take light from this order. Finally, the power at the specimen plane in the strong first order is about 1.5% of the power from the laser. The corresponding peak intensities are given in the last column. There are two first order beams, a "strong" $(+1)$ and a "weak" (-1) beam. The -1 beam has about 35% as much power as the $+1$ beam. When the intensity is too low or the exposure time is too short, no polymerization occurs, when intensity is too high or the exposure time is too long, the resist boils and a bubble is visible [96]. It is the range in between these two extremes in which patterning is possible.

According to Zeiss specifications the transmission expected through the objectives used in this research range from 60-80%. For ease of calculation, a 70% transmission will be assumed for all objectives. After taking the objective transmission into account, the most accurate peak intensity estimates are given in Table 3. The pulse energy after the objective in the strong first order was measured to be 0.37 μJ of the original 24 μJ coming from the laser.

Table 2: Parameters for determining upper bound of peak intensity for each objective (assuming 14.4 kW peak power and 100 % transmission through each objective). The +1st order of the phase grating is the "strong" first order beam.

Obj.	Beam Radius (μm)	Area (cm^2)	P. I. (GW/cm^2)	P. I. 0th (GW/cm^2)	P. I. +1st (GW/cm^2)
10×	10	3.14e-6	4.6	1.06	0.51
20×	5	7.85e-7	18.63	4.28	2.05
40×	2.5	1.96e-7	73.8	16.97	8.12
63×	1.6	8.04e-8	180	41.4	19.8
100×	1	3.14e-8	461	106	50.7

Table 3: Parameters for determining upper bound of peak intensity for each objective (assuming 14.4 kW peak power and 70 % transmission through each objective). The +1st order of the phase grating is the "strong" first order beam.

Obj.	Beam Radius (μm)	Area (cm^2)	P. I. (GW/cm^2)	P. I. 0th (GW/cm^2)	P. I. +1st (GW/cm^2)
10x	10	3.14e-6	3.2	0.74	0.36
20x	5	7.85e-7	13.0	3.0	1.44
40x	2.5	1.96e-7	51.7	11.9	5.7
63×	1.6	8.04e-8	126	29.0	13.9
100×	1	3.14e-8	323	74.2	35.5

4.7 PRELIMINARY EXPERIMENTS

Two resists were tested, although one resist was used with 5 different photoinitiators. The first resist to be tested was ma-N 2410. The other resist was OrmoComp©. The OrmoComp© was used with 1.8% Irgacure 369XP, 1% Irgacure 184XP, Irgacure 127XP, OXE01XP, and TPO. The ma-N 2410 resist was found to cure with available laser power but could only be spun in film thicknesses of about 1 micrometer which is too thin for 3D DMHL. The OrmoComp© with TPO as its photoinitiator was not cured by any available laser powers. All the other photoinitiators showed curing in OrmoComp© and performed similarly, but the 1.8% Irgacure 369XP was most readily available and chosen for all subsequent patterning. The fact that the pillars cure at peak intensities far below the maximum available (see Table 2) implied that DMHL would be possible. Moreover, the fact that the pillars are taller than a micrometer (approximate axial voxel for the 100× objective) proves that OrmoComp© can be spun thick enough to be used for 3D DMHL. OrmoComp© is known to shrink by a few percent by volume after curing [78]. This works out to an expected 1% reduction in lateral dimension.

The general procedure for making samples goes as follows:

1. Spin coat a layer of resist for 30 seconds at 3000 rpm on a glass coverslip (Corning Cover Glass, No. 1.5, 25 mm sq., Cat. No. 2870-25). The resist is normally between 50-100 μm thick for OrmoComp©.
2. Place coated coverslip on a small piece of aluminum foil
3. Pre-bake substrate on hot plate at 80° C for 2 minutes.
4. Expose
5. Post-bake substrate on hot plate at 80° C for 2:30 (2 min. and 30 sec.).
6. Develop substrate in OrmoDev for 3 minutes
7. Rinse with IPA
8. Put back in developer for 15 seconds.
9. Rinse with IPA again
10. Dry with compressed air for 1 minute.
11. Sputter coat with palladium for SEM analysis.

Preliminary experiments were run to find the ablation threshold of the glass slides used as a substrate and the boiling and curing threshold of the resist. These thresholds are exposure time-dependent. The peak intensity was chosen as the unit in which the thresholds would be expressed and an exposure time of 0.1 seconds was chosen as a representative exposure in this research. There are no voxels exposed for less than 0.1 seconds in any experiments described here. The ablation threshold for the glass substrate was found to be around 12 GW/cm^2. Ablated glass was initially mistaken as cured resist, but SEM EDAX spectroscopy was performed to confirm that the material was glass. The boiling threshold for the resist was found to be about 6 GW/cm^2. This puts an upper bound on usable peak intensities for patterning. The curing threshold for OrmoComp© with 1.8% Irgacure 369XP was found to be about 2.7 GW/cm^2 during serial line-scanning with an exposure time of 0.1 seconds per voxel.

Using a value of 0.37 μJ per pulse, the 0.1 second exposure that this threshold was derived from, and the fact that the exposure was made with the 100x objective which has a spot size area of 3.14×10^{-8}cm^2 the threshold dose is about 44.6 J/cm^2. The suggested dose of UV light for OrmoComp© is 0.5-1.5 J/cm^2, but two-photon absorption is known to require much higher doses.

4.7.1 Sputter coating process and SEM induced damage

To ensure that SEM analysis was not altering the sample, it was necessary to confirm that the sputter coating process and SEM use did not do any damage to cured OrmoComp©. The environmental SEM (ESEM) does not require the sample to be coated in palladium and allows for comparison before and after coating. It was during this test that it was noticed that the electron beam was doing damage to the cured resist. Figure 51 shows that a 20 kV electron beam can damage cured resist. Figure 52 shows the progression from development, to uncoated sample in the ESEM, to coated sample in the SEM. Normal SEM operation uses a 10 kV electron beam which does not appear to do damage. Therefore, the result of this study is that coating the sample with palladium and using the SEM at 10 kV provides an accurate gauge of the DMHL process.

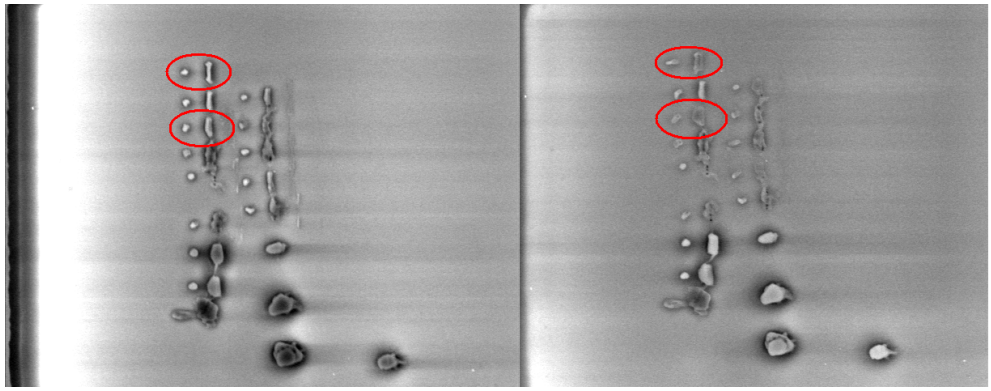

Figure 51: Both images are from the ESEM before the sample was coated with palladium. On the left is the sample viewed with a 20 kV electron beam early in viewing. On the right is the same area viewed about 10 minutes later. There seems to be damage done by the electron beam.

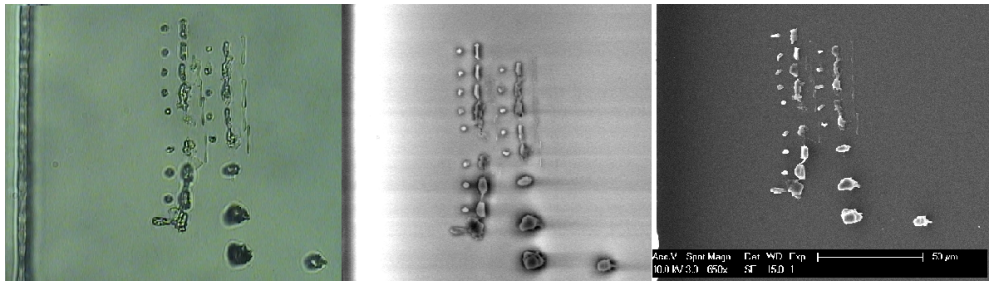

Figure 52: On the left is the optical microscope image taken after development with the 40x objective. In the center is the early (before electron beam damage) ESEM image. On the right is the same area viewed with the SEM.

5.0 2D PATTERNING RESULTS AND DISCUSSION

DMHL can be used to make 2D patterns both serially and in parallel. To use DMHL most effectively, it is important to characterize the patterning resolution and standard deviation for each patterning mode. This section discusses the 2D DMHL results including calibrations and determinations of the process resolution. The best achievable linewidth of patterned lines and the minimum distance between patterned lines were found. First the results from the serial mode will be presented, then the parallel mode.

A single beam can be scanned (serial mode) or whole images can be displayed (parallel mode) to cure a pattern. The choice between these patterning modes depends upon the sensitivity of the resist and the available laser power. In some instances, the resist is not sensitive enough to cure when the available laser power is divided among many points in an intensity pattern. In these situations, single beam scanning is the only possible patterning mode.

5.1 2D SERIAL PATTERNING

The beam positioning for 2D serial patterning is effectively continuous as explained in Chapter 2. Therefore the lateral dimensions of the cured voxel limit the achievable linewidth. To make smooth lines and other features, voxels must be exposed in an overlapping manner. As explained above, the diffraction efficiency of displayed phase holograms drops off with spatial frequency. This necessitates the use of higher patterning intensities and longer exposure times to ensure that patterning is possible over a larger patterning area, or dwell-time compensation. There are then three critical numbers to define for 2D serial DMHL: small

area resolution (linewidth in areas close enough to the zero order that they do not require dwell-time compensation), large area resolution (linewidth in the whole patterning area when a higher intensity is used with dwell-time compensation), and pitch which is the minimum center-to-center distance between patterned lines. The pitch is not equal to the linewidth because there is a small zone around an exposed line that is partially-cured after exposure, but would still be removed by the developer [81]. This partially-cured zone becomes cured if another feature is exposed too close to it (if partially-cured zones overlap). In this section experimental realities that affect patterning will be discussed and the three process resolution benchmarks will be given.

5.1.1 Experimental results

The experimental results for 2D serial DMHL showed some unexpected characteristics that are useful to know for future experimental design. Sensitivity of linewidth to the axial position of the objective and the possibility that resist is curing thermally were important discoveries. Lines were scanned serially at various speeds (voxel exposure times) and various peak intensities to find their relationship with linewidth. The voxel spacing was 265±15 nm unless otherwise specified.

5.1.1.1 Sensitivity to Objective Axial Position The linewidth of cured lines is very sensitive to the axial position of the objective with respect to the substrate. Even 100 nm movements can significantly increase or decrease the linewidth. The limited size of the usable patterning area required the microscope stage to be moved by hand throughout the making of a given sample. These movements sometimes led to axial displacements between the objective and the substrate. The axial thickness of the line is greatest when the objective is focused exactly at the substrate/resist interface, with the widest part of the voxel being in contact with the substrate. If it is focused slightly below, the ellipsoidal voxel gets cut-off and a smaller linewidth results. It was also found that when the focus is further below the substrate surface, the cured features are wider than expected for an ellipsoidal voxel (discussed below). Figures 53 and 54 show how serially scanned features can vary just based

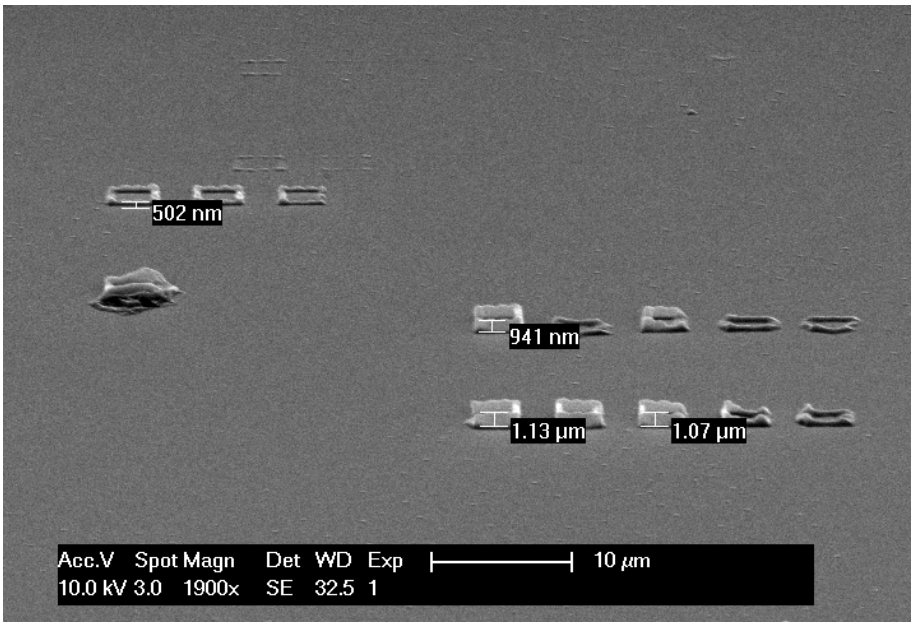

Figure 53: The upper-left trio of squares was serially scanned at a shallow depth, while the set of 10 on the lower right were made with a deeper focus.

on where the objective is placed axially. The linewidth for a given intensity, exposure time and dot density, was found to vary $\pm 15\%$ due to objective axial positioning error.

The best way to control the axial position would be to use a Fresnel lens instead of moving the fine focus knob of the microscope, but adding a Fresnel lens changes the effective number of pixels per grating period, and therefore, the diffraction efficiency. From initial diffraction efficiency maps that were measured with the CCD camera, very small Fresnel lens constants ($|C_{\text{lens}}| < 15$) might be used without appreciable effects. This allows a 1.5 μm axial positioning range with the 100× objective.

5.1.1.2 Possible Thermal Curing In several samples that included lines exposed when the centroid of the focus was within the substrate, the linewidths were wider than lines exposed when the focus was closer to the substrate (see Figure 55). As the axial position of the laser focus comes up through the surface of the glass and into the resist, the linewidth is actually wider, then gets thinner, and then wider again (evident in Figure 54). If the

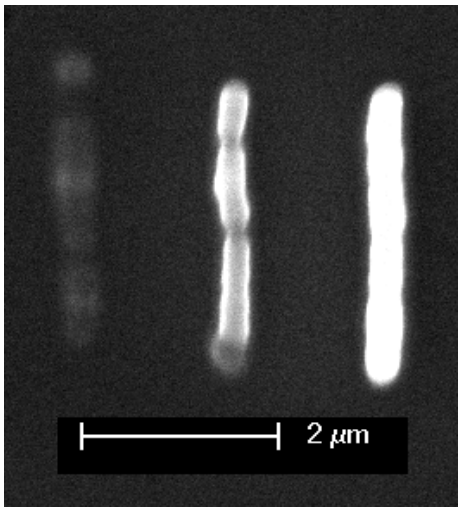

Figure 54: These lines were made with increasing depth into the sample from left to right. The contrast of the lines is proportional to their axial height and it can be seen that the width of the most shallow line is wider than the middle line.

shape of a voxel were ellipsoidal, one would expect the first tip of the voxel to be very small. One possible explanation for this behavior is that while the focus of the laser is still inside the glass, it heats up the glass enough to *thermally* cure the resist. This thermally cured feature is more "smeared" than the photocured resist made when the focus is deeper in the resist layer. The chemical structure of the thermally cured resist is probably identical to the photocured resist, therefore it is impossible to tell the method of curing. It might be possible to determine the degree of curing with FTIR or Raman spectroscopy [13]. The only way to experimentally test thermal curing would be to use a substrate with a significantly different thermal conductivity or absorption of green light.

5.1.1.3 Shape of the voxel In theory, the voxel is ellipsoidal based on the shape of the focal region. At higher intensities and longer exposures, the DMHL process resulted in voxels with bulbs on the ends not touching the substrate, while the lines that are laying on their sides appear to have more of the expected ellipsoidal shape. This is most evident in Figure 56 and appears to happen when lines are overexposed. One hypothesis is that each

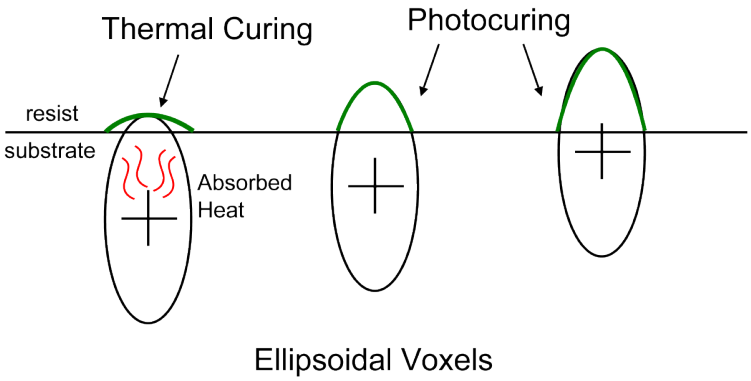

Figure 55: This is a schematic explanation of possible thermal curing when the focus is too deep within the substrate. Once the centroid of the focus is closer than some threshold distance, normal photocuring begins to occur.

pulse of light alters the refractive index of the gradually-curing resist, and this changes the shape of the focal region, putting more intensity toward one end of the voxel [73]. Also, side views like Figure 57 show that the bottom of the line flares out where it is attached to the substrate (likely due to thermal curing).

5.1.2 Patterning resolution

As discussed above in Chapter 3, the beam intensity and exposure time determine the diameter of a voxel. The diameter of the voxel for constant intensity varies as [54, 91]:

$$d(t) = A_1\sqrt{\ln B_1 t} \tag{5.1}$$

where t is the exposure time and A_1 and B_1 are constants determined by the laser parameters and the photochemistry. The diameter of the voxel for constant exposure time, t varies as:

$$d(I) = A_2\sqrt{\ln B_2 I^2} \tag{5.2}$$

where I is the average intensity of the laser, and A_2 and B_2 are other constants. Plots of data with both constant exposure time (see Figure 58) and constant peak intensity (see Figure 59) both have good fits to the theoretical models. The peak intensity is proportional to the average intensity and only changes the coefficient in the fit. Below are results for the three resolution metrics used in this research.

5.1.2.1 Small Area Linewidth The best measured lateral resolution for a serially exposed square can be seen in Figure 60, but only one of the set of 10 squares cured properly (see Figure 61). This justifies the need for a "small area linewidth" because the minimum linewidth is not achievable over the whole patterning area. The low intensities required for small linewidths are not high enough to cure the resist when the first order beam is far from the zero order.

To make sure that a particular linewidth measurement was not thin due to the focus being underneath the substrate surface, a series of 2D serial lines (see Figure 62) were made that were displaced axially with a Fresnel lens ($C_{\text{lens}} = -15, -10, -5, 0$). The thickest linewidth

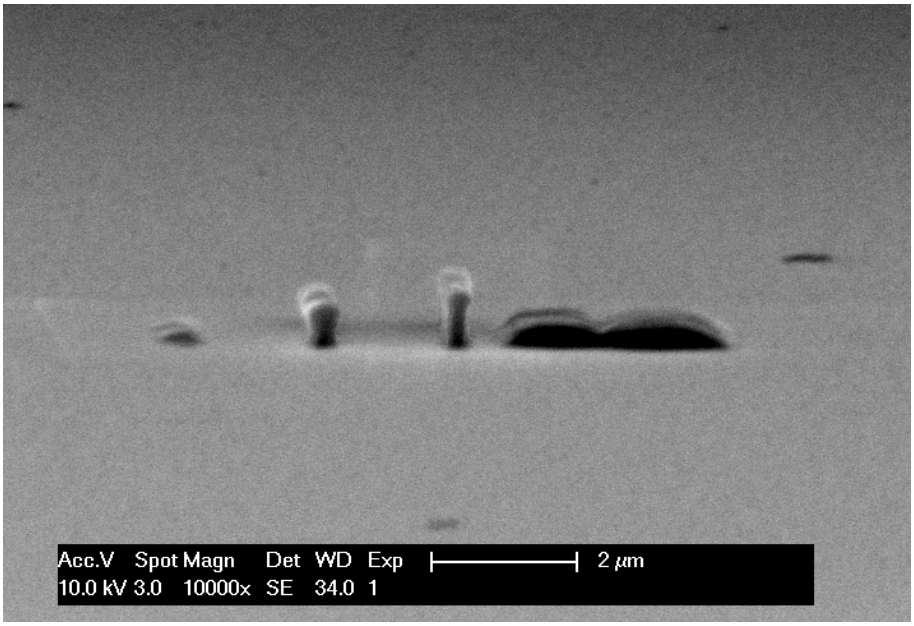

Figure 56: These lines were made with a peak intensity of about 3.1 GW/cm^2 and an exposure time of 0.3 sec. per voxel. The objective was moved up about 500 nm between each line.

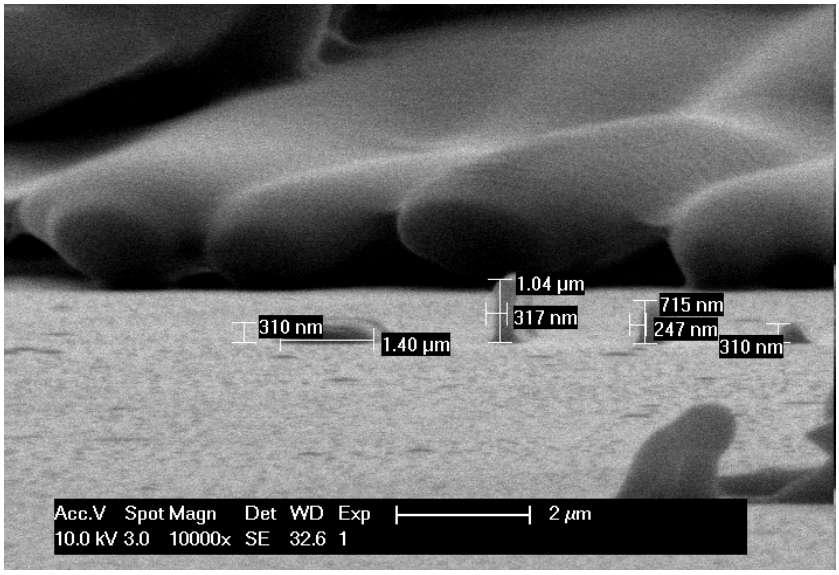

Figure 57: This set of lines was made with a peak intensity of about 2.7 GW/cm^2 and an exposure time of 0.3 sec. per voxel.

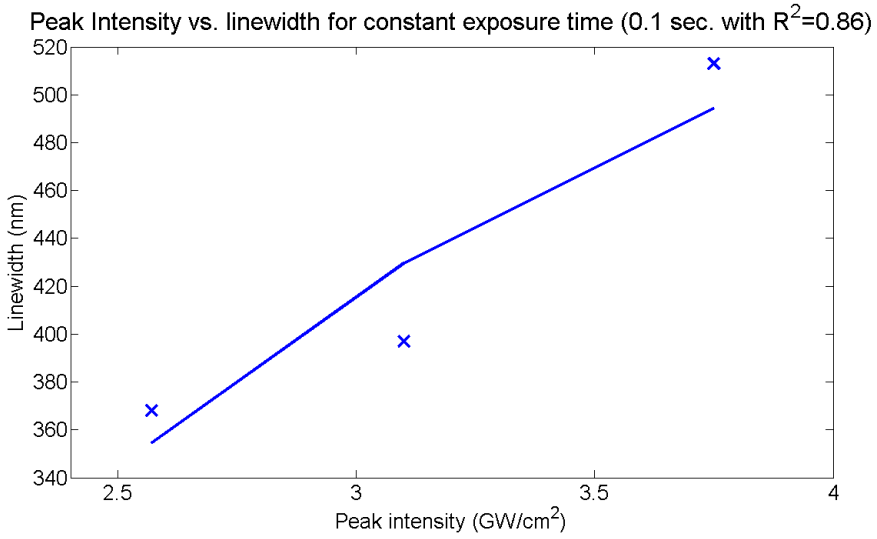

Figure 58: This is a fit of theoretical voxel diameter for constant exposure time at several peak intensities.

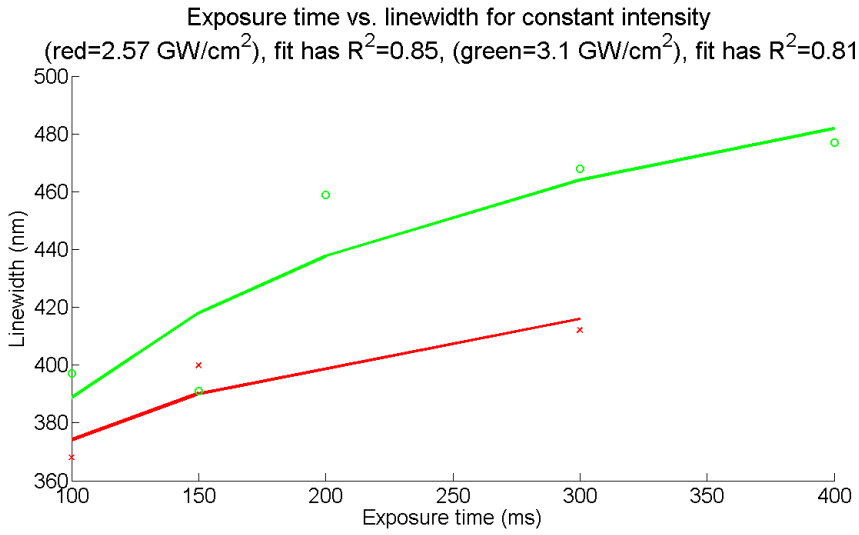

Figure 59: This is a fit of theoretical voxel diameter for two constant exposure peak intensities at several exposure times.

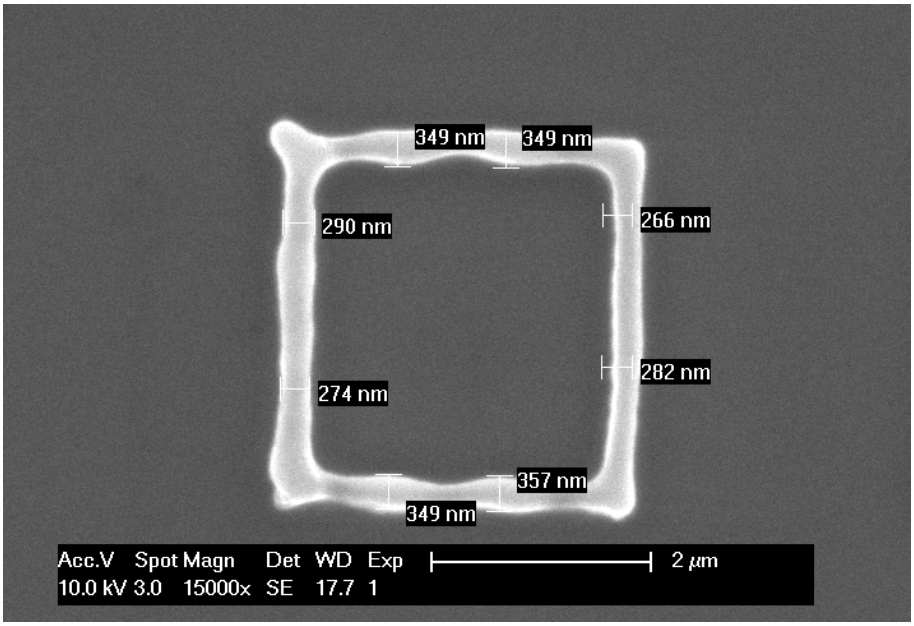

Figure 60: This square was made with a peak intensity of about 2.7 GW/cm^2 and an exposure time of 0.1 sec.

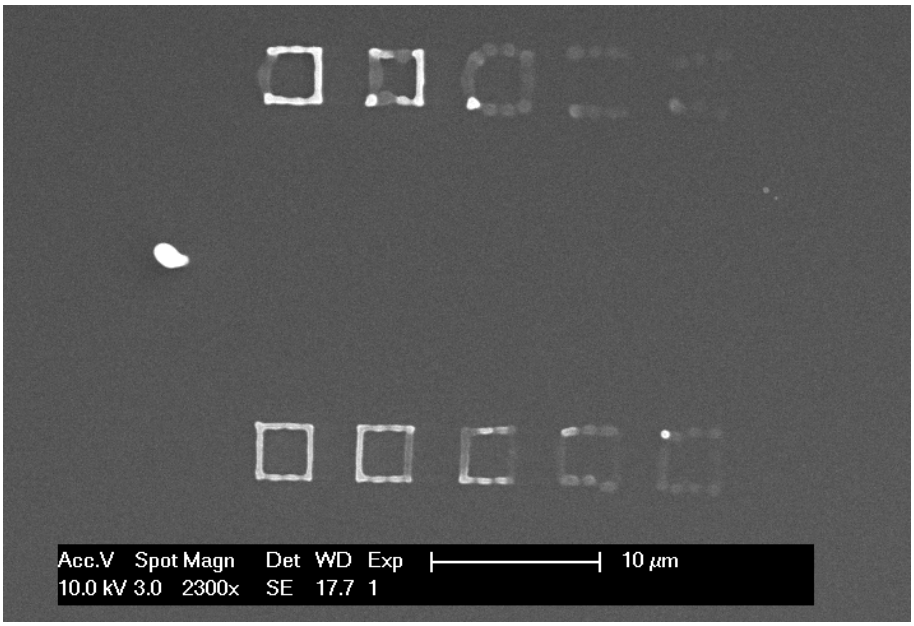

Figure 61: These squares were made with a peak intensity of about 2.7 GW/cm^2 and an exposure time of 0.1 sec. Only the bottom left feature was cured as designed.

would then be the most accurate measurement for the exposure conditions. Small lens constants were used so as not to add the confounding factor of reduced diffraction efficiency as lens constants increase. As mentioned above in Chapter 4, small intensity fluctuations throughout the patterning area mean that lines that are placed next to each other might be made at different intensities depending on their distance from each other. Again in order to get the largest, worst case measurement of linewidth for given exposure conditions, the intensity fluctuations were measured beforehand to make sure each line was placed at an intensity maximum.

The patterning resolution for a peak exposure intensity of 2.7 GW/cm^2 (ND= 0.7) and an exposure time of 0.15 sec. with a voxel spacing of about 280 nm was found to be 400±24 nm from 18 data points. The data for determining the patterning resolution for small areas is shown in Figures 62 and 63. The smallest half of these data points was thrown out to account for the axial positioning and intensity fluctuation uncertainty. The variation quoted is the standard deviation of those remaining 9 data points. This is the small area linewidth.

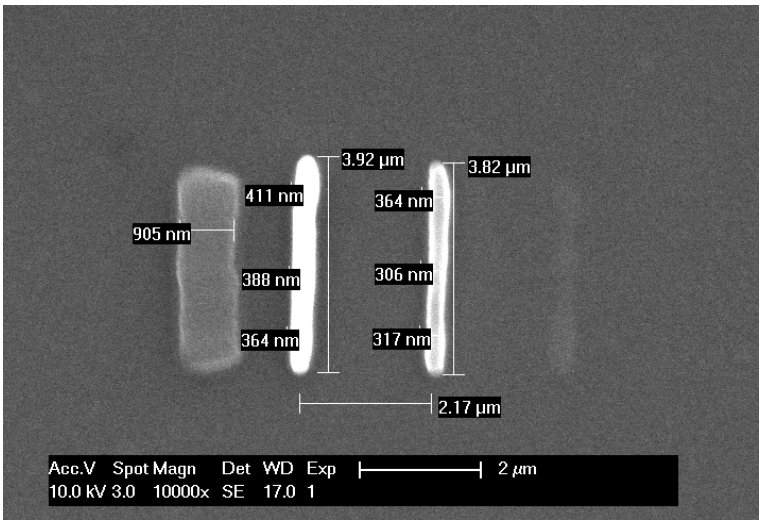

Figure 62: This set of lines was made with a peak intensity of about 2.7 GW/cm^2 and an exposure time of 0.15 sec. per voxel.

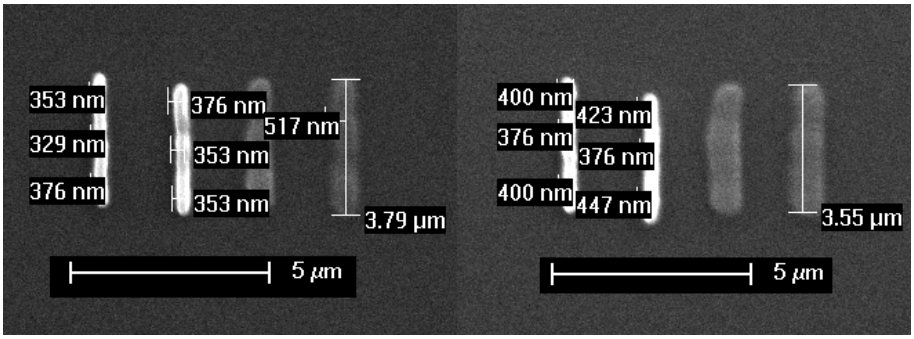

Figure 63: These linewidth data points were used for the determination of the small area patterning resolution. The two lines on the right of both sets were underexposed.

5.1.2.2 Large Area Linewidth The second metric, large area linewidth is necessary because the diffraction efficiency of blazed phase gratings decrease as the grating period decreases. Small periods are needed for large displacements in the patterning area. Due to this loss in intensity at high displacements, the patterning beam must be made more intense. Also in order to minimize the amount the intensity must be increased (because this increases linewidth) longer exposure times are also used.

Dwell-time compensation will be explained in more detail below, but the large area linewidth was defined with a set of 2D serially patterned squares with an exposure time that increased as the squares were placed further from the zero order. The large area linewidth with a peak intensity of 3.1 GW/cm^2 (near the zero order), an exposure time per voxel starting at 0.2 sec. and a voxel spacing of about 280 nm was found to be 468±57 nm (see Figure 64).

5.1.2.3 Minimum Pitch The minimum pitch measurement is important because partial curing can become total curing if lines are placed too close together. The pitch experiments had several line pairs that did not touch each other. The minimum distance between two separated lines was 627 nm. The average distance between between lines was 710±47 nm (see Figure 65). The measurements quoted above are made "by hand" with a measurement tool in the SEM program. The SEM program allows a line to be drawn between two points on an image and gives the appropriate distance. A Simulink model that used SEM images as an input was able to come within 5% of pitch measurements made "by hand". In the future, pitch measurements could be automated. Finally Table 4 shows all the 2D serial DMHL resolution values.

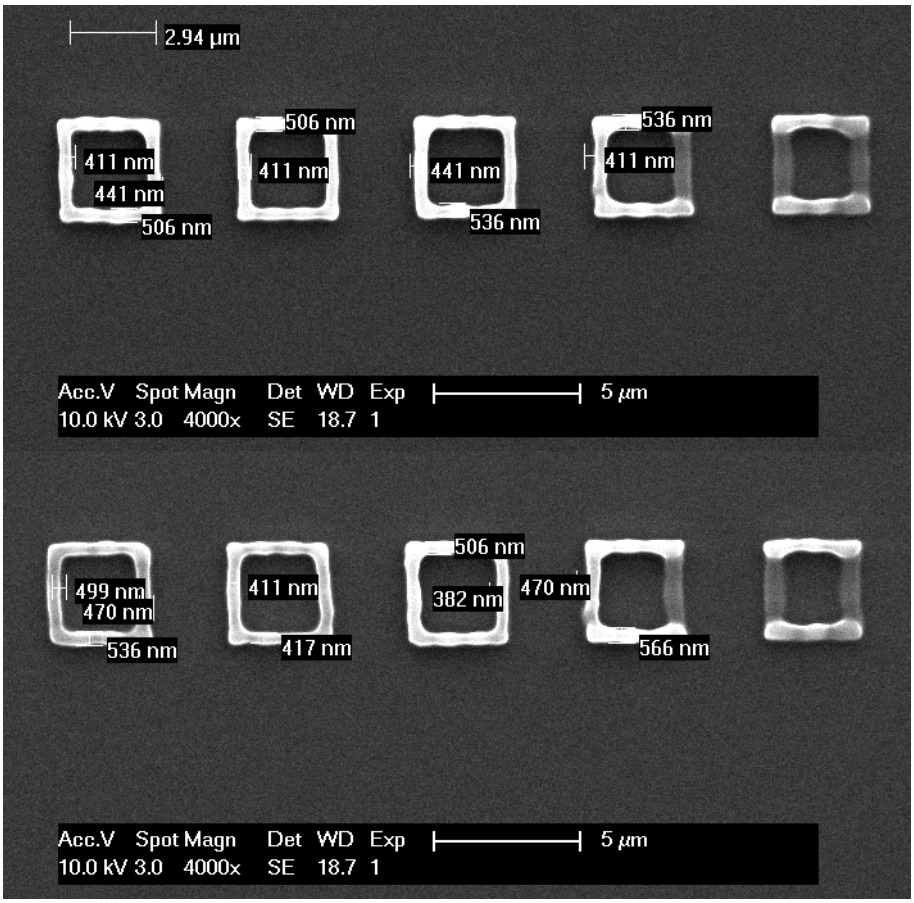

Figure 64: These squares were used to find the large area patterning resolution. Dwell-time compensation was used. The two squares on the right had an exposure time of 0.2 sec. per voxel, then the middle was 0.3 sec, the next was 0.55 sec. and the last was 0.7 sec.

Table 4: Resolution for 2D serial DMHL.

Resolution Type	Best achievable (nm)
Small Area Linewidth	400±24
Large Area Linewidth	468±57
Minimum pitch	710±47

5.1.3 Dwell-time Compensation

The pixelated nature of the SLM causes it to have a reduced diffraction efficiency and some anomalies in its light steering capabilities. There have been studies on these effects [38, 15, 106, 6], but not with respect to pixelation's affect on DMHL or how it might be compensated.

As discussed in Chapter 2, as the spatial frequency of a phase grating displayed on an SLM increases, the diffraction efficiency drops and it becomes more difficult to create uniform features throughout the patterning field. This is a well-known problem in phase holograms produced with several phase retrieval algorithms including the Gerchberg-Saxton algorithm [30, 93]. When using one of these algorithms, the drop off in intensity with distance from the zeroth diffraction order can be compensated by applying an appropriate intensity gradient to the target image. Holographic optical tweezer applications in which arrays of traps are displayed can have weights assigned to each trap as another way to compensate for reduced intensity [23]. Unfortunately these methods are only possible when there is an "input image" used as the target intensity pattern and cannot be implemented when simple gratings are used to steer a single beam.

The two factors that affect the size of the cured voxel of resist and, therefore, the uniformity of the pattern, are the intensity of the exposing light and the amount of time that the resist at that particular point is exposed. The only degrees of freedom available for controlling the intensity of a single beam with a grating (using the SLM alone) are the phase depth and grating profile, assuming the laser has no intensity control available. The phase depth is

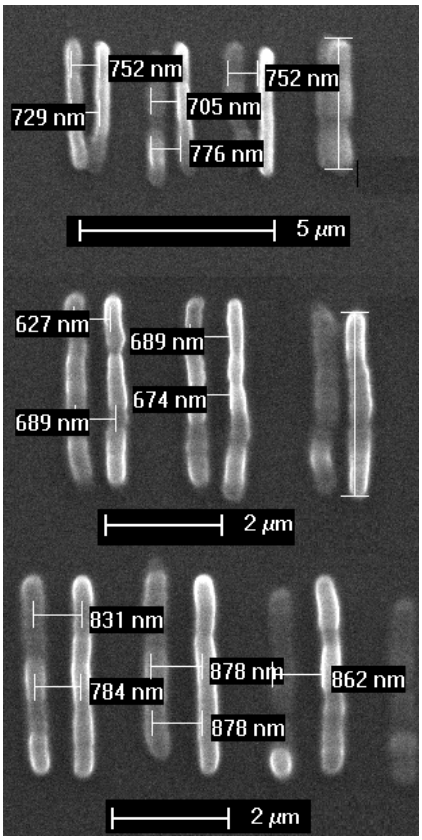

Figure 65: The data points for the determination of the minimum pitch come from these line pairs.

the amount of phase delay each grating period adds to transmitted or reflected light and the grating profile is the shape of each period (normally triangular). It is possible to control the intensity of the beam (before or after the SLM) by using polarizers, but this would require a complex control system to rotate a polarizer as the phase hologram is updated.

A simpler method for improving the uniformity of micro-manufactured features over a large patterning area is presented here. It is possible to make a 3D beam intensity map of the entire patterning volume. Knowing the beam intensity at every point allows for adjustments to be made to make each voxel of cured resist uniform in size. To use the available laser power most efficiently, an increased dwell time per voxel can compensate for reduced intensity at each point in the patterning area.

5.1.3.1 Actual vs. Theoretical Patterning Beam Intensity To confirm that the SLM behaved as expected, the actual intensity of the first order patterning beam was measured with a power meter at the first location where the beam comes to a focus outside the microscope. The data from the power meter measurement almost exactly matches the theoretical model (see Figure 66) presented in Chapter 2. The theoretical values from Equation 2.40 are derived with $N = 512\sqrt{2}$ because this is the actual number of pixels across the face of the SLM for all diagonal blazed gratings. The only two gratings with 512 pixels are horizontal or vertical gratings.

5.1.3.2 Implementing Dwell-time Compensation As explained in Chapter 3 the shape of a cured voxel is approximately ellipsoidal and therefore has a length and diameter associated with it. Simplified versions of the voxel diameter and length are [54, 91]:

$$d(I,t) = A_1\sqrt{\ln(BI^2t)} \tag{5.3}$$

where I is the intensity of the laser spot, t is the exposure time and A_1 and B are constants determined by the laser parameters and the photochemistry and:

$$l(I,t) = A_2\sqrt{\sqrt{(BI^2t)} - 1} \tag{5.4}$$

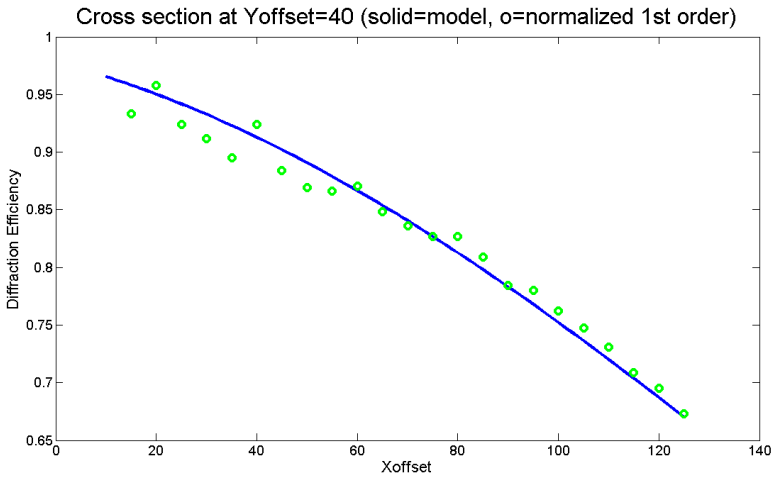

Figure 66: The normalized diffraction efficiency for the patterning beam (first diffraction order) compared with that derived from the model. The beam power was measured with a power meter. The number of periods in the displayed horizontal blazed grating is twice the number of X_{offset} units.

where l is the length of the voxel along the optical axis. The constant, A_2 is different from equation 5.3, while constant, B is the same. Conveniently, the same product, I^2t must be kept constant to produce uniform voxel diameter and length.

To perform dwell-time compensation, it is necessary to know the intensity of the patterning beam at every point in the patterning area. To automate the process for each specific pattern, a "diffraction efficiency map" of the patterning area is taken before each sample is made. The patterning beam intensity (and proportional diffraction efficiency) is measured by taking a series of images with a CCD camera and integrating the intensity of the laser spot (assuming that the image of the spot is not saturated). The CCD derived data (not shown) was taken at a much higher resolution than the power meter data in Figure 66 and has periodic fluctuations that vary about the model. As mentioned above in Chapter 4, this is most likely due to the fact that the actual phase patterns displayed on the SLM cause aliasing and loss of efficiency for certain values of grating period. The fluctuations are more pronounced on one axis than the other. Dwell-time compensation can also be used to make

uniform features in the face of these fluctuations, but for the purposes of this experiment, a small number of points were mapped at the five chosen locations given in Table 5. In this case the compensation is only applied based on the x-coordinate of the line location because beam intensity does not change appreciably along the length of the line.

5.1.3.3 Experimental Results The dwell-time compensation is determined by measuring the intensity in the patterning field with the CCD camera. This "map" is used to find a specific dwell-time for each point in the patterning field. In the case of this experiment, five lines are made, so the intensity need only be mapped in five narrow areas. A nominal exposure time is chosen for the part of the patterning field with the greatest intensity (closest to the zero order). Then the other dwell times are determined by setting the value $I_1^2 t_1$ to a constant where I_1 is the intensity at the first patterning location and t_1 is the chosen nominal exposure time. The necessary dwell time for the next patterning location, t_2, is found by:

$$t_2 = \frac{I_1^2 t_1}{I_2^2} \tag{5.5}$$

where I_2 is the measured intensity at the second patterning location.

In case the calculated dwell time is not be enough to compensate for the reduced intensity in practice, the effect of *overcompensation* must also be tested, so five lines are also exposed with dwell-times derived with an exponent of 2.5 (instead of 2) to increase the exposure time. To quantify the effect of dwell-time compensation, a set of uncompensated lines is patterned as well. The patterning locations (which correspond to the number of periods, N_λ in the displayed grating) and derived dwell times for the compensated and overcompensated sets are given in Tables 5 and 6, respectively. The lines in Figures 67a, 67b and 67c were exposed with a peak intensity of about 3.2 GW/cm^2 (near the zero order).

Table 5: Dwell-time compensation derived from measured patterning intensity.

N_λ	Dwell time (s)
32.66	0.20
80.00	0.22
134.66	0.45
193.34	0.52
251.4	1.00

Table 6: Dwell-time overcompensation

X_{offset}	Dwell time (s)
32.66	0.20
80.00	0.22
134.66	0.55
193.34	0.66
251.4	1.50

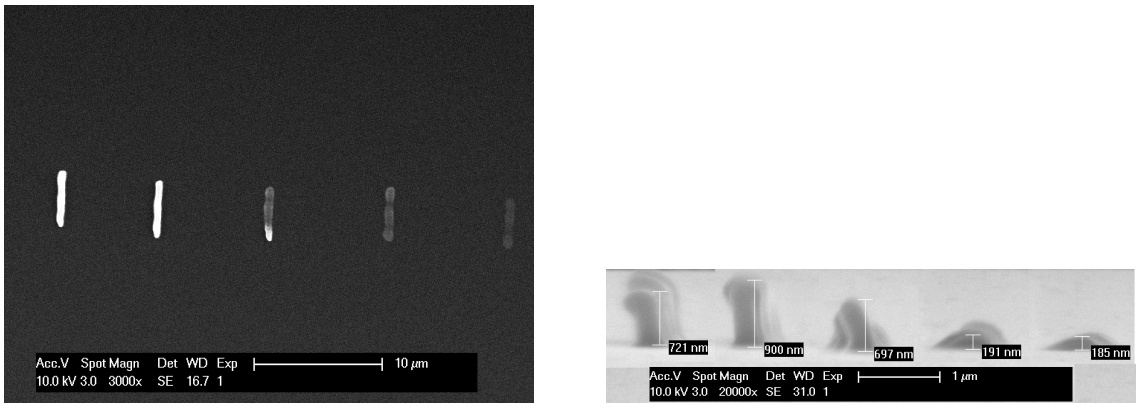

Figure 67a: Top and side view of uncompensated lines.

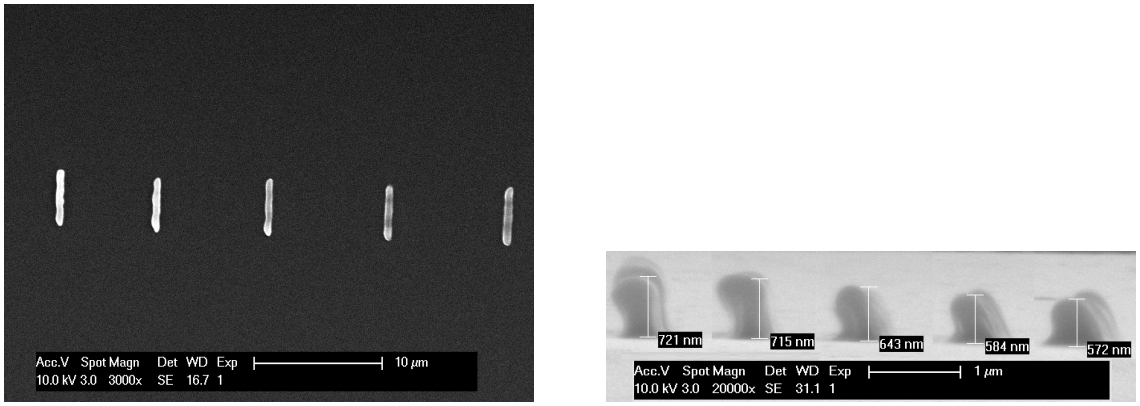

Figure 67b: Top and side view of dwell-time compensated lines.

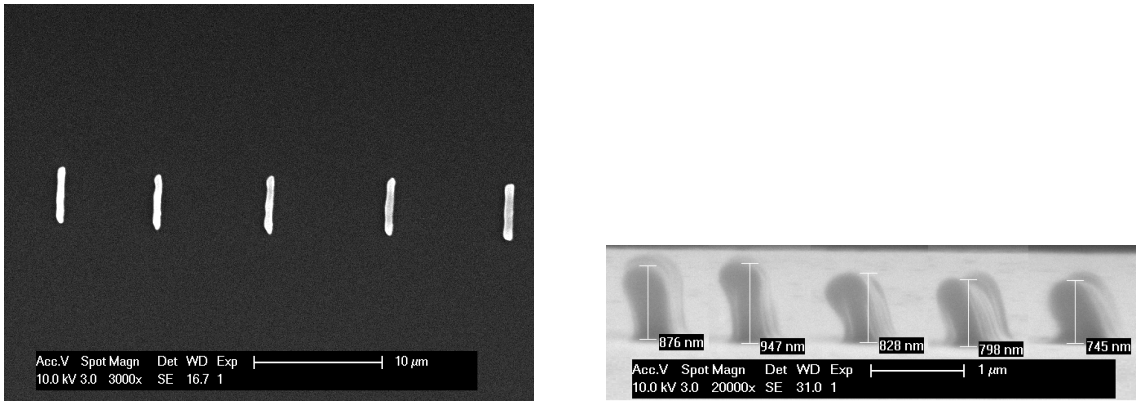

Figure 67c: Top and side view of overcompensated lines.

The lengths of the voxels were found to vary more than the voxel diameters. Therefore, the length was used to evaluate the effectiveness of the dwell-time compensation procedure. The reason for this is that the constants A_1 and A_2 are not equal and therefore the proportionality between voxel diameters could be different from the proportionality between voxel heights in this particular exposure regime. Also note that the measured value is not the true voxel height, but some fraction of it. A full voxel would not adhere to the substrate and be washed away during development. Each feature has the same fraction though, allowing for comparison with theory.

The experimental results (see Figure 68) show that dwell-time compensation has a significant effect on feature uniformity over a large patterning area. However, longer dwell-times are necessary than the measured intensities suggest. One possible reason for this is that the measured power is *integrated* in the CCD image. The actual power at the sample is a Gaussian distribution in which only the central portion is above the threshold to cause photopolymerization. It is also known that the nature of voxel growth depends on the exposure intensity [55]. At high intensities, the voxel grows more rapidly axially than radially, while at lower intensities, voxel growth is more uniform. It is possible that dwell-time compensation works best in a small intensity range. Outside this range, the extra dwell-time could cause the features to grow laterally as well as axially, actually decreasing feature uniformity. This can already be seen to be happening in the "overcompensated" set of lines. The longest exposed line on the right in Figure 67c is slightly wider laterally than the others. Future experiments can be done to test the performance of dwell-time compensation in different intensity regimes.

5.2 2D PARALLEL PATTERNING

Parallel patterning is done by creating a target image and finding an appropriate phase hologram with the GS algorithm. Each pixel in the target image (512×512) corresponds to a point on a grid in the specimen plane. The spacing of this grid, or the imaging resolution, for the 100× objective is 160 nm (see Chapter 4). As discussed above, the minimum linewidth

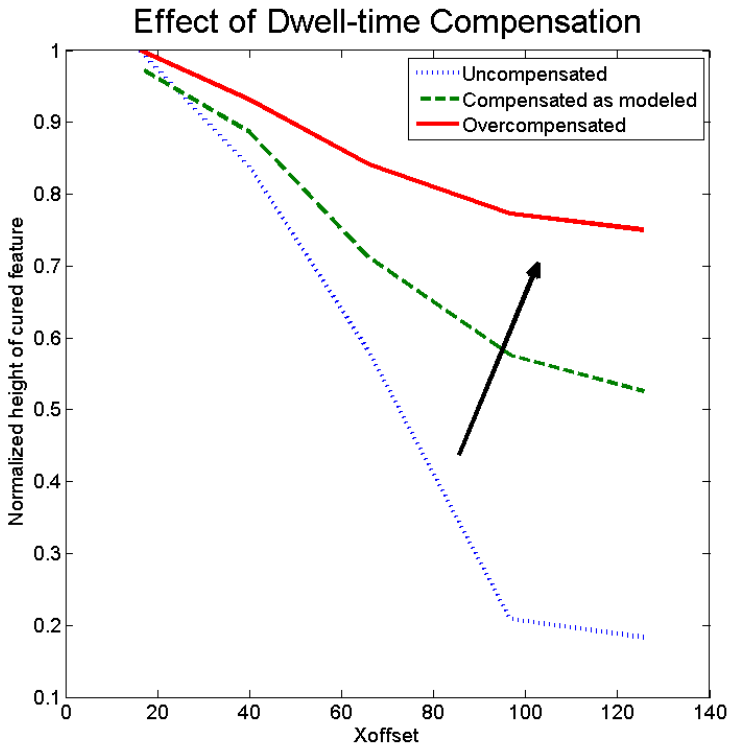

Figure 68: Normalized height of cured lines made at different distances from the zero order. The $X_{textoffset}$ value is proportional to spatial frequency of the grating in the x-direction and also the displacement of the beam from the zero order. Here, the number of periods in the blazed grating is twice the value of the corresponding $X_{textoffset}$. As the distance increases, the patterning intensity decreases and dwell-time compensation becomes necessary. It can be seen that dwell-time compensation significantly improves the uniformity of features. By definition, theory predicts that all compensated features should have a normalized height of 1. Performance is even better if even more dwell-time is added (overcompensation).

is more than twice this amount and therefore still the limiting factor. Another limiting factor for the minimum possible linewidth achievable in this patterning mode is speckle. Holographic systems with coherent light sources suffer from speckle. Instead of a smooth, solid intensity in the target image, some points of the image are very bright, and some are dim. There are methods to compensate for speckle that will be discussed below, but parallel patterning requires that portions of a pattern must be overexposed to ensure that the dimmer parts are cured at all. This increases the minimum achievable linewidth.

Also, as discussed above, the whole patterning field does not fit on the sensor in the CCD camera. The actual area in which a target image can be placed in the 512×512 pixel target imaging field is about 350×250 pixels (56 μm by 40 μm area in the specimen plane). The zero order is in the center of the image, but can be blocked without causing much disturbance to the patterning field. The whole field cannot be used at once due to the very limited laser power available.

The peak intensity per pixel can be used as a metric to determine whether a certain target feature is possible. As shown in Table 3, the available peak intensity in the strong first diffraction order for the 100× objective is 35.5 GW/cm^2. The curing threshold is around 2.7 GW/cm^2 for 0.1 second exposures, so target intensity patterns with up to 13 well separated pixels should be possible. A longer exposure time can reduce the apparent curing threshold. For 2 second exposures, the curing threshold was measured to be 0.36 GW/cm^2. Most parallel-exposed patterns were exposed for longer than 0.1 seconds and in practice the number of pixels in a target image could reach up to 80 pixels for this system. Another factor that enables larger than expected patterns is that spacing between adjacent pixels is less than a cured voxel diameter and multiple pixels can be thought of as contributing to a single voxel. Table 7 shows the peak intensity per pixel for several simple target patterns. Even a 30×30-pixel square is too big for the available laser power.

A 100-pixel target intensity pattern would produce a cured feature that takes up about 4.75 μm^2. The parallel patterning characterization done here can only be on a rudimentary level due to the lack of available laser power. The area of the largest possible cured feature is only about 0.2% of the available 2240 μm^2. Parallel 2D DMHL has been done by segmenting the target image into pieces small enough to be cured by available laser power [4].

Table 7: Number of pixels for certain patterns (Parallel Patterning). These are assumed to be made with images that are 512×512 pixels using the strong first diffraction order.

Pattern	Pixels	P.I. per pixel w/100× (GW/cm^2)	P.I. per pixel w/63× (GW/cm^2)
10×10 square	36	0.99	0.39
20×20 square	76	0.47	0.18
30×30 square	116	0.31	0.12
diameter 20 circle	52	0.68	0.27
diameter 30 circle	84	0.42	0.16

The dwell time concept also applies here. The required exposure time for a certain image is inversely proportional to the square of the average intensity. The average intensity varies with the number of pixels in the feature. For example, a 20×20 square has about twice as many pixels and needs to be exposed for $4\times$ the amount of time as a 10×10 square because the average intensity will be one half.

5.2.1 Speckle Reduction

Speckle is a phenomenon in which coherent light scatters off a material that is not optically smooth [31]. Each point in the material is a scattering source and in the far field, each of these sources can interfere to produce a random pattern of light and dark spots. In this research, the random phase distribution used at the beginning of the GS algorithm acts as a diffuser, and introduces speckle to the reconstructed image in the specimen plane, but a continuously variable random initial phase reduces speckle better than a binary random phase [1]. One method of reducing the effect of speckle in parallel lithographic patterning is to expose the same feature with several independently derived holograms. This has the same effect as moving the diffuser during exposure to spatially average out the speckles.

An equation for speckle contrast, C, is given by: [31]

$$C = \sigma/\langle I \rangle = 1/\sqrt{N} \tag{5.6}$$

where σ is the standard deviation of the intensity, $\langle I \rangle$ is the average intensity, and N is the number of images added. The ideal situation is $C = 0$. In most experiments done here, N ranges from 5 to 10, resulting in a speckle contrast reduction from about 1 to 0.447 (for $N = 5$) to 0.316 (for $N = 10$). There is a finite transition time between holograms, so the actual exposure is less than implied by the number of holograms multiplied by hologram exposure time.

5.2.2 Experimental Results

Hollow squares of 10×10, 20×20 and 30×30 pixels were attempted with the $63\times$ objective (see Figures 69 and 70). Movies of N holograms were used to average out the speckle. The fact that the 10×10-pixel squares were overexposed ($N = 5$, 0.1 sec. each), the 20×20-pixel squares were adequately exposed ($N = 10$, 0.2 sec. each), and the 30×30-pixel squares were underexposed ($N = 20$, 0.5 sec. each) is not surprising if it is assumed that about 2 pixels contribute to each voxel for the 2 second exposure of the 20×20-pixel square.

Circular target intensity patterns were used to show the process is capable of curvilinear features. The 30-pixel-diameter circles (see Figure 71) had a similar peak intensity as the successful 20×20-pixel square patterns, but only segments of the circles cured. This may be due to the fact that the intensity is not uniform enough in the particular part of the patterning field.Actually the circle exposure pattern had many more than the 84 pixels given in Table 7 because the circle was more than one pixel thick, but the fact that the spacing between pixels is much less than the spacing between voxels means the peak intensity is effectively the same.

In an effort to see if a different region of the patterning field was more uniform, the location of the circle in the patterning field (see Figure 72) was adjusted slightly and a whole circle cured. It was made with $N = 10$ holograms, each exposed for 0.1 seconds.

The parallel-exposed circles in Figure 73 were made with a peak intensity per pixel of ~ 0.35 GW/cm^2 instead of 0.42 GW/cm^2 to reduce linewidth. They also were unevenly exposed.

The three sets of four parallel-exposed circles in Figure 74 were each made without moving the microscope objective, but in separate exposures. It can be seen in Figure 47 that even about the center of the patterning area, one half has higher intensity than the other. This is also evident in Figure 74 in that the top pair in each group of four is more cured than the bottom pair. This can be compensated with dwell time compensation as or graylevel scaling as explained below.

The features exposed in this research are too small to show the effects of a drop-off in diffraction efficiency between points on the feature nearest and furthest from the zero order.

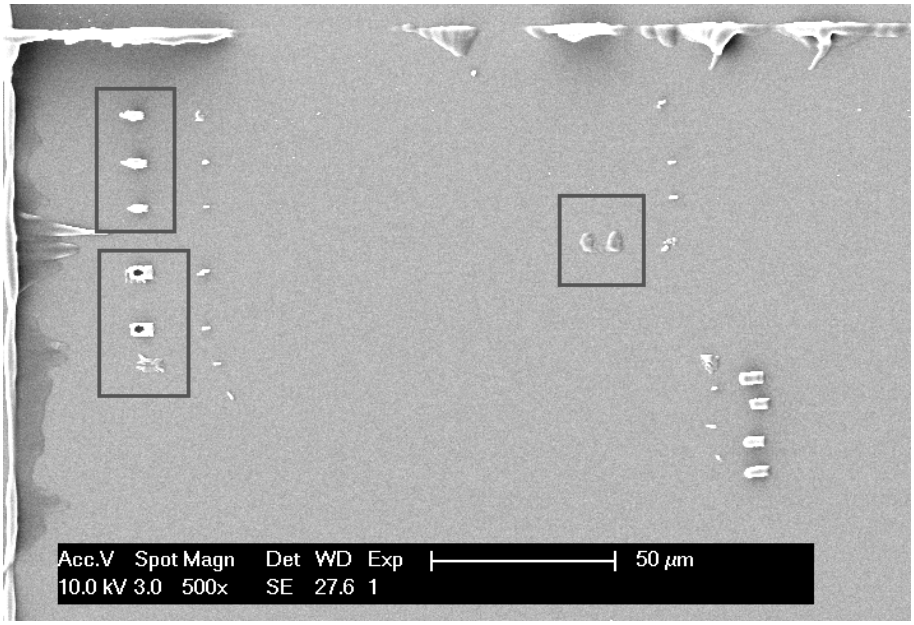

Figure 69: This is the whole Litho 43 sample. The three sets of interest have boxes around them. Clockwise from the top left are 10x10 squares, 30x30 squares, and 20x20 squares. This is the first instance of a parallel feature being exposed properly (20x20 squares in bottom left).

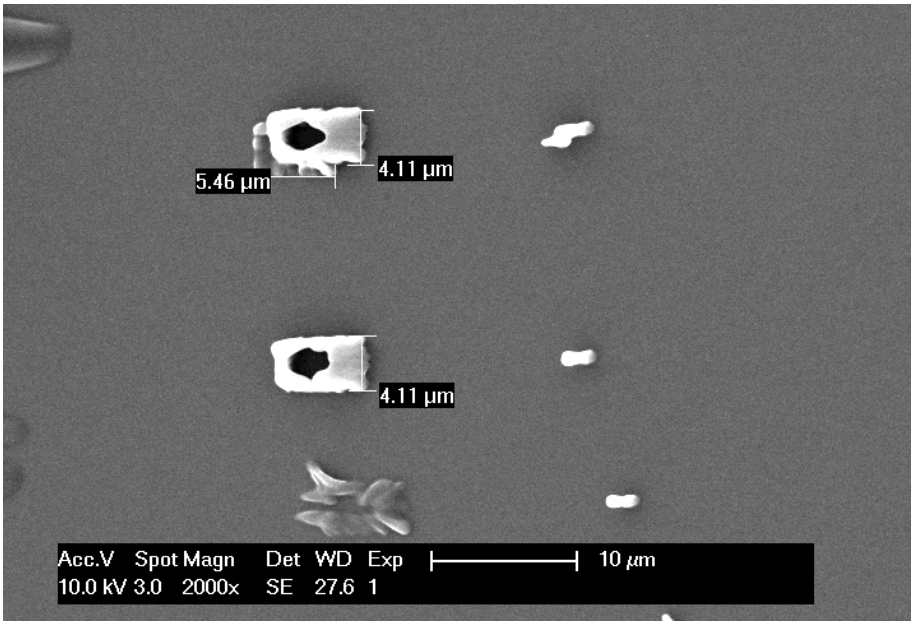

Figure 70: The two good-looking squares were made with $ND = 0$ and 10 holograms each exposed for 0.2 seconds. The top one was exposed twice.

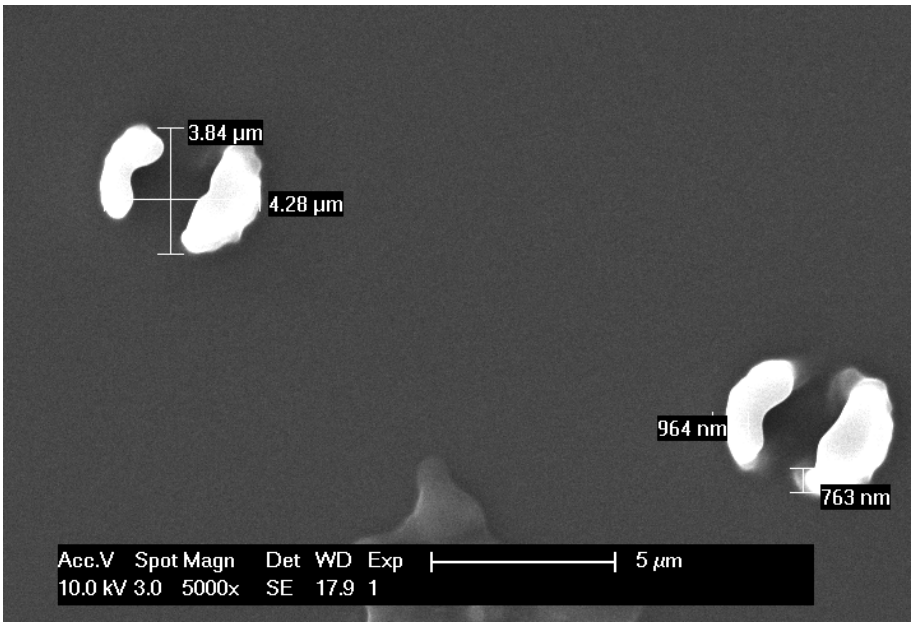

Figure 71: Segments of circles (Top: $N = 10$, Bottom: $N = 5$) in parallel exposures.

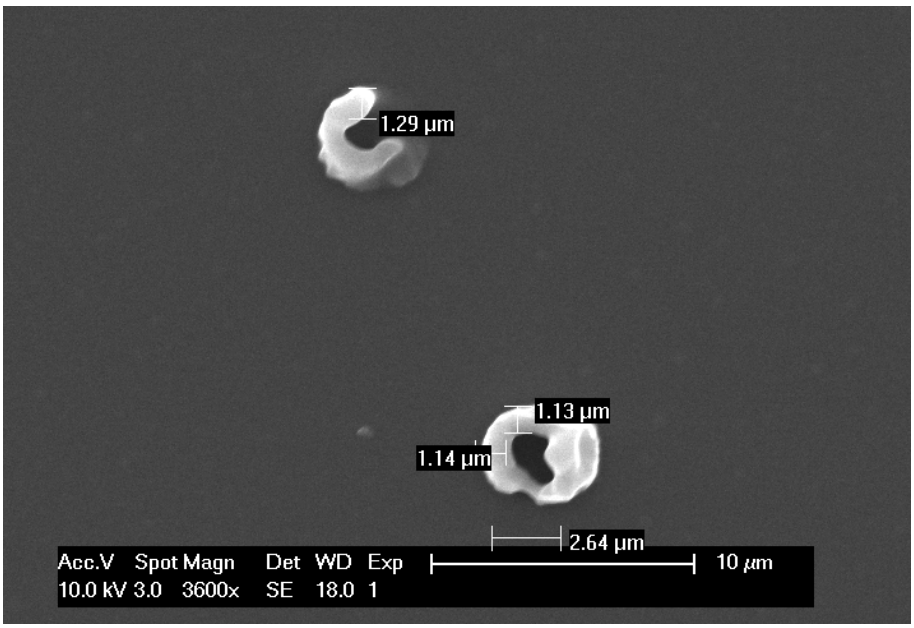

Figure 72: These circles were exposed separately, with the objective being moved between exposures.

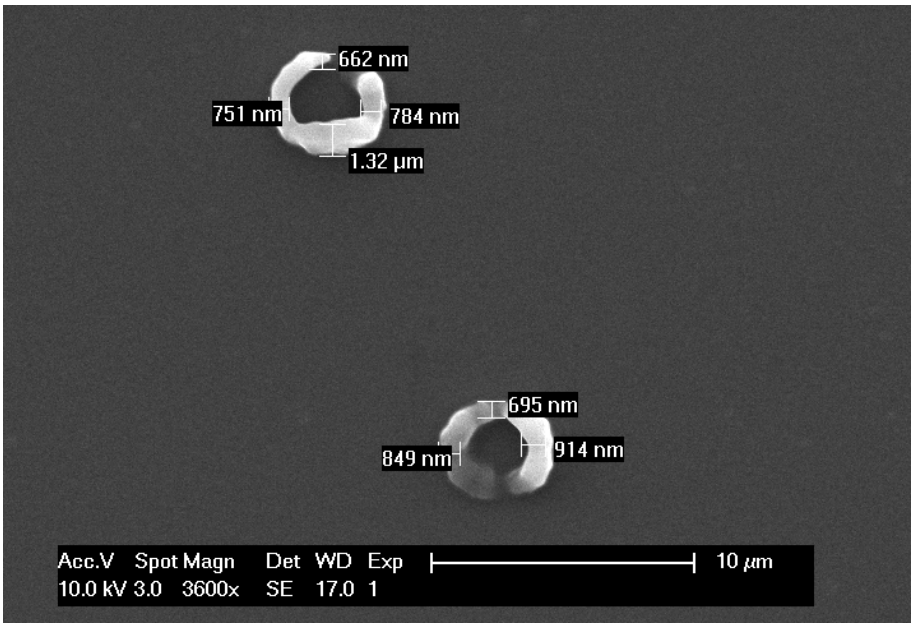

Figure 73: This set was made with $N = 10$ holograms and an exposure time per hologram of 0.3 sec.

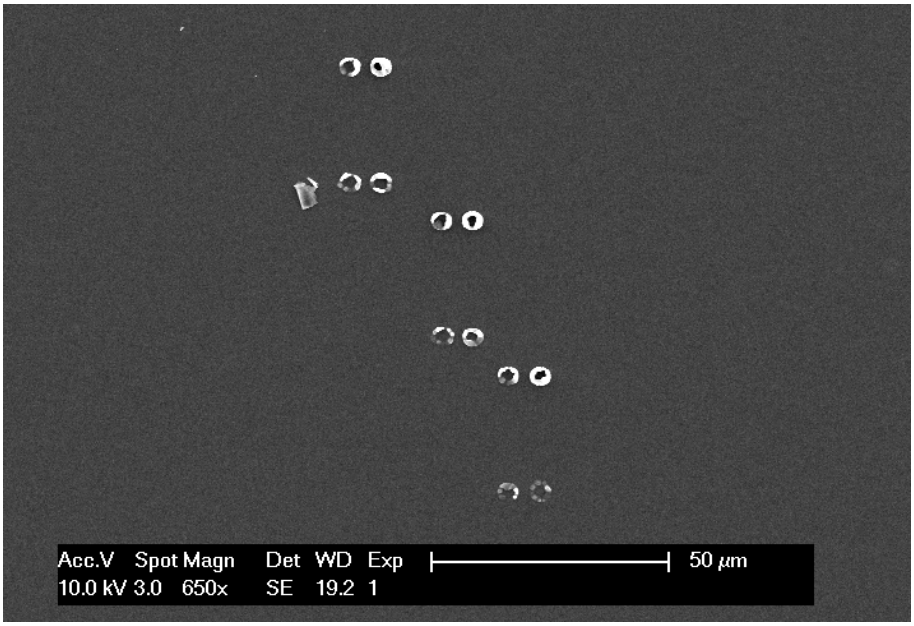

Figure 74: This set was made with $N = 10$ holograms. The top left set had an exposure time of 0.25 sec. per hologram, the middle set, 0.2 sec. per hologram, and the bottom right set, 0.15 sec. per hologram.

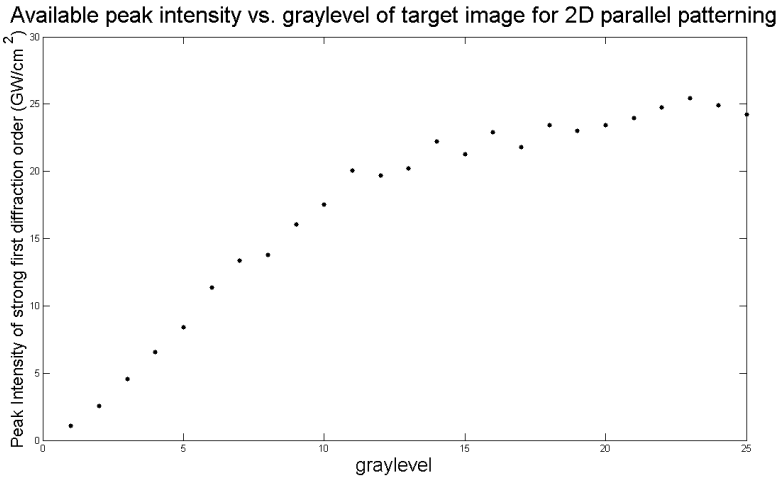

Figure 75: This plot shows how the available peak intensity in the strong first diffraction order changes as the flat graylevel applied to the target image is changed.

On the other hand, whole features can be noticeably underexposed as they get further from the zero order. One way to compensate for this is to adjust the graylevel of the target image. The graylevel of the feature to be placed furthest from the zero order can be left as the maximum graylevel, white (graylevel=255/3=85), while the closer features can be adjusted accordingly. The graylevel on a scale from 0 to 85 is a consequence of RGB decomposition of the input image in MATLAB. This is equivalent to applying a crude gradient to the target images that brightens them with distance from the zero order. Unfortunately, the peak intensity in the strong first diffraction order does not change linearly (as assumed in these samples). The intensity is practically constant from graylevel= 85 all the way down to about graylevel= 25. It then varies as shown in Figure 75.

To account for the decreasing diffraction efficiency in parallel exposures, a different graylevel was applied to each target image in Figure 76. Each parallel-exposed, 30-pixel-diameter circle was exposed separately. All six in a set were made without moving the objective.

Other holograms are known to produce circular beams. A Bessel beam can be created with an axicon (a conical lens) and has an extended focus, propagating with minimal

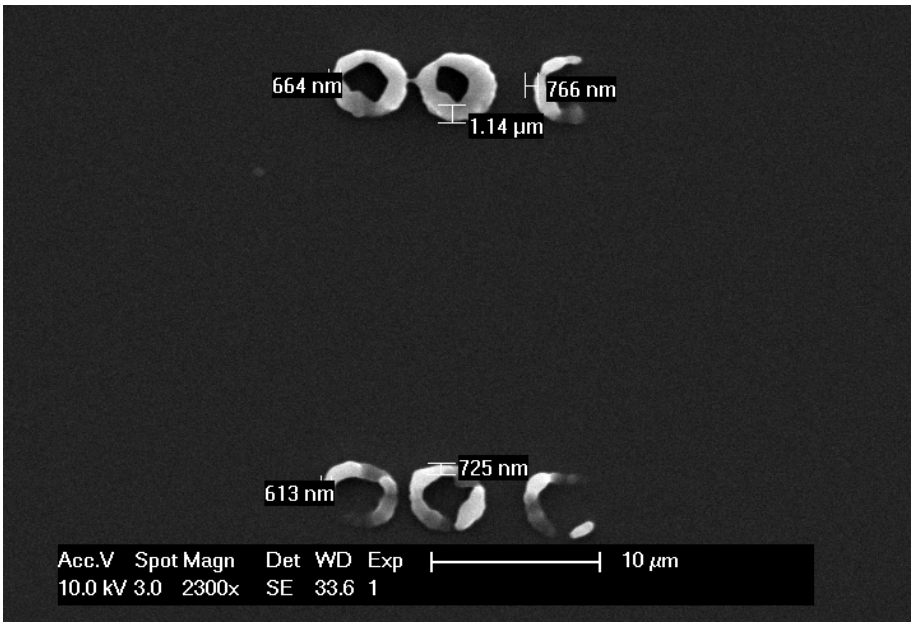

Figure 76: This set was made with $N = 10$ holograms each exposed for 0.25 sec. The graylevel decreases from left to right with increasing distance from the zero order.

diffraction [24]. The equation for the phase hologram is [18]:

$$\phi(x, y) = \exp\left[\frac{-i2\pi r}{r_o}\right] \tag{5.7}$$

where $r = \sqrt{x^2 + y^2}$ and r_o is a constant. Displaying a phase axicon allowed for more uniform rings that did not appear to suffer from speckle (see Figure 77). Ways to take advantage of this should be investigated in future work.

The calculated average linewidth for 2D parallel DMHL is 938±292 nm. The data set has a large standard deviation due to the lack of uniformity over the patterning area and the need to overexpose a particular feature to make sure the whole target image cures. For a similar reason the large area serial resolution is larger than the small area serial resolution in the section above. Parallel patterning inherently has worse resolution because speckle requires long exposures to fill in all parts of the pattern evenly. Parallel-exposed features are very sensitive to their placement in the patterning field. The illumination of the SLM is not

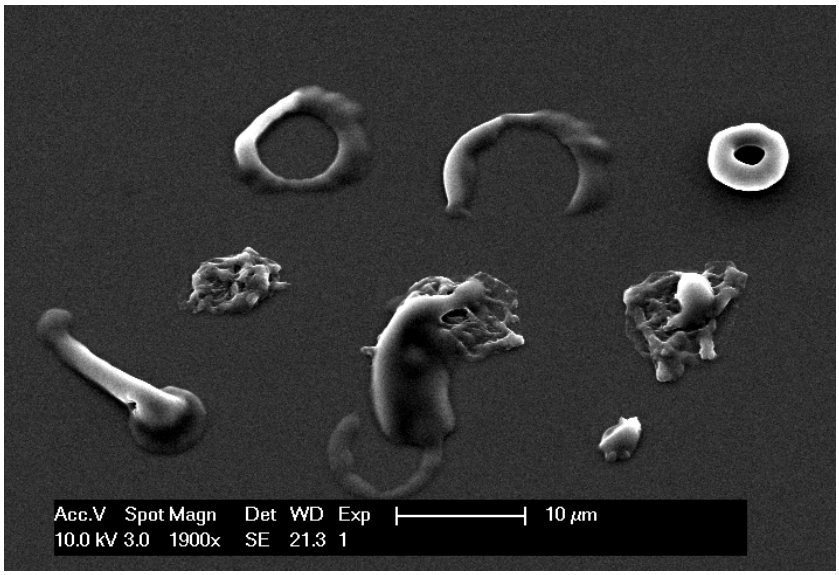

Figure 77: Several parallel-exposed circles made with Bessel beams. Each column is a separate exposure with the Bessel beam of a different r_o value. The center row is the over exposed zero order.

uniform enough for parallel patterning to be very viable. The 2D parallel- exposed circles show the potential for 500 nm resolution, but speckle and nonuniform illumination make it difficult to achieve consistently.

5.3 IN BETWEEN 2D AND 3D

Various methods of patterning are difficult to categorize as 2D or 3D. One method of making 3D features is to expose a single feature with parallel 2D DMHL, and then expose another feature on top of it by displacing the feature axially with a Fresnel lens. Figures 78 and 79 show the results of a horizontal line segment being exposed, and then a vertical line segment being exposed at a variety of depths into the sample. Each input image was a white line segment 20 pixels by 3 pixels on a black background (512x512).

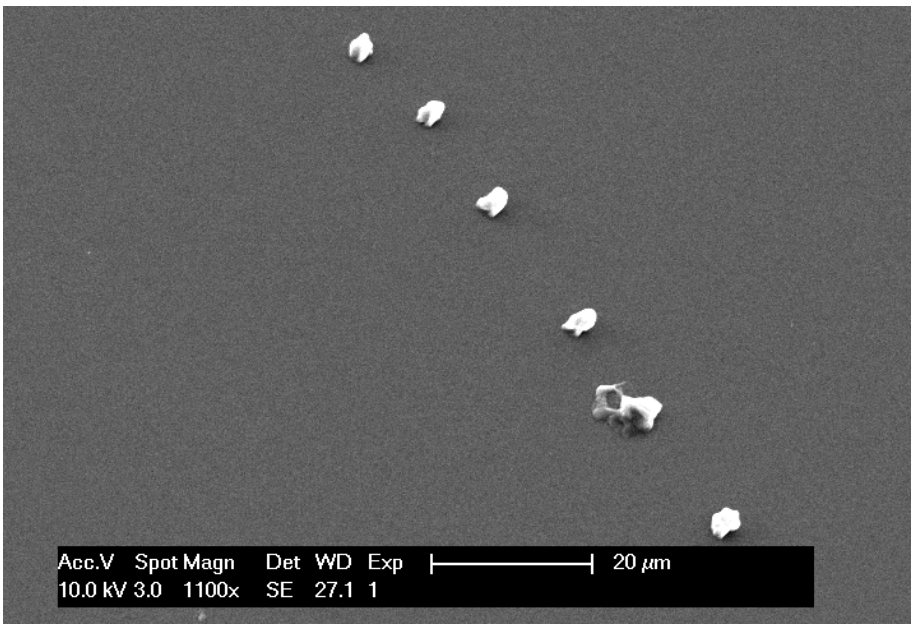

Figure 78: One parallel line segment was exposed, then an orthogonal line segment was cured at various depths to create a cross ($N = 5$ holograms with an exposure time of 0.15 sec.).

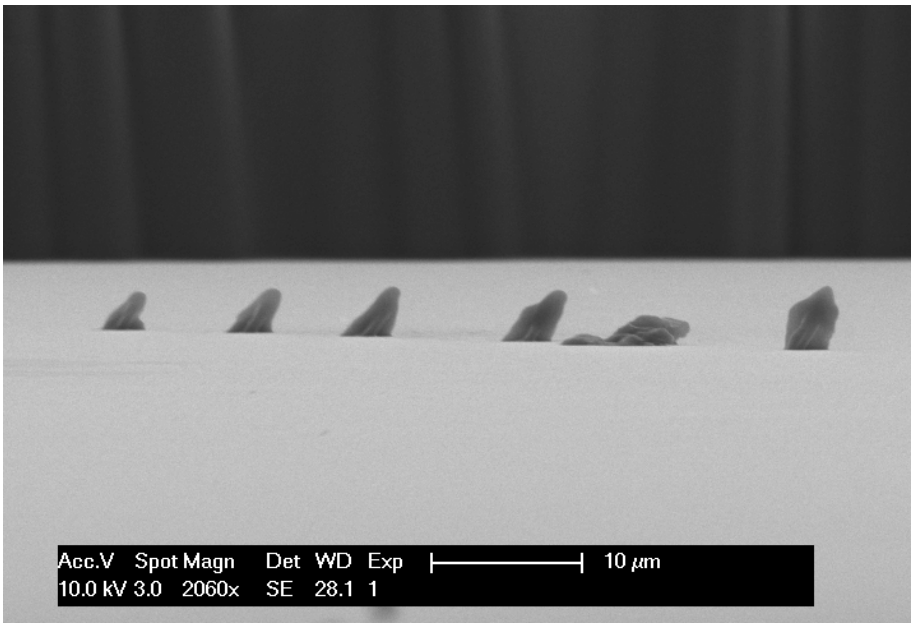

Figure 79: One parallel line segment was exposed, then an orthogonal line segment was cured at various depths to create a cross.

Also, multiple holograms can be summed together to create a single hologram that makes a 3D intensity pattern. This requires that all but one of the holograms to be summed have a Fresnel lens superimposed on it to displace it axially in the pattern. One method that works well is described by Davis and Cottrell [17].

6.0 3D PATTERNING RESULTS AND DISCUSSION

The main benefit of using phase holograms for patterning is that the beam focus or whole intensity pattern can be moved in three dimensions without any moving parts. By adding a Fresnel lens to a blazed grating, it is possible to move the focus of the first order beam axially. A sequence of these holograms can be displayed to build a feature serially. Aberration correction can be used to maximize the intensity in the focal volume and increase the potential patterning volume. Also, phase holograms allow for entire volumetric intensity patterns to be displayed in the resist. Whole features can then be cured in a single shot.

6.1 3D SERIAL PATTERNING

The 3D serial patterning mode is very similar to the 2D serial mode except that each hologram now has a Fresnel lens added to it, defining its axial position in the patterning volume. The axial positioning resolution of each voxel is essentially continuous as it was for lateral positioning. The process resolution for 3D serial patterning is necessarily worse than that of 2D serial patterning because the features must not only survive the development process but be able to support their own weight as well.

6.1.1 Measuring Axial Voxel Length

In order to design features with the necessary amount of voxel overlap, the axial voxel length must be found. The axial voxel length can be estimated in two ways. The first is to suspend a one-voxel-thick line in the air and the other is to make a series of lines at increasing depths

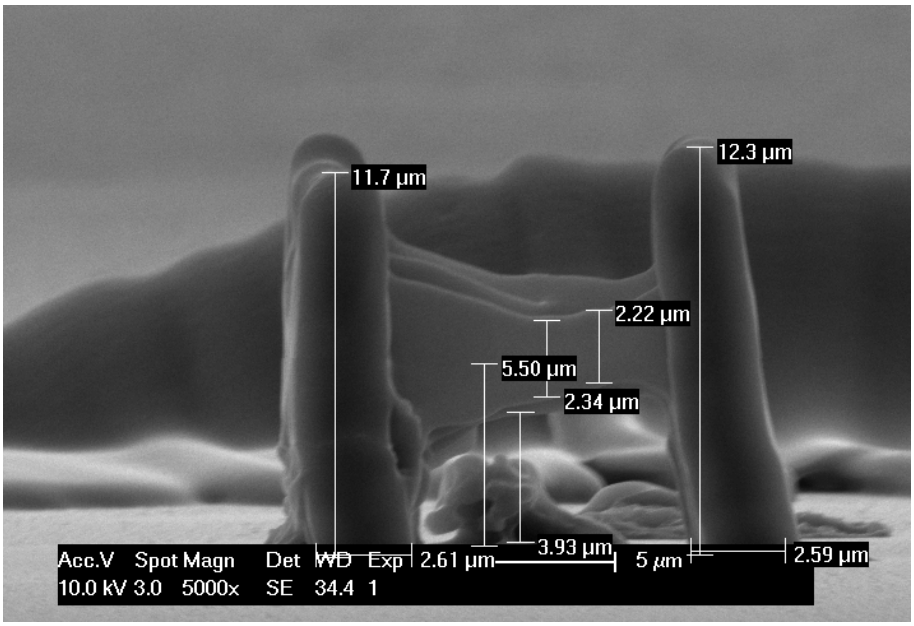

Figure 80: Cured lines were hung in the air using 3D serial patterning.

into the resist layer. When there is not enough cured resist adhering to the substrate, the line falls over. This measurement puts a lower bound on the axial voxel length. In tandem, these methods provide a robust value for the axial voxel length. Although the "true" axial voxel length can be thought of as the value found using the first method, the more practical number comes from the second. Most of the axial voxel length data quoted here is from the second method.

Using the first method, one-voxel-thick, 2D serially-exposed lines were suspended in the air using the 63× objective (see Figure 80). The voxel thickness is over 2 μm because a high intensity and slow scan speed were used. All the data given in this section will be synthesized and plotted to show the relationship between peak intensity and axial voxel length (see Figure 83).

The method of making lines with increasing depth into the resist layer was used at three different exposure peak intensities and two different dwell times. The voxel spacing was about 250 nm. An example of the experimental results are shown in Figures 81 and 82. The

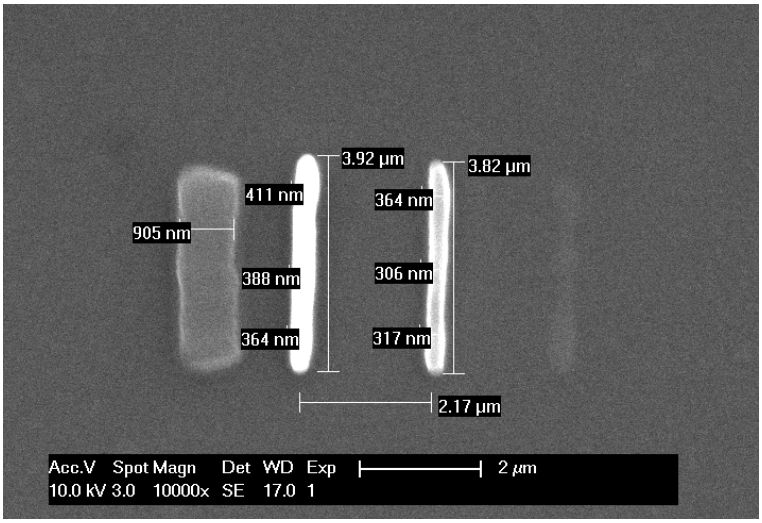

Figure 81: This set of lines was made with an exposure time of 0.15 sec. per dot and a peak intensity of about 2.7 GW/cm^2. The line on the left has fallen over indicating that the axial voxel length is being approached.

length of the fallen line is taken as the usable axial voxel length for fitting data to the model. A model of the axial voxel length for a point exposure is given in Chapter 3 but is repeated here: [54]

$$l(P_t, t) = 2z = \frac{2\lambda}{\pi[\tan\theta]^2}\left[\left(\frac{4\pi^2 P_t^2 t[\tan\theta]^4}{\lambda^4 E_{th}}\right)^{1/2} - 1\right]^{1/2} \tag{6.1}$$

where d is the voxel diameter, l is the voxel length, E_{th} is the threshold energy, P_t is the laser power, and t is the exposure time. Rewriting the equation without the constants,

$$l(P_t, t) = A[(BP_t^2 t)^{1/2} - 1]^{1/2} \tag{6.2}$$

gives two fitting parameters, A and B. The serially-exposed axial voxel length data fits well with the given theory (see Figure 83). The estimated axial voxel length for the "standard patterning parameters" given in Chapter 5 (exposure peak intensity of about 2.7 GW/cm^2 and a dwell time of 0.15 sec. per voxel) is then about 1.2 μm.

Although the hanging lines in Figure 84 were made in a parallel exposure, they are still one voxel thick. They were exposed at a designed height of 4.0 μm, and were found

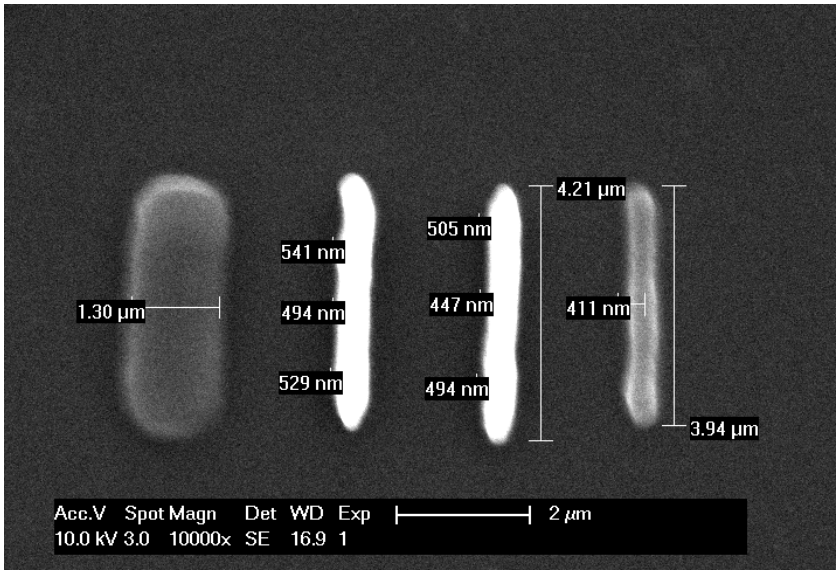

Figure 82: This set of lines was made with an exposure time of 0.3 sec. per dot a peak intensity of about 2.7 GW/cm^2. The line on the left has fallen over indicating that the axial voxel length is being approached.

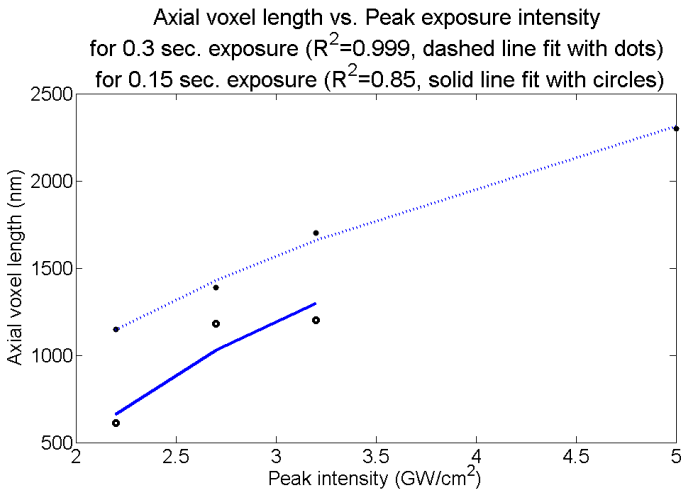

Figure 83: Plot of axial voxel length vs. exposure peak intensity for two different dwell times. The data is fit to an equation for the axial voxel length given in Chapter 3.

to be about 3.7 μm above the substrate surface which is within the axial placement error ($\pm$750 nm, a half-increment on the fine focus knob of the microscope) inherent in using a microscope with no motorized stage. The thickness of the parallel features hanging in the air are between 500 nm and 1.5 μm. The results from this parallel exposure are consistent with those of the serial exposures.

6.1.2 Aspect ratio limit

The mechanical strength of the resist limits possible aspect ratio of a cured feature. Several tests were done to find this limit for Ormocomp©, first with DMHL and then without.

Two serial 3D pillars were made with the weak first order. This experiment also tested the depth to which patterning can be done with the 63× oil immersion objective without aberration correction. The first pillar was made with a peak intensity of 8.45 GW/cm^2 and 0.3 sec. exposure per voxel, and fell over. The expected lateral dimensions were about 2 μm × 2 μm. The spacing between layers of the pillar was about 600 nm. It was designed to be about 25 μm tall but turned out to be about 5 μm taller than expected (to be discussed below). The axial voxel length at this peak intensity is around 3 μm, which cannot explain the extra 5 μm in the pillar. The other pillar (see Figure 85) was made with a peak intensity of 6.78 GW/cm^2 and 0.3 sec. exposure per voxel, and was designed to be the same height. The resulting pillar was only 15 μm tall, but did not fall over. It is likely that spherical aberration reduced the power at greater depths into the sample, preventing curing at this lower peak intensity. It should be noted that this pillar shows the best obtained aspect ratio from using DMHL in this research ($\sim$6.9). To make sure that the DMHL process itself was not limiting the aspect ratio, the 10× objective was used without the SLM to make a free-standing pillar (see Figure 86). The aspect ratio achieved ($\sim$ 12) is almost double that achieved with DMHL so far. This suggests that thinner pillars could be made with DMHL, but that the height of features may be limited by aberration.

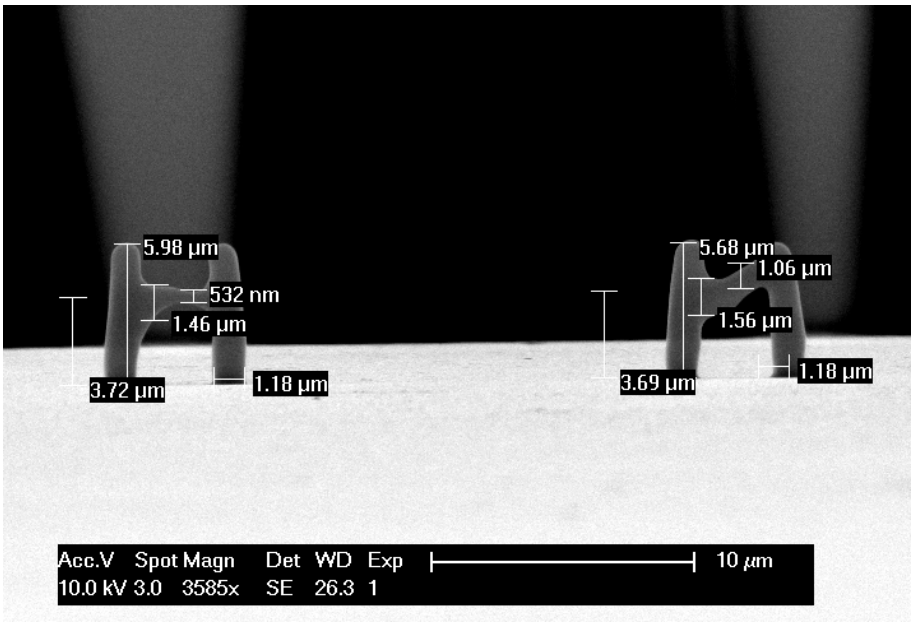

Figure 84: Sets of pillars were made from which to hang parallel-exposed features. The horizontal beam connecting the two vertical pillars is one voxel thick. Both hanging features were made with two separate exposures. The feature on the left was made with a horizontal beam exposed first and an orthogonally placed beam exposed next that did not cure. Each exposure was with $N = 5$ holograms and an exposure time of 0.15 sec. each. The feature on the right is similar except that the second exposure was of a Bessel beam, which also appears not to have cured.

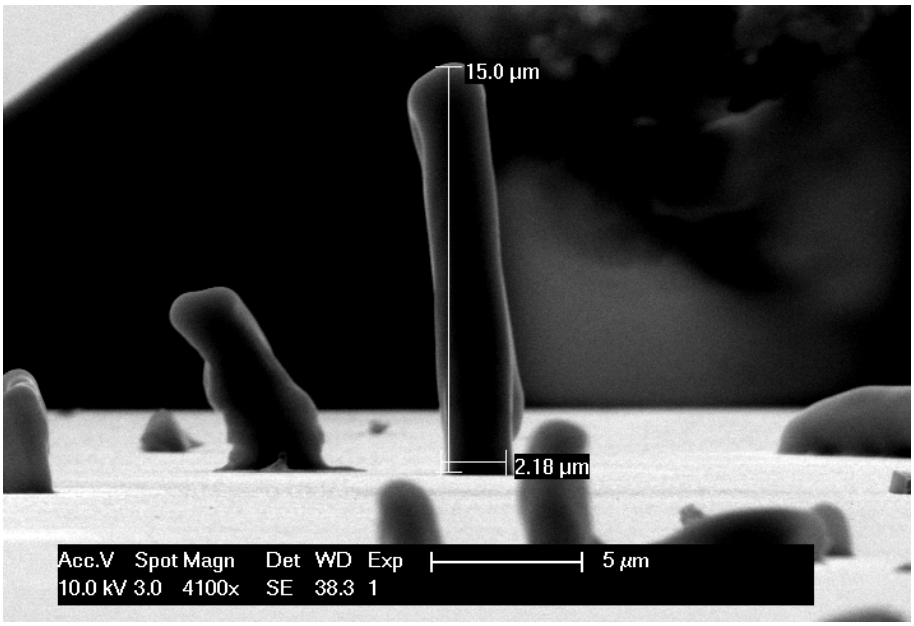

Figure 85: The pillar made with 6.78 GW/cm^2 peak intensity and 0.3 sec. exposure per voxel.

6.1.3 Patterning volume - Aberration correction for DMHL

With 3D serial DMHL resolution determined, the next process characterization to make is the potential patterning volume. Aberrations can limit the patterning volume by reducing the peak intensity at the intended voxel location. Holographic aberration correction has been done mostly in holographic optical tweezers [108] but the same concepts can be applied to DMHL. Aberration correction has also been done recently in microscope systems using deformable mirrors [9, 80, 103].

There are two main aberrations (see Chapter 4) that occur in a DMHL set up and degrade the quality of features that can be produced. The first is spherical aberration due to the refractive index mismatch between the immersion oil that is used with a high-NA objective, and the photoresist being cured [86]. The second is astigmatism due to poor flatness across the SLM face [108]. This is especially true for transmissive SLMs that have large (on the

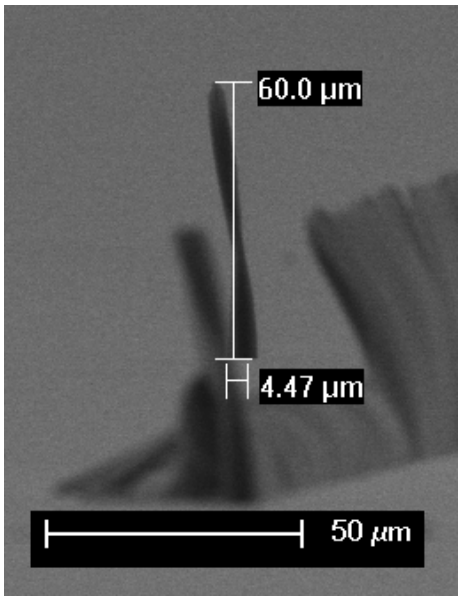

Figure 86: The pillar was not made with DMHL. With no SLM, the 10× objective created a free standing pillar with an aspect ratio of 12. This gives a better idea of the physical limits of the mechanical strength of the resist.

order of 1 cm^2) apertures. The result of the aberrated system is a decrease in potential patterning volume or an increase in patterning time if dwell-time compensation is used [69]. Aberrations also reduce pattern fidelity.

To implement aberration correction in a DMHL system, the aberrations in the optical system must first be characterized. This can be done by applying a series of Zernike polynomials (see Chapter 4) to the SLM and measuring the "sharpness" of the laser spot focused on a coverslip with the CCD camera. The set of Zernike coefficients that provide the sharpest spot is then chosen for aberration correction. Finally, the increase in potential patterning volume due to aberration correction is quantified.

6.1.3.1 Sharpness Metrics The quality of the focused laser spot in the specimen plane is determined with a sharpness metric. One such metric has a global minimum when all aberrations have been corrected. The metric looks like [108]:

$$M_s = \left(\sum_{ij} I_{ij} \right)^2 / \sum_{ij} I_{ij}^2 \tag{6.3}$$

where I_{ij} is the intensity of the ijth pixel.

Another sharpness metric takes the integral of the intensity within a pupil that is centered on the location of the original laser spot at zero defocus. It is given by [75]:

$$S = \int P(x,y) I(x,y) dx dy \tag{6.4}$$

where $P(x,y)$ is a circular pupil. This type of sharpness metric is appropriate when the pupil function is the same shape as the undistorted image, which in this case is a diffraction-limited circular dot. If the pupil is small enough, this metric is a maximum at zero distortion.

The sharpness metric chosen for use in this work is the one in Equation 6.3 because it accounts for both the shape of the laser spot and its intensity, and does not require an arbitrary pupil function. At first each set of coefficients for a particular Zernike polynomial is tested individually. Then linear combinations of Zernike polynomials are tested to find a global minimum in the sharpness metric. A MATLAB script is used to display a hologram with a certain combination of Zernike polynomials, grab an image of the laser spot, and then

apply the sharpness metric. This method does not work for spherical aberration because focusing the laser spot on a coverslip does not cause the same kind of spherical aberration as that of focusing the spot into the resist. Testing the effects of spherical aberration correction can only be done by SEM inspection after producing a lithographic feature.

6.1.3.2 Experimental results The experimental set up with an added aberration that needs to be corrected is shown in Figure 87. An image of the focused spot is taken with a CCD camera while different aberrations are applied and a sharpness metric is used to quantify the quality of the spot as explained above. The actual phase delay applied by a particular pixel in the SLM is the sum of the delays due to each aberration.

First the x- and y-astigmatism values were varied independently about zero correction, then their linear combination was tested. The linear combination which gives the best sharpness is simply a sum of the two optimum aberrations:

$$W_{\text{opt}}(x,y) = Z_5(x,y)a_{5\text{opt}} + Z_6(x,y)a_{6\text{opt}} \tag{6.5}$$

where $W_{\text{opt}}(x,y)$ is the optimum phase aberration added to each pixel of the patterning hologram, $a_{5\text{opt}}$ is the x-astigmatism coefficient found to provide the optimum sharpness and $a_{6\text{opt}}$ is the y-astigmatism coefficient found to provide the optimum sharpness. By multiplying W_{opt} by a scaling factor, c, it is possible to test a cross-section of the $a_5 - a_6$ vector space. Values of c from -2 to 2 are tested to confirm that the best sharpness occurs at $c = 1$ (see Figures 88 and 89):

$$W(x,y) = cW_{\text{opt}}(x,y) \tag{6.6}$$

Figures 88 and 89 show the measured maximum intensity and sharpness of the laser spot for each set of applied Zernike coefficients. The sharpness metrics are normalized to the sharpness value obtained for a Zernike coefficient of zero (no correction). The sharpness data is fit to a parabola around the point of best sharpness. Because the aberration added to the system was a simple rotation of a lens on one axis, it is not surprising to see that one Zernike coefficient (a_5) is significantly larger than the other. The phase holograms corresponding to $a_{5\text{opt}}$, $a_{6\text{opt}}$, and their linear combination with $c = 1$ are given in Figure 90.

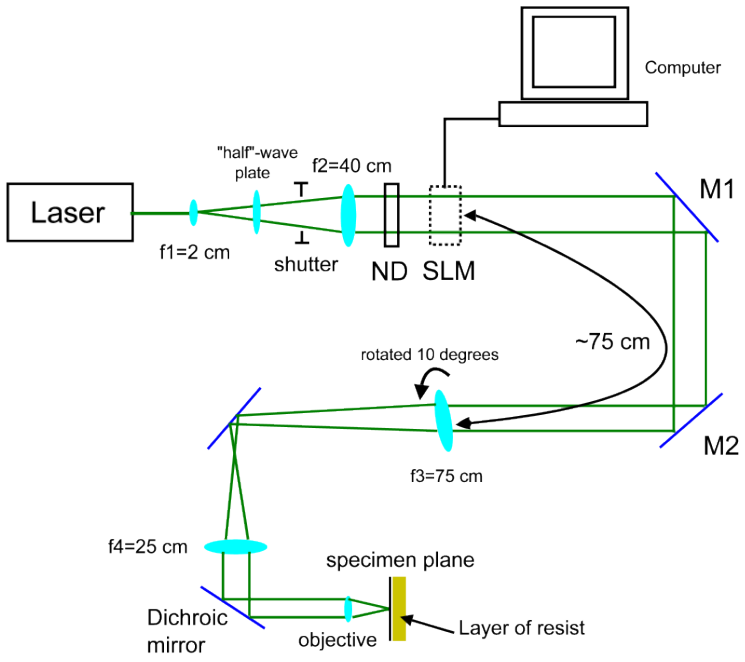

Figure 87: The first lens after the SLM is placed about one focal length away to perform a Fourier transform and is rotated by about 10 degrees to add enough aberration to the system to affect patterning.

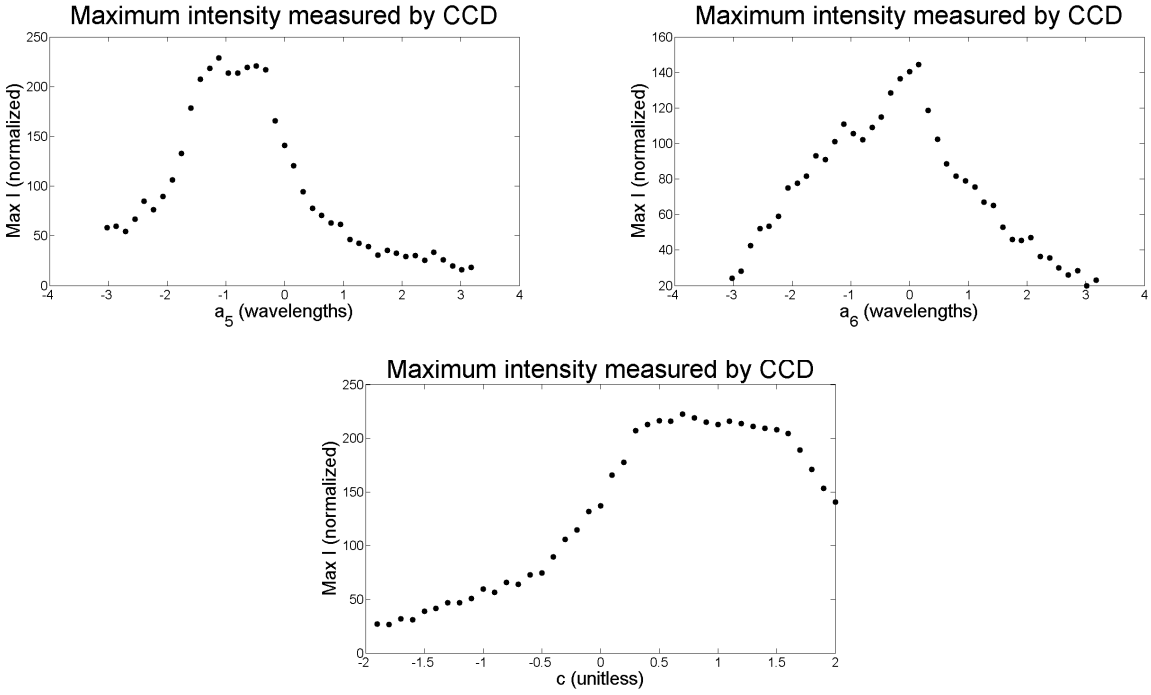

Figure 88: Maximum intensity of laser spot from CCD image for different degrees of aberration correction. The patterning volume is proportional to the maximum laser intensity. Therefore it is best to find a set of aberration correction coefficients that also provide high intensity along with sharpness.

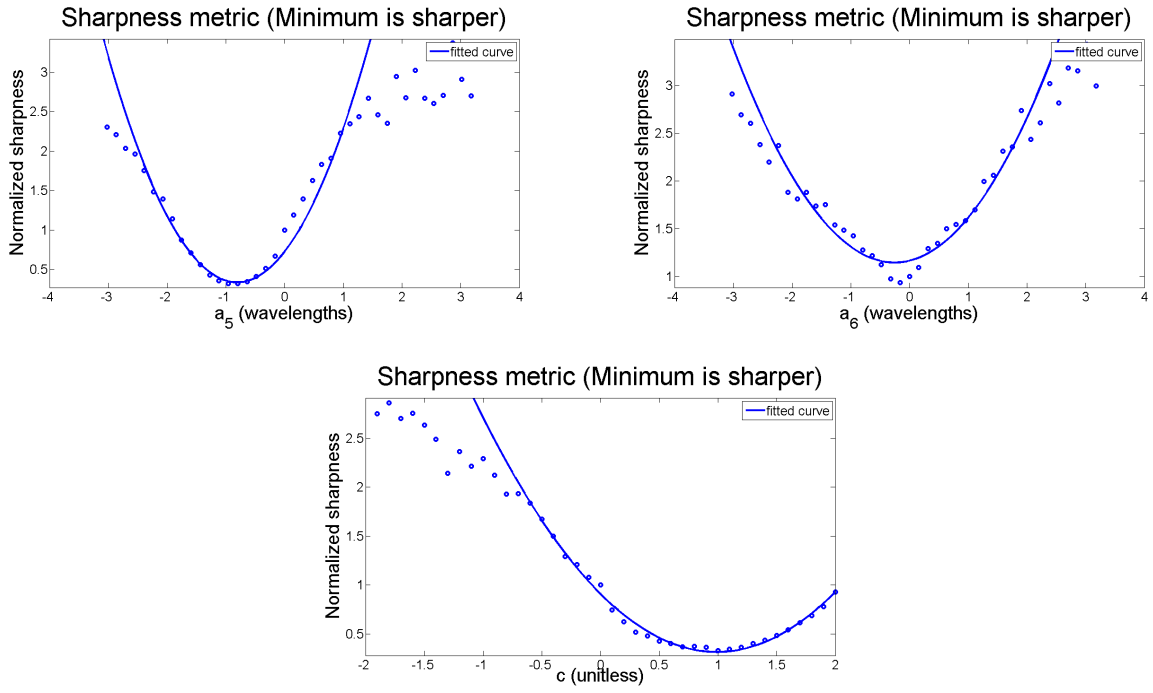

Figure 89: Sharpness of laser spot from CCD image for different degrees of aberration correction. The most efficient use of laser power is to focus the light into the sharpest point possible.

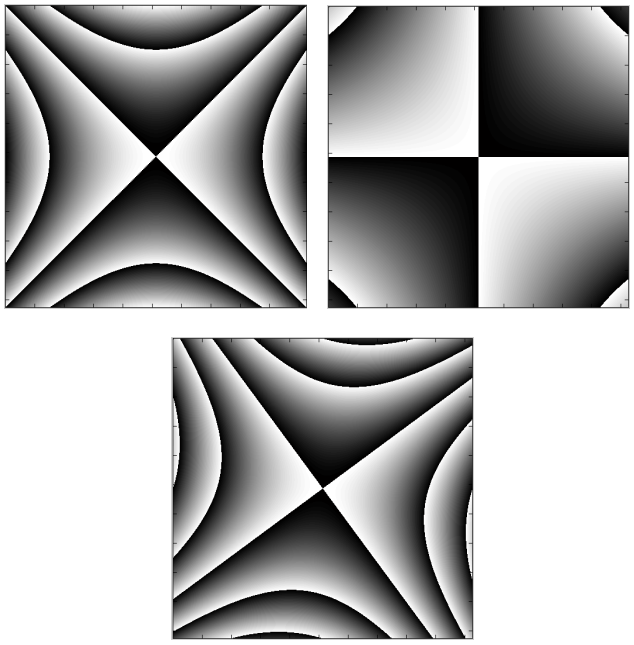

Figure 90: The determined aberration corrections. X-astigmatism with -0.81λ (top left) and Y-astigmatism with -0.25λ (top right) are added to get the total correction (center). The color relates to the phase of the pixel. Black corresponds to a delay of 0 and white corresponds to a delay of 2π.

To demonstrate the effectiveness of aberration correction in DMHL, a 3D feature was designed. The feature is a hollow cube of line segments. Four features were made under identical exposure conditions (same laser power incident on the SLM) except for the amount of aberration correction applied to the patterning holograms. The four amounts of aberration correction correspond to $c = 0$, 0.2, 0.4, and 1.0. These values were chosen because they provide an approximately even sampling of sharpness values between zero correction and optimum correction (sharpness = 1, 0.62, 0.48, 0.33 respectively).

The example features were made through a series of point exposures. Each hologram directed the patterning beam to a single point in space. The peak intensity was about 2.2 GW/cm^2 and the exposure time per voxel was 0.25 sec. The pattern consisted of 4908 points for a total patterning time of about 20 minutes per feature (not including hologram calculation time which pushes total time per feature to about 50 minutes).

The astigmatism compensating aberration can be quantified in units of wavelengths as:

$$W_{\text{ast}}(c) = \pm c\sqrt{(a_{5\text{opt}})^2 + (a_{6\text{opt}})^2} \tag{6.7}$$

This value aids in quantifying the magnitude of aberration that the DMHL system can tolerate. The value of each optimum aberration correction is $W_{\text{ast}} = -0.81\lambda$ when $a_5 = a_{5\text{opt}}$ and $a_6 = 0$ and $W_{\text{ast}} = -0.25\lambda$ when $a_5 = 0$ and $a_6 = a_{6\text{opt}}$. When both Zernike coefficients are set to their optimum values, $W_{\text{ast}} = -0.85\lambda$.

It is difficult to compare resolution between different amounts of aberration correction because linewidth is strongly coupled with laser power. Even if one laser spot is sharper than another, a beam with lower power might produce a line with the same dimensions. Therefore patterning volume is used as the figure of merit.

There is a clear progression in pattern fidelity as the scale factor, c, is increased from zero in the upper left to 1 in the lower right of Figure 91. The side walls of the structure have fallen over in the uncorrected features. This is due to the fact that the beam was not intense and focused enough at the deeper parts of the feature to cure the upper segments of the cube. This puts a lower bound of a 68% increase in patterning volume from uncorrected to corrected. The upper segments of the cube (see Figure 93) begin at a height of about 3.4 μm and reach up to a height of 5.7 μm (5.7/3.4 = 1.68). Even at an intermediate sharpness

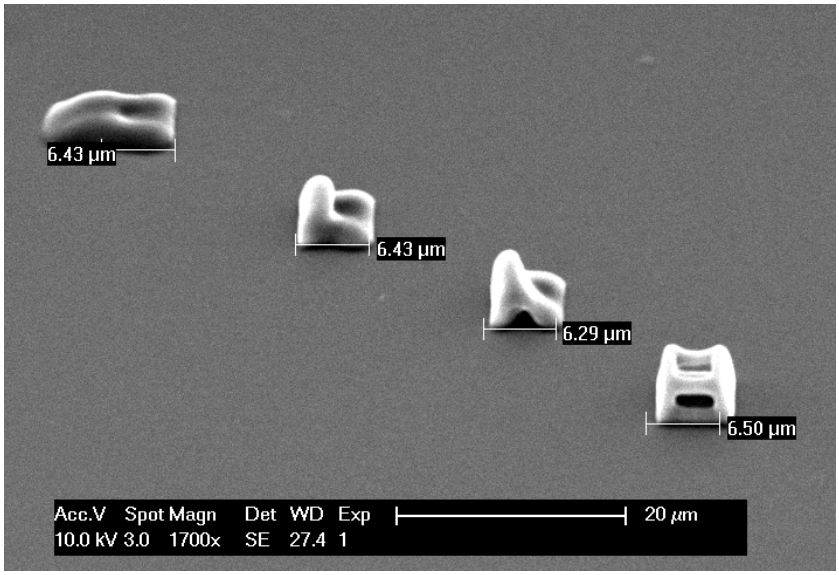

Figure 91: This is an oblique view of four features made with a varying amount of aberration correction. The aberration correction increases from the top left to the bottom right, and there is clear evidence that aberration correction improves pattern fidelity.

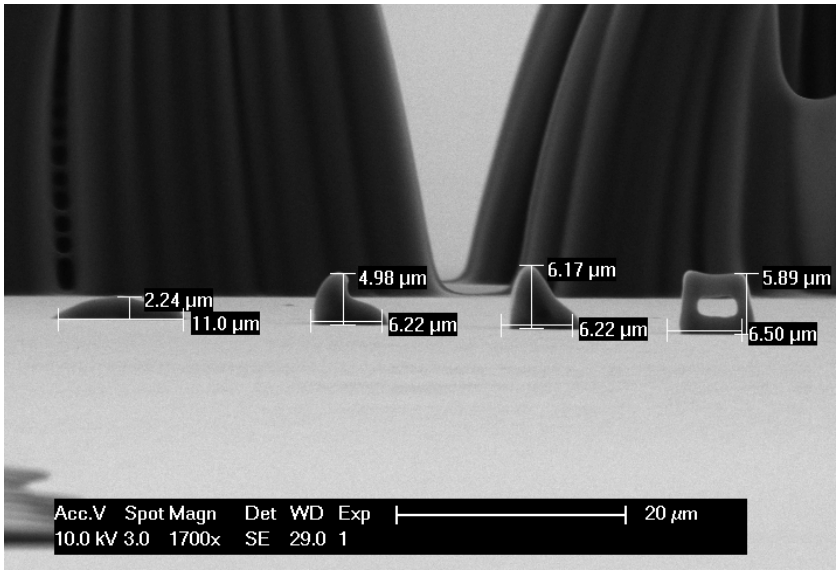

Figure 92: This is a side view of four features made with varying amount of aberration correction. The aberration correction increases from the left to the right.

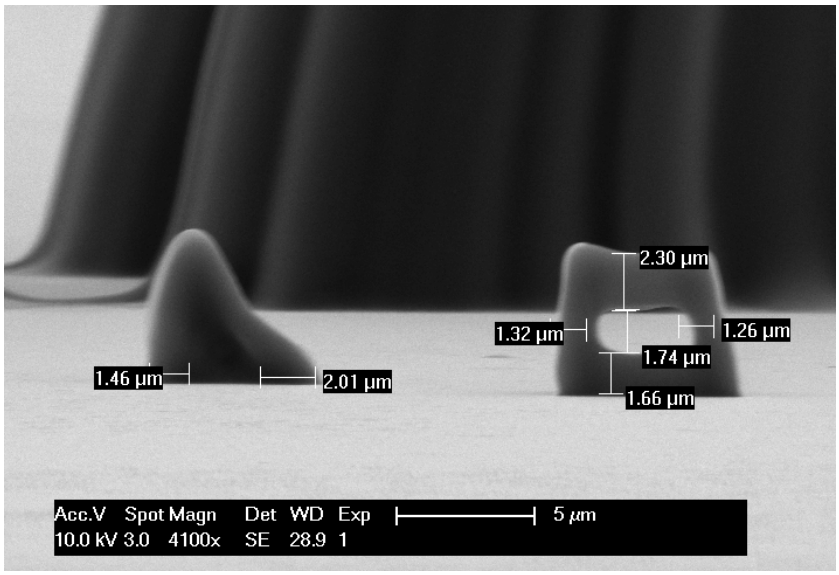

Figure 93: This is a side view of the two features made with the most aberration correction applied. There is still a significant improvement from $W_{\text{ast}} = -0.34\lambda$ on the left and $W_{\text{ast}} = -0.85\lambda$ on the right.

value of 0.48 corresponding to a scale factor of $c = 0.4$, pattern fidelity is poor. The scale factor $c = 0.4$ also corresponds to an applied $W_{\text{ast}} = -0.34\lambda$ and puts a lower bound on the maximum allowable W_{ast} magnitude. The optimum W_{ast} is -0.85λ and shows that this DMHL system cannot tolerate more than a half wavelength of astigmatism aberration. Also it should be noted that in Figure 88 the intensity of the beam is approximately the same from $c = 0.3$ to 1.6 which corresponds to $W_{\text{ast}} = -0.3\lambda$ to -1.3λ. This implies that sharpness is more important than beam intensity in predicting pattern fidelity.

Aberration correction has been shown to transform an optical system incapable of 3D patterning into a system with potentially double the patterning volume. This method allows even inexpensive and poorly aligned components to be used for micromanufacturing.

6.1.4 Anomalous curing - height of features

An interesting phenomenon was seen over and over again through the making of micro-features in Ormocomp© with 1.8% Irgacure 369. If a serially-exposed pillar was designed to be a certain height, it always turned out taller than designed (assuming it was designed to be shorter than the depth limit discussed above). A hypothesis is that the partially-cured region at the top of the feature becomes completely cured through repeated exposure even at the very low intensities far from the geometric center of the focus. This occurs due to the diffusion of radicals in a "weakly polymerized region" that expands with exposure time [81].

Three sets of four pillars were made using 3D serial DMHL to test this hypothesis. The pillar was built up layer by layer with two different exposure times per voxel and two different axial spacings between layers. Each set was designed to have pillars of 1.1 μm, 3.1 μm, 5.1 μm and 7.1 μm in height. The patterning conditions for each set is given in Table 8 and the results are given in Figure 95. As expected, all pillars were taller than designed, but Sets B and C were both taller than Set A. Sets B and C were approximately the same height and had identical total exposure times. This implies that total exposure time determines how much extra curing will occur in a given feature. To achieve optimal results, the shortest exposure time should be used that still creates a feature strong enough to survive the development process.

Table 8: Patterning conditions for anomalous curing experiment.

Set	Axial layer spacing (nm)	Exposure time per voxel (s)
A	500	0.25
B	250	0.25
C	500	0.5

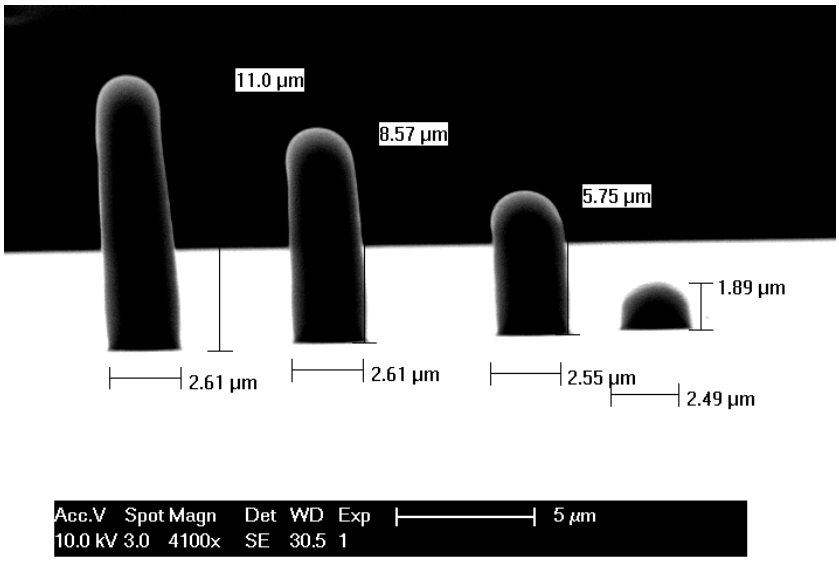

Figure 94: Set A was made with the shortest exposure time and has pillars that are closest to the designed height.

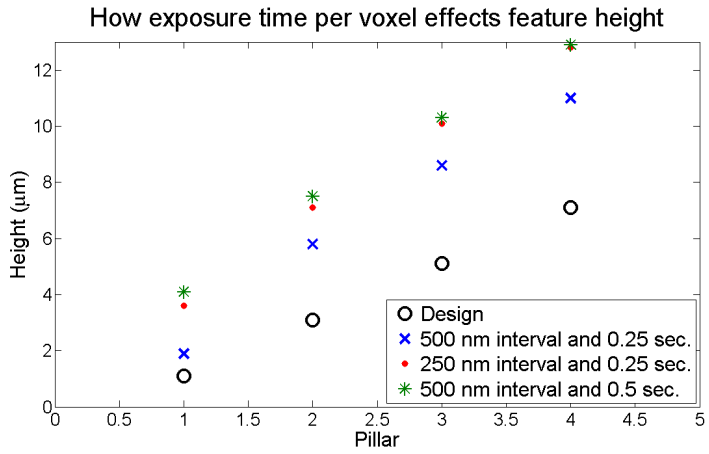

Figure 95: This plot shows the effect of different 3D serial patterning methods. The axial spacing between layers and the exposure time per voxel was varied. All methods produced pillars much taller than designed, but longer exposure time per voxel (set C) and more voxels in a given volume (set B) produce larger deviations from design.

6.2 3D PARALLEL PATTERNING

The majority of micro-feature devices are made with a stationary laser beam (or set of beams) that cures photopolymer on a moving stage. The stage movements must be accurate to the order of nanometers. Also, due to the damage threshold of the photoresist used in these processes, much of the power of an industrial strength laser might need to be blocked and wasted. A more efficient technique for micro-manufacturing is to use 3D light intensity patterns that cure whole features in a single exposure without scanning the patterning beam.

For components that are made of hundreds or thousands of voxels, a significant increase in throughput can be made with 3D parallel patterning. Even when parallel beams are used in serial methods, each voxel of the part must be exposed separately. There are also limits based on the difficulty of adding an arbitrary number of beams to an image field, the size of the feature (limits to how close each beam can be to the other) and the damage threshold of the resist. Even if a powerful laser has its power spread into many beams, the damage threshold of the resist will limit the number of features that can be made at one time because each beam is focused to a single high-intensity point. With 3D parallel exposures, the laser light is spread in all three dimensions, preventing damage due to overexposure and increasing the number of features that can be made in a single patterning field.

There are two ways of accomplishing 3D parallel DMHL. The first is the gratings and lenses method in which a set of voxels is defined, they are summed, and the resulting hologram puts a point of light at each desired location. The second uses a 3DGS algorithm to take a desired 3D target volume and iterates until a hologram is obtained that reasonably approximates the target volume in the focal volume of a microscope objective. The preliminary experimental results from 3D parallel DMHL show that there are some unexpected design constraints pertaining to interference within the 3D intensity pattern. The two methods each have different ways of dealing with this interference problem.

The design of 3D volumetric features is constrained by physical laws and experimental limitations, and realizable 3D intensity patterns must satisfy the wave equation. If a desired pattern is significantly different from the closest realizable pattern, it could suffer from defects. For example, interference can make intensity high where it is intended to be low

and vice versa. The experimental limitations have to do with the available laser power and the mechanical properties of the resist. The amount that each voxel must overlap to create a stable feature is determined by the mechanics of the cured resist. In particular, the overlap between voxels needed to create a stable feature depends upon the mechanics of the cured resist and the extent of partially-cured regions [81]. In this context, a partially-cured region is one that would be washed away by developer after a single exposure, but becomes over-cured if the partially-cured region of at least one neighboring voxel overlaps with it. These considerations separate HOT from DMHL.

6.2.1 Gratings and Lenses Approach

This section presents the first results from 3D DMHL using the gratings and lenses approach (see Chapter 2) for micro-manufacturing. Multiple voxels can be summed to generate arbitrary patterns by summing the complex amplitudes for each voxel. A hologram generating the complete pattern is the phase argument of this complex sum. The equation for a sum of l voxels is:

$$\phi_{mn} = \arg \sum_{l=1}^{N} \exp i\psi_{mn}^{l} \tag{6.8}$$

where ϕ_{mn} is the phase of the (m, n)th pixel of the hologram, and N is the number of voxels making the 3D pattern.

Because this is a new micro-manufacturing method, pertinent design considerations are not well known. Preliminary experiments found that areas of a feature with high voxel density would suffer from over-curing; for example, the apex of a tripod would be much larger than designed. This likely occurred because partially-cured regions of several voxels were overlapping. The intensity of the voxel affects the extent of the partially-cured region. To remedy this problem, weights are used to reduce the intensity of voxels that have several near neighbors. The number of neighbors, N_n, each voxel has within a user-defined threshold distance, d_t, is used to determine weight of the lth voxel:

$$w_l = 1 - c(N_n - 1) \tag{6.9}$$

where c is a user-defined constant; how this constant is chosen will be discussed later. Including the weights, the hologram equation becomes

$$\phi_{mn} = \arg \sum_{l=1}^{N} w_l \exp i\psi_{mn}^{l} \tag{6.10}$$

The way the weights are defined, the intensity of the voxels with more near neighbors should be reduced while the voxels with the fewer near neighbors remain unchanged. In practice, as some voxels are dimmed, others were found to increase in intensity. This actually uses the available laser light more efficiently than if the extra power were just deflected into higher diffraction orders.

6.2.1.1 Results and Discussion To demonstrate 3D volumetric patterning, a tripod shape was chosen for its simplicity, demonstrating designed 3D structure with a minimum number of voxels. In the tripod morphology (see Figure 96), the threshold distance (850 nm) was chosen to be just greater than the two least neighbor-neighbor distances (665 nm and 843 nm). The shading of the voxels in Figure 96 corresponds to N_n, with the lightest colored voxels having the fewest neighbors nearer than the threshold distance and the darkest colored voxels having the most.

The physical extent of the voxel depends on the exposure time and intensity [54]. Calibration experiments showed the voxel to be about 350 nm in diameter near the threshold peak exposure intensity of the resist. The length of the voxel (parallel to the direction of light propagation) near the threshold exposure intensity was found to be about 1.3 μm. A lateral voxel spacing of 384 nm and an axial voxel spacing of 750 nm was found to produce structures that could support their own weight and withstand development.

The tripod micro-features (see Figure 97) were made with an exposure time of 0.2 seconds and an average peak intensity per voxel of 1.6 GW/cm^2. As the c value is increased, the relative intensity of the voxels with many near neighbors is decreased from this value. Each tripod is composed of 22 voxels and the designed dimensions are $4.4 \times 5.0 \times 6.0$ μm. Without reducing the intensity of the voxels near the apex, the feature is severely overexposed (see

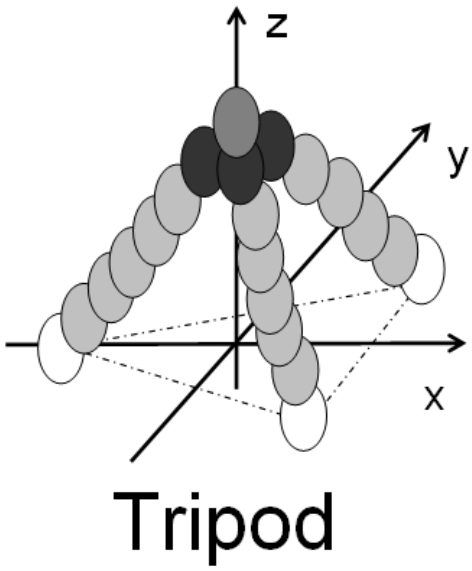

Figure 96: Model of desired feature. Each oval corresponds to a voxel and the color corresponds to the weight. White is the highest intensity. The highest weights are at the base of the feature because the voxels at the base have the fewest near neighbors.

Figure 97). The introduction of weights with $c = 0.1$ (center) and $c = 0.2$ (right) improve the pattern fidelity. The error in the height of the micro-feature is reduced from 45% with $c = 0$ to 26% with $c = 0.2$.

There was a consistent systematic error of 10% for the lateral dimension of each feature. Each feature was measured to be smaller than designed. This was found to be due to the objective lens being placed a few hundred nanometers too shallow. The substrate is not on a computer-controlled stage, and must be aligned axially by hand with the fine focus knob of the microscope. A single fine-focus knob increment moves the substrate by 1500 nm. Future work using a more accurate stage will solve this problem.

Features were attempted at lower peak intensities to demonstrate the possibility of making patterns with more voxels, but the mechanical integrity of the cured resist could not withstand the development process, leading to pattern collapse. It was found that the peak intensity per voxel has more of an effect on the resulting feature than the exposure time. Below a certain intensity, no curing occurs no matter how long the exposure. Therefore the available intensity is very important in the design of 3D micro-feature.

These preliminary results suggest that the voxels need not overlap at all to obtain stable features that can survive the development process. This is likely because there is a small region around a voxel that becomes partially-cured from exposure.

In a subsequent sample, a larger range of c values was tested ($c = 0, 0.2, 0.4$) without any more improvement in the pattern fidelity. The apex of the tripod was still larger than designed. It is possible that the gratings and lenses method with weights applied has inherent limits. Therefore a second 3D parallel DMHL method was investigated.

6.2.2 3D Gerchberg Saxton Algorithm

The 3DGS algorithm was discussed in Chapter 2. It takes a volume of points and uses a 3D FFT to find the closest realizable intensity pattern to the desired intensity pattern. It takes into account the interference and propagation effects that the gratings and lenses algorithm ignores, and therefore could have better performance. The best achievable lateral resolution for this method was given above in Chapter 4. For this SLM, the grid spacing in

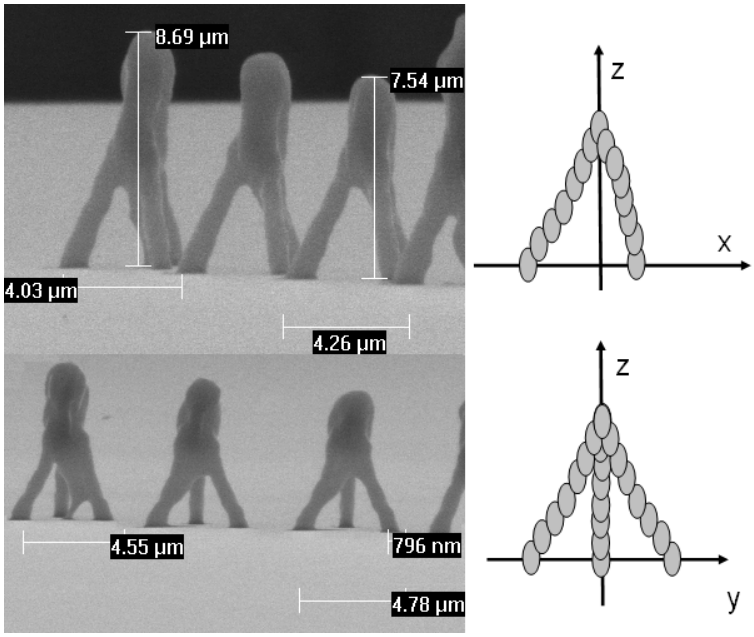

Figure 97: Examples of hollow tripods made with a single exposure with 3D volumetric holograms. Two orthogonal views are given. From left to right, the value of c increases from 0 to 0.1 to 0.2. The application of weights reduces the overexposure at the top of the feature. Each tripod was made in a separate exposure. On the right, the corresponding views of the ideal morphology are given.

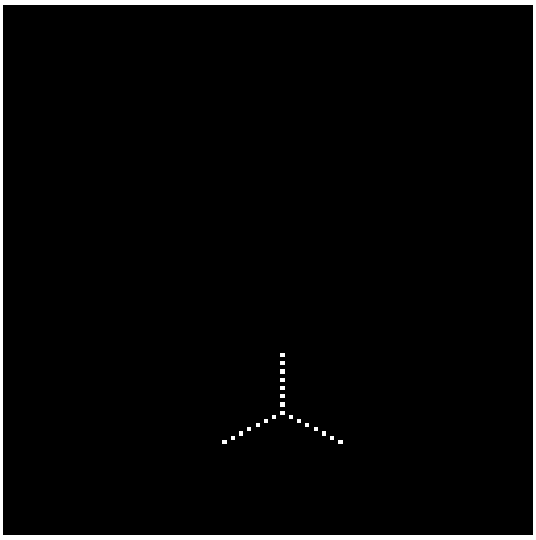

Figure 98: This is the projection from above of the 128×128 pixel input pattern. The input is actually a set of 8 images at different axial displacements.

the specimen plane is 160 nm. One of the drawbacks of the 3DGS method is that voxels can only be placed at points on this grid. With the gratings and lenses method explained above, the lateral voxel spacing ranged from 200-400 nm, but the only reasonable choices are 320, 358, and $320\sqrt{2} \approx 453$ nm for 3DGS.

The target intensity pattern is a volume of $128 \times 128 \times 128$ pixels with a set of 8 input bitmaps that are 128×128 pixels because MATLAB runs out of memory when $256 \times 256 \times 256$ pixel volumes are used. The "dimension" of the target intensity pattern was $33 \times 33 \times 16.5$ μm in MATLAB, and $\tau/k = 0.01$. Calibration experiments determined that one pixel of axial displacement in the target volume is equivalent to an axial displacement of 90 nm when the 100× objective is used. A projection of the target intensity pattern from above is shown in Figure 98. It is a tripod with 6 pixels$\approx$ 540 nm, between each voxel layer. This corresponds to a designed dimension of about $3.7 \times 4.8 \times 4.5$ μm (see Figure 99).

A set of weights similar to those used in the gratings and lenses approach above was implemented for the 3DGS algorithm to account for voxel density. This time, the weight, c was multiplied by the grayscale value of the pixel in the target intensity pattern. The

grayscale value corresponding to white is 255/3 = 85 and black is 0. Unlike with the gratings and lenses approach, the 3DGS algorithm actually managed to get the height of the cured feature to be under the design height (see Figure 100) The tripods were made with no ND filter and a 0.2 second exposure. The strong effect of reducing the graylevel of the target intensity is unexpected because it was found in Chapter 5 that the intensity of a voxel does not start to significantly decrease until the graylevel is reduced to 25.

6.2.3 Ways to improve uniformity

All "parallel" patterning is done with the assumption that each voxel has the same intensity. Even when weights are applied depending on the position of the voxel, the calculation of the weights is done with only the voxel location, without any information about the actual intensity of the voxel. This leads to problems with pattern uniformity. Uniformity is very sensitive to the phase error. A scaling error of 1% in the phase of a hologram can lead to a uniformity error of almost 10% [28]. This highlights the need for the maximum number of phase levels to be available on an SLM because coarse phase quantization can cause poor uniformity.

It is possible to make the uniformity of the set of voxels in the patterning volume a variable to be optimized [23]. This "weighted Gerchberg-Saxton" method improves uniformity while keeping good efficiency in an array of traps. It has about the same speed as the GS algorithm, but produces better uniformity. It does not require the measurement of intensities, but calculates the theoretical intensity at each trap due to the displayed phase hologram. Future work could include the use of adaptable weights to improve uniformity. In this work, the number of voxels per pattern was so low that voxel proximity overwhelmed any effects that might be caused by lack of uniformity.

It has been demonstrated that micro-features with full 3D design can be made with two-photon absorption using a single hologram and a single exposure. With further development, pattern fidelity can be increased and this method could be used to vastly increase micro-manufacturing throughput.

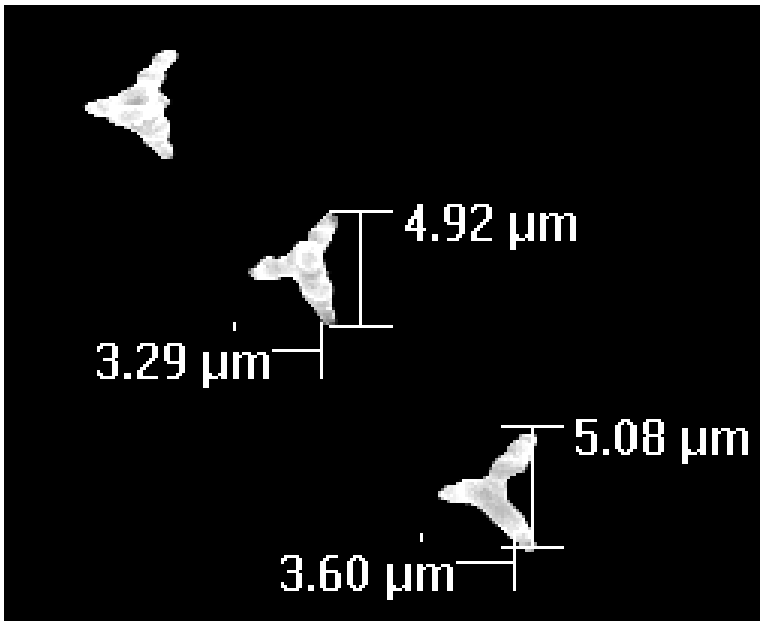

Figure 99: This is a top view of the set of 3 tripods made with the 3DGS algorithm. The top left tripod did not had no weights applied, the middle tripod had $c = 0.2$ and the bottom right tripod had $c = 0.4$. It seems that a weight of $c = 0.2$ is sufficient to make the tripod come out as designed.

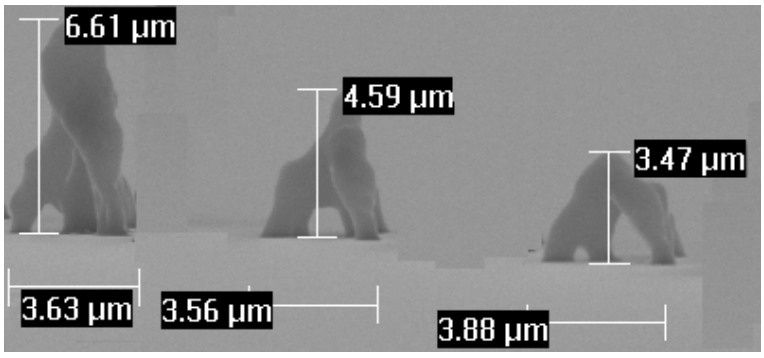

Figure 100: This is a set of 3 tripods made with the 3DGS algorithm. The top left tripod did not had no weights applied, the middle tripod had $c = 0.2$ and the bottom right tripod had $c = 0.4$. It seems that a weight of $c = 0.2$ is sufficient to make the tripod come out as designed.

7.0 SUMMARY AND CONCLUSION

In this research a DMHL system was designed and implemented. The display of phase holograms on a liquid-crystal SLM allowed for the creation of intensity patterns in the focal volume of a microscope objective without needing a separate mask for each pattern. Four different patterning modes were demonstrated and characterized. The four modes were 2D serial, 2D parallel, 3D serial, and 3D parallel. All but the last had been demonstrated before, but not with two-photon absorption. The three that had been demonstrated previously were extended by incorporating various methods to improve performance.

The first objective of the project involved demonstrating two-photon DMHL in two dimensions and characterizing the process in more detail than was currently available. In the literature, the most common information available about photolithographic micro-manufacturing processes is the cured voxel size. The voxel size varies with laser power and exposure time. Most available information is only applicable to the particular laser/resist pair used in each particular journal article. The results of this research are more extensive, and more general in the sense that the uncertainty associated with achieved linewidths has more to do with the SLM and the optics than the particular laser or photoresist. The sources of uncertainty in the linewidth measurements were mainly axial drift of the objective and intensity fluctuations due to the SLM. Both serial and parallel patterning modes were demonstrated. The minimum linewidth of 2D parallel patterns is necessarily larger than in 2D serial patterns due to speckle.

Another aim of this research was to improve the resolution of the DMHL process. The most obvious way to do this would be to use a shorter wavelength to expose the resist, but many liquid-crystal SLM displays would be destroyed by light of UV wavelengths or shorter. UV wavelengths can also require reflective optics and a vacuum environment due

to absorption. Two-photon absorption bypasses this problem by using a longer wavelength of light. Linewidths of less than 400 nm were achieved, which did not quite reach the goal of 300 nm set in the proposal. This is likely due to low two-photon absorption of the resist at the laser wavelength and could be improved with a titanium-sapphire femtosecond pulsed laser. On the other hand, the goal of 1.5 μm axial resolution was exceeded with an achieved 1.2 μm axial voxel.

Adding a third dimension to microstructures can increase their functionality and density. There are two ways to cure objects holographically in 3D: 1) scan a holographic dot (or any other image) through the whole volume of the feature using Fresnel lens holograms to displace the image axially, or 2) use a hologram that creates a whole 3D intensity pattern. These 3D intensity patterns can be used to cure whole micro-components in a single shot and this type of almost-arbitrary, nonperiodic, 3D patterning has never before been demonstrated. In this work two ways of making a complete 3D micro-feature in a single exposure, were demonstrated. The first technique used a "gratings and lenses" approach in which a set of holograms corresponding to single voxels was summed to obtain a single hologram that places light at each designed location. The second method used a 3DGS algorithm to find the closest realizable 3D intensity pattern that still obeys the physical constraints of Maxwell's equations. This 3D parallel patterning research also resulted in the discovery of new micro-manufacturing design considerations. For example, the intensity of certain voxels in a 3D pattern must be decreased in areas of high voxel density to prevent unintended curing and retain pattern fidelity.

Several experimental limitations were overcome over the course of the project. The pixelation of the SLM, and resulting diffraction efficiency variation in the patterning field, was compensated in a unique way with dwell-time compensation. Aberration correction was also introduced to increase the potential patterning volume and allow for inexpensive, improperly aligned optics to be used for high-quality DMHL.

This research made the following contributions to the field of photolithographic micro-manufacturing:

1. Design and implementation of two-photon DMHL system.
2. Demonstration of dwell-time compensation to improve uniformity in serial DMHL.

3. First demonstration of aberration correction to increase potential patterning volume.
4. First demonstration of 3D parallel patterning (whole 3D feature being cured in a single-shot with no beam scanning).
5. Introduction of weights to improve pattern fidelity in 3D parallel patterning.

7.1 FUTURE WORK AND RECOMMENDATIONS

Several aspects of the experimental setup limited the types of patterns that could be cured:

1. The SLM had an asymmetry in its diffraction efficiency and large intensity fluctuations. Better SLMs from companies like Boulder and Hammamatsu have pixels that are driven individually instead of through a raster scan. This could improve the quality of the displayed holograms and therefore the quality of the intensity patterns in the focal volume.
2. The average power of the laser was only about 10 mW and severely limited the size of features that could be made with parallel patterning modes. To fully use the advantages of increased throughput from DMHL, a more powerful laser, or a resist with a higher two-photon absorption is necessary.
3. Finally, a motorized stage would increase the throughput of the system so that more features can be patterned. It is difficult to see the features as they are made because of very low index contrast, and when the stage is moved by hand it is easy to overwrite a pattern or misalign what is meant to be a neat array of features. A 3D motorized stage would also help control the axial drift of the substrate as it is moved.

APPENDIX A

SLM BACKGROUND

Some background research on SLM physics might be helpful to future researchers. The information here is meant to supplement that given in Chapter 4. Most of the information pertains to the use of a liquid-crystal device for the display of phase holograms. Much of what is discussed here was accounted for in the experimental design, but the extra wave plates and polarizers were found to be insignificant to the results. The following section explains the theory behind using an SLM for phase-mostly operation [19, 74, 85, 2]. At the end, several more aspects of the physical characteristics of SLMs are given, including a comparison between parallel aligned and twisted LC layers, and the effects of fringing fields and flyback.

A.1 SLM THEORY AND CHARACTERIZATION

Jones matrices describe what optical elements do to a particular input polarization which is described by a Jones vector. A Jones vector describes the polarization of light. For example light that is linearly polarized parallel to the horizontal of the laboratory frame has a unit-magnitude Jones vector of [32]:

$$\begin{pmatrix} 0 \\ 1 \end{pmatrix} \tag{A.1}$$

and right-handed circularly polarized light is described as:

$$\frac{1}{\sqrt{2}}\begin{pmatrix}1\\-i\end{pmatrix} \tag{A.2}$$

The common components used in a phase-mostly experimental setup include polarizers and wave plates. The Jones matrix for a polarizer is [32]:

$$P(\varphi) = \begin{bmatrix}\cos^2\varphi & \sin\varphi\cos\varphi\\ \sin\varphi\cos\varphi & \cos^2\varphi\end{bmatrix} \tag{A.3}$$

where φ is the angle that linearly polarized input light must make with the horizontal of the reference frame for it to be transmitted.

The Jones matrix of a retarding wave plate is given by [32]:

$$W(\Gamma) = \begin{bmatrix}1 & 0\\ 0 & e^{-i\Gamma}\end{bmatrix} \tag{A.4}$$

where the retardation Γ is [32]:

$$\Gamma = \frac{2\pi d}{\lambda_o}(n_x - n_y) \tag{A.5}$$

where λ_o is the vacuum wavelength of light, n_x is the refractive index for the component of polarization in the x-direction, n_y is the refractive index of the component of polarization in the y-direction, and d is the plate thickness. The most common wave plates are quarter-wave plates which generally convert linearly polarized light into circularly polarized light and half-wave plates which generally rotate the angle at which light is linearly polarized.

The Jones matrix of a wave plate that is rotated at some angle, θ with respect to the x-axis of the reference system, is given by:

$$W_\theta = R(-\theta)W_0R(\theta) \tag{A.6}$$

where $R(\theta)$ denotes the rotation matrix:

$$R(\theta) = \begin{bmatrix}\cos\theta & \sin\theta\\ -\sin\theta & \cos\theta\end{bmatrix} \tag{A.7}$$

It is possible to model a twisted-nematic liquid crystal as many slices of a homogeneous uniaxial crystal described by a specific Jones matrix. The whole thickness of the device can then be modeled as the product of this set of Jones matrices [59]. The Jones matrix of a single SLM pixel is [85]:

$$M(\beta) = e^{-i\beta} R(\alpha) \begin{bmatrix} \cos\gamma - i\beta\frac{\sin\gamma}{\gamma} & -\alpha\frac{\sin\gamma}{\gamma} \\ \alpha\frac{\sin\gamma}{\gamma} & \cos\gamma + i\beta\frac{\sin\gamma}{\gamma} \end{bmatrix} \tag{A.8}$$

where β is the birefringence of the liquid crystal, given by

$$\beta = \frac{\pi d}{\lambda}(n_e - n_o), \tag{A.9}$$

where d is the thickness of the liquid crystal layer in the cell, n_o is the ordinary index of refraction and n_e is the extraordinary index of refraction for light propagated along the z-axis, and γ is defined by

$$\gamma = \sqrt{\alpha^2 + \beta^2} \tag{A.10}$$

α is the total twist angle of the molecules in the cell and $R(\alpha)$ denotes the rotation matrix. It should be noted that for each voltage applied, the above parameters β and γ adopt different values. The maximum birefringence, $\beta_{\max}$ is simply the value in the absence of an applied voltage:

$$\beta_{\max} = \frac{\pi d}{\lambda}(n_{e\max} - n_o) \tag{A.11}$$

The liquid crystals in the SLM tilt at a voltage-dependent angle, ψ such that [94]:

$$\psi = \frac{\pi}{2} - 2\tan^{-1}\left(\exp\left[-\left(\frac{V_{rms} - V_c}{V_o}\right)\right]\right) \tag{A.12}$$

for $V_{rms} > V_c$ and $\psi = 0$ otherwise, where V_c is the threshold voltage below which no tilting of the molecules occurs and V_o is the excess voltage. It is assumed that the LC molecules all tilt at the same angle, ψ, when an electric field is applied. When this electric field is applied, the new extraordinary index of refraction is defined as [85]:

$$\frac{1}{n_e^2(\psi)} = \frac{\sin^2\psi}{n_o^2} + \frac{\cos^2\psi}{n_e^2} \tag{A.13}$$

A.1.1 Phase-mostly operation

There are many physical parameters that must be measured before use of a specific twisted-nematic SLM [21]. They include the magnitude and rotational sense of the twist angle, α, of the display, the maximum (off state) birefringence, $\beta_{\max}$ of the display, and the orientation angle, Ψ_D, of the extraordinary index of refraction for the liquid crystal molecules at the input side relative to the laboratory frame. This is related to the director (see Chapter 4).

The only thing assumed to be known in the following series of experiments are the angles of the polarizer and the analyzer relative to an external laboratory coordinate system (0° =laboratory vertical). The rest of the SLM parameters must be determined. For crossed polarizers, the transmitted intensity is given by [94]:

$$T_{crossed} = A\left([\sin\alpha\cos\gamma - \left(\frac{\alpha}{\gamma}\right)\cos\alpha\sin\gamma]^2 + [\left(\frac{\beta}{\gamma}\right)\sin\gamma\sin(\alpha + 2\Psi_D - 2\theta_1)]^2\right) \quad \text{(A.14)}$$

where A is a scaling factor, α is the "twist angle", $\gamma = \sqrt{\alpha^2 + \beta^2}$, Ψ_D is the angle of the molecular director at the input face ($\Psi_D = \theta_1 + \Psi_1$), and the angle of the polarizer is θ_1. After setting the polarizer and analyzer to be crossed, and then rotating them simultaneously, the transmitted intensity should be predicted by equation A.14. Some curve-fitting is necessary to tease out these 4 unknowns. From equation A.14, the first minimum in transmitted intensity occurs at $\Psi_D = (2\theta_1 - \alpha)/2$ [94]. To determine the sign of α, set the analyzer to zero and rotate the polarizer through 180 degrees. Using the already determined magnitude of alpha, two predictions can be made using both signs. The experimental data will more closely match whichever sign for α is correct. Keep in mind that the model only approximates the effect of applied voltage, so there will probably not be a precise relationship between β and graylevel [94]. In this way the three variables that determine the properties of an SLM, α, β and Ψ_D can be found.

Davis et al. [21] describe another approach for finding the extraordinary axis of the LC layer in order to confirm results found with the above method. It involves illuminating the SLM with linearly polarized light, and varying a constant phase value on all the pixels. When the light is polarized along the ordinary axis, the diffraction pattern does not change with graylevel, but if the light is polarized along the extraordinary axis, the diffraction pattern

does "change". For example, for one particular device, when the polarizer is aligned with the ordinary axis, the diffraction pattern of the SLM does not change with grayness value, but when the polarizer is aligned with the extraordinary axis, the 5th and 6th diffraction orders became much brighter as the displayed graylevel value was increased. For other devices the behavior could be different [21]. After reaching some maximum change, as the graylevel value continues to increase, the diffraction pattern will return to its original intensity. It is possible that this change in intensity is due to a "blazing effect" due to an electric field gradient across each pixel causing the effective optical thickness to vary from one side of the pixel to the other [21]. The graylevel value that causes the molecules to tilt at 45 degrees will cause the largest blazing effect.

Phase-mostly operation can be achieved by compensating for the range of elliptical polarizations of the light transmitted through (or reflected from) the SLM. Ponce et al. [85] employed an optimization to find the best set of orientations for two polarizers and a quarter-wave plate to give the smallest variation in amplitude with the largest variation in phase. The parameters of their optimization were the orientation angle, φ, and ellipticity, ε, of the input elliptical polarization state and the orientation of the output polarizer, Ψ_{P2}, after the SLM. The optimal ellipticity of the input determines the relative rotation between the first linear polarizer and the wave plate. The authors measured the phase and amplitude modulation experimentally by displaying a binary grating and measuring the relative intensities of the grating diffraction orders. Arrizon et al. [2] describe another method that simplifies the setup by one polarizer, only using a polarizer and quarter-wave plate before the SLM. Although transmissive SLMs can simplify the layout of the optical setup, they can require extra components to compensate for the polarization effects of the LC layer. Reflective SLMs have better phase-only modulation characteristics because of the double pass through the LC cell which cancels out some complex modulation effects [83].

A.1.2 Differences between Parallel aligned and Twisted LC cells

Parallel aligned LC SLMs can perform both phase-only and amplitude modulations [50]. Parallel-aligned LC cells can provide more phase change for a given LC layer thickness than

twisted cells [50]. A twisted cell is insensitive to wavelength for an amplitude-modulation condition as long as $d\Delta n/\lambda >> 1$ is satisfied where d is the thickness of the cell and Δn is the difference between the ordinary and extraordinary refractive indices. A parallel-aligned cell on the other hand is highly sensitive to wavelength in the visible range [50].

A.1.3 Fringing Fields

In an SLM, there is a potential difference between adjacent backplane electrodes that causes field coupling (fringing fields) [90]. These fields can cause LC molecules to twist as opposed to only rotating which adds complex phase modulation to the desired phase-only modulation [90]. The fringing field is greatest when the difference in voltage between two electrodes is greatest. This occurs at phase reset regions where the desired phase value jumps from 0 to 2π or vice versa. The twist from the fringing field can occur over the space of several electrodes, causing the greatest drop in diffraction efficiency to occur at high spatial periods [90]. When cells are closely spaced and thick, the electric field is "smeared" across the LC layer [6]. To combat the fringing effect, cells must be made as thin as possible, which requires a higher operating voltage because the LCs near the electrode surfaces have interactions which require energy to overcome. Thus an engineering trade off is introduced between the operating voltage and the effect of fringing fields. The LC layer thickness also effects the time response (see Chapter 4).

A.1.4 Flyback

At the phase resets of a blazed grating, the phase does not discontinuously change from zero to 2π. The small region in which the phase changes is called the "flyback region". The periodicity of the flyback region can produce sidelobes that reduce diffraction efficiency to the patterning beam [90]. By incorporating flyback a more accurate value of the diffraction efficiency can be found by multiplying the calculated efficiency, η by the flyback factor [71]:

$$\eta_f = \left(1 - \frac{\Lambda_F}{\Lambda}\right)^2 \tag{A.15}$$

where Λ_F is the width of the flyback region and Λ is the period of the programmed grating. Depending on the size of the flyback region with respect to the grating period, this effect can be significant. A general rule of thumb says that the thickness of the flyback region is approximately equal to the thickness of the LC layer [71].

APPENDIX B

MATLAB CODE

B.1 AVERAGE PHASE CHANGE

Code for avgphasechange.m:

```
for p=1:15

% Creates matrix for generation of grating
ysize=512;
%xsize=round(1.333*ysize);
xsize=ysize;

x = linspace(-1,1,xsize); y = linspace(-1,1,ysize);
[Y,X]=meshgrid(x,y);

const(p)=p*(25); Xoffset=0; Yoffset=0;

phi_lens = const(p)*(X.^2 + Y.^2);
grating =  (2*pi)*(X.*Xoffset + Y.*Yoffset);  %this creates a BLAZED grating

theta = atan2(X,Y); rho = sqrt(X.^2+Y.^2);
```

```
%variables called by the zernike polynomials
a1 = 0;  %tilt y  (300 is one box) (just moves dot like a grating constant)
a2 = 0;  %tilt x  (300 is one box) (just moves dot like a grating constant)
a3 = 0;  %power (spreads) ("defocus")
a4 = 0;  %astig x   (wavelengths = a4/(2*pi))
a5 = 0;  %astig y
a6 = 0;  %coma y (10 is to the left and -10 is to the right)
a7 = 0;  %coma x
a8 = 0;  %primary spherical (spreads)
[phi1, phi2, phi3, phi4, phi5, phi6, phi7, phi8] = zernike(rho,
theta,...
    a1, a2, a3, a4, a5, a6, a7, a8);
phi=phi_lens+grating+phi1+phi2+phi3+phi4+phi5+phi6+phi7+phi8;
maxvalue=max(max(phi))

whole=mod(phi,2*pi);

wholecorr=whole;

figure(3) imagesc(wholecorr); axis('square') colormap('gray')
title('grating') set(gcf,'Position', [1338 383 661 661])
    c=0;
    for b=256 %pick a row in the center of the hologram
        totaldiff=0;
        for a=1:511
            totaldiff=totaldiff+abs(wholecorr(b,a)-wholecorr(b,a+1));
        end
        avgchangeperpixel(p)=totaldiff/512;
            if avgchangeperpixel(p)>2
```

```
                'spatial frequency is too high'
            end
    end
pause(1) end %%

figure(100) plot(const,avgchangeperpixel) ylabel('Average Phase
change per pixel (rad.)') xlabel('lens const') title('Average change
in phase per pixel for the middle row of the hologram - Fresnel
lens')
```

B.2 MAKING PHASE GRATINGS

Code for `adaptivegratinghigh.m`:

```
% Creates matrix for generation of grating
ysize=512;
%xsize=round(1.333*ysize);
xsize=ysize;

x = linspace(-1,1,xsize); y = linspace(-1,1,ysize); [Y,X] =
meshgrid(x,y); deltax=abs(x(2)-x(1));

%NOTE:This script uses a scaling that is different than
%all other scripts because of 'zernikehigh' function and the modulo 2pi
%function is not applied until the phi_lens and grating are already summed!
constax=0; const=0; Xoffset=10; Yoffset=0;
phi_axicon =constax*angle(exp(-1i*2*pi*(sqrt(X.^2+Y.^2))/1));  %from Davis93
phi_lens = const*(X.^2 + Y.^2);
grating =  (2*pi)*(X.*Xoffset + Y.*Yoffset);  %this creates a BLAZED grating
```

```
theta = atan2(X,Y); rho = sqrt(X.^2+Y.^2);

%variables called by the zernike polynomials
a1 = 0;  %tilt y  (300 is one box) (just moves dot like a grating constant)
a2 = 0;  %tilt x  (300 is one box) (just moves dot like a grating constant)
a3 = 0;  %power (spreads) ("defocus")
a4 = 0;  %astig x   (wavelengths = a4/(2*pi))
a5 = 0;  %astig y
a6 = 0;  %coma y (10 is to the left and -10 is to the right)
a7 = 0;  %coma x
a8 = 0;  %primary spherical (spreads)
a9 = 0; a10= 0; [phi1, phi2, phi3, phi4, phi5, phi6, phi7, phi8,
phi9, phi10] = zernikehigh(rho, theta,...
    a1, a2, a3, a4, a5, a6, a7, a8,a9,a10);
phi=phi_lens+grating+phi1+phi2+phi3+phi4+phi5+phi6+phi7+phi8+phi9+...
phi10+phi_axicon;
maxvalue=max(max(phi))

whole=mod(phi,2*pi);

wholecorr=whole;

wholecorr(1,1)=0; wholecorr(ysize,xsize)=2*pi;

figure(3) imagesc(wholecorr); axis('square') colormap('gray')
set(gcf,'Position', [1338 383 661 661])
```

Code for function `zernikehigh.m`:

```
function [phi1, phi2, phi3, phi4, phi5, phi6, phi7, phi8, phi9,
phi10] = zernikehigh(rho,... theta, a1, a2, a3, a4, a5, a6, a7, a8,
```

```
a9, a10)

%from Noll76 (and normalized, unlike zernike.m)

Z1 = 2*rho.*cos(theta); Z2 = 2*rho.*sin(theta); Z3 =
sqrt(3)*(-1+2*rho.^2); Z4 = sqrt(6)*rho.^2.*cos(2*theta); Z5 =
sqrt(6)*rho.^2.*sin(2*theta); Z6 =
sqrt(8)*rho.*(3*rho.^2-2).*cos(theta); Z7 =
sqrt(8)*rho.*(3*rho.^2-2).*sin(theta); Z8 = sqrt(5)*(1 - 6*rho.^2
+6*rho.^4); Z9 = sqrt(8)*rho.^3.*cos(3*theta); Z10=
sqrt(8)*rho.^3.*sin(3*theta);



%a1 = tilt y  (300 is one box)
%a2 = tilt x  (300 is one box)
%a3 = defocus (moves focus axially)
%a4 = astig x
%a5 = astig y
%a6 = coma y
%a7 = coma x
%a8 = primary spherical (spreads)
%a9 = trefoil?
%a10= trefoil?

phi1 = a1*Z1; phi2 = a2*Z2; phi3 = a3*Z3; phi4 = a4*Z4; phi5 =
a5*Z5; phi6 = a6*Z6; phi7 = a7*Z7; phi8 = a8*Z8; phi9 = a9*Z9;
phi10= a10*Z10;
```

B.3 MEASURING PHASE RESPONSE OF SLM

Code for `fringedisplacement.m`:

```
vidobj=videoinput('winvideo', 1, 'RGB24_720x480'); set(vidobj,
'SelectedSourceName', 'svideo'); pause(0.5) snapshot =
getsnapshot(vidobj); I0=snapshot(:,:,1); I0=double(I0); figure(30)
imagesc(I0)

closepreview

figure(2) plot(I0(170:220,425)) title('Cross section vertically')
hold on %%
vidobj=videoinput('winvideo', 1, 'RGB24_720x480'); set(vidobj,
'SelectedSourceName', 'svideo'); pause(0.5) snapshot =
getsnapshot(vidobj); I1=snapshot(:,:,1); I1=1.3*double(I1);
figure(31) imagesc(I1)

closepreview

figure(2) plot(I1(170:220,425),'r') hold on

%%
correlation=xcorr(I0(170:280,425),I2(170:280,425)); figure(5)
plot(correlation)

%%
vidobj=videoinput('winvideo', 1, 'RGB24_720x480'); set(vidobj,
'SelectedSourceName', 'svideo'); pause(0.5) snapshot =
getsnapshot(vidobj); I2=snapshot(:,:,1); I2=1.0*double(I2);
figure(31) imagesc(I2)
```

```
closepreview

figure(2) plot(I2(170:220,425),'m')

%%
peaks1=fft(I0(180:220,430)); peaks1a=abs(peaks1).^2;
peaks1p=angle(peaks1); figure(3) plot(peaks1a)

figure(4) plot(peaks1p)

%%
graylevel=[0 25 50 75 85 100 125 150 175 200 225 255];
phaseshift=([0 0 0 2 4 6 7 9 9 9.9 9 10]/11)*360;

figure(5) plot(graylevel,phaseshift,'bo') xlabel('Gray level')
ylabel('Phase (deg.)') title('Phase modulation of LC 2002 (B:100,
C:255, P:0^o, A:45^o)')
```

B.4 MAPPING DIFFRACTION INTENSITY IN PATTERNING FIELD

Code for `mapdiffeff pupil polarize.m`:

```
%This cell determines the xoffset, yoffset and axial focus constant
%vectors.
yoffvector=[]; xoffvector=[];
    Npts=7;
    Nlines=5;
    start1=13;
    stop1=17;
```

```
    start2=38;
    stop2=42;
    start3=66;
    stop3=70;
    start4=94;
    stop4=98;
    start5=123;
    stop5=127;

    xoffvector=[linspace(start1,stop1,Npts) linspace(start2,stop2,Npts)...
                linspace(start3,stop3,Npts) linspace(start4,stop4,Npts)...
                linspace(start5,stop5,Npts)];
    yoffvector=[-40*ones(1,Npts*Nlines)];

%%
%This loop in this cell moves a dot around in the first diffraction order.
%It uses a vector to define the xoffset, yoffset, and axial focus constant.
%The actual output is a series of holograms that are displayed for the
%exposure time set in the above cell.
%pause(6)
intensity=zeros(Npts*Nlines,1); for d=1:2
    for i=1:Npts*Nlines
        % Creates matrix for generation of grating
        x = linspace(-1,1,512);
        y = linspace(-1,1,512);
        [Y,X] = meshgrid(x,y);
        X=single(X);
        Y=single(Y);

        Xoffset=xoffvector(i);
```

```
Yoffset=yoffvector(i);
const=0;
phi_lens = single(const*(X.^2 + Y.^2));
grating =  single((2*pi)*(X.*Xoffset + Y.*Yoffset));
%this creates a BLAZED grating
holo=grating+phi_lens;
hologram=single(mod(holo,2*pi));
%blazed gratings direct more power into one order

i,d

figure(3)
imagesc(hologram)
colormap('gray');
axis('square');
title('grating');
set(gcf,'Position', [1338 383 661 661]); %for 512by512 holograms

vidobj=videoinput('winvideo', 1, 'RGB24_720x480');
set(vidobj, 'SelectedSourceName', 'svideo');
pause(0.5)
snapshot = getsnapshot(vidobj);
I0=snapshot(:,:,1);

delete(vidobj);  %this is extremely important because otherwise the
                 %camera stores them and runs out of memory after
                 %about 100 pictures...
I0=single(I0);
figure(30)
imagesc(I0)
```

```
        sim('determinecoefsfast')
        closepreview
        load beamtrack  %variable name= trail

        ysetpoint=round(trail(2,1));
        xsetpoint=round(trail(3,1));
        [sizex sizey sizez]=size(snapshot);
        M=single(zeros(sizex,sizey));

        for a=1:32
            for b=1:32
                if sqrt((a-16)^2+(b-16)^2) < 9
                    M(a+ysetpoint-16,b+xsetpoint-16)=1;
                end
            end
        end
        intensity(i,d)=sum(sum(M(:,:).*I0(:,:)));
        if max(max(I0(:,:)))>250
            'camera saturating'
        end
        figure(40)
        imagesc(M.*I0)
    end
end

intensitymean=(intensity(1:Npts*Nlines,1)+intensity(1:Npts*Nlines,2))/2;

figure(1) plot(xoffvector, intensity,'b.') xlabel('Xoff value') %%
figure(2) plot(xoffvector, intensitymean,'b') xlabel('Xoff value')
```

```
ylabel('Normalized intensity') title('Yoff=-40, Xoff=') hold on
%% determining dwell time (by taking the max of each intensity)
const=0.2; I=[max(intensitymean(1:Npts,1))
max(intensitymean(Npts+1:Npts*2,1))...
   max(intensitymean(Npts*2+1:Npts*3,1))...
   max(intensitymean(Npts*3+1:Npts*4,1))...
    max(intensitymean(Npts*4+1:Npts*5,1))];

counter=1; for c=1:Nlines
    for d=1:Npts
     if intensitymean(d+(c-1)*Npts,1)==max(intensitymean(1+...
                     (c-1)*Npts:Npts+(c-1)*Npts,1))
      xoffI(counter)=xoffvector(d+(c-1)*Npts);
      counter=counter+1;
      end
    end
end
Inorm=I./max(I)     %normalizes measured intensity with itself
dwelltime=const./Inorm.^2 dwelltime2p5=const./Inorm.^2.5

figure(2) plot(xoffI,I,'o')
%% determining dwell time (by emphasizing drop-off...)

const=0.2; Ie=[max(intensitymean(1:Npts,1))
               max(intensitymean(Npts+1:Npts*2,1)) ...
               max(intensitymean(Npts*2+1:Npts*3,1))...
               min(intensitymean(Npts*3+1:Npts*4,1))...
               min(intensitymean(Npts*4+1:Npts*5,1))];

counter=1; for c=1:Nlines
```

```
for d=1:Npts
        if intensitymean(d+(c-1)*Npts,1)==max(intensitymean(1+(c-1)...
           *Npts:Npts+(c-1)*Npts,1)) && c==1
        xoffIe(counter)=xoffvector(d+(c-1)*Npts);
        counter=counter+1;
        'i am satisfiying if condition 1'
        end
        if intensitymean(d+(c-1)*Npts,1)==max(intensitymean(1+(c-1)...
           *Npts:Npts+(c-1)*Npts,1)) && c==2
        xoffIe(counter)=xoffvector(d+(c-1)*Npts);
        counter=counter+1;
        'i am satisfiying if condition 2'
        end
        if intensitymean(d+(c-1)*Npts,1)==max(intensitymean(1+(c-1)...
          *Npts:Npts+(c-1)*Npts,1)) && c==3
        xoffIe(counter)=xoffvector(d+(c-1)*Npts);
        counter=counter+1;
        'i am satisfiying if condition 3'
        end
        if intensitymean(d+(c-1)*Npts,1)==min(intensitymean(1+(c-1)...
           *Npts:Npts+(c-1)*Npts,1)) && c==4
        xoffIe(counter)=xoffvector(d+(c-1)*Npts);
        counter=counter+1;
        'i am satisfiying if condition 4'
        end
        if intensitymean(d+(c-1)*Npts,1)==min(intensitymean(1+(c-1)...
           *Npts:Npts+(c-1)*Npts,1)) && c==5
        xoffIe(counter)=xoffvector(d+(c-1)*Npts);
        counter=counter+1;
        'i am satisfiying if condition 5'
```

```
            end

    end
end
Inorm=Ie./max(Ie)     %normalizes measured intensity with itself
dwelltime=const./Inorm.^2 dwelltime2p5=const./Inorm.^2.5

figure(2) plot(xoffIe,Ie,'ro')

%% determining dwell time (averaging each region...)
const=0.2; Iavg=[mean(intensitymean(1:Npts,1))
mean(intensitymean(Npts+1:Npts*2,1))...
      mean(intensitymean(Npts*2+1:Npts*3,1))...
      mean(intensitymean(Npts*3+1:Npts*4,1))...
       mean(intensitymean(Npts*4+1:Npts*5,1))];

counter=1; for c=1:Nlines
    mindiff=3000;
    for d=1:Npts
      if abs(intensitymean(d+(c-1)*Npts,1)-mean(intensitymean(1+(c-1)...
        *Npts:Npts+(c-1)*Npts,1)))<mindiff

        mindiff=abs(intensitymean(d+(c-1)*Npts,1)-mean(intensitymean(1+...
                       (c-1)*Npts:Npts+(c-1)*Npts,1)));
        xoffIa(counter)=xoffvector(d+(c-1)*Npts);
        end
    end
    counter=counter+1;
end
Iavgnorm=Iavg./max(Iavg)     %normalizes measured intensity with itself
```

```
dwelltime=const./Iavgnorm.^2 dwelltime2p5=const./Iavgnorm.^2.5

figure(2) plot(xoffIa,Iavg,'o')
%% model diff eff
xoffset=10:1:136; yoffset=10:1:136; [X,Y]=meshgrid(xoffset,yoffset);
flybackinpixels=10/32;

pitch=32e-6; activepixel=24e-6;

SLMtotalpixels1D=512;
SLMtotalpixels2D=512*sqrt(2); %I am really unsure about this number...
for a=1:127
    for b=1:127
    periods(a,b)=2*xoffset(a)+2*yoffset(b);
    pixelsperperiod(a,b)=SLMtotalpixels2D./periods(a,b);
    diff_eff(a,b)=(sin((activepixel*pi)/(pitch*pixelsperperiod(a,b)))/...
                ((activepixel*pi)/(pitch*pixelsperperiod(a,b))))^2;
    flyback_diff_eff(a,b)=diff_eff(a,b)*(1-...
                        flybackinpixels/pixelsperperiod(a,b))^2;

    end
end

Iavgnormmod=Iavgnorm*diff_eff(5,31) %%
figure(4) plot(xoffset,diff_eff(:,31)) title('Cross section at
Yoffset=40 (solid=model, o=norm 1st order)') xlabel('Xoffset')
ylabel('Diffraction Efficiency model') hold on
plot(xoffIa,Iavgnormmod,'o')

figure(5) plot(xoffIa,dwelltime,'o') xlabel('xoffset')
```

```
ylabel('Dwell-time compensation (s)') %%
dropoff10=[xoffvector' intensitymean];
save('SLMpolarize10','dropoff10')

%%
load('SLMpolarize0','dropoff0')
dropoff0(:,2)=dropoff0(:,2)*max(dropoff0(:,2)); %to normalize all plots
figure(100) plot(dropoff0(:,1),dropoff0(:,2),'b') hold on

load('SLMpolarize10','dropoff10')
dropoff10(:,2)=dropoff10(:,2)*max(dropoff10(:,2));
plot(dropoff10(:,1),dropoff10(:,2),'g')
```

B.5 3DGS

Code for `near3DGStripod.m`:

```
xsize=128; ysize=xsize; zsize=128;

deltac=6;   % number of pixels between voxels in axial direction
threshold=650; %in units of nm
decrement=0.4; %controls how much the intensity drops off

Xoffset=     [0 -2 -4 -6 -8 -10 -12 -14 -16 1 2 3 4...
              5  6  7  8  1  2  3  4   5   6   7   8]+34;
Yoffset=     [0  0  0  0  0   0   0   0   0 2 4 6 8...
              10 12 14 16 -2 -4 -6 -8 -10 -12 -14 -16]+2;
const=deltac*[8  7  6  5  4   3   2   1   0 7 6 5 4...
              3  2   1  0  7  6  5  4   3   2   1   0];
Ntot=25;
```

```
% determine all nearest neighbor distances
Xactual=Xoffset*160e-9; Yactual=Yoffset*160e-9;
constactual=const*90e-9;

coords=[Xactual' Yactual' constactual']; D =
pdist(coords,'euclidean'); D=squareform(D); Dnm=D*1e9

%associate the number of nearest neighbors below threshold
%with each particular voxel
for b=1:Ntot
    [Numnearest(b) throwaway]=size(find(Dnm(:,b)>0 & Dnm(:,b)<threshold))
end

%an example set of weights
weights=1-(Numnearest-1)*decrement

A=1e-2*ones(xsize,ysize,zsize);
%it makes a difference if this is zero or not...
for b=1:Ntot
A(xsize/2+1+Xoffset(b),ysize/2+1+Yoffset(b),((zsize)/2)+1+...
  const(b))=85*weights(b);
end

lambda=532e-9;    %wavelength is 532 nm
k=(2*pi)/lambda; tauoverk=0.01; tau=tauoverk*k;

latres=160e-9;          %known lateral resolution of SLM/optical system
dimx=2*16.5e-6; dimz=16.5e-6;
```

```
xdim=dimx           %the physical size of the target intensity
ydim=dimx           %effects the momentum space
%zdim=size*lambda/2;
%zdim=size*lambda/40;
zdim=dimz

x=linspace(-xdim/2,xdim/2,xsize);   %the spacing effects momentum space too
y=linspace(-ydim/2,ydim/2,ysize);
z=linspace(-zdim/2,zdim/2,zsize);   %for just z>0, I need 0:lambda:zdim/2?
%z=-zdim/2:lambda:zdim/2;

deltax=abs(x(2)-x(1)) deltay=abs(y(2)-y(1)); deltaz=abs(z(2)-z(1))

fsx=1/deltax fsz=1/deltaz

kzmax=pi*fsz; ratio=kzmax/k

A=fftshift(A);    %this is key!
phi = 2*pi*rand(xsize,ysize,zsize);

for q=1:4

ud = A.*exp(1i*phi);    %this is now the desired field distribution...
u_d=fftn(ud);

%find the field magnitude at each point in k-space...
W=zeros(xsize,ysize,zsize);

%this set of nested for loops takes all the points in u_d, and imposes
%physical constraints on them
```

```
for pp=1:zsize
    for mm=1:xsize
        for nn=1:ysize
           fx=((mm-(xsize+1)/2)/xsize)*fsx;
           %this centers the k-sphere on kx=0
           fy=((nn-(ysize+1)/2)/ysize)*fsx;
           %this centers the k-sphere on ky=0
           fz=((pp-(zsize+1)/2)/zsize)*fsz;
           kx=2*pi*fx;
           ky=2*pi*fy;
           kz=2*pi*fz;
           kvector=[kx ky kz];
           kmag(mm,nn,pp)=norm(kvector);

           if kz<0
               W(mm,nn,pp)=0;
               %this makes the sphere just the half that is kz>0
           else
               W(mm,nn,pp)=exp(-(kmag(mm,nn,pp)-k)^2/(2*tau^2));
           end


        end
    end
end

u_c=W.*u_d;

u_k=ifftn(u_c);         %closest physically
                        %realizable field to the target field...
```

```
    phi=angle(u_k);
end

% Derive 2D hologram to display on the SLM from u_c

slmhologram1=zeros(xsize,ysize); for b=1:xsize
       for c=1:ysize
            slmhologram1(b,c)=angle(sum(u_c(b,c,:)));
       end
end

slmhologramnograting=mod(slmhologram1,2*pi);
slmhologramnograting(1,1)=0; slmhologramnograting(1,2)=2*pi;

figure(4) imagesc(slmhologramnograting) title('Actual hologram to
display on SLM without grating?') axis('square') colormap('gray')
set(gcf,'Position', [1338 383 661 661])
```

BIBLIOGRAPHY

[1] Jun Amako, Hirotsuna Miura, and Tomio Sonehara. Speckle-noise reduction on kinoform reconstruction using a phase-only spatial light modulator. *Applied Optics*, 34, No. 17:3165–3171, 1995.

[2] Victor Arrizon, Luis A. Gonzalez, Rodrigo Ponce, and Alfonso Serrano-Heredia. Computer-generated holograms with optimum bandwidths obtained with twisted-nematic liquid-crystal displays. *Applied Optics*, 44, No. 9:1625–1634, 2005.

[3] Tommaso Baldacchini and et al. Christopher N. LaFratta. Acrylic-based resin with favorable properties for three-dimensional two-photon polymerization. *Journal of Applied Physics*, 95, No. 11:6072–6076, 2004.

[4] Christoph Bay, Nils Hubner, Jon Freeman, and Tim Wilkinson. Maskless photolithography via holographic optical projection. *Optics Letters*, 35, No. 13:2230–2232, 2010.

[5] Kevin D. Belfield, Katherine J. Schafer, Yong Liu, Xiaobin Ren, and Eric W. Van Stryland. Multiphoton-absorbing organic materials for microfabrication, emerging optical applications and non-destructive three-dimensional imaging. *Journal of Physical Organic Chemistry*, 13:837–849, 2000.

[6] N. Bennis, M. A. Geday, X. Quintana, B.Cerrolaza, D. P. Medialdea, A. Spadlo, R. Dabrowski, and J. M. Oton. Nearly-analogue blazed phase grating using high birefringence liquid crystal. *Opto-Electronics Review*, 17, No. 2:112–115, 2009.

[7] Alain Bergeron, Jonny Gauvin, Francois Gagnon, Denis Gingras, Henri H. Arsenault, and Michel Doucet. Phase calibration and applications of a liquid-crystal spatial light modulator. *Applied Optics*, 34, No. 23:5133–5139, 1995.

[8] A. Bertsch, J. Y. Jezequel, and J. C. Andre. Study of the spatial resolution of a new 3d microfabrication process: the microstereophotolithography using a dynamic mask-generator technique. *Journal of Photochemistry and Photobiology A: Chemistry*, 107:275–281, 1997.

[9] Martin J. Booth, Mark A. A. Neil, Rimas Juskaitis, and Tony Wilson. Adaptive aberration correction in a confocal microscope. *Proceedings of the National Academy of Sciences*, 99, No. 9:5788–5792, 2002.

[10] Max Born and Emil Wolf. *Principles of Optics*. Cambridge University Press, 1999.

[11] et al. Brian H. Cumpston. Two-photon polymerization initiators for three-dimensional optical data storage and microfabrication. *Nature*, 398:51–54, 1999.

[12] Ciba Specialty Chemicals. Photoititiators for uv curing. http://forums.reprap.org/file.php?184,file=30,filename=Photoinitiator_UVCURING_March05.pdf.

[13] Klaus Cicha, Zhiquan Li, Klaus Stadlmann, Aleksandr Ovsianikov, Ruth Markut-Kohl, Robert Liska, and Jurgen Stampfl. Evaluation of 3D structures fabricated with two-photon-photopolymerization by using ftir spectroscopy. *Journal of Applied Physics*, 110:064911, 2011.

[14] James V. Crivello. The discovery and development of onium salt cationic photoinitiators. *Journal of Polymer Science*, 37:4241–4254, 1999.

[15] George Curatu and James E. Harvey. Analysis and design of wide-angle foveated optical systems based on transmissive liquid crystal spatial light modulators. *Optical Engineering*, 48(4):043001, 2009.

[16] Jennifer E. Curtis, Brian A. Koss, and David G. Grier. Dynamic holographic optical tweezers. *Optics Communications*, 15:169–175, 2002.

[17] Jeffrey A. Davis and Don M Cottrell. Random mask encoding of multiplexed phase-only and binary filters. *Optics Letters*, 19, No. 17:496–498, 1994.

[18] Jeffrey A. Davis, Jarod Guertin, and Don M. Cottrell. Diffraction-free beams generated with programmable spatial light modulators. *Applied Optics*, 32, No. 31:6368–6370, 1993.

[19] Jeffrey A. Davis, Ignacio Moreno, and Philbert Tsai. Polarization eigenstates for twisted-nematic liquid-crystal displays. *Applied Optics*, 37, No. 5:937–945, 1998.

[20] Jeffrey A. Davis, Brian A. Slovick, C. Stewart Tuvey, and Don M. Cottrell. High diffraction efficiency from one- and two-dimensional nyquist frequency binary-phase gratings. *Applied Optics*, 47, No. 15:2829–2834, 2008.

[21] Jeffrey A. Davis, Philbert Tsai, Kevin G. D'Nelly, and Ignacio Moreno. Simple technique for determining the extraordinary axis direction for twisted-nematic liquid crystal spatial light modulators. *Optical Engineering*, 38:929–932, 1999.

[22] Winfried Denk, James H. Strickler, and Watt W. Webb. Two-photon laser scanning fluorescence microscopy. *Science*, 248:73–77, 1990.

[23] Roberto DiLeonardo, Francesca Ianni, and Giancarlo Ruocco. Computer generation of optimal holograms for optical trap arrays. *Optics Express*, 15, No. 4:1913–1922, 2007.

[24] J. Durnin, J.J. Miceli, and J. H. Eberly. Diffraction-free beams. *Physical Review Letters*, 58:1499–1501, 1987.

[25] U. Efron, S. T. Wu, and T. D. Bates. Nematic liquid crystals for spatial light modulators: recent studies. *J. Opt. Soc. Am. B*, 3, No. 2:247–252, 1986.

[26] E. Ericksson, S. Keen, J. Leach, M. Goksor, and M. J. Padgett. The effect of external forces on discrete motion within holographic optical tweezers. *Optics Express*, 15, No. 26:18268–18274, 2007.

[27] Peter Galajda and Pal Ormos. Complex micromachines produced and driven by light. *Applied Physics Letters*, 78, No. 2:249–251, 2001.

[28] Michael T. Gale, Markus Rossi, Helmut Schutz, Peter Ehbets, Hans Perter Herzig, and Damien Prongue. Continuous-relief diffractive optical elements for two-dimensional array generation. *Applied Optics*, 32, No. 14:2526–2533, 1993.

[29] Justyna K. Gansel, Michael Thiel, Michael S. Rill, Manuel Decker, Klaus Bade, Volker Saile, Georg von Freymann, Stefan Linden, and Martin Wegener. Gold helix photonic metamaterial as broadband circular polarizer. *Science*, 325:1513, 2009.

[30] R. W. Gerchberg and W. O. Saxton. A practical algorithm for the determination of phase from image and diffraction plane pictures. *Optik*, 35, No. 2:237–246, 1972.

[31] J. W. Goodman. Some fundamental properties of speckle. *J. Opt. Soc. Am.*, 66, No. 11:1145–1150, 1976.

[32] Joseph W. Goodman. *Introduction to Fourier Optics*. Roberts and Company Publishers, 2005.

[33] Herbert Gross. *Handbook of Optical Systems*. Wiley-VCH Verlag GmbH and Co., 2005.

[34] T. Haist, M. Schonleber, and H. J. Tiziani. Computer-generated holograms from 3d-objects written on twisted-nematic liquid crystal displays. *Optics Communications*, 140:299–308, 1997.

[35] Satoshi Hasegawa, Yoshio Hayasaki, and Nobuo Nishida. Holographic femtosecond laser processing with multiplexed phase fresnel lenses. *Optics Letters*, 31, No. 11:1705–1707, 2006.

[36] Wojciech Haske and et al. 65 nm feature sizes using visible wavelength 3-d multiphoton lithography. *Optics Express*, 15:3426–3436, 2007.

[37] Yoshio Hayasaki, Takashi Sugimoto, Akihiro Takita, and Nobuo Nishida. Variable holographic femtosecond laser processing by use of a spatial light modulator. *Applied Physics Letters*, 87:031101, 2005.

[38] Michinori Honma, Yoshikazu Akagawa, Masanori Ogasawara, and Toshiaki Nose. Diffraction efficiency improvement in liquid crystal blazed gratings with spatially distributed hybrid orientation domains. *Japanese Journal of Applied Physics*, 49:051702, 2010.

[39] Takashi Ito and Shinji Okazaki. Puishing the limits of lithography. *Nature*, 406:1027–1031, 2000.

[40] Richard James, F. Anibal Fernandez, Sally E. Day, Milos Komarcevic, and William A. Crossland. Modeling of the diffraction efficiency and polarization sensitivity for liquid crystal 2d spatial light modulator for reconfigurable beam steering. *J. Opt. Soc. Am. A*, 24, No. 8:2464–2473, 2007.

[41] Nathan J. Jenness, Ryan T. Hill, Angus Hucknall, Ashutosh Chilkoti, and Robert L. Clark. A versatile diffractive maskless lithography for single-shot and serial microfabrication. *Optics Express*, 18, No. 11:11754–11762, 2010.

[42] Frederic J. Kahn. Electric-field-induced orientational deformation of nematic liquid crystals: Tunable birefringence. *Applied Physics Letters*, 20, No. 5:199–201, 1972.

[43] W. Kaiser and C. G. B. Garrett. Two-photon excitation in caf2:eu2+. *Physical Review Letters*, 7, No. 6:229–231, 1961.

[44] Lorand Kelemen, Sandor Valkai, and Pal Ormos. Integrated optical motor. *Applied Optics*, 45, No. 12:2777–2780, 2006.

[45] Lorand Kelemen, Sandor Valkai, and Pal Ormos. Parallel photopolymerization with complex light patterns generated by diffractive optical elements. *Optics Express*, 15, No. 22:14488–14497, 2007.

[46] S. M. Kennedy and F. E. Lytle. p-bis(o0methylstyryl)benzene as a power-squared sensor for two-photon absorption measurements between 537 and 694 nm. *Anal. Chem.*, 58:2643–2647, 1986.

[47] Kil Suk Kim and et al. Temperature-dependent conformational change of meso-hexakis(pentafluorophenyl)[28]hexaphyrins(1.1.1.1.1.1) into mobius structures. *J. Phys. Chem.*, 113:4498–4506, 2009.

[48] Woo-Soo Kim, Ruth Houbertz, Tae ho Lee, and Byeong-Soo Bae. Effect of photoinitiator on photopolymerization of inorganic-organic hybrid polymers (ormocer). *Journal of Polymer Science: Part B: Polymer Physics*, 42:1979–1986, 2004.

[49] David A. Kleinman. Laser and two-photon processes. *Physical Review*, 125, No. 1:87–88, 1962.

[50] N. Konforti, E. Marom, and S.-T. Wu. Phas-only modulation with twisted nematic liquid-crystal spatial light modulators. *Optics Letters*, 13, No. 3:251–253, 1988.

[51] Stephen T. Kowel, Philipp Kornreich, and Akbar Nouhi. Adaptive spherical lens. *Applied Optics*, 23, No. 16:2774–2777, 1984.

[52] Stephen M. Kuebler and et al. Optimizing two-photon initiators and exposure conditions for three-dimensional lithographic microfabrication. *Journal of Photopolymer Science and Technology*, 14, No. 4:657–668, 2001.

[53] Ju Young Lee, Byung Hee Hong, Woo Youn Kim, Seung Kyu Min, Yukyung Kim, Mikhail V. Jouravlev, Ranojoy Bose, Keun Soo Kim, In-Chul Hwang, Laura J. Kaufman, Chee Wei Wong, Philip Kim, and Kwang S. Kim. Near-field focusing and magnification through self-assembled nanoscale spherical lenses. *Nature*, 460:498–501, 2009.

[54] Kwang-Sup Lee, Dong-Yol Yang, Sang Hu Park, and Ran Hee Kim. Recent developments in the use of two-photon polymerization in precise 2D and 3D microfabrications. *Polymers for Advanced Technologies*, 17:72–82, 2006.

[55] Kwang-Sup Lee, Dong-Yol Yang, Sang Hu Park, Tae Woo Lim, and Ran Hee Kim. Improvement of spatial resolution in two-photon stereolithography. In *Biophotonics, Nanophotonics and Metamaterials*. IEEE, 2006.

[56] Uriel Levy, David Menlovic, Zeev Zalevsky, Gal Shabtay, and Emanuel Marom. Iterative algorithm for determining optimal beam profiles in a three-dimensional space. *Applied Optics*, 38, No. 32:6732–6736, 1999.

[57] J. Liesener, M. Reicherter, T. Haist, and H.J. Tiziani. Multi-functional optical tweezers using computer-generated holograms. *Optics Communications*, 185:77–82, 2000.

[58] Adolf W. Lohmann, David Mendlovic, Zeev Zalevsky, and Gal Shabtay. The use of ewald's surfaces in triple correlation optics. *Optics Communications*, 144:170–172, 1997.

[59] Kanghua Lu and Bahaa E. A. Saleh. Theory and design of the liquid crystal tv as an optical spatial phase modulator. *Optical Engineering*, 29, No. 3:240–246, 1990.

[60] Michal Makowski, Maciej Sypek, Andrzej Kolodziejczyk, and Grzegorz Mikula. Three-plane phase-only computer hologram generated with iterative fresnel algorithm. *Optical Engineering*, 44:125805, 2005.

[61] Michal Makowski, Maciej Sypek, Andrzej Kolodziejczyk, Grzegorz Mikula, and Jaroslaw Suszek. Iterative design of multiplane holograms: experiments and applications. *Optical Engineering*, 46:045802, 2007.

[62] Andres Marquez, Claudio Iemmi, Ignacio Moreno, Juan Campos, and Maria J. Yzuel. Anamorphic and spatial frequency dependent phase modulation on liquid crystal display. optimization of the modulation diffraction efficiency. *Optics Express*, 13, No. 6:2111–2119, 2005.

[63] Shoji Maruo, Koji Ikuta, and Hayato Korogi. Force-controllable, optically driven micromachines fabricated by single-step two-photon microstereolithography. *Journal of Microelectromechanical Systems*, 12, No. 5:533–539, 2003.

[64] Shoji Maruo and Satoshi Kawata. Two-photon-absorbed near-infrared photopolymerization for three-dimensional microfabrication. *Journal of Microelectromechanical Systems*, 7, No. 4:411–415, 1998.

[65] Shoji Maruo, Osamu Nakamura, and Satoshi Kawata. Three-dimensional microfabriacation with two-photon-absorbed photopolymerization. *Optics Letters*, 22:132–134, 1997.

[66] Shoji Maruo, Akira Takaura, and Yohei Saito. Optically driven micropump with a twin spiral microrotor. *Optics Express*, 17, No. 21:18525–18532, 2009.

[67] Materials Research Society Symposia. *Single State Absorption Spectra of Novel Nonlinear Optical Materials*. CSA Illumina, 2000.

[68] Roy M. Matic. Blazed phase liquid crystal beam steering. In *Laser Beam Propagation and Control*, 1994.

[69] Daniel R. McAdams and Daniel G. Cole. Using a dwell-time increase to compensate for pixilation-limited diffraction efficiency in dmhl. In *Advanced Fabrication Technologies for Micro/Nano Optics and Photonics V*, Advanced Fabrication Technologies for Micro/Nano Optics and Photonics V. SPIE, 2012.

[70] F. B. McCormick, F. A. P. Tooley, T. J. Cloonan, J. M. Sasian, H. S. Hinton, Keith O. Mersereau, and A. Y. Feldblum. Optical interconnections using microlens arrays. *Optical and Quantum Electronics*, 24:S465–S477, 1992.

[71] Paul F. McManamon, Terry A. Dorschner, David L. Corkum, Larry J. Friedman, Douglas S. Hobbs, Michael Holz, Sergey Liberman, Huy Q. Nguyen, Daniel P. Resler, Richard P. Sharp, and Edward A. Watson. Optical phased array technology. In *Proceedings of IEEE*, volume 84, pages 268–298, 1996.

[72] Micro Resist Technology. Ormocomp absorption spectra. http://www.microresist.de/products/ormocers/pdf/pi_ormocomp_en_07062201_ls_neu.pdf.

[73] M. Miwa, S. Juodkazis, T. Kawakami, S. Matsuo, and H. Misawa. Femtosecond two-photon stereo-lithography. *Applied Physics A*, 73:561–566, 2001.

[74] Ignacio Moreno, Jeffrey A. Davis, Kevin G. D'Nelly, and David B. Allison. Transmission and phase measurement for polarization eigenvectors in twisted-nematic liquid crystal spatial light modulators. *Optical Engineering*, 37, No. 11:3048–3052, 1998.

[75] Richard A. Muller and Andrew Buffington. Real-time correction of atmospherically degraded telescope images through image sharpening. *Journal of the Optical Society of America*, 64, No. 9:1200–1210, 1974.

[76] Le Huong Nguyen, Martin Straub, and Min Gu. Acrylate-based photopolymer for two-photon microfabrication and photonic applications. *Advanced Functional Materials*, 15, No. 2:209–216, 2005.

[77] Robert J. Noll. Zernike polynomials and atmospheric turbulence. *Journal of the Optical Society of America*, 66, No. 3:207–211, 1976.

[78] Samuel Obi, Michael T. Gale, Christiane Gimkiewicz, and Susanne Westenhofer. Replicated optical MEMS in sol-gel materials. *IEEE Journal of Selected Topics in Quantum Electronics*, 10, No. 3:440–444, 2004.

[79] George Odian. *Principles of Polymerization*. John Wiley and Sons, Inc., 1991.

[80] Taisuke Ota, Satoshi Kawata, Tadao Sugiura, Martin J. Booth, Mark A. A. Neil, Rimas Juskaitis, and Tony Wilson. Dynamic axial-position control of a laser-trapped particle by wave-front modification. *Optics Letters*, 28, No. 6:465–467, 2003.

[81] Sang Hu Park, Tae Woo Lim, Dong-Yol Yang, Nam Chul Cho, and Kwang-Sup Lee. Fabrication of a bunch of sub-30-nm nanofibers inside microchannels using photopolymerization via a long exposure technique. *Applied Physics Letters*, 89:173133, 2006.

[82] Martin Persson, David Engstrom, Anders Frank, Jan Backsten, Jorgen Bengtsson, and Mattias Goksor. Minimizing intensity fluctuations in dynamic holographic optical tweezers by restricted phase change. *Optics Express*, 18, No. 11:11250–11263, 2010.

[83] J. L. Pezzaniti and R. A. Chipman. Phase-only modulation of a twisted nematic liquid-crystal tv by use of the eigenpolarization states. *Optics Letters*, 18, No. 18:1567–1569, 1993.

[84] Polymer Science Learning Center. Polyacrylates. http://pslc.ws/macrog/acrylate.htm.

[85] Rodrigo Ponce, Alfonso Serrano-Heredia, and Victor M. Arrizon. Simplified optimum phase-only configuration for a tnlcd. In Khan M. Iftekharuddin and Abdul Ahad S. Awwal, editors, *Photonic Devices and Algorithms for Computing IV*, volume 5556, pages 206–213. SPIE, 2004.

[86] Alexander Rohrbach and Ernst H. K. Stelzer. Trapping forces, force constants, and potential depths for dielectric spheres in the presence of spherical aberrations. *Applied Optics*, 41, No. 13:2494–2507, 2002.

[87] Yael Roichman, Alex Waldron, Emily Gardel, and David G. Grier. Optical traps with geometric aberrations. *Applied Optics*, 45, No. 15:3425–3429, 2006.

[88] Mariacristina Rumi and et al. Structure-property relationships for two-photon absorbing chromophores: Bis-donor diphenylpolyne and bis(styryl)benzene derviatives. *J. Am. Chem. Soc.*, 122:9500–9510, 2000.

[89] Christian H. J. Schmitz, Joachim P. Spatz, and Jennifer E. Curtis. High-precision steering of multiple holographic optical traps. *Optics Express*, 13, No. 21:8678–8685, 2005.

[90] S. Serati and J. Stockley. Advanced liquid crystal on silicon optical phased arrays. In *Proc. IEEE Aerospace Conf.*, 2002.

[91] J. Serbin and et al. Femtosecond laser-induced two-photon polymerization of inorganic-organic hybrid materials for applications in photonics. *Optics Letters*, 28, No. 5:301–303, 2003.

[92] Gal Shabtay. Three-dimensional beam forming and ewald's surfaces. *Optics Communications*, 226:33–37, 2003.

[93] G. Sinclair, P. Jordan, J. Leach, M. J. Padgett, and J. Cooper. Defining the trapping limits of holographical optical tweezers. *Journal of Modern Optics*, 51, No. 3:409–414, 2004.

[94] Colin Soutar and Kanghua Lu. Determination of the physical properties of an artbitrary twisted-nematic liquid crystal cell. *Optical Engineering*, 33, No. 8:2704–2712, 1994.

[95] C. Sun, N. Fang, D. M. Wu, and X. Zhang. Projection micro-stereolithography using digital micro-mirror dynamic mask. *Sensors and Actuators A*, 121:113–120, 2005.

[96] Hong-Bo Sun, Takeshi Kawakami, Ying Xu, Jia-Yu Ye, Shigeki Matuso, Hiroaki Misawa, Masafumi Miwa, and Reizo Kaneko. Real three-dimensional microstructures fabricated by photopolymerization of resins through two-photon absorption. *Optics Letters*, 25, No. 15:1110–1112, 2000.

[97] Hong-Bo Sun, Kenji Takada, Moon-Soo Kim, Kwang-Sup Lee, and Satoshi Kawata. Scaling laws of voxels in two-photon photopolymerization nanofabrication. *Applied Physics Letters*, 83, No. 6:1104–1106, 2003.

[98] G. J. Swanson. Binary optics technology: The theory and design of multi-level diffractive optical elements. Technical report, Lincoln Laboratory - MIT, 1989.

[99] Edward A. Sziklas and A. E. Siegman. Mode calculations in unstable resonators with flowing saturable gain. 2: Fast fourier transform method. *Applied Optics*, 14, No. 8:1874–1889, 1975.

[100] Hidetomo Takahashi, Satoshi Hasegawa, and Yoshio Hayasaki. Holographic femtosecond laser processing using optimal-rotation-angle method with compensation of spatial frequency response of liquid crystal spatial light modulator. *Applied Optics*, Vo. 46, No. 23:5917–5923, 2007.

[101] Hidetomo Takahashi, Satoshi Hasegawa, Akihiro Takita, and Yoshio Hayasaki. Sparse-exposure technique in holographic two-photon polymerization. *Optics Express*, 16, No. 21:16592–16599, 2008.

[102] Tomokazu Tanaka, Hong-Bo Sun, and Satoshi Kawata. Rapid sub-diffraction-limit laser micro/nanoprocessing in a threshold material system. *Applied Physics Letters*, 80, No. 2:312–314, 2002.

[103] Eirini Theofanidou, Laurence Wilson, William J. Hossack, and Jochen Arlt. Spherical aberration correction for optical tweezers. *Optics Communications*, 236:145–150, 2004.

[104] Charles M. Titus, John Pouch, Hung Nguyen, Felix Miranda, and Philip J. Bos. Diffraction efficiency of thin film holographic beam steering devices. Technical report, NASA, 2003.

[105] V. M. Treushnikov, N. V. Frolova, and A. V. Oleinik. Spectrophotometric analysis of photochemical reactions in a polymer-azide system. *Zhurnal Prikladnoi Spectroskopii*, 34, No. 5:879–884, 1981.

[106] Xu Wang, Daniel Wilson, Richard Muller, Paul Maker, and Demetri Psaltis. Liquid-crystal blazed-grating beam deflector. *Applied Optics*, 39, No. 35:6545–6555, 2000.

[107] Graeme Whyte and Johannes Courtial. Experimental demonstration of holographic three-dimensional light shaping using a gerchberg-saxton algorithm. *New Journal of Physics*, 7:117, 2005.

[108] Kirt D. Wulff, Daniel G. Cole, Robert L. Clark, Roberto DiLeonardo, Jonathan Leach, Jon Cooper, Graham Gibson, and Miles J. Padgett. Aberration correction in holographic optical tweezers. *Optics Express*, 14, No. 9:4170–4175, 2006.

[109] Jun Xia and Hanchun Yin. Three-dimensional light modulation using phase-only spatial light modulator. *Optical Engineering*, 48:020502, 2009.

[110] Zheng Zhang, Guowen Lu, and Francis T. S. Yu. Simple method for measuring phase modulation in liquid crystal televisions. *Optical Engineering*, 33, No. 9:3018–3022, 1994.

[111] Susanne Zwick, Tobias Haist, Michael Warber, and Wolfgang Osten. Dynamic holography using pixelated light modulators. *Applied Optics*, 49, No. 25:F47–F58, 2010.